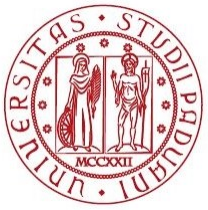

UNIVERSITÀ DEGLI STUDI DI PADOVA

Dipartimento di Ingegneria Industriale

Corso di Laurea Magistrale in Ingegneria Energetica

Numerical Investigation of the Effect of Passive Vortex Generators for Wind Turbine Airfoils Applications

Relatore
Prof. Ernesto Benini

Laureando
Andrea Franco
Matr.1099714

Anno Accademico 2018/2019

Abstract

As the transition towards a more sustainable energy production is becoming increasingly more important, the interest in renewable sources of energy such as wind power increases, due to its potential of satisfying large power demands. Wind energy companies are, therefore, seeking improvements in the amount of energy generated from wind turbines, together with solutions to improve the efficiency of such machines. One possible solution to improve the aerodynamic efficiency of wind turbines is to consider the application of flow control devices on the blades' surface, to help in preventing undesired flow conditions that would otherwise occur. A category of devices that achieve such purposes comprises passive flow control techniques. Among the different solutions proposed for passive flow control, the use of Vortex Generators (VGs) has seen a growing interest for their easy installation and efficiency improvements obtained.
For this reason, in this thesis, the effects on aerodynamic performance of VGs placed on a wind turbine's blade sections are investigated. This is achieved through Computational Fluid Dynamics (CFD) simulations using the SU2 collections of tools for partial differential equations. The aim of this thesis is to explore the capabilities of the SU2 incompressible solver in resolving the flow features of different VGs configurations placed on two reconstructed blade sections. The blade sections considered are the FFA-W3-241 and the FFA-W3-301. The configurations explored are related to VGs of two different heights and at two streamwise locations, as well as the Smooth configuration (e.g without VGs).
First, a number of test cases is run to determine the most suitable CFD-configurations set-up for the final simulations. With the information obtained, the cases of interest are simulated, focusing on near-stall and stall-developed flow conditions. From these conditions, the effect of vortex generators on the flow field is clearly evaluable.
The results are first compared with the corresponding experimental reference data, showing a noticeable deviation of the simulations' values from the experiments. In addition to this, the results are also analyzed from a qualitative perspective, to ascertain how the difference of the simulations from the experimental values influences the data obtained. The analysis of the results by means of airfoil surface data, such as pressure coefficient and skin friction values, demonstrates how flow separation is effectively prevented, as would be expected through the presence of VGs in the flow field. The vortices influence on the flow field, investigated by displaying the vorticity magnitude and the velocity components on planes perpendicular to the airfoil streamwise direction, exhibit the typical flow patterns found in related reference sources. A 2D boundary layer investigation clearly presents the characteristic velocity and vorticity magnitude profiles' shape, with an identifiable inflection of these profile curves in the streamwise direction, due to the application of VGs. A final three dimensional evaluation highlights how the vortices can be identified using the state-of-the-art techniques for flow visualization. A skin friction flow visualization shows, however, how further considerations from a three dimensional point of view would not be possible, since the actual results are far from being accurate enough to display such information. In light of this, a detailed vortices structure analysis will not be addressed.
From this evaluation, it can be stated that the relevant flow modifications introduced by the VGs presence are captured by the simulations, although further testing and validation is needed to improve the results obtained. Nevertheless, the simulated data can be regarded to be significative enough for modeling purposes.

Riassunto Esteso

A causa della crescente necessità di produzione di energia da fonti rinnovabili, le realizzazioni di impianti eolici hanno visto un aumentato interesse nell'ultimo decennio determinato dalla possibilità di produrre notevoli quantità di energia, anche attraverso la costruzione di impianti off-shore. Le aziende che producono turbine eoliche ricercano pertanto soluzioni per aumentare la produzione di energia, insieme a strategie per migliorare l'efficienza di questa tipologia di macchine. Una delle possibili applicazioni che permettono un aumento dell'efficienza aerodinamica delle pale di queste turbine prevede l'utilizzo di strumenti per il controllo del flusso d'aria, che aiutano a prevenire condizioni di funzionamento indesiderate che potrebbero verificarsi. Una delle categorie tra quelle identificabili per queste strategie di controllo è quella comprendente soluzioni di controllo passivo del flusso. Tra queste, gli strumenti più utilizzati correntemente sono i Generatori di Vortici (Vortex Generators, VGs), a causa della loro facilità di installazione e dei miglioramenti in termini di efficienza che comportano.

I VGs sono costituiti da piccole sottili lame rigide, di varie forme geometriche, comunemente triangolari o rettangolari, che vengono applicate su strisce metalliche, perpendicolarmente alle stesse. Queste strisce metalliche sono poi apposte in diverse posizioni sulle pale eoliche, lungo la direzione principale del flusso e generalmente nelle zone più vicine alla radice della pala, dove le condizioni di flusso risultano facilmente in stallo aerodinamico.

In questa tesi vengono investigati gli effetti dell'applicazione di VGs sull'efficienza aerodinamica di sezioni di pale di turbine eoliche, attraverso simulazioni di fluidodinamica computazionale, utilizzando le librerie SU2 per la risoluzione di problemi alle derivate parziali di natura fluidodinamica. Lo scopo principale di questo elaborato è l'esplorazione delle possibilità e capacità delle librerie SU2 di definire le caratteristiche del flusso d'aria di diverse configurazioni di VGs, posizionate sulla superficie di due sezioni differenti di pale eoliche. Queste sezioni sono riprodotte con le modalità riportate nella pubblicazione scientifica di riferimento, che ne illustra i relativi risultati sperimentali. Le sezioni di pala considerate sono relative ai profili aerodinamici FFA-W3-241 e FFA-W3-301. Le configurazioni investigate sono relative a due altezze dei VGs e a due posizioni sulla superficie delle sezioni, lungo la direzione principale del flusso. Oltre a queste, viene considerata anche la configurazione senza VG, per poter valutare successivamente l'effetto dei VG stessi rispetto a condizioni di flusso non disturbate dalla loro presenza.

Nel Capitolo 1 una breve introduzione all'argomento della tesi spiega le motivazioni e gli obbiettivi delle successive analisi condotte.

Nel Capitolo 2 è riportata una descrizione degli aspetti teorici necessari per la comprensione dei risultati ottenuti dalle simulazioni.

Nel Capitolo 3 vengono presentati i risultati principali ottenuti finora in ambito sperimentale ed accademico, discutendo i principali aspetti e caratteristiche fisiche del flusso influenzato dai VGs.

Nel Capitolo 4 vengono descritti i test case realizzati per determinare la configurazione dei parametri che permettono di ottenere i risultati migliori dalle simulazioni.

Nel Capitolo 5 viene riportata la metodologia riguardante la creazione dei modelli tridimensionali da simulare e l'impostazione delle simulazioni da realizzare con le librerie di SU2. Le simulazioni finali vengono impostate tenendo conto solo di condizioni di flusso vicine allo stallo, o in condizioni di stallo sviluppato. Tali condizioni

di flusso infatti permettono di verificare chiaramente l'influenza dei VGs rispetto alle condizioni di flusso indisturbate.
Nel Capitolo 6 si analizzano infine i risultati ottenuti, confrontandoli con i dati sperimentali di riferimento. I risultati ottenuti dalle simulazioni evidenziano uno scostamento considerevole dai dati sperimentali. Per questo motivo, si procede all'analisi delle simulazioni da un punto di vista qualitativo, per verificare quanto lo scostamento rilevato influenzi la significatività dei risultati. Utilizzando i dati estratti dalla superficie delle sezioni simulate, ovvero coefficiente di pressione e di sforzo d'attrito, si rileva come la separazione del flusso, che si verificherebbe per i casi simulati in assenza di VGs, sia effettivamente evitata come ci si aspetterebbe. Analizzando il modulo della vorticità insieme a ciascuna componente di velocità su piani perpendicolari alla superficie delle sezioni di pala investigate, si nota che queste quantità mostrano gli andamenti tipici dovuti alla presenza di vorticosità nello strato limite, come riportato nelle fonti bibliografiche reperite. Per quanto riguarda lo strato limite, i profili di velocità e del modulo della vorticità presentano gli andamenti attesi. I profili di velocità evidenziano l'inflessione tipica dei profili a valle dei VGs, che, a causa della loro presenza, di fatto costituiscono un ostacolo al flusso. I profili del modulo della vorticità illustrano il decadimento della vorticosità introdotta nel flusso dai VGs. La valutazione delle caratteristiche tridimensionali del flusso, mediante tecniche di visualizzazione apposite, mostra come sia possibile catturare la forma e l'evoluzione del tubo di flusso vorticoso a valle dei VGs. Invece, per quanto riguarda la visualizzazione delle linee dello sforzo d'attrito sulla superficie della sezione considerata, si vede come non sia possibile identificare gli andamenti caratteristici di queste linee. Questo indica che ulteriori valutazioni ed analisi tridimensionali non possono essere prese in considerazione, dal momento che i risultati comunque presentano una discrepanza non trascurabile rispetto ai dati sperimentali, tenendo conto inoltre dei modelli di turbolenza non accurati abbastanza per tali scopi. E' comunque possibile affermare che le modifiche principali introdotte dai VGs al flusso d'aria, vicino alla superficie della pala, sono identificabili nei risultati, anche se ulteriori verifiche e simulazioni sono ritenute necessarie per un loro miglioramento. Nonostante ciò, si ritiene che i dati ottenuti dalle simulazioni possano comunque essere utilizzati per la creazione iniziale di modelli che riproducano l'effetto dei VGs sul flusso indisturbato, senza dover ricorrere a simulazioni di fluidodinamica computazionale che presentano tempi notevolmente lunghi.

Acknowledgements

First of all, I would like to express my sincere gratitude to Huseyin Özdemir for giving me the opportunity to do an internship at the Energy research Centre of the Netherlands (ECN). The period spent working under his supervision was a very valuable working experience, one that I will always remember, for both my personal and professional growth.
I would also like to thank all the people and colleagues I met at ECN, with whom I had the chance to interact, for all the friendly memories. The multicultural working environment that I was exposed to at ECN allowed me to broaden my horizons, proving it to be an interesting learning experience as well.
A special thank to Vanessa, for her help with LaTeX and LyX during the writing of this thesis.
Finally, I must give my gratitude to my parents and family for the support given in the pursue of this experience abroad.

Andrea

Contents

List of Figures

List of Tables

Chapter 1

Introduction

The renewable energy sector is expected to grow fast in the next decades, due to technological cost reduction and specific policies to promote and support a transition towards clean and sustainable energy production. According to [1], energy production by renewable sources has risen at a rate of 2.8% per year in 2017.
Among these sources, the most prominent are solar and wind energy, as a result of the increasing support of more countries and the increased cost effectiveness over time.
In Figure 1.1, the growing importance of wind energy can in fact be observed: it is expected to reach an installed capacity of 2.5 trillion kWh in 2040.
Moreover, according to the International Energy Agency (IEA), the percentage of electricity generated from wind energy will increase up to 18% around 2050. For this reason, during the next years wind power production will most likely experience a continuos development.

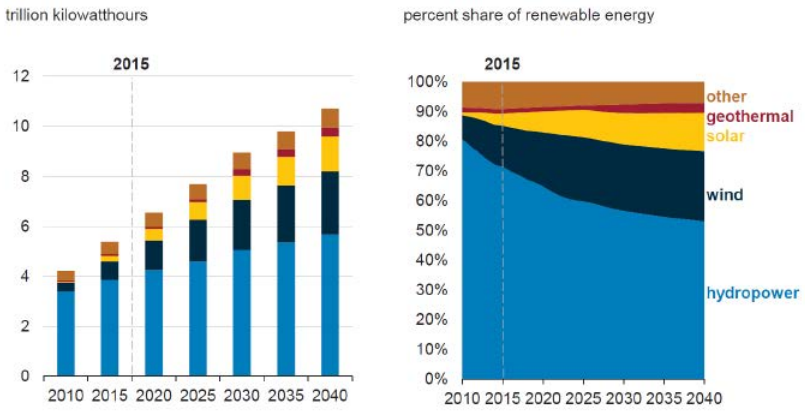

Figure 1.1: World net electricity generated from renewable sources [1]

Following the growth lines of the past years, larger turbines can be expected to be manufactured in the future, expecially regarding offshore installations. As a matter of fact, from the mid-eighties an increase in the dimensions of wind turbines installations is noticeable; from an average capacity of the installations of 30 kW, with turbines having a rotor diameter of 15 m, in 2017 the Enercon E-126 turbine installation had already reached a capacity of 7.5 MW, with a diameter of 127 m.

In addition to that, not only larger rotor diameters could be predicted, but also taller wind turbines. Due to the growth of the offshore sector, it will be possible to reach greater heights and thus exploit the increased wind speeds that follow: this would be achieved without incurring in possible environmental impacts issues related to the otherwise excessive dimensions for common onshore installations. Being the power produced given by a cubic relation of the wind speed, together with the considerations about a large rotor size, the expected power output will therefore be considerable. From Figure 1.2, this increase in dimensions and installed power over the years can be observed.

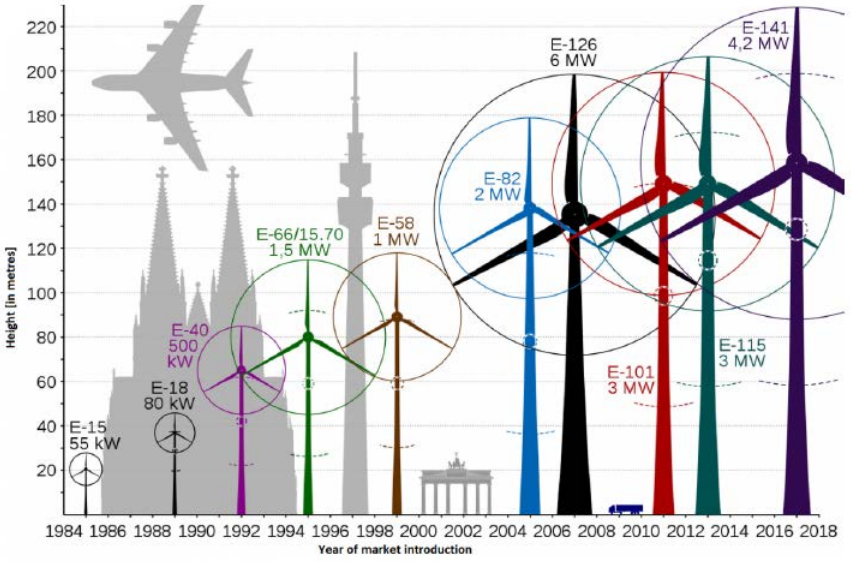

Figure 1.2: Wind turbines size evolution over decades [2]

Even if larger rotors and taller turbines would be the most probable wind turbine manufacturing developing sectors, a report from Fraunhofer Institute for Wind Energy and Energy System Technology (IWES) indicates that as the blade length, width and thickness will possibly increase, so will weight and related costs, proportionally with the cube of the blade length. Taking this into consideration, wind turbines companies are advancing also with regard to design optimization strategies and blade quality, to tackle the production challenges of the future [24].
From this perspective, various solutions are being evaluated, of which increasing the aerodynamic performance of the blades is with no doubt one that has seen a constant interest throughout the years [21],[2].

1.1 Thesis Motivation

This thesis therefore investigates the effectiveness of a class of flow control devices to increase aerodynamic performance of wind turbines blades.
Flow control techniques could be divided in two main categories [25], passive and active flow control techniques.
Passive flow control techniques do not need an energy input since the desired control is achieved through compact geometrical modifications in desired locations on the blade, whereas active flow control techniques require an extra energy input, and as a consequence of this they need regular maintenance.
Among all the possible alternatives for these devices, the use of passive flow control ones is one of the most promising, and it already proved to be effective in the aeronautical sector, reason for which wind turbine applications were soon considered.
A significant amount of passive flow control techniques has been developed in the aeronautical sector, including Vortex Trapping Airfoils, Passive Aspiration, Fences, Trailing Edge Effectors, Riblets, Porous Airfoils, Winglets, and Vortex Generators, which can be seen in Figure 1.3:

- Vortex Trapping Airfoils sections are constructed with the use of a vortex cell that aids in mantaining a formed vortex trapped. This concept is difficult to manufacture since the vortex has to be mantained as close as possible to the airfoil surface, in order to improve the lift coefficient. However, the drag coefficient will increase as a consequence of the vortex cell, so this solution can be used when it does not penalize significantly the lift to drag ratio [26].

- Passive Aspiration uses passive blowing as vortex generator jets: these jets pass through openings on the airfoil surface that create a primary vortical structure in the chordwise direction. This solution excludes the extra drag formation present in mechanical devices applied to the airfoil surface [4].

- Fences are used to control the radial flow movement that could occur at the hub of a wind turbine blade under stalled-flow conditions, which could propagate throughout the blade span. They are mostly useful when strong spanwise pressure gradients are experienced during operational conditions [5].

- Trailing Edge Effectors modify the flow at the trailing edge of the airfoil, increasing the camber, hence the lift. Among these devices, the most known are Gurney flaps [6].

- Riblets are cavities on the blade surface, created in the streamwise direction. They reduce turbulent skin friction, thus reducing the total drag coefficient [7].

- Porous Airfoils are manufactured as an airfoil surface covered with small holes, through which air is injected, creating small vortices in the boundary layer. Overall, the effect of all these vortical structures is to globally enhance the lift coefficient while decreasing also the drag coefficient [8].

- Winglets are used at the blade tip to reduce the tip flow between pressure side and suction side of the airfoil profile. These devices help to reduce the induced drag in this blade location [27].

- Vortex Generators are simple solid geometries placed perpendicular to the blade surface, at a given chordwise position and at a given angle with respect to the incoming flow. These devices help in reducing flow separation, but at low angles of attack they show an undesirable drag increase. Nevertheless, this is one of the most known and used technique in preventing flow separation and increasing aerodynamic performance that has been studied for more than 30 years [28].

For this reason, in this thesis the effect of vortex generators will be investigated through numerical simulations using the SU2's open source collection of tools for partial differential equations, in order to ascertain their influence in the flow field [29]. This could subsequently allow future modelling approaches to characterize the flow field and the overall performance enhancements for wind turbines blades.

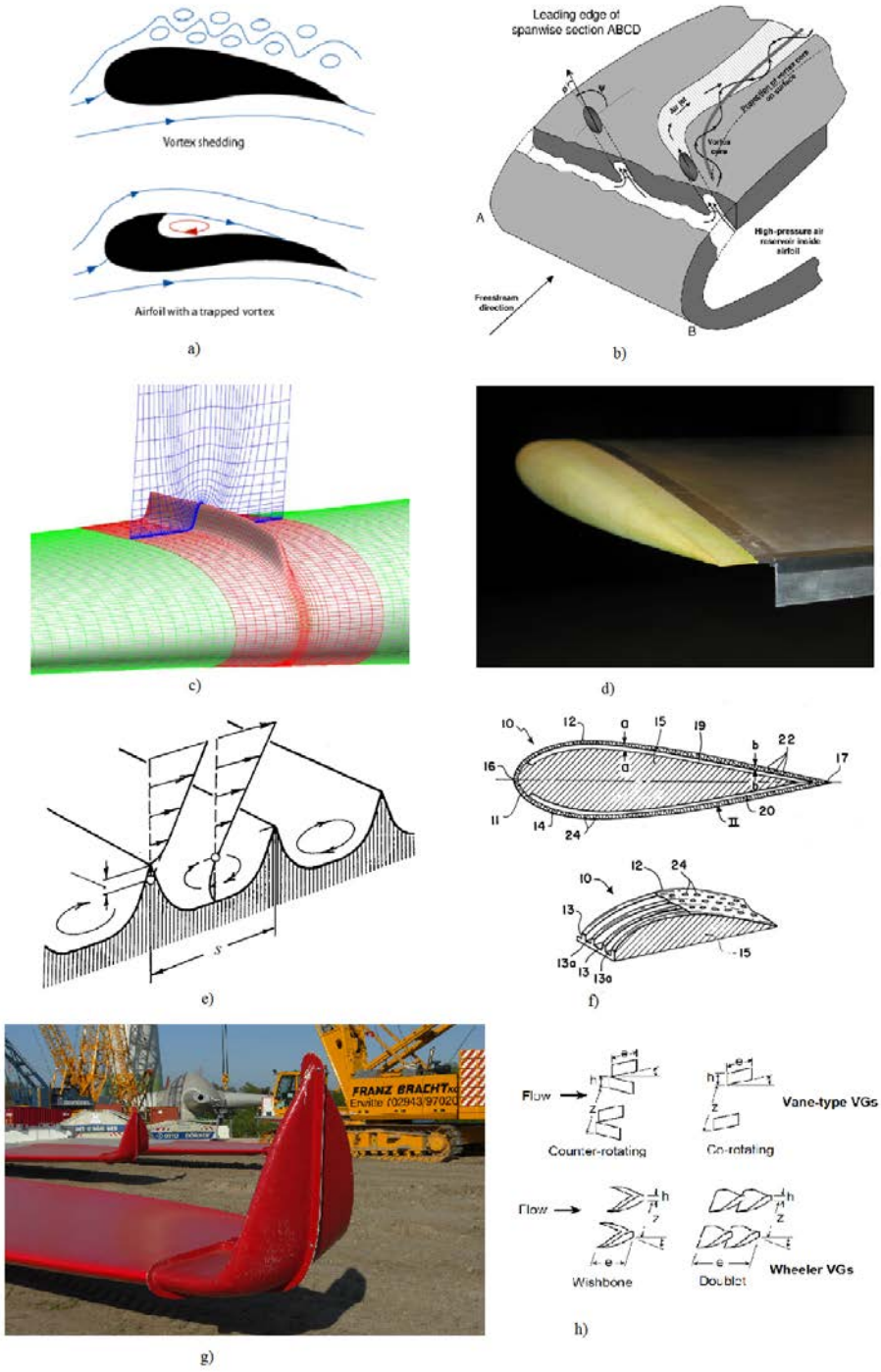

Figure 1.3: Different passive flow control techniques. a) Vortex Trapping Airfoil [3]. b) Passive Aspiration [4]. c) Fences [5]. d) Gurney Flaps [6]. e)Riblets [7]. f) Porous Airfoil [8]. g) Winglets [9]. h) Vortex Generators [10].

1.2 Research Questions

Given the information described in the previous sections, the research questions for this thesis are proposed as follows:

1. Is the current SU2's incompressible solver implementation able to reproduce vortex generators' experimental results up to a reasonable degree of accuracy?
2. Are the results obtained from the simulations qualitatively describing the relevant flow modifications?
3. Is a 2D boundary layer analysis showing the expected essential qualitative aspects?
4. Is a 3D qualitative flow visualization analysis displaying the important flow features?

1.3 Thesis Outline

This thesis explores the potentiality of the current SU2's incompressible solver in solving different vortex-generators-related flow fields configurations. These configurations are reproduced using the wind tunnel results introduced in [23], where experimental pressure data of wind turbine blades sections with and without vortex generators are reported. These data are compared with the data obtained from the numerical simulations performed, and the effectiveness of the solver is assessed. Complementing that, additional flow analysis and visualization techniques are considered, examining the results collected.
The present work begins with a brief presentation of the relevant theoretical background in Chapter 2, to allow a better understanding of the results obtained. In Chapter 3 the vortex generators are presented; the flow modifications that such devices introduce are explained in more detail, and an outline of the current research and applications, in particular for wind turbines, is provided. Chapter 4 will investigate the ability of SU2 in solving standard flow configurations, considering the FFA-W3-241 wing section of [23] without vortex generators. The results are compared with the experimental ones; this chapter represents the test case section of the thesis, based on which the final simulations setup will be decided. In Chapter 5 the methodology followed in obtaining the final results is described; the pre-processing, simulations set-up and post processing is also reported. In Chapter 6, the results are presented and the research questions are discussed. Finally the conclusions are outlined in Chapter 7, providing an answer to the proposed research questions.
The appendices are presented at the end of the thesis. They contain the reference equations of the theoretical background chapter, together with a detailed description of the computational grids creation-process and the relevant programming scripts used in analyzing the data collected.

Chapter 2

Background Theory

In this chapter the background theory necessary to understand the separated-flow phenomenon is presented, because the main advantage of the use of vortex generators is in fact delaying flow separation.
A brief introduction of general aerodynamics concepts related to wind turbines is presented first, introducing the importance of boundary layers for wind turbine performance.
A simple introduction about the boundary layer model and its equations follows.
With the equations provided, the qualitative behaviour of boundary layer flows is then emphasysed; this will permit to interpret the final results of this work. Related to this section, an integral boundary layer overview about the main equations is also reported next, so that overall properties of this flows could be evaluated.
At the end of this chapter, the flow separation phenomenon is described, using the knowledge obtained in the previous sections; in this section the favourable effects of turbulence are highlighted, suggesting how they could be exploited in order to prevent flow separation.

2.1 Aerodynamics Introduction

The Wind turbines aim is to transform the kinetic energy from the wind resource and convert it to mechanical energy and subsequently to electric energy.
The appearance of wind turbines resembles the one of propellers, with a number of blades connected to a rotating shaft, which can be placed in the horizontal direction (Horizontal Axis Wind Turbine) or in the vertical direction (Vertical Axis Wind Turbine).
In the early 20th century, the performance successes obtained in the propellers field for aerodynamic applications showed that exploiting the lift aerodynamic force, instead of the drag force, leads to increased efficiency during their functioning. The aerodynamics knowledge obtained during that time allowed to improve the wind turbines design concepts and performance throughout the 20th century [11].
Wind turbine manufacturers began to use airfoils developed with aircraft applications in mind, but these were not optimized for high angles of attack, being this a working condition that is frequently experienced by wind turbines during their operation period. For this reason the blades of a wind turbine are currently manufactured from 2D dedicated airfoil profiles, extruding the blades final shape considering different profiles at different spanwise positions, given a chord and a twist distribution.
During the design process of a wind turbine, power production is an essential requirement to satisfy.
Equation (2.1) allows a simple evaluation of the power produced by a wind turbine,

$$P = 1/2\dot{m}U_{\infty}^2 = 1/2\rho A U_{\infty}^3 \tag{2.1}$$

where $\dot{m}$ is the mass flow, ρ is the air density, A is the rotor swept area and U_{∞} the freestream wind velocity.

Therefore, it can be seen that for a given wind velocity U_∞, increasing the area A swept by the rotor would increase the power output generated. This area is given by $A = \pi L^2$, with L as the blade length, so in order to increase the area L has to increase.
From this simple evaluation, it is possible to comprehend why technological developments regarding the radial extension L of the blades were soon been considered by manufacturers.
For the reason described above, modern blades are usually long structures, making it possible to assume that the local velocity direction will be predominantly streamwise, with negligible spanwise component.
This assumption allows in the design stage to treat the flow as two dimensional (2D), so that the corresponding airfoil theory's well-known-concepts and models could be used, together with its flow characterization as in Figure 2.1.
It should be pointed out that to consider a true 2D flow, an infinite span wing should be created from a constant chord and shape airfoil profiles. In reality, chord and twist change along the span of the blade and the blade itself is of finite length, hence 2D flow conditions cannot represent the real flow development. In order to implement successfully the 2D theory, the trailing vortices behind the wing should be considered and the angle of attack corrected accordingly.

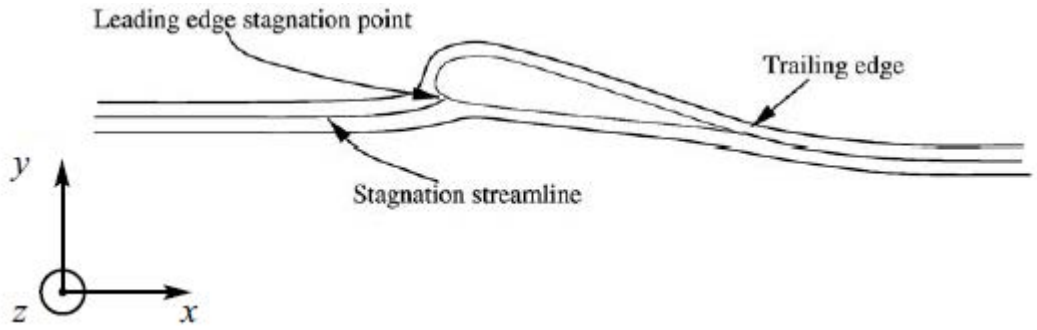

Figure 2.1: 2D airfoil profile with generic streamlines [11]

From the 2D airfoil theory, when considering an airfoil shape in a uniform flow, the reacting force from the flow experienced by the airfoil is usually decomposed, with respect to the freestream velocity, in a component perpendicular to it (Lift force L) and a component parallel to it (Drag force D).
From a physical point of view, lift is caused by the pressure difference between the upper side and the lower side of the airfoil. This pressure difference is the consequence of the streamlines curvature induced by the presence of the airfoil in the flow field, that cause a local pressure gradient.
In aircraft applications, the lift force is the force that is responsible for lifting mass off the ground in order to prevail over gravity, whereas the drag force is the force responsible for the decrease in fluid velocity relative to the airfoil in the fluid path.
In wind turbine applications, the decomposition of lift and drag forces on the plane of rotation of the blade, at a given spanwise position and multiplied by it, results in the contribution to the overall torque that ensures the desired power output. With these definitions, the lift and drag force can be made adimensional as follows, introducing the lift coefficient C_L and the drag coefficient C_D:

$$C_L = \frac{L}{1/2\rho U_\infty^2 c} \quad C_D = \frac{D}{1/2\rho U_\infty^2 c} \tag{2.2}$$

In Equation (2.2), c is the chord distance on the chord line.
In Figure 2.2, the definition of the chord line is displayed: this is the ideal line that connects the leading edge to the trailing edge of an airfoil; in the same figure, α is defined as the angle of attack measured between the chord line and the free stream direction.

Therefore, it is important to maximize the ratio C_L/C_D in aerodynamic applications.
For aircrafts, this maximizes the lifting action off the ground. For wind turbines, the influence of lift and drag forces on the power production can be evinced from Blade Element Momentum (BEM) theory; this is a successful 2D model used in the design and manufacturing process to determine the loads on the blade and the power output.
Considering the Equation (2.3) for the torque contribution dM at a given spanwise position r and for a given number of blades B:

$$dM = Bp_T r dr \tag{2.3}$$

where $p_T = Lsin(\phi) - Dcos(\phi)$ and ϕ is the relative flow angle, it is then clearly displayed that increasing the lift force, while mantaining a low drag force, increases the contribution dM of the given blade section to the total torque and power production.

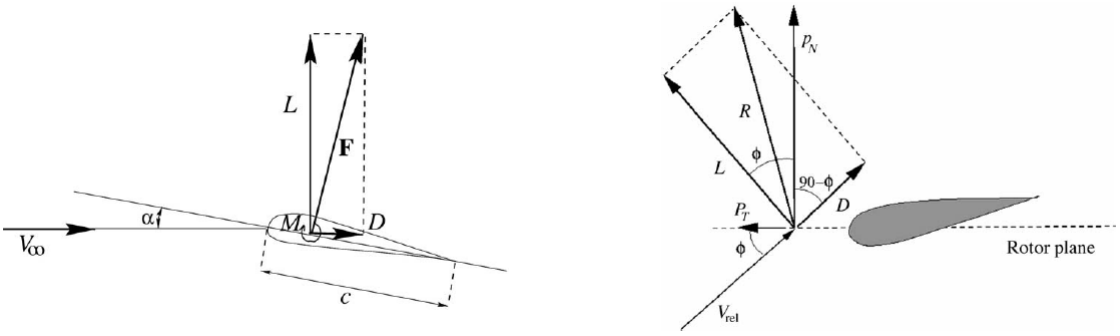

Figure 2.2: Lift and Drag definition [11]

The lift and drag coefficients are generally functions of the angle of attack α, the Reynolds number Re and the Mach number Ma. For wind turbine applications, the two coefficients can be considered indipendent of the Mach number, since tipically flow conditions are characterized by $Ma < 0.3$, that is to say subsonic flow conditions.

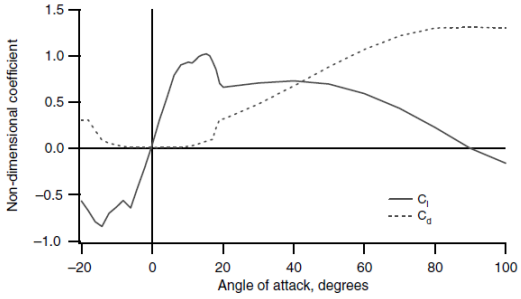

Figure 2.3: Lift and Drag coefficients for the S809 airfoil [12]

In Figure 2.3 the typical lift coefficient and drag coefficient curves are displayed.
The behaviour of lift coefficient, as a function of α, is linear up to a maximum for a certain value of α. After that, the airfoil experiences aerodynamic stall, a condition where airfoil performance decrease abruptly. In this situation, the lift values decrease in a typical way for each airfoil considered.

Regarding the drag coefficient, it shows an almost constant value for α below the corresponding stall angle, and it increases rapidly in stall flow conditions.
The aerodynamic stall conditions are greatly influenced by the fluid flow phenomena occurring in the region close to the airfoil surface, named Boundary Layer following the studies of Prandtl.
According to Prandtl [30], this region is described as the region where the fluid adheres to the wall surface of a body immersed in a fluid, with a zero relative velocity between the fluid and this wall surface. Under the circumstances of a very small viscosity value and a short fluid path along the wall, the velocity in this model will reacquire its freestream value rapidly in a direction normal to the wall. The boundary layer is therefore the region where the viscous effects are not negligible, and where sharp changes of velocity occur even with small friction.
The boundary layer can be characterized by laminar or turbulent flow conditions. The first is related to the assumption of fluid layers sliding over each other, with few fluid particles interchange. The latter is described by layers that exchange a greater momentum between each other, inducing additional shearing forces.
Having introduced this information about the boundary layer, as mentioned before the stall condition is highly dependent on the way this flow region develops around a given airfoil geometry.
In fact, when the boundary layer separates from the upper side of the airfoil surface, stalled conditions manifest.
If separation occurs at the airfoil trailing edge and it does not develop much under greater angles of attack flow condition, a so called soft stall is observed. If early separation is seen, that is to say separation close to the leading edge, a strong stall is observed, with a considerable loss in lift coefficient.
The dependency from the Reynolds number Re for lift and drag coefficients is related closely to the laminar or turbulent boundary layer behaviour just described. In particular, it is associated to the chordwise position on the airfoil surface after which the boundary layer transitions to turbulent flow conditions.
The Reynolds number influence, in particular for the drag coefficient, is negligible when reaching a critical value Re_{CRIT}, after which the boundary layer becomes predominantly turbulent.
From this brief introduction to aerodynamics theory, the importance of boundary layers regarding airfoil performance has been pointed out. Hence, in the next sections boundary layers are treated more in detail.

2.2 Boundary Layer Equations

The reference equations for fluid motion are the Navier-Stokes equations. These equations are obtained from the laws of conservation of mass, momentum and energy. When they are coupled with relations for viscous stresses, heat conduction and the equations of state, they characterize the entire flow field.
For the purposes of the following explanation, 2D incompressible Navier-Stokes equations are introduced, allowing a more intuitive description of the boundary layer region.
In Equation (2.4), Equation (2.5) and Equation (2.6), u and v are the components of the velocity in the x and y directions respectively, p is the pressure, μ is the dynamic viscosity and ρ is the fluid density, so that $\nu = \mu/\rho\,[m^2/s]$ is the kinematic viscosity; the body forces will be neglected for simplicity, and a steady flow will be assumed. The following equations are respectively the continuity (Equation (2.4)), x-momentum (Equation (2.5)) and y-momentum (Equation (2.6)) equations.
In Figure 2.4 the corresponding coordinate system is displayed.

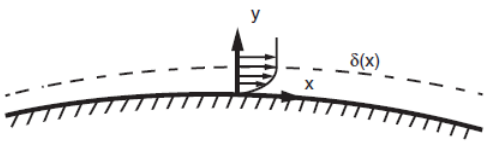

Figure 2.4: Coordinate system for the boundary layer equations [13]

The set of equations for fluid motion is therefore:

$$\frac{\partial u}{\partial x} + \frac{\partial v}{\partial y} = 0 \tag{2.4}$$

$$u\frac{\partial u}{\partial x} + v\frac{\partial u}{\partial y} = -\frac{1}{\rho}\frac{\partial p}{\partial x} + \nu\,(\frac{\partial^2 u}{\partial x^2} + \frac{\partial^2 u}{\partial y^2}) \tag{2.5}$$

$$u\frac{\partial v}{\partial x} + v\frac{\partial v}{\partial y} = -\frac{1}{\rho}\frac{\partial p}{\partial y} + \nu\,(\frac{\partial^2 v}{\partial x^2} + \frac{\partial^2 v}{\partial y^2}) \tag{2.6}$$

The assumptions behind Prandtl boundary layer model are that, for high Reynolds number, the viscous forces can be neglected in the whole flow field except for a thin region in the proximity of solid boundaries. This region is characterized by its own thickness, that is the boundary layer thickness, which becomes smaller as viscosity approaches a zero value. This boundary layer thickness is assumed to be very small compared to the characteristic length of the object (for airfoils it would be the chord length c), therefore written as in Equation (2.7):

$$\delta \ll c \tag{2.7}$$

Following the approach of Veldman [16], the boundary layer equations can now be derived with an analysis of the order of magnitude of the terms in Equation (2.4), Equation (2.5) and Equation (2.6), as explained in Section §A.1.
To determine the corresponding factors to nondimensionalize the 2D Navier-Stokes equations, first an order-of-magnitude analysis is performed.
Subsequently, it is possible to derive the nondimensional boundary layer equations, applying the nondimensionalization to the original variables with the estimated quantities obtained at the previous step.
The final step is to calculate the limit for large Reynolds numbers, since this is the assumption for the viscous forces to be neglected. In the end the final nondimensionalized boundary layer equations Equation (2.8), Equation (2.9) and Equation (2.10) are obtained:

$$\frac{\partial u'}{\partial x'} + \frac{\partial v'}{\partial y'} = 0 \tag{2.8}$$

$$u'\frac{\partial u'}{\partial x'} + v'\frac{\partial u'}{\partial y'} = -\frac{\partial p'}{\partial x'} + \frac{\partial^2 u'}{\partial y'^2} \tag{2.9}$$

$$0 = \frac{\partial p'}{\partial y'} \tag{2.10}$$

With this approach, information about the terms to neglect was obtained.
Simplifying the corresponding terms in the original Navier-Stokes equations (Equation (2.4), Equation (2.5) and Equation (2.6)), the boundary layer equations can be derived using the information obtained from the order of magnitude analysis and the nondimensionalization.

The equations for a 2D steady laminar boundary layer are shown in Equation (2.11), Equation (2.12) and Equation (2.13):

$$\frac{\partial u}{\partial x} + \frac{\partial v}{\partial y} = 0 \tag{2.11}$$

$$u\frac{\partial u}{\partial x} + v\frac{\partial u}{\partial y} = -\frac{1}{\rho}\frac{\partial p}{\partial x} + \nu\frac{\partial^2 u}{\partial y^2} \tag{2.12}$$

$$0 = \frac{\partial p}{\partial y} \tag{2.13}$$

Through Equation (2.11), Equation (2.12) and Equation (2.13), an important result is highlighted in particular by Equation (2.13): the pressure in the boundary layer can be assumed constant in the normal direction. The boundary conditions to apply to the boundary layer domain are the following:

- zero velocity at the wall (No-slip condition) $u(x, 0) = 0$ and $v(x, 0) = 0$, and
- velocity at the edge of the boundary layer $u(x, \infty) = U_\infty(x)$.

The velocity edge boundary condition applied on the x-momentum equation Equation (2.12) results in the relation shown in Equation (2.14):

$$U_\infty\frac{\partial U_\infty}{\partial x} = -\frac{1}{\rho}\frac{\partial p_\infty}{\partial x} \tag{2.14}$$

Equation (2.13) states that there is no pressure gradient in the y-direction, then it is possible to assume the pressure gradient in the x-direction equal to the one at the edge of the boundary layer, relation expressed in Equation (2.15):

$$\frac{dp}{dx} \sim \frac{dp_\infty}{dx} \tag{2.15}$$

The x-momentum equation can then be written as in Equation (2.16):

$$u\frac{\partial u}{\partial x} + v\frac{\partial u}{\partial y} = U_\infty\frac{\partial U_\infty}{\partial x} + \nu\frac{\partial^2 u}{\partial y^2} \tag{2.16}$$

The final 2D steady laminar boundary layer set of equations is given in Equation (2.17) and Equation (2.18):

$$\frac{\partial u}{\partial x} + \frac{\partial v}{\partial y} = 0 \tag{2.17}$$

$$u\frac{\partial u}{\partial x} + v\frac{\partial u}{\partial y} = U_\infty\frac{\partial U_\infty}{\partial x} + \nu\frac{\partial^2 u}{\partial y^2} \tag{2.18}$$

For the 2D incompressible turbulent boundary layers, it is possible to follow the same approach as the one for the laminar set of equations.
In this case, the Reynolds averaging process will be used, which separates a given variable into a mean value and a fluctuating quantity [14].

For a generic variable Q, the mean value $\overline{Q}$ is given by the integral shown in Equation (2.19):

$$\overline{Q} = \frac{1}{T}\int_{t_o}^{t_o+T} Q dt \tag{2.19}$$

where T is an integration interval larger than the fluctuation period, and t_o is a starting time.
The fluctuation is then defined as the subtraction from the velocity Q of the mean value $\overline{Q}$, as in Equation (2.20):

$$Q' = Q - \overline{Q} \tag{2.20}$$

This fluctuation by definition has a zero-mean value, $\overline{Q'} = 0$. Because of this, to characterize the magnitude of the fluctuation the mean square value is used as in Equation (2.21):

$$\overline{Q'^2} = \frac{1}{T}\int_{t_o}^{t_o+T} Q'^2 dt \tag{2.21}$$

Under the assumption of independency of the integrals from the starting time t_o, the fluctuation is said to be statistically stationary, as can be seen in Figure 2.5.

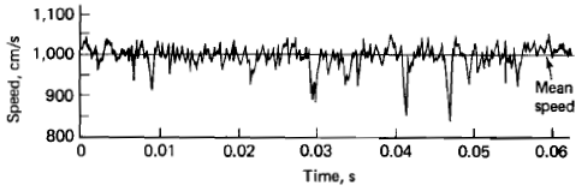

Figure 2.5: Mean and fluctuating values of Reynolds averaging [14]

It is now possible to write an expression for the fluid quantities of interest for an incompressible turbulent flow, as shown in Equation (2.22):

$$u = \overline{u} + u', \quad v = \overline{v} + v', \quad p = \overline{p} + p' \tag{2.22}$$

From the definitions of Q and Q', the statements in Equation (2.23), Equation (2.24) and Equation (2.25), useful for the derivation of the turbulent set of equations, can be written for any two turbulent quantities f and g, and a generic space coordinate s [14]:

$$\overline{f'} = 0, \quad \overline{\overline{f}} = \overline{f}, \quad \overline{f\overline{g}} = \overline{f}\,\overline{g} \tag{2.23}$$

$$\overline{f'\overline{g}} = 0, \quad \overline{f+g} = \overline{f} + \overline{g}, \quad \overline{\frac{\partial f}{\partial s}} = \frac{\partial \overline{f}}{\partial s} \tag{2.24}$$

$$\overline{fg} = \overline{f}\,\overline{g} + \overline{f'g'}, \quad \overline{\int f ds} = \int \overline{f} ds \tag{2.25}$$

The final equations are obtained through the same procedure of the laminar set of equations and are presented in Equation (2.26), Equation (2.27) and Equation (2.28).

The turbulent set of equations for a 2D steady incompressible turbulent boundary layer are:

$$\frac{\partial \overline{u}}{\partial x} + \frac{\partial \overline{v}}{\partial y} = 0 \tag{2.26}$$

$$\overline{u}\frac{\partial \overline{u}}{\partial x} + \overline{v}\frac{\partial \overline{u}}{\partial y} = \frac{1}{\rho}\frac{\partial \tau}{\partial y} + U_\infty \frac{\partial U_\infty}{\partial x} \tag{2.27}$$

$$\tau = \mu \frac{\partial \overline{u}}{\partial y} - \rho \overline{u'v'} \tag{2.28}$$

where $\overline{u}$ and $\overline{v}$ are the mean components of the velocity in the same x and y directions displayed also in Figure 2.4, u' and v' are the fluctuating components of the corresponding velocities (with $\overline{u'v'}$ the mean value of their product), U_∞ the freestream velocity, μ is the dynamic viscosity, ρ is the fluid density and τ is the total shear stress.

2.3 Boundary Layer Flow Description

Having introduced in Section §2.2 the boundary layer equations for both laminar and turbulent flow conditions, this flow conditions can now be described qualitatively with the help respectively of Equation (2.17)-Equation (2.18) and Equation (2.26)-Equation (2.27)-Equation (2.28).

2.3.1 Laminar Boundary Layer

Throughout the boundary layer, the fluid is decelerated essentially for two reasons: the presence of the wall (no-slip condition) and of momentum diffusion, which is also referred to as viscous diffusion since it is characterized by viscosity.
Intuitively, this deceleration is the result of the interaction between each fluid layer, from the wall surface up to the potential flow region. The layer of fluid next to the wall will need to have the wall's zero velocity (no-slip condition), so when considering this together with the viscosity of the other layers, each layer, including the first, will exert shear stresses on the next layer up, causing it to accelerate or decelerate. This process is continued up through the fluid because of the momentum diffusion due to the shear stresses between the layers; the development of this process is faster in more viscous fluids.
The fluid will move in the general direction of the inviscid outer flow. Considering a positive direction with respect to a given reference frame, the velocity profiles in the region of the boundary layer closer to the wall will be characterized by a positive slope trend.
This generic trend of the shape of velocity profiles is influenced by two main forces, that can alter the profiles shape significantly [13]:

- the *Shear Stress* τ, and
- the *Streamwise Pressure Gradient* dp/dx.

The *Shear Stress* is proportional to the derivative of the streamwise component of the velocity with respect to the normal coordinate to the wall, as in Equation (2.29):

$$\tau \sim \mu \partial \overline{u} / \partial y \tag{2.29}$$

For a given velocity profile in a 2D laminar boundary layer with constant viscosity, the shear stress has a zero value outside this region, and grows in magnitude as it approaches the wall.

For a turbulent boundary layer, the relation between the shear stress and the derivative of the velocity has a different expression, but it is again proportional to $\partial\overline{u}/\partial y$. Generally, in a turbulent boundary layer a larger gradient of the velocity exists at the wall, causing a higher shear stress.
With the definition of the shear stress in Equation (2.29), it follows that the calculated shear stress gradient in the y normal direction to the wall is therefore proportional to the second derivative of the streamwise velocity, i.e $\partial^2\overline{u}/\partial y^2$.
At this point, the explanation of the force introduced by the shear stress can be combined with the boundary conditions on the derivative, which imply a region with a negative shear stress gradient.
This negative shear stress gradient contributes to a net viscous force on the fluid parcels tending to decelerate them. In most of the boundary layer flows, this force dominates; the above explained effect of decelerating the fluid parcels allows the boundary layer to become thicker as it flows in the streamwise direction.
The *Streamwise Pressure Gradient* is described by Equation (2.30) and it causes an additional acceleration that modifies the velocity profiles:

$$\partial p_\infty/\partial x = -1/\rho[U_\infty(\partial U_\infty/\partial x)] \tag{2.30}$$

When considering the acceleration of a given fluid particle in a Lagrangian frame of reference, this acceleration would be nearly the same for all fluid parcels, with no appreciable difference of this force along the normal coordinate to the wall. This can be proved recalling the Lagrangian acceleration formula for a 1D steady flow given by $Du/Dt = u\partial u/\partial x$, where it can be seen that the same acceleration of the particle can be obtained if u is small and $\partial u/\partial x$ is large, or if u is large and $\partial u/\partial x$ is small.
Applying this last statement in the bottom region of the boundary layer, where u is small, results in a larger velocity gradient $\partial u/\partial x$, hence the fluid particles respond to a modification in the streamwise pressure gradient, $\partial p_\infty/\partial x$, with correspondingly a larger spatial rate of change of the streamwise velocity, $\partial U_\infty/\partial x$. This acceleration is linked to a corresponding force. Based on its sign, the streamwise pressure gradient can be therefore defined as follows:

- Adverse Pressure Gradient (APG) when $\partial p_\infty/\partial x > 0$, since it reduces more the velocity of the lower region of the boundary layer compared to what happens in the upper part of it ($\partial U_\infty/\partial x < 0$);
- Favourable Pressure Gradient (FPG) when $\partial p_\infty/\partial x < 0$, since it tends to increase the velocity of the lower region of the boundary layer ($\partial U_\infty/\partial x > 0$).

The predominant decelerating behaviour of the fluid parcels in the boundary layer, mentioned at the beginning of the section, has an exception when considering the region closer to the wall under an APG.
In this situation, $\tau > 0$ at the wall, and farther out it becomes zero and subsequently negative; $\tau > 0$ at the wall corresponds to a net viscous force that accelerates the parcels. Therefore, this constitutes a favourable effect under APGs, since it allows the flow to resist the main deceleration due to the combined effect of the negative τ and the APG in the outer region of the boundary layer, as shown in Figure 2.6.

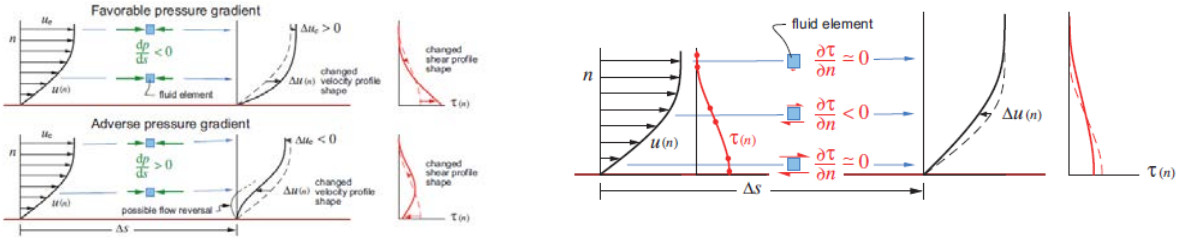

Figure 2.6: Velocity changes due to the influence of pressure gradient (left) and shear stress gradient (right) [15]

2.3.2 Turbulent Boundary Layer

The boundary layer behaviour described so far becomes more complex when considering turbulent boundary layers [13].
In 2D turbulent boundary layers, there are very large velocity gradients at the wall, with the highest gradient in a very thin region called viscous sublayer; in this region the shear stress is completely viscous and therefore negligible, with no contribution from Reynolds stresses, i.e the term $-\rho\overline{u'v'}$ in Equation (2.28).
The fact that there is a negligible turbulent shear stress does not imply a zero-turbulence condition in the sublayer. In this region the flow is quite turbulent, with large velocity fluctuations with respect to the mean velocity, but the particularity of this region is that the Reynolds stress is instead nearly zero because of the constraints that the near wall imposes on the turbulence phenomenon. Therefore, in the viscous sublayer, the viscous shear stress dominates. In the outer region, the turbulent shear stress dominates over the viscous stress; the velocity profile is however still affected by the viscosity, because the presence of the viscous sublayer has a considerable effect on the profile shape, even in the part where the turbulent shear stress has more influence.
Another characteristic of turbulent boundary layers is related to inflection points under APGs:

- For a laminar boundary layer, the inflection point has to be present since there is a change of sign of $\partial^2\overline{u}/\partial y^2$, from a positive value near the wall, to a negative value farther away.
- For a turbulent boundary layer, the inflection is present both in the viscous sublayer and farther out: a region of $\partial^2\overline{u}/\partial y^2 > 0$ can in fact occur in a 2D turbulent profile under a very strong APG, or an APG that has been present for long enough. The inflection point is not as pronounced as the laminar case, so it is difficult to see it from experiments and is mostly argued from the outer flow behaviour with physical reasoning.

Outside the viscous sublayer, a distinctive feature of turbulent velocity profiles is a "corner", in which $\partial^2\overline{u}/\partial y^2 \ll 0$.
In the outer region of the turbulent boundary layer, the eddy viscosity increases rapidly with increasing y, and the velocity gradient diminishes accordingly to the lower levels of the outer part of the boundary layer. In this region, it is assumed that the transport of momentum is completely turbulent and that the velocity profile is not directly viscosity dependent. The velocity profile in the outer region approaches the value of the inviscid outer flow at the edge of the boundary layer, and it has to merge with the velocity profile characterizing the wall region in proximity of the "corner" of the profile mentioned previously, as can be seen in Figure 2.7.
The outer region can be thought as a boundary layer characterized by a slip velocity at the distinction between sublayer and outer layer. In contrast with the no-slip velocity at the real wall, this slip velocity is then the velocity present at the boundary with the real wall-region profile. Because the flow in the outer region is not influenced by the velocity relative to the wall, the velocity that influences this layer is the velocity defect $(U_\infty - u)$, with u being the slip velocity. The outer region is therefore often called the defect layer.

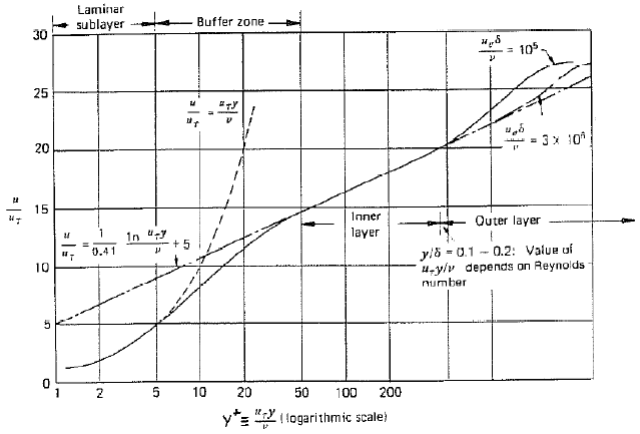

Figure 2.7: Turbulent boundary layer velocity profile [16]

2.3.3 3D Boundary Layer

What described so far about the generic behaviour for 2D flows of the boundary layer region and the forces acting on it, becomes more complex when considering 3D boundary layers, because of the presence of cross-flow velocity profiles.
The cross-flow profile is linked to pressure gradients in the same cross-flow direction, since, when considering flows over a stationary wall, it is necessary that the pressure gradient in a cross-flow direction has a cross-flow profile.
With respect to the cross-flow direction, a cross-flow pressure gradient has an effect similar to a streamwise pressure gradient in 2D flows. This means that, inside the boundary layer, it has almost the same value along the normal to the wall, with a more appreciable effect in the region closer to the wall. This effect is again restrained by the viscosity, as in 2D flows. The viscous forces in this case are produced by the negative second derivative of the cross-flow profile, in a region that starts at the wall until the peak of the cross-flow velocity profile, as shown in Figure 2.8.

Figure 2.8: Schematic of a 3D velocity profile, and different types of cross-flow profiles: a) Shear driven cross-flow due to the motion of the wall, b) pressure driven cross-flow increasing c) pressure driven cross-flow reversing [13]

The presence of the cross-flow in a 3D boundary layer affects considerably the momentum transport and consequently the development of the flow, contrary to what would happen in a 2D flow under the same streamwise pressure gradient.
The momentum deficit convection phenomenon in a 2D Boundary Layer is in the streamwise direction, from upstream to downstream. In a 3D Boundary Layer the momentum deficit is convected in the local direction of the flow, which varies.
Cross-flow is therefore an important aspect to take into consideration when describing a 3D boundary layer flow, due to the lateral momentum transport present in some regions of the boundary layer. Moreover, if there are patterns of increasing or decreasing cross-flow velocity in the 3D boundary layer, this leads to a convergence or divergence of the flow, which affects the velocity component normal to the wall (through continuity balance) and indirectly also momentum transport, modifying the development of the boundary layer as can be seen in Figure 2.9.

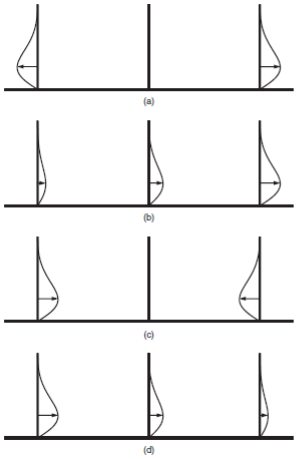

Figure 2.9: Examples of cross-flow convergence or divergence: a) divergence to either side of a location b) divergence all of one sign c) convergence to either side of a location d) convergence all of one sign [13]

2.4 Integral Boundary Layer Equations

In Section §2.2, Equation (2.26) and Equation (2.27) describe the turbulent flow field inside the boundary layer, but often when analyzing it, the global parameters are of major interest, since they allow a more immediate analysis of the flow.
Equation (2.26) and Equation (2.27) can be therefore integrated, introducing integral quantities that are used, together with the equations just mentioned, to describe quantitatively the flow separation phenomena in Section §2.5.
The two integrated equations that will be considered in the following analysis are the Von Kàrmàn integral momentum equation, and the integral kinetic energy equation.

2.4.1 Von Kàrmàn Integral Momentum Equation

The Von Kàrmàn integral momentum equation in dimensional form results in Equation (2.31) (the derivation of the Von Kàrmàn integral momentum equation is presented in Section §A.2):

$$\frac{\partial}{\partial x}(\rho U_\infty^2 \theta) = \tau_w - \rho U_\infty \frac{\partial U_\infty}{\partial x}\delta^* \tag{2.31}$$

The parameters introduced through the integral boundary layer formulation in Equation (2.31) are:

- Displacement Thickness $\delta^* = \int_0^\delta (1 - \frac{\overline{u}}{U_\infty})dy$
- Momentum Thickness $\theta = \int_0^\delta [\frac{\overline{u}}{U_\infty}(1 - \frac{\overline{u}}{U_\infty})]dy$

Equation (2.31) can be also formulated in its corresponding nondimensional form, expanding the derivative $\frac{\partial}{\partial x}(\rho U_\infty^2 \theta)$ as in Equation (2.32):

$$\frac{\partial}{\partial x}(\rho U_\infty^2 \theta) = \theta \frac{\partial}{\partial x}(\rho U_\infty^2) + \rho U_\infty^2 \frac{\partial \theta}{\partial x} = 2\theta \rho U_\infty \frac{\partial U_\infty}{\partial x} + \rho U_\infty^2 \frac{\partial \theta}{\partial x} \tag{2.32}$$

Equation (2.32) is substituted in Equation (2.31), and after rearranging and dividing all the terms by ρU_∞^2 yields the non dimensional Von Kàrmàn integral momentum equation in Equation (2.33):

$$\frac{\partial \theta}{\partial x} = \frac{c_f}{2} - (H+2)\frac{\theta}{U_\infty}\frac{\partial U_\infty}{\partial x} \tag{2.33}$$

The parameters introduced through the integral boundary layer formulation in Equation (2.33) are the following:

- Shape Parameter $H = \frac{\delta^*}{\theta}$
- Skin Friction Coefficient $c_f = \frac{\tau_w}{1/2\rho U_\infty^2}$

2.4.2 Integral Kinetic Energy Equation

The integral kinetic energy equation in its dimensional form is shown in Equation (2.34)(the derivation of the integral kinetic energy equation is presented in Section §A.3):

$$2D = \frac{\partial(\rho U_\infty^3 \theta^*)}{\partial x} \tag{2.34}$$

The parameters introduced through the integral boundary layer formulation in Equation (2.34) are:

- Energy Thickness $\theta^* = \int_0^\delta [\frac{\overline{u}}{U_\infty}(1 - \frac{\overline{u}^2}{U_\infty^2})]dy$
- Dissipation Integral $D = \int_0^\delta \tau \frac{\partial \overline{u}}{\partial y} dy$

To obtain the nondimensional form of the same equation, the RHS can be differentiated as in Equation (2.35):

$$2D = \rho U_\infty^3 \frac{\partial \theta^*}{\partial x} + \rho 3\theta^* U_\infty^2 \frac{\partial U_\infty}{\partial x} \tag{2.35}$$

Dividing Equation (2.35) by ρU_∞^3 yields the nondimensional form of the integral kinetic energy equation shown in Equation (2.36):

$$\frac{\partial \theta^*}{\partial x} = 2c_D - 3\frac{\theta^*}{U_\infty}\frac{\partial U_\infty}{\partial x} \tag{2.36}$$

The parameters introduced through the integral boundary layer formulation in Equation (2.36) are the following:

- $c_D = \frac{D}{\rho U_\infty^3}$ Dissipation Coefficient

2.4.3 Integral Parameters Physical Meaning

The two equations obtained, the Von Kàrmàn integral momentum equation and the integral kinetic energy equation, govern the evolution of the momentum thickness θ and the energy thickness θ^* respectively.
These two parameters, together with the displacement thickness δ^*, are the main parameters that describe the boundary layer from a global perspective in the streamwise direction.
Their pysical meaning can be described introducing the concept of a strictly-potential flowfield named Equivalent Inviscid Flow (EIF). The EIF is characterized by values of velocity and pressure that are the same as the ones at the edge of the boundary layer; this concept is used mostly in integral boundary layer codes, where it becomes useful for viscous-inviscid coupling.
At this point, the following interpretation can be made regarding the three integral parameters [15]: assuming a thin boundary layer, with respect to the radius of curvature of the airfoil geometry, the EIF will almost exactly match the flow outside the boundary layer and will have constant values through the boundary layer thickness. Under these conditions, using a control volume approach in treating the integral quantities of interest, it can be seen that if the same cross section is taken in the normal direction to the airfoil surface, the EIF will have a mass flow greater than the real flow situation, being the flow slowed down by the presence of the surface itself in the latter.
To account for this mismatch, the flow can be thought as being displaced by a certain distance from the wall, so that the EIF through the new cross-section will have the same mass flow as the real situation. The distance to displace the EIF flow from the wall is the displacement thickness δ^*; these considerations are depicted in Figure 2.10.

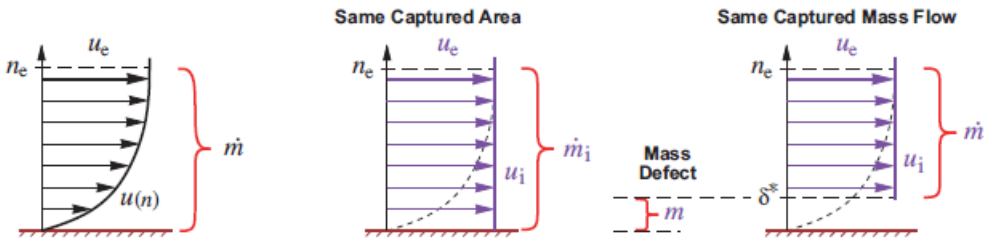

Figure 2.10: Real and EIF flow [15]

For the momentum θ and energy thickness θ^*, the momentum flow as well as the kinetic energy flow is considered to be carried by mass flow. Considering the control volume approach, the momentum flow can be seen as the force acting on a fictitious barrier that captures all the mass flow and slows down the fluid to zero velocity, whereas the kinetic energy flow can be seen as the power from an ideal arrays of turbines which brings the stream velocity to zero reversibly.
When considering the same mass flow for both the real flow and the EIF, the EIF has more momentum and kinetic energy than the real flow. The ipotetic barrier and the turbine array just introduced are shorter by a quantity equal to the displacement thickness δ^*, as shown in Figure 2.11.
In this case, the thicknesses interpretation for momentum and kinetic energy is related to the corresponding defect of the real case when compared to the EIF. The defect in momentum is characterized by the momentum thickness θ, whereas the defect in kinetic energy is characterized by the energy thickness θ^*.
It can be proved that the momentum thickness from a physical point of view is associated with drag force, whereas the energy thickness is associated to viscous dissipation and drag as well [15].

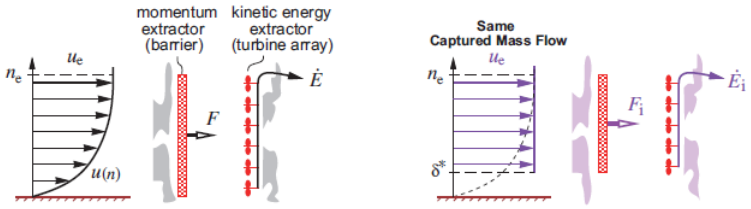

Figure 2.11: Momentum thickness and Energy thickness interpretation [15]

For the particular case of incompressible flows, like the one considered in this thesis, another intepretation of the mentioned thicknesses is possible.
This approach considers a geometric interpretation of the normalized velocity profile U. The thicknesses formulation is rewritten as shown in Equation (2.37) and Equation (2.38):

$$U = \frac{u}{U_\infty} \tag{2.37}$$

$$\delta^* = \int_0^\delta (1-U)dy, \quad \Rightarrow \quad \theta = \int_0^\delta (U-U^2)dy, \quad \Rightarrow \quad \theta^* = \int_0^\delta (U-U^3)dy \tag{2.38}$$

These incompressible thicknesses definitions allow to consider them as the geometric areas under the profiles U, U^2, U^3, as seen in Figure 2.12. Using the normalized velocity profile results in a unit length in the plots, so that comparisons between these geometric areas could be performed even for different flow situations.

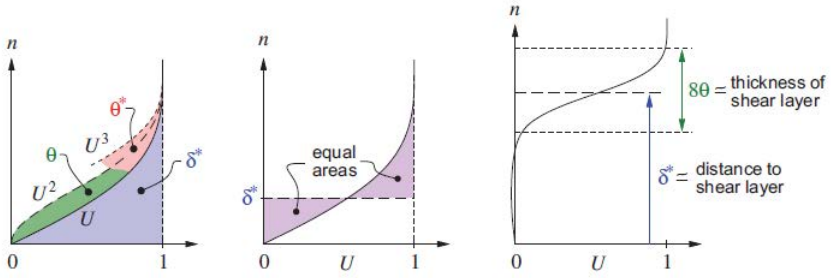

Figure 2.12: Integral thicknesses interpretation for an incompressible flow [15]

The displacement thickness δ can also be interpreted, along the normal direction to the surface, as the distance of the horizontal line that results in equal geometric areas between this line and the U profile.
The last consideration regarding displacement and momentum thickness is related to a separated flow region; this is a situation of interest in this work since the vortex generators provide a mean to control flow separation. In a separated flow condition, the fluid of the boundary layer with its associated vortices is lifted off the airfoil surface. This flow constitutes a free shear layer that separates 2 flow regions: the outer potential flow and the recirculating flow region near the surface. Therefore, the displacement thickness is the distance from the wall of the free shear layer centerline, while the momentum thickness can be considered as the thickness of this layer.

2.5 Flow Separation

Having introduced the boundary layer both qualitatively and quantitatively, flow separation can be now addressed, being the influence of this flow phenomenon of great importance for the remainder of this thesis. The main application of vortex generators is in fact preventing flow separation and as a consequence the performance of wind turbine blades.
When flow separation occurs, a region of flow reversal is seen next to the wall, with a negative slope of the velocity profile. The process from attached to separated flow requires then a change on the slope of velocity from positive to negative at the wall, passing through the condition of zero slope at the separation point, which is the point after which separation occurs.
An APG is required for separation to occur [13]. This requirement can be explained considering that a negative slope of the velocity profile at the wall can appear only if in that region the velocity profile has a positive second derivative. Therefore in a laminar boundary layer, or in the lower region of a turbulent boundary layer, a convex velocity profile ($\partial^2\overline{u}/\partial y^2 > 0$) implies a positive shear stress gradient ($\partial\tau/\partial y \sim \partial^2\overline{u}/\partial y^2 > 0$), which is characteristic of an APG.
In APG flows, the resulting positive shear stress gradient on its own is a favourable viscous force, sustaining the flow at the bottom of the boundary layer and allowing it to stay attached for a while and not separate immediately. If viscous forces where not present (e.g purely inviscid flow), immediate separation would instead happen.
An APG is not sufficient then to cause flow separation. This phenomenon can only happen relative to the combined action of an APG, of the viscous force and of the no-slip condition. If viscosity and the no-slip condition are absent, the inviscid flow remains attached throughout the whole length of the wall, but when they are present, they slow down the flow enough to be subject to the flow separation phenomenon.
Recalling the general development of an attached boundary layer flow, this would be characterized by an increase in the boundary layer thickness as it proceeds downstream, since viscosity and the no-slip condition together have the effect of decelerating the flow. But when it is subjected to an APG, it presents instead in the lower region the combination of 2 forces acting along opposite directions; these forces are due to viscosity and the positive shear stress gradient respectively.
Until the force due to the positive shear stress gradient has a decreasing rate low enough to allow the flow to still stay attached (even with flow reversal), there will not be separation. When viscosity is so that the decrease rate of the positive shear stress gradient will not be low enough anymore, the boundary layer experiences separation; this is the physics mechanism at the root of this phenomenon.
Nevertheless, the APG is an important factor, and its effect is different when considering a laminar or turbulent boundary layer:

- A laminar boundary layer cannot resist separation long enough, since the favourable viscous force experienced under APG comes only from molecular shear stress, which is usually small.
- In a turbulent boundary layer instead, the favourable net viscous force is stronger, and this is due to the fact that there is only a thin sublayer near the wall where the eddy viscosity is almost zero, while outside this sublayer the eddy viscosity is much greater than the one in a laminar boundary layer.

As for turbulence in particular, this has an important and favourable effect on delaying separation. Intuitively, the greater resistance to separation of the turbulent boundary layer can be explained imagining the mixing part of the flow pulling the top of the lower sublayer along, mantaining the velocity-profile slope and the skin-friction positive.

These considerations made so far about flow separation are valid for 2D flows. When considering 3D flows, the definition of separation becomes more complex, since it is not due anymore only to a streamwise pressure gradient, but also to a cross flow one. This can be intuitively explained considering that the reversal of velocity could happen also in the cross-flow direction. This idea of cross-flow velocity reversal is though not uniquely linked to separation, since flow reversal in the cross-flow direction could happen also in other flow conditions.
The most general definition of flow separation in 3D flows that can be stated is some flow that leaves the surface, forming a shear layer somewhat separated from the surface [13].
To identify separation regions in 2D flows, the commonly accepted procedure is to identify zero skin friction C_f values, but in 3D flows the identification of a separation is complicated by the presence of an additional dimension.
To identify separation in this case, the separation line concept can be used. A separation line identified on the airfoil surface is a geometrical entity dividing this surface in regions where the flow from different directions converges to it; the local direction of the flow defines the direction of the surface shear stress, or skin friction lines, thus the separation line is a skin friction line towards which other skin friction lines converge.
For these lines, even if the skin friction magnitude is not zero, the skin friction component perpendicular to the surface will present a zero value, as in 2D flows. This last characteristic is present for every other skin friction line, and not only for the separation line in particular. Moreover, the converging behaviour of the lines previously described is not sufficient either to identify uniquely a separation line, reason for which a different definition of a separation line is necessary.
McLean [13] proposes a definition of separation line that is related to the locations of origin of the skin friction lines and their converging movement towards a particular line. If skin friction lines originating from distant locations on the surface are converging to a particular skin friction line, then the chances the identified line is a separation line are higher.
In this way it is possible to identify two main distinct types of separation lines, as shown in Figure 2.13:

- The first one identifies the separation region referred to as *Close Separation*. The separation line divides the surface into a region where the boundary layer is fed by the outer flow flowing from upstream, and a separation bubble identifying the Close Separation area.
- The second one identifies an *Open Separation*. In this case, the separation line does not divide areas of the flow identified by different kinds of flow, but it can be noticed that from both sides of this line the boundary layer is fed by the outer flow.

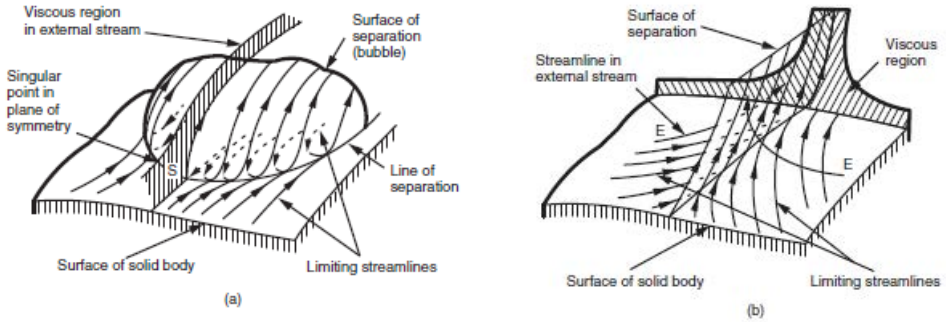

Figure 2.13: Illustration of the two types of separation lines. a) Closed type ("bubble") b) Open type ("free shear layer") [13]

To describe the turbulent phenomena and the vortical structures arising when considering the flow separation situation, the mathematical tool to consider is vorticity.
Vorticity is a vector quantity proportional to the angular momentum of a fluid element. It is generally a function of position and time, e.g $\overrightarrow{\omega} = \overrightarrow{\omega}(x, y, z, t)$, and it is defined as in Equation (2.39):

$$\overrightarrow{\omega} = \overrightarrow{\nabla} \times \overrightarrow{V} \quad \Rightarrow \quad \overrightarrow{\omega} = \omega_x \overrightarrow{i} + \omega_y \overrightarrow{j} + \omega_z \overrightarrow{k} \quad \Rightarrow \quad \overrightarrow{\omega} = (\frac{\partial w}{\partial y} - \frac{\partial v}{\partial z})\overrightarrow{i} + (\frac{\partial u}{\partial z} - \frac{\partial w}{\partial x})\overrightarrow{j} + (\frac{\partial v}{\partial x} - \frac{\partial u}{\partial y})\overrightarrow{k} \tag{2.39}$$

Vorticity originates at the fluid boundaries, diffusing into the fluid where it experiences convection, stretching (vortices increase their characteristic length) and associated intensification (the vorticity component in the stretching direction becomes greater because of angular momentum conservation). Moving away from flow domain boundaries, viscous effects are generally neglected (inviscid flow region) and therefore vortex lines are transported together with the outer fluid [31].
Vorticity is governed by the so called vorticity equation, that can be obtained taking the curl of the Navier-Stokes equation for conservation of the angular momentum. From the incompressible formulation, where $\overrightarrow{V}$ is the velocity vector, p the static pressure, ρ the density and f a generic force field, the vorticity equation results in Equation (2.40):

$$\frac{\partial \overrightarrow{V}}{\partial t} + \overrightarrow{V} \cdot \nabla \overrightarrow{V} = f - \frac{\nabla p}{\rho} + \nu \nabla^2 \overrightarrow{V} \quad \Rightarrow \quad \overrightarrow{\nabla} \times (\frac{\partial \overrightarrow{V}}{\partial t} + \overrightarrow{V} \cdot \nabla \overrightarrow{V}) = \overrightarrow{\nabla} \times (f - \frac{\nabla p}{\rho} + \nu \nabla^2 \overrightarrow{V})$$
$$\Rightarrow \quad \frac{D\omega}{Dt} = \omega \cdot \nabla \overrightarrow{V} + \nu \nabla^2 \omega \tag{2.40}$$

The time and spatial evolution of vorticity is influenced by the vortex intensification phenomenon just mentioned, which is quite pronounced in turbulent flows and flow separation situations. For this reason, in these kind of flows a progressive decrease of the scales of flow variation (i.e the movements of flow particles) is experienced. This chain of events is referred to as an energy cascade, leading to small fluctuations in the flow field that are mainly governed by viscosity dissipation, which therefore cannot be neglected when considering these small scale phenomena.
The energy dissipation occurring at small scales influences vortical structures evolution. This is of importance when considering flow separation control devices that generally exploit the idea of adding vortices in the flow field to energize it, such as vortex generators.

2.6 Conclusions

In this chapter, flow separation has been presented as a key physical phenomena that has to be delayed or prevented in order to improve wind turbine blades aerodynamical performance. The connection between flow separation and physical interpretations was highlighted based on boundary layer theory. This theory was introduced both from a quantitative and a qualitative point of view, through the constitutive equations and the related integral ones, and physical reasoning using the results obtained from these relations was presented. Using these concepts, it was pointed out that one way to improve the aerodynamic performance of wind turbine blades with respect to flow separation is exploiting the positive effects of turbulence in delaying separation. This could be achieved by means of devices that induce additional turbulence and flow mixing in the flow such as vortex generators, as it will be described in the next chapter.

Chapter 3

Vortex generators

In this chapter vortex generators are introduced as devices that allow separation prevention under otherwise stalled circumstances.
Their effect on the flow field is addressed first, describing the modifications that they introduce. Even if still not complete from a physical point of view, the main models describing them are also reported.
The current research branches regarding vortex generators are then briefly summarized, and the main applications are presented.
In the last section applications regarding wind turbines are highlighted, focusing mostly on ongoing research and flow field characterization efforts.

3.1 Vortex Generators Physics

In Chapter 2 it was introduced the fact that a turbulent boundary layer is more effective than a laminar boundary layer at resisting separation, because of the higher eddy viscosity outside the sublayer therefore contributing to a higher turbulent shear stress gradient. Following this, it would seem beneficial for preventing flow separation to introduce even more turbulent mixing in the boundary layer, so that the favourable effect of turbulence just mentioned could be even more effective.
One way of achieving such an effect is generating streamwise vortices in the boundary layer, upstream of where separation would be likely to occur, to "enhance mixing". The device that allows the introduction of such streamwise vortices is called Vortex Generator (VG).
A VG can have various geometrical shapes: the most common shape is a low-aspect ratio vane, with a plane form that could be rectangular, triangular (delta shape) or trapezoidal. Other shapes have been manufactured too, such as doublets, wishbones, as can be seen in Figure 3.1. They are attached perpendicular to the wall, and placed at an angle of attack to the local flow that varies between 15°-20° [18].

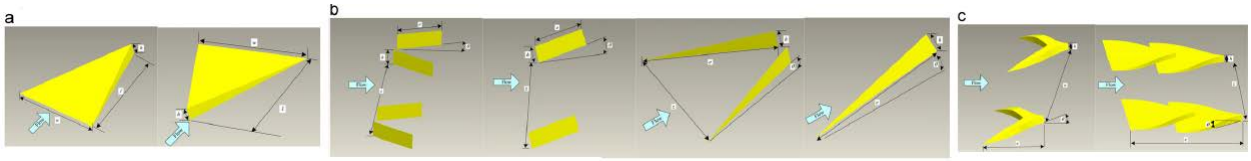

Figure 3.1: Types of VGs. (a) Forward and backward facing wedge or ramp (b) Counter and co rotating vane (c) Wishbone and doublet type Wheeler vanes [17]

VGs can have a height comparable to the boundary layer thickness (h $\approx$ δ), or they could have a much smaller height (h $<<$ δ): in this case they would be defined as Submerged Vortex Generator (SVG).
The explanation of the effectivenes of the VGs, using the "enhanced mixing" idea, is approximative. When talking of a large VG (h $\approx$ δ), the effect of those VGs on the flow is more similar to a strong side force pushing the flow strongly to the side, with a major rearrangement of the meanvelocity field [13].
A satisfactory and comprehensive explanation of the VG physics has not yet been given, since it involves complex turbulence phenomena that are still subject to study and speculation in fluid dynamics. Nevertheless, it is possible to find research papers that provide interesting insights on how VG modify the flow field, to understand better their effectiveness in practical applications. These speculations are mainly qualitative; some interesting modelling suggestions were provided by Velte in [18].
In this Phd thesis, passive rectangular vanes VG (h $\approx$ δ) were considered mounted on a flat plate, and the embedded vortices were studied by Stereoscopic Particle Image Velocimetry. The VGs were considered in a turbulent flow condition. It was shown that the embedded vortices induced by VGs are characterized by helical symmetry for a device angle of attack $20° \leq \beta \leq 40°$, which are the typical angles used in practical applications.
From the experimental flow field, it was possible to highlight two main vortical structures: a primary and a secondary one. The secondary vortex is constantly present for all the angles considered: this introduces an asymmetric disturbance in the ideal helical symmetric flow field. In the case of smaller angles ($\beta < 15°$) an additional vortex structure arises, complicating the flow field even more. For angles $\beta > 40°$, the streamwise vorticity component will decrease resulting in higher spanwise component that induces a vortex shedding from the VG and a disappearance of the simmetry highlighted before. The vortex radius was seen to be increasing weakly as the angle of attack β of the vortex generator increases, while the circulation was increasing considerably under the same conditions of larger angles [18].
Moreover, a separation control with VGs was also addressed, studying a triangular pair of vanes on top of a bump that created counter-rotating vortices. In this experiment, it was shown that the flow separation that would otherwise be experienced after the bump was significantly reduced by the presence of VGs. The flow experiences rotation, with a distortion, so that the high momentum flow transfers in the near wall region. The boundary layer therefore becomes thinner in this region, and the fluid with low momentum is transported upwards in the area between two vortices.
The donwstream development of the flow sees initially vortices isolated from each other, and then gradually integrated and mixed with the boundary layer, becoming submerged in it and lifting away from the wall in the end as can be seen in Figure 3.2. The main effect of the VGs is the primary vortex structure that generates additional shear layers.
In [32, 33] the 3D evolution of the vortices induced by a counter-rotating VG pair was studied. It was shown that the vortices move down towards the wall, with the boundary layer below and between the vortices being thinned by a lateral divergent flow movement pattern. The divergent movement causes the skin friction coefficient to increase approximately 10% in the central region. On the sides of the vortices lateral convergence can be seen, causing reduced skin-friction. Overall, the flow experiences a lateral contraction, reattaches in the central region and separates at the sides where secondary flow patterns develop. This flow development and the skin friction behaviour just described were depicted also in [19], where wall flow visualization was used to display the skin friction lines on the surface, as seen in Figure 3.3.

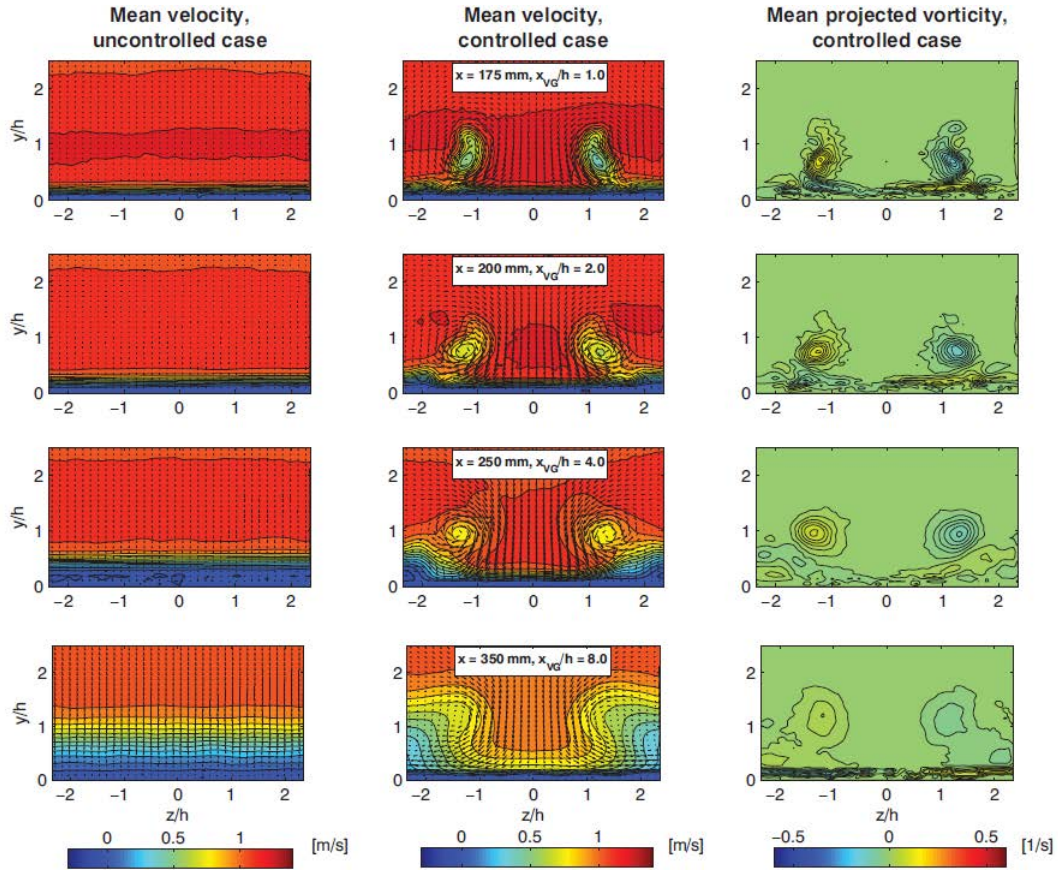

Figure 3.2: Example of flowfield average velocity and vorticity. The terms uncontrolled and controlled refer to flowfields without and with VGs. Image produced from experimental results of VGs placed on top of a bump. [18]

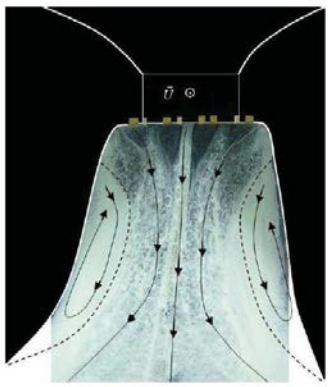

Figure 3.3: Example of flow visualization behing VGs [19]

As it is observed from the research papers mentioned before, and practical engineering applications too, VGs are generally used in arrays, having two main configurations, characterized by whether the vortices are all of the same sign (co-rotating) or of alternating signs (counter-rotating) [13].
The counter-rotating VGs configuration has the effect of producing regions of strong flow divergence, where the boundary layer is thinned considerably, increasing its resistance to separation. Regions of flow convergence appear too, in which the boundary layer is thickened, reducing presumably the resistance to separation. As the vortices move laterally, the regions of divergence become wider, and the regions of convergence narrower, until these pairs of vortices converge on each other, rising from the surface. The rising vortices lift some of the low-energy fluid at the wall away from it, and in doing so, this process contributes to a less tendency to separate.
If counter-rotating VGs are placed not upstream enough of where separation will manifest, a flow separation will occur in the convergence regions mentioned previously, since the converged vortex pairs will rise too far and lose their effectiveness.
The placement of an array of VGs, relative to its spacing, is thus a balancing act, still subject to research in optimization methods. So far, most of the successful configurations rely strongly on best-practices guidelines and not on many empirical observations. A common practice about counter-rotating arrays is to group the devices usually in pairs, such that vortex convergence and liftoff are delayed farther downstream than they would be with uniform spacing.
The co-rotating VGs configuration has a similar behaviour to the counter-rotating configuration, producing regions of divergence (thinning) and convergence (thickening), but not as pronounced as those produced by counter-rotation.
The following points summarize the positive and negative effects of the two types of configurations, described by Figure 3.4:

- Counter-Rotating Arrays can be more effective in short distances, since they produce a stronger divergence. When the vortices merge, the effectiveness for the remaining portion of the airfoil is reduced. The enhanced performance of this configuration can be degraded consistently if the vortices produced in a pair are not of equal strength [34]: this situation could happen with flow direction changes that cause different angles of attack for each single vane. In 3D flows with strong cross-flow in the boundary layer, the two vortices in a pair behave differently, with a less favourable effect on delaying separation than a co-rotating configuration, which would be preferred in this case.

- Co-Rotating Arrays are less effective in the immediate downstream flow region, but the vortices are able to persist farther downstream than a counter-rotating solution. A co-rotating configuration is used more in cases with strong boundary-layer cross-flow. In the case when the main vortex from the VG has the same rotation as the background cross-flow vorticity in the outer part of the boundary layer, the vortex will diffuse more rapidly, than it would do when it rotates in the opposite direction, with a co-rotating configuration. The vortices from VGs will then decay two to three times faster than they would in a comparable 2D flow [35].

To briefly consider the effect of a VG configuration in the design process, a rule of thumb about the direction of the force exerted by VGs is provided in [13]: this force should push the flow in the direction opposite to the direction of the crossflow.

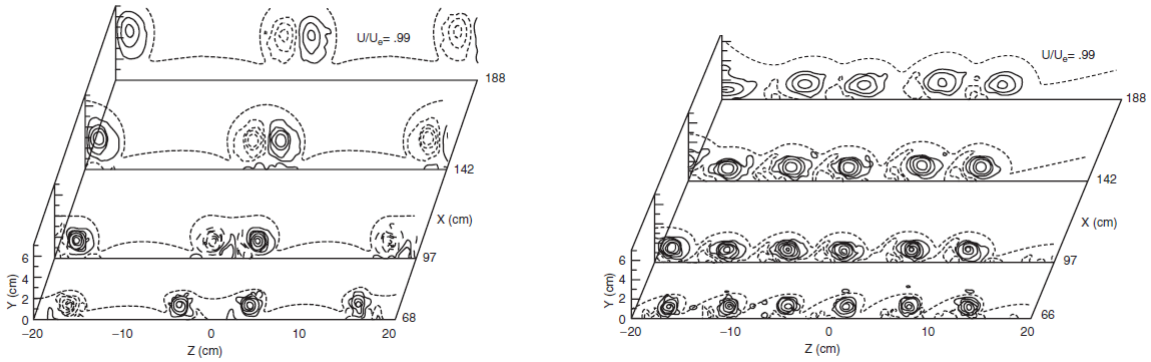

Figure 3.4: Mean velocity field behing VGs. The left plot shows a counter-rotating configuration, the right plot a co-rotating one [20]

In these previous papers cited, VGs were placed in locations were separation was expected to occur. Separation is a flow phenomenon influenced by a pressure gradient, which in aerodynamics applications is induced by airfoil profiles curvature. For this reason, in [36] numerical experiments investigated the development of modelled vortex pairs in turbulent boundary layers, considering the influence of both streamwise curvature and pressure gradients.
Two different types of counter-rotating vortex pairs were studied, common flow between them towards the wall and away from the wall. These two vortices configurations were then considered in three different curvature situations in the boundary layers: flat, convex and concave surface, leading to 6 total configurations studied. The modeled vortex pairs were introduced to the Reynolds Averaged Navier Stokes solver by means of inlet boundary conditions. A semi-empirical model was developed allowing the user to choose the size, strength and location of vortices related to the VG geometry considered. Velocity and turbulence distributions in the vortices dowstream of the VG were calculated.
The results show that:

- the combination of common-flow-down vortices with concave-wall boundary layer leads to the formation of secondary vortices outside the primary vortices, which remain closer to each other (as compared with flat plate or convex wall cases).
- circulation of both common-flow-down and common-flow-up vortices becomes larger as the flow proceeds downstream in a concave surface case, but decreases when considering a flat plate or a convex wall. This can be explained, with respect to the other cases, by the different primary longitudinal vorticity caused by a concave surface.
- for the peak vorticity in the curved duct geometry considered, it can be seen that in the case of concave wall:
  - in the initial part, it decreases rapidly due to adverse longitudinal pressure gradient present during transition from flat to curved surface.
  - in the final part, it increases rapidly due to favourable longitudinal pressure gradient present during transition from curved surface to flat.
- common-flow-down vortices on a convex wall remain closer to the wall due to the normal pressure gradients accompanying streamwise curvature, thus reducing their magnitude rapidly.
- common-flow-up vortices on convex wall are quickly attenuated as well, being replaced by secondary vortices forming below them. Even if this is the case of common-flow-up vortices, the final effect is similar to that of the common-flow-down configuration.

The models and physical explanations given so far were related to subsonic flows VGs applications. There is also a considerable number of supersonic applications in which SVGs are used, mainly concerning the prevention and reduction of Shock Boundary Layer Interaction (SBLI).
In [17] results from numerical investigations involving SVG are presented, related to high-speed flow applications and SBLI. Wedge type SVG were considered in supersonic flow conditions, that is $Ma = 1.4$ and $Ma = 2.5$. The SVG model proposed by Babinsky [37] was confirmed in [17], with the characteristic separation bubble forming right after the VG leading-edge, caused by a SBLI phenomenon. This model predicts a pair of weak trailing vortices in the vicinity of the leading edge corner separation, in which a horseshoe geometry is observed, with a primary vortex pair stronger than the previous that is been shed from the edges of the SVG. The presence of other generic minor secondary vortices is also considered. This model is shown in Figure 3.5.

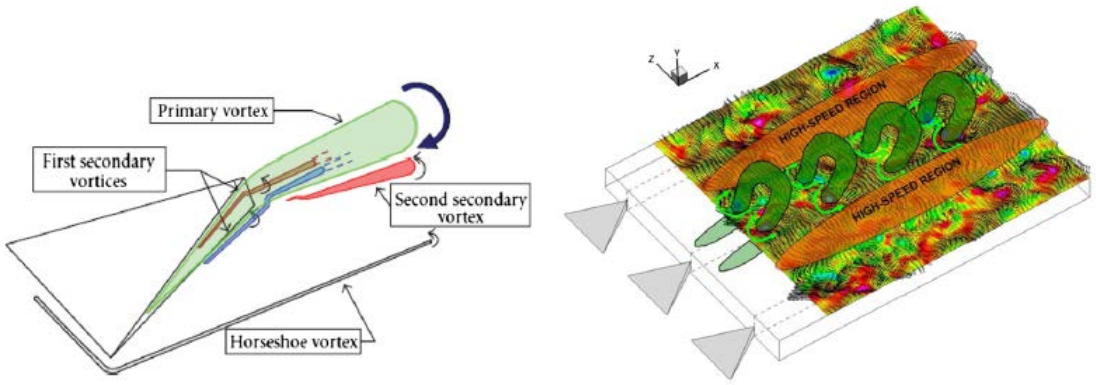

Figure 3.5: The left plot shows the vortex model postulated for VGs in high speed flow, the right a numerical visualization of the vortices behind VGs in high speed flow [17]

The following points summarize the main physical behaviour of vortices due to vortex generators:

- when a single device is considered, depending on the angle of attack relative to the incoming flow, if this angle of attack is positive or negative the flow experiences a vortex with circulation of a different sign. This vortex initially moves closer to the wall, entraining the high momentum fluid in the lower region near the surface. The vortex then tends to move laterally due to the presence of secondary vortices, and at a certain streamwise location, it starts to lift off of the surface, creating an additional shear layer in the boundary layer.

- when multiple devices are considered, they are usually grouped in pairs and their effect on the flow-field depends on the configuration chosen, that can producing counter-rotating or co-rotating vortices. In the counter-rotating configuration, the two primary vortices created by each device converge on each other, creating a unique primary vortical structure that at some location will move away from the wall. The vortex intensity measured by circulation decays as the vortex moves donwstream and the primary vortex radius tends to increase during its movement. In the co-rotating configuration, the primary vortices do not converge on each other and they tend to move laterally downstream of the VG, with a direction depending on the VG angle of attack with the incoming flow. These vortices are characterized by a smaller radius and a lower circulation.

- depending on their mutual position, the counter-rotating configuration can be divided into two other subcategories: one that produces a flow between them that tends to move closer to the wall (common flow-down) and one that is characterized by a flow between them moving away from the wall (common

flow-up). When these two configurations are considered together with the effect of a streamwise pressure gradient created by different curvatures of the base where VGs are mounted, it can be seen that in the common flow-down configuration, the primary vortices remain closer to each other than the other flow-field pattern, with a stronger circulation. When considering a concave base curvature, secondary vortices arise near the primary vortices. If a convex base curvature is taken into consideration, the primary vortices will remain closer to the base surface due to the pressure gradient generating from the type of curvature introduced.

3.2 Vortex Generators Ongoing Research

The research about low profile VGs can be divided in two main branches [10]:

- the first focuses on studying the efficiency of different devices for flow-separation control, and
- the second is focused instead on the characterization of the vortical flowfield induced downstream by devices. The aim of this type of research is to produce correlations to be used later in numerical simulations during the design process of VGs configurations

Flow Separation Control
In the first research branch, two sub-categories can be indentified, *Adverse Pressure Gradients (APG) at low speeds* and *Normal Shocks at supersonic speeds*.
For *APG at low speed*, the most effective group of flow separation control devices is the one that generates streamwise vortices, such as SVGs and Conventional VGs. These types of devices are the ones to which the term vortex generator relates directly. In theory, there is also another group of devices that could be considered, that is to say devices that generate transverse vortices (spanwise cylinders, transverse grooves, etc.). This other group of devices is generally less efficient than SVGs and Conventional VGs.
The term Conventional VGs considers devices with $h/\delta \sim 0.8$, where h is the VG height and δ is the boundary layer thickness, placed approximatively at $6h$ upstream of the baseline separation. Results from experimental investigations on a backward facing ramp indicate that pairs of counter rotating VGs provide mostly an attached flow directly downstream of the ramp trailing edge. The flow in this region is highly 3D, with areas of recirculating flow on the separation ramp between adjacent attached-flow regions, as can be seen from Figure 3.6.

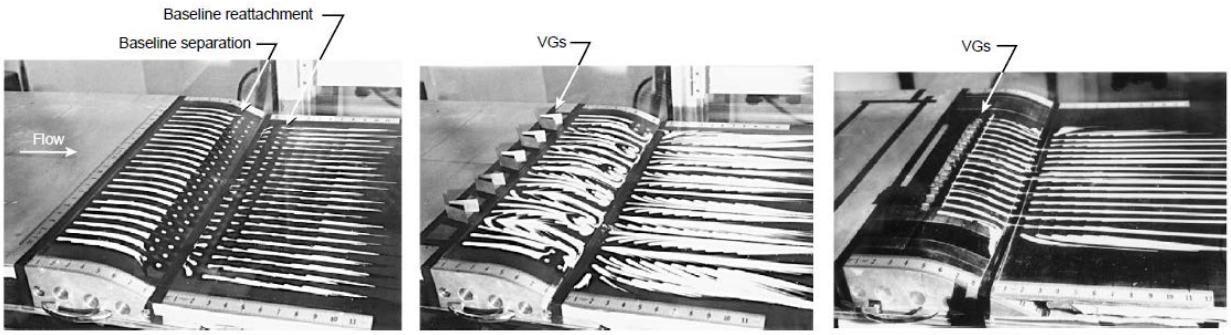

Figure 3.6: Oil flow visualization of VGs over a backward facing ramp. The leftmost plot shows the case without VGs, the middle plot shows the case with VGs with height $h = 0.8\delta$ and the rightmost plot shows the case with VGs with height $h = 0.2\delta$ [10]

The recirculating flow region on the separation ramp is thought to be an indication of the excessive strength of the vortices, reason for which another type of VGs was introduced in research, called SVGs. This type is

smaller than the Conventional type ($h/\delta \sim 0.2$), and generally placed at approximately $10h$ upstream of the baseline separation. The main difference is that these new devices can produce weaker streamwise vortices to overcome flow separation in the areas of recirculating flow. The reduction of separation was of almost 90%. The effectiveness of the SVGs can be explained considering that when comparing the height of low-profile VG relative to the boundary layer velocity profile, for $h/\delta \sim 0.2$, the local velocity is already over 75% of the free stream value. This means that any further increase in height will consider only an additional small fraction of the corresponding velocity profile, thus providing only a moderate increase in local velocity and a dramatical increase in the drag of the device.
VGs substantially lose their effectiveness when lowering $h/\delta < 0.1$. The most effective location range of low profile VGs is determined to be about $5h \div 30h$ upstream of the baseline separation. The device induced streamwise vortices could last up to $100h$.
The other subcategory, *Normal Shocks at supersonic speeds*, is related to a physical phenomenon present in many aerodynamics applications such as transonic inlets, diffusers or airfoils. The Normal Shock has the effect of increasing the drag and lowering the pressure recovery dramatically, when interacting with a turbulent boundary layer. In this case, the use of SVGs shows that they can significantly suppress the shock-induced separation bubble, improving consequently the boundary layer characteristics downstream of the shock: the boundary layer becomes thinner and contains lower mixing losses.

Vortex Characterization
In the second research branch, related to vortex characterization and correlation, the vortex strength measured by the circulation Γ is usually determined through flowfield measurements or numerical experiments.
Ashill et al. [38], introducing the concept of device effective height h_e, showed that it is possible to generalize the correlation of a non-dimensional circulation parameter with respect to this h_e. h_e is selected ensuring that the maximum value of non-dimensional circulation is independent of device geometry, so that it is possible to combine a family of circulation curves for various VGs into a single curve. The correlation introduced enables the prediction of vortex strength just downstream of the VGs for a wide range of Reynolds numbers.
Being still an active research field, modelling and optimization has therefore not reached a mature state yet. The main modelling approaches used to represent these flow features are *Statistical Models*, *Velocity-Profile based Models*, *the Wendt Model*, *the BAY Model* and *the jBAY Model.* These approaches are described as follows:

- as for the *Statistical Models* approach, there are *Statistical Models based on the Lamb-Oseen vortex model*, used also in the work of Velte [18], or *Statistical Models based on Second-Order statistics* of the initial vortices computed using a vortex model in combination with the Prandtl Lifting Line theory. In the last case, the statistics are added as additional turbulence stress terms to the governing equations.

- *Velocity-Profile based Models* are useful in cases in which only the dowstream effects of the VG are thought to be relevant (and not the local effects near the VG). Smooth velocity distributions in 3D simulations can be specified in regions where the vortex generation is to be modeled, including some additional control of the upstream influence to increase the additional velocities from zero to those desired. The main forms of velocity imposition that can be used are:

  - Direct Forcing, which sets the velocity directly as a boundary condition (best performance, but difficult to implement in commercial solvers), and
  - Proportional Control Feedback Forcing, which gives reasonable performance in terms of setting the velocity, but it has a steady-state error which cannot be entirely removed.

- *The Wendt Model* is an empirical model suited for subsonic flows with adverse pressure gradients, which simulates the VG by adding vorticity as a step change at a given axial station (the VG should have a height comparable to the one of the Boundary Layer).

- *The Bender, Anderson and Yagle (BAY) Model* is a lift-force model applicable to a wide range of flows, including supersonic and sub-boundary layer VGs. This model adds a source term to the momentum and energy equations, that simulates the lift force introduced by a VG, aligning the local flow velocity with the vane VG. The BAY Model introduces a non-physical Boundary Condition that explicitly modifies flow properties, with the intention of modeling the effect of the presence of the VG on a given flow.

- *The jBAY Model* is based on lifting force theory developed by Bender, Anderson and Yagle. This new model introduces a novel technique for defining control points on which to apply the simplified model, allowing a better user experience, with improved accuracy.

In [39], the validation results for a single vane in subsonic flow, an array of vanes in a subsonic S-duct diffuser, and a pair of counter-rotating vanes in supersonic flow are considered, using *the BAY Model* and the *Wendt Model*. These models, in particular *the BAY Model*, provide comparable numerical results to those of gridded vanes simulations. The author concludes that *the BAY Model* is easier and accurate enough to use than gridded vanes.
In [40], different methods of modelling vortex generators in Computational Fluid Dynamics codes without meshing are investigated, focusing on large scale applications, such as using vortices for force augmentation or directing the flow. The different methods considered fall under two main categories: direct VG modelling (*BAY Model*), useful in cases such as presence of Strakes, and modelling the vortex alone without VG, using *Velocity Profile based Models*. The calculation using a *Velocity Profile based Model* with Direct Forcing directly from Navier Sokes equations has not provided good results, because it requires an accurate discretization of the domain for complex cases. The *BAY Model* provided good results, as already proved also in the other papers.
In [41], the *Lamb-Oseen statistical vortex model* is proposed. This model was applied to an APG boundary layer flow, and evaluated qualitatively against experimental and fully resolved Vortex Generators computational simulations. The test cases considered were a 2D clean flat plate, a 2D flat plate with the VG Model implemented, and a 3D Model that fully resolved the VGs on a flat plate. Different streamwise positions and set-ups (co-rotating or counter-rotating) are presented. The model is compared against distributions of wall pressure and skin-friction coefficient obtained experimentally. The results of the investigation successfully predicts both attached and separated flow states, and it is capable also of predicting flow control sensitivity with respect to the streamwise position.
In [42], a *Statistical Model based on Second-Order statistics* was implemented. Numerical simulations of a flat plate in zero and APG conditions, and of a plane axisymmetric diffuser are performed. The models used are in the order: the proposed statistical model, the fully resolved simulations, and the experimental results. The application of the model in flat plate boundary layer has shown that it generally underpredicts the stresses downstream of the VG, since the vortices are not the ones actually induced by the VG, but they are only modeled. Qualitatively it is possible to produce correct results in trends and tendencies of the flow quantities considered.
The jBAY Model was considered in [43]. Numerical simulations were conducted for a single Vortex Generator on a flat plate, on an S-Duct air intake and for a high lift configuration. Good agreement was shown when comparing the results against fully gridded CFD results and experimental ones. The limitation for this model is that it does not take into account the thickness of the vortex generator.
In [44] *the BAY Model* was implememented and tested for an array of vortex generators. This model was calibrated, comparing the results against fully gridded numerical simulations and experimental results for a single SVG vane, with the height of this being just a fraction of the boundary layer thickness. The BAY Model allowed a reduction of approximately 70% of the grid resolution, when compared with the full grid, with a good accuracy in the prediction of shape and size of vorticity and velocity contours. It was also possible to predict well the peak vorticity location and vortex circulation.

3.3 Vortex Generators Applications

VG applications can be summarized into two main categories [10]:

- the first includes investigations that focus on *flow separation control* applications for various airfoils and wings, and
- the second is about investigations for *non-airfoil applications*, seeking performance improvement through flow control.

In the *flow separation control* category, 4 different subcategories can be identified: *Low Reynolds Airfoils*, *High Lift Airfoils*, *Highly Swept Wings* and *Transonic Airfoils:*

- The *Low Reynolds Airfoils* subcategory includes many modern airfoil applications operating in a Low-Reynolds regime, such as remotely piloted vehicles, high-altitude aircraft, compressor blades, and wind turbines. In these cases, usually airfoils operate at $Re < 1000000$, experiencing a laminar separation bubble for angles of attack below stall. Even though these separation bubbles are small, with a little effect on the airfoil lift, they can cause a thicker turbulent boundary layer, which results in a significant drag increase and consequent decrease of airfoil efficiency. Therefore reducing the separation bubble will result in a thinner turbulent boundary layer downstream, extending the range of application. As a note, a significant drag reduction over the entire midrange of the lift coefficient was shown to be possible, when using SVGs.
- In the *High Lift Airfoils* subcategory are included high-lift systems of modern commercial transport aircrafts. In particular, the focus is on flow separation on multielement high-lift airfoils, which is a complicated function of geometry and flight conditions. In previous research conducted, it was shown that certain high-lift configurations exhibit boundary-layer separation on the flap at low angles of attack. To prevent this low-angle-of-attack separation, altering the geometrical configuration is an option, but this would cause an important reduction on the maximum lift obtainable. An effective countermeasure is employing flap-mounted, SVGs, that allow the airfoil to maintain high maximum-lift values while attenuating boundary-layer separation at low angles of attack.
- In the *Highly Swept Wings* subcategory, including wings with sweep-back greater than 40%, used mostly for supersonic combat or transport aircraft, the interest is on reducing the large lift-dependent drag, so that the aircraft could maneuver more efficiently at subsonic speeds. An effective application of VGs on swept wings is a co-Rotating vane-type configuration, which can give a great improvement in terms of maximum lift for modern fighter aircrafts. In fact, during aggressive maneuvers in flight regimes characterized by highly separated flowfields and sometimes strong vortical flows, this measure aids in reducing the drag force.
- In the *Transonic Airfoils* subcategory, the applications are aimed at increasing the lift coefficient of aircrafts during high-speed turning maneuvers. During these, very large APGs are present in the streamwise direction, and also shock waves over the wing's upper surface. The use of SVGs, in particular wedges and split vanes, can improve lift and overall performance. In particular, the use of wedges seems to provide the greatest reduction of shock strength, probably due to compression waves induced by the wedges. On the other hand, using split vanes produces instead the largest shock strength, and this could be due to the reduced growth of the boundary-layer caused by the split vanes upstream of the shock. Weaker compression waves strength could cause this effect.

In the *non-airfoil applications* category, 3 main subcategories can be found: *Noise Reduction*, *Engine Face Distortion Management in Compact Inlets* and *Heat Exchangers:*

- As for *Noise Reduction*, the interest is in lowering noise that could arise from small region of shock-induced boundary-layer flow separation at high Mach numbers. From experiments it was shown that the low-frequency noise known as "Mach rumble" is produced by vibrations caused by an unsteady vortex separation, which might be excited by a von Karman vortex street shed from the shock wave. To prevent this phenomenon, SVGs placed attached to the fuselage upstream of the shock are successful in suppressing the formation of the Karman vortex street in the wake region: they very effectively reduce both the Mach rumble and the vibration.

- As for *Engine Face Distortion Management in Compact Inlet*s, the applications are on flow-control methods to manage the flowfield inside compact inlet configurations. Modern S-duct inlet configurations are being created more compact (shorter) to achieve weight, volume and cost reduction. This reduction in size comes with the price of high flow distortion and low pressure recovery caused by extreme wall curvature and strong secondary flow gradients. In the flow configuration without VGs, counter-rotating vortices form in the forward section of the duct, leading to vortex lift-off in the back section; this lift-off (3D separation phenomenon) is the primary distortion mechanism in compact inlet systems, and consequently the flow phenomenon that must be controlled. The VGs are usually placed inside and around the surface of the duct in a co-rotating configuration, closer to the region of separation and with a device height on the order of the boundary-layer momentum thickness, in order to evenly redistribute the boundary-layer flow around the circumference of the fan face. The purpose of these VGs is to create vortices that merge quickly to form a single overall secondary flow pattern that remains within the "thin" boundary layer next to the wall. This induced secondary flow pattern adjacent to the wall prevents the formation of the pair of counter-rotating vortices described before, and the undesirable effects of the vortex lift-off phenomenon. The near-wall low-momentum fluid is effectively spread out circumferentially, suppressing 3D flow separation from the wall.

  - In [45], Vortex Generators effect was studied in External Compression Inlets of supersonic aircrafts. These inlets are characterized by a reduction in Mach number from supersonic to subsonic, obtained using shocks and an area expansion region. The performance is influenced by the interactions between shocks and viscous regions. Vortex Generators are used in this article since they reduce the need for bleeding the flow at the shock impingement; they cause though the side effect of increasing parasitic drag when VG height is comparable to Boundary Layer thickness. In general, the use of a counter-rotating VG configuration reduced the total separation area and increased the spanwise variation compared to the solid wall case.
  - In [46]a design of SVGs in a rectangular S-duct diffuser is presented. The use of VGs in this type of diffuser is necessary because the separation inside the duct, due to its geometry and high curvature, lowers the performance considerably. Numerical simulations were performed for S-Ducts without and with SVGs, in different configurations. It was shown that it is possible to obtain a reduction in the distortion coefficient of the inlet flow by 27%, thus making the flow more uniform at the inlet. A drop in momentum thickness by 61.54% at the exit plane is achieved too with the Vortex Generators considered, when comparing this values with the bare S-Duct diffuser.

- As for the *Heat Exchangers* subcategory, the successful application of VGs on S-duct Engine Compact Inlets, improving their performance by means of a reduction of flow distortion and an increase in pressure recovery, stimulated the interest for VGs being used also for thermal applications in Heat Exchangers. One such example of these new applications is described in [47]. In this paper, novel fin-tube surfaces are presented, with the aim of reducing pressure losses and pressure loss penalty, increasing heat transfer. On this novel surfaces delta winglet pairs of Vortex Generators were introduced, through a punch out from the surface, only from the larger fin area around the first transverse row of tubes. In particular,

the Vortex Generators were designed with the angle of attack of the delta winglet to be modest: a large angle of attack would lead to a pressure drop increase, whereas a small angle of attack would cause less heat transfer enhancement. To increase the leading edge of the delta winglet pairs, which was seen to cause an heat transfer enhancement, a large fin area around the first transverse row of tubes can be used. The height of the VGs for this configuration has been chosen as 0.9 times the fin pitch (distance between centerlines of fins). Numerical simulations were conducted, showing that it is possible to achieve enhancements in both heat transfer and pressure drop reduction, with the proper configuration of the location, size and angle of attack of the VGs.

3.4 Vortex Generators Research and Applications for Wind Turbines

In the last decades, the renewed interest for VGs as devices to enhance aerodynamic performance was due also to a discovery of new possible usages, such as wind turbines applications.
VGs have proved to be effective devices in improving aerodynamic performance expecially for large wind turbines. Related to wind turbines applications, they are generally mounted in multiple strips in the hub region of the blades, as can be seen in Figure 3.7, where the stall phenomenon manifests sooner than other radial positions. Their aim is to delay as much as possible the presence of stall flow conditions in this region, increasing the tolerable range of optimum angles of attack and therefore power production.

Figure 3.7: Installation of VGs on the root section of the blade [21]

As a consequence of their capability of delaying separation and therefore stall conditions, VGs are also able to address the noise reduction problem due to vortex shedding from the blade. When energizing the flow through induced vortices, the result is a stronger attached flow and a decrease in vortices recirculation area, with an associated noise reduction.
The research regarding applications for wind turbines is focused currently on flow characterization through CFD simulations. There are also efforts in modeling their effect in lower fidelity simulation codes, employing for example panel code techniques coupled with an Integral Boundary Layer formulation.
Regarding the research about flow characterization through CFD simulations, this is aimed mainly at understanding and representing the flow field adequately. This branch includes turbulence model selection and meshing strategies to resolve properly the flowfield discretization; in some cases, the use of the BAY Model is considered, to reduce the computational effort.
In [48], VGs were studied considering their height influence on the flow field physics. CFD simulations were performed, with these devices placed at approximatively 20% chord on the blunt trailing-edge airfoil DU97-W-300. A counter-rotating configuration was used, with five pairs of VGs in total. Different geometric parameters of these devices were analyzed. It was shown that increasing the VG height under the same VG streamwise position causes an increase of the maximum lift coefficient, but a larger increase in the drag coefficient too: this was explained as due to the additional shear stresses introduced with the greater device height. When considering different devices length, an increase of this parameter involves stronger vortices but

also a greater drag coefficient. Therefore increasing the devices length, even if it produces more circulation, involves also additional shear stresses that can result in abrupt additional drag under high angles of attack. With regards to VG pair intra-spacing, a change of this quantity does not produce appreciable effects in terms of lift and drag coefficients, but when considering a larger value both for the long and short spacing, it can be seen from the analysis of the flow field that the vortices tend to remain closer to the airfoil surface, with a slight beneficial effect in flow separation control.
In [49], the effect of VGs on the CAS-W2-350, CAS-W2-400 and CAS-W1-450 thick wind turbine airfoils was presented through experiments carried out at a Reynolds number of 1 million. Different configurations of VG height, chordwise position and VG pair spanwise spacing were considered, together with the analysis of a second row of VGs. From the results obtained, it can be seen that the maximum lift coefficient has a greater value when VGs are placed closer to the leading edge position of the airfoil. When the chordwise position is lower than 20% of the chord distance, the lift coefficient decreases at lower angles of attack with respect to the smooth configuration.
As for the drag coefficient, an overall increase is noticed at low angles of attack when using VGs, and the larger values could be reduced if the VGs are placed gradually at greater chordwise positions. Related to VG height sensitivity analysis, an increase of this parameter causes the minimum pressure drag coefficient. The spanwise spacing has a negligible effect on the performance of the airfoils. It was noted a further performance enhancement when using a second row of VGs, depending on the chordwise position and the VGs dimensions of this additional VG strip.
In [22] the aerodynamic performance of the NREL S809 airfoil with and without VGs was investigated through CFD simulations. A counter-rotating configuration was investigated, with rectangular VGs characterized by a height equal to 1% of the chord distance. Both one and two rows of VGs were analyzed: for the single row configuration, the devices were placed at respectively 10%, 20% and 40% of the chordwise position, whereas for the double row configuration, the two rows were placed in two main configurations, that is (10% - 20%) and (10% - 40%) of the chord distance. It was seen that in the single-row 40%-chordwise-position case, the lift coefficient is increased. In this case though, the stall phenomenon at high angles of attack occurs early in the position along the streamwise direction, therefore the stall delay is not very effective. For the other single-row configurations, the 20%-chordwise-position is the one that produces the highest lift coefficients, in accordance to what found generally in the previous articles referenced. For double VGs row configurations, they generally increase lift values. For angles of attack greater than the critical value, they have a main beneficial effect in reducing drag as compared to the single row cases.
Regarding the flow field investigation, the double row configuration shows interesting results in terms of pressure coefficient and velocity profiles. The pressure coefficient behaviour shows a considerable decrease of values at the suction side, where VGs are placed. This causes a larger integration area between the two curves of the suction side and pressure side, resulting in a greater lift coefficient. As for velocity profiles, it can be seen that the increase in momentum in the region close to the airfoil surface is considerable, with respect to the single row configuration. Consequently, a more energized fluid stays attached by a notably large portion of the surface: for a high angle of attack such as 18°, the profiles in fact show the reversed flow behaviour but not the separating one at the trailing edge. These considerations are shown in Figure 3.8.
The vorticity development for a VG pair in the streamwise direction is characterized by the presence of the two corresponding vortex cores, related each to the corresponding VG. In the article, the single-row configuration at 10% chordwise position is analyzed for the angle of attack of 18°. The contour plots show that the vortex induced by the presence of the VGs diffuses rapidly already at a streamwise position of 20% of the chord distance, thus implying that the momentum increase is not able to resist separation for long enough. This behaviour, with the proper distinctions regarding different configurations, is a typical flowfield development of the vortices induced by a counter-rotating VG configuration, such as the one considered in the rest of this thesis.

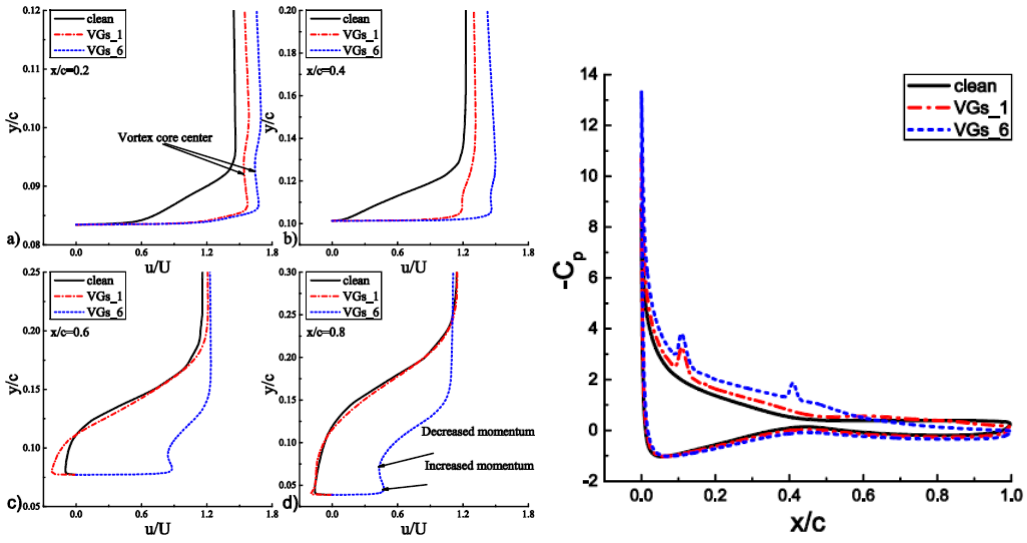

Figure 3.8: CFD results of the NREL S809 equipped with VGs. The left plot shows the velocity profiles for different streamwise locations, the right plot shows the pressure coefficient. Two different VGs configurations are considered here: VGs_1 is a single VG of height $h = 0.1 * c$ placed at a streamwise location of $x/c = 0.1$; VGs_6 is a double strip VG configuration, with VGs of height $h = 0.1 * c$ placed at a streamwise location of $x/c = 0.1$ and $x/c = 0.4$ [22]

In [50], CFD simulations of two airfoils, FFA-W3-301 and FFA-W3-360, are performed, for both cases with and without VGs. The peculiarity of this paper is that it is one of the very few describing the meshing process for fully resolved VGs simulations, allowing the reader to try to test and repeat the results more easily than other papers. The meshing steps consist of an initial VG blocking meshing strategy, realized using an in house optimization meshing solver to create the surface grids in this region. From this step interesting indications on a fast and generalizable meshing strategy could be obtained. The remaining airfoil surface grids are then generated, followed by a single normal hyperbolic extrusion creating the final flow domain. The Reynolds number considered in these simulations is 3 million, and the $k - \omega$ SST with the $\gamma - \widetilde{Re_\theta}$ transition models were employed in the simulations. The computations are then compared with experimental results from wind tunnel measurements, comparing pressure coefficient, lift and drag coefficient. The fully resolved simulations do not capture exactly the measured performance, although the results obtained show that it is possible to compare VGs setups qualitatively, with respect to chordwise position, inner and intra spacing.
In the papers mentioned previously, fully resolved CFD simulations are used in analyzing the flow field, in substitution of experiments: these simulations are generally quite expensive from a computational point of view, if good accuracy in the results is to be achieved. Usually Reynolds Averaged Navier Stokes (RANS) simulations are performed, allowing a lower computational time at the cost of a lower resolution in the results obtained. The flow resolution accuracy of the results could be improved by using more computationally intensive models such as Detached Eddy Simulations (DES) and Large Eddy Simulations (LES).
If the interest in VGs simulations is related to global parameters and performance estimation accuracy, it is possible to further simplify the calculations and simulations by using lower fidelity models such as the BAY model or Integral Boundary Layer codes.
Examples of these simplifications are present in [51], in which a modified version of the BAY model is tested, together with another analytical model. In this paper, two different models of VGs are compared, considering a test case of a single vortex generator mounted on a flat plate. The two models considered are Actuator

Vortex Generator Model (AcVG), based on the lifting force theory used in the BAY Model, and the analytical model developed by Velte [18], proposed considering the recognizable helical structure of the vortices for a given range of VG geometrical parameters. The AcVG Model permit the user to simulate in CFD codes the effect of VGs, without creating and grid-resolving the real geometry of the VG. These two models were compared with a fully resolved simulation and experimental results. It was shown that the analytical model deviates quite importantly from experiments values, whereas the AcVG model predicts well the flow field after the VG, saving computational time when compared to the fully grid resolved simulation.
In [52] instead, an Integral Boundary Layer approach was introduced. In this paper, the well-known aerodynamic tool XFOIL was modified to account for the additional dissipation due to the vortices in the boundary layer along the streamwise direction. The influence of the VG was considered forcing transition at the actual VG streamwise location on the airfoil profile. A semi-empirical relation is implemented, and according to the authors, the results show that the effect of the devices in the flow is well captured, considering different parameters such as VG height, VG angle of attack and chordwise position. The polar curves for the airfoils examined are in good agreement with the experimental data.

3.5 Conclusions

In this chapter vortex generators are described considering first the flow field modifications that they introduce. Their main effect is to create additional vortices in the boundary layer moving towards the base surface. During this movement, they entrain the high momentum fluid from the outer zones to the region near the wall surface. The vortex generally shows a lateral movement due to the presence of secondary vortices, and at a particular position in the streamwise direction, it moves away from the surface, creating a free shear layer region in the boundary layer. VGs are usually grouped in pairs, and depending on the configuration chosen, that is producing either counter-rotating or co-rotating vortices, they affect the flow field in a different way. In the counter-rotating one, the two primary vortices, characteristic of the pair configuration considered, converge on each other, creating a single primary vortex that will again lift off the wall at a given location, as in the single VG case. In the co-rotating configuration, the primary vortices do not converge on each other, but they move laterally as described for the single VG situation. They are characterized by a smaller radius and a lower circulation. For the counter-rotating configuration it is possible to identify two other subcategories based on their position with respect to each other: common flow-down and common flow-up, if respectively the flow between them moves down or away the wall.
The current research developments are then summarised. These are divided in two branches, the first focuses on flow-separation control, while the second is focused instead on flowfield characterization.
The main engineering applications are then presented, which can be divided in flow separation control for airfoils and wings, and non-airfoil applications. Flow separation control is related to Low Reynolds Airfoils, High Lift Airfoils, Highly Swept Wings and Transonic Airfoils; non-airfoil applications are subdivided in Noise Reduction, Engine Face Distortion Management in Compact Inlets, and Heat Exchangers.
In the end of the chapter, wind turbines applications are considered more in detail. VGs are generally placed in the hub portion of the blades, and generally in multiple strips. In this part of the radial blade development, the stall phenomenon manifests sooner than other radial positions, hence their purpose is delaying the presence of such flow conditions. In doing so, they tend to increase the angles of attack working range, enhancing power production. They suppress noise formation too, decreasing the vortex shedding phenomenon and its associated frequency.
The research in this field is related currently to CFD simulations for flowfield characterization and modelling efforts in lower fidelity simulation codes (e.g panel codes with Integral Boundary Layer formulations).

Chapter 4

Test Cases

In this chapter, the test case simulations that were initially run to verify the SU2 solver capabilities are described.
First, the reference paper from which the test cases were designed is briefly summarized, describing how the experimental data were obtained. This paper also contains the experimental values of the VG configurations considered in Chapter 5 and Chapter 6. Then, the SU2 solver is introduced, reporting the current incompressible solver implementation used. The complications that were found during this thesis, regarding the convergence of the solver formulation, are highlighted using appropriate references.
The test cases run consist of a comparison of the turbulence models implemented in SU2 at the time of writing this thesis. This is followed by a mesh dependency of the simulations conducted and by a verification of the influence of the farfield boundary condition that is to be used. The procedure to generate these test cases is described, from the Pre-Processing phase involving the CAD model creation and the mesh-grid generation, to the CFD simulations setup and results discussion.

4.1 Reference Paper

The reference paper for the experimental data, to compare the simulations with, is [23]. The airfoils presented in this paper are the FFA W3-241 and FFA W3-301, first presented by Bjork [53], and the NACA 63-430. The experimental data were obtained from a measurement campaign in the VELUX wind tunnel. This wind tunnel is of the closed-return type, characterized by an open test section. The cross-section of the test section has an area of $7.5 * 7.5\, m^2$, with a length of $10.5\, m$. The cross section of the jet of air in the wind tunnel is $3.4 * 3.4\, m^2$. The maximum flow velocity achievable is $45\, m/s$. The airfoils tested were manufactured with a chord of $0.6\, m$, extruding the airfoil profile with a span of $1.9\, m$. The manufactured airfoils profiles were positioned at a height of $1.7\, m$ on the test-stand used, at a distance of $3.2\, m$ from the exit of the nozzle, from which the air is blown into the wind tunnel. The wind tunnel reference pressure was measured using three Pitot tubes at different locations, as shown in Figure 4.1. These Pitot tubes were used also to estimate the turbulence level.
The airfoils pressure data were measured using a pressure-scanning module recording the pressure signals received. This module was mounted on the test-stand outside of the airfoil section, with tubes characterized by an equal length that were guided from the airfoil section considered to the pressure module. On the airfoils sections' surface, 62 pressure taps were placed along the chord at the centre of the extruded airfoil profile. These taps were positioned in a staggered configuration, to minimize the disturbances for each tap from the sorroundings ones. The taps positions for the airfoil sections considered in this thesis, the FFA-W3-241 and the FFA-W3-301, can be seen in Figure 4.2. Wind tunnel corrections were applied for the streamline curvature and the downwash, when considering the experimental results.

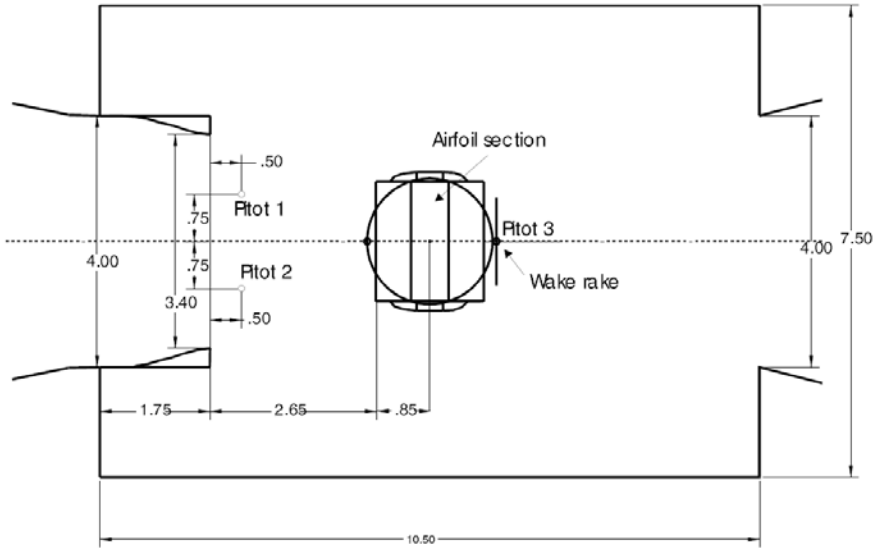

Figure 4.1: Wind tunnel dimensions, displaying the position of the Pitot tubes as well.

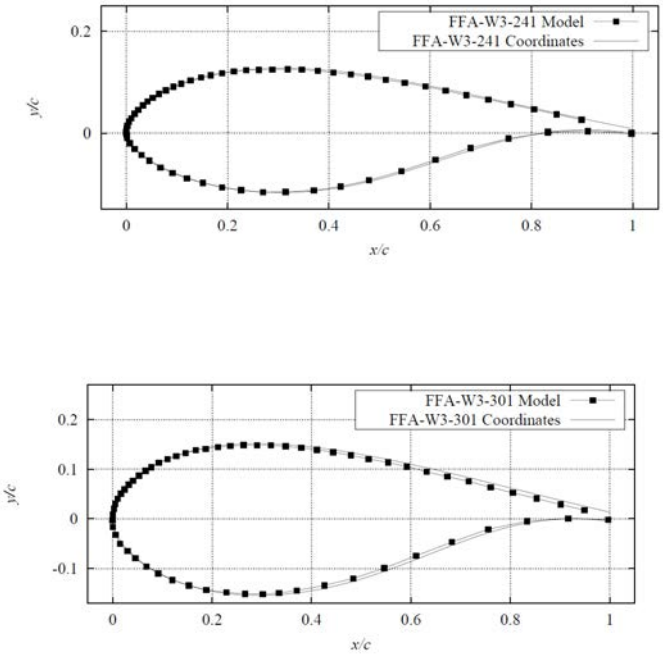

Figure 4.2: Pressure taps positions for the airfoil sections considered in this thesis. The pressure taps are located in correspondence to the reconstructed profile points indicated by the filled squares. The reconstructed model used in the experimental tests is derived from the original points of the airfoil sections, denoted by the continuos line without the filled squares.

4.2 SU2 Solver

The generic class structure of the SU2 solver can be described by Equation (4.1) [54]:

$$\partial_t U + \nabla \cdot \overrightarrow{F}^c - \nabla \cdot \overrightarrow{F}^v = Q \tag{4.1}$$

where U is the state variables vector, $\overrightarrow{F}^c(U)$ is the vector of the convective fluxes, $\overrightarrow{F}^v(U)$ is the vector of the viscous fluxes, and $Q(U)$ is the vector of the source terms.
This generic equation can be solved for a specific problem defining the vectors U, $\overrightarrow{F}^c(U)$, $\overrightarrow{F}^v(U)$, and $Q(U)$, together with the appropriate boundary and temporal conditions that are characteristic of the problem considered.
Different forms of the Reynolds Averaged Navier Stokes (RANS) equation are implemented in SU2. For the purposes of this thesis, only the incompressible formulation is considered, being wind turbine applications described by the incompressible set of RANS equations.
The incompressible solver formulation used in the SU2 collection of tools to solve Partial Differential Equations is described by Equation (4.1), with the following vectors:

$$U = \begin{pmatrix} P \\ \rho v_1 \\ \rho v_2 \\ \rho v_3 \end{pmatrix}, \qquad \overrightarrow{F}^c_i(U) = \begin{pmatrix} \beta^2 v_i \\ \rho v_i v_1 + P\delta_{i1} \\ \rho v_i v_2 + P\delta_{i2} \\ \rho v_i v_3 + P\delta_{i3} \end{pmatrix}, \qquad \overrightarrow{F}^v_i(U) = \mu_{tot} \begin{pmatrix} \cdot \\ \partial_i v_1 \\ \partial_i v_2 \\ \partial_i v_3 \end{pmatrix}, \qquad Q(U) = \begin{pmatrix} \cdot \\ \cdot \\ \cdot \\ -\frac{\rho}{Fr^2} \end{pmatrix}$$

where $i = 1, \ldots, 3$ refers to the related quantity component along the x, y, and z coordinate.
In these vectors the following variables are introduced:

- P is the pressure
- ρ is the density
- v_i is the velocity component
- δ_{ij} is the Kronecker delta function, with $j = 1, \ldots, 3$ related to the x, y, and z coordinate directions
- β^2 is the artificial compressibility parameter
- Fr is the Froude number
- $\mu_{tot} = \mu_{dyn} + \mu_{tur}$ is the total viscosity, sum of the dynamic viscosity μ_{dyn} and of the turbulent viscosity μ_{tur}

The boundary conditions available in SU2 for this incompressible solver formulation are: Euler wall (flow tangency), no-slip wall (adiabatic), far-field, symmetry boundaries, inlet boundaries (total conditions or prescribed mass flow), and outlet boundaries (back pressure prescribed).
This particular incompressible implementation is based on the artificial compressibility formulation by Chorin [55], that is valid only for steady-state problems definition.
A typical problem regarding this particular formulation is the convergence speed of the calculations using an Euler implicit integration scheme, expecially for low Mach number flows [56].
However, implicit Euler schemes are the most robust ones and are widely used for CFD applications, reason for which its usage in the remainder of the thesis.
Related to the convergence issue that is experienced with this kind of solvers, the choice of the optimal value for the β parameter influences considerably the convergence capabilities of the calculations.
In [56], a sensitivity study regarding the artificial compressibility factor for a low Mach number flows has been performed, showing that the optimal value is believed to be around $\beta = 1$. This optimal value allows a clear improvement in the convergence speed. This value is confirmed by an order of magnitude analysis of β that is conducted in [57]. If values greater or lower than $\beta = 1$ are considered, the convergence speed decreases drastically.

4.3 Turbulence Models Test Case

Given the previous considerations, during the test case phase of this thesis, a significant number of simulations were conducted, in order to investigate the solver capabilities and identify a suitable solver set-up for the final simulations. In the remainder of the chapter, the most significant results of all the simulations run is presented. As an initial test case, it was decided to compare the turbulence models implementations present in SU2, to test their accuracy. The aim of this test case was to reproduce the experimental data of the lift, drag and pressure coefficient of the FFA-W3-241 airfoil section. Since the computational time required to run a 3D simulation was already seen to be considerably high at this stage of the thesis, only 2D simulations were considered, reproducing the *Smooth* airfoil configuration experimental data.

4.3.1 Pre-Processing

In the Pre-Processing phase, the CAD model and the mesh grid are generated. The complete description of the mesh generation process can be found in Appendix B.
As for the CAD model, a zero-thickness surface delimited by the airfoil profile was created. This was done in *SolidWorks,* importing the airfoil coordinates through the *Curve Through XYZ Points* feature, and subsequently using the *Filled Surface* function for the generation of the zero thickness surface. The airfoil chord considered is the unitary chord $c = 1$.
The CAD model created was imported in *Pointwise* to generate the mesh of the 2D flow domain for the subsequent calculations. Connectors were created on the model imported, with the *Connectors On Database Entities* feature. After this, 250 nodes were assigned to the connectors on the suction side and on the pressure side of the airfoil, and 3 nodes to the connector of the blunt trailing edge. The O-Grid domain was created using the *Hyperbolic Normal Extrusion* feature, selecting all the connectors of the airfoil profile. The settings for the Normal Extrusion performed were:

- Method: Geometric Progression
- Initial $\Delta s = 4.56e-6$
- Growth Rate: 1.088
- Stop Conditions: Total Height=500

The initial Δs was calculated from the flat plate boundary layer theory as presented in [14]:

$$Re_x = \frac{\rho U_\infty c}{\mu} \;\Rightarrow\; C_f = \frac{0.026}{Re_x^{1/7}} \;\Rightarrow\; \tau_{wall} = \frac{C_f \rho U_\infty^2}{2} \;\Rightarrow\; U_{fric} = \sqrt{\frac{\tau_{wall}}{\rho}} \;\Rightarrow\; \Delta s = \frac{y^+ \mu}{U_{fric}\rho} \tag{4.2}$$

where ρ is the air density, U_∞ the free-stream velocity, c the airfoil chord, μ the dynamic viscosity, Re_x the Reynolds number related to the airfoil chord length, C_f the skin friction coefficient, τ_{wall} the shear stress at the wall, U_{fric} the friction velocity, and y^+ the dimensionless wall distance. To calculate the Δs spacing, the values of ρ, U_∞, c, and μ have to be given together with the desired y^+. For these test cases, a $y^+ = 1$ is specified. The resulting Δs value is halved, since it was seen that when using the original value computed with Equation (4.2), a y^+value slightly greater than 1 was obtained in the results. To resolve properly the boundary layer region, a $y^+ \leq 1$ should be ensured in all parts for the cells adjacent to the airfoil profile. The Growth Rate value was chosen to allow a sufficient number of cells in the normal direction to the airfoil profile, up to a distance $d = c$, with c being the airfoil chord. Resolving with a proper number of cells the region around the airfoil, up to a distance of one airfoil chord from the profile, was seen to ensure a good accuracy in the results from the simulations. With a Growth Rate of 1.088, 70 nodes in the normal direction were achieved. The Total Height value of the Stop Conditions ensures a domain boundary distant enough from the airfoil profile, to avoid the influence of the farfield boundary condition used for this domain boundary. The fluid domain external boundary is, therefore, distant from the airfoil profile 500 times the airfoil chord.

4.3.2 CFD Simulations Set-up

After creating the mesh grid, the CFD simulations can be run. All the turbulence models available in the SU2 solver were tested, that is, the Menter's Shear Stress Transport (SST), without a transition model [58], and the Spalart–Allmaras (SA), with the Bas-Cakmakcioglu (B-C) transition model [59]. The SU2 solver is set up through a configuration text file for each case considered. In this text file, the initial conditions specified are the free-stream flow properties, that is:

- the free-stream density ρ and the dynamic viscosity μ, and
- the free-stream velocity components as $(u, v, w) = U_\infty(cos(\alpha), sin(\alpha), 0)$.

In addition to these conditions, the Reynolds reference length c, corresponding to the airfoil chord, is specified as well. These values are introduced as an input in nondimensionalized quantities, allowing an easier set-up for each case. Considering the free-stream density ρ and the free-stream velocity magnitude U_∞, nondimensionalizing these values by the free-stream flow conditions result in unitary values $\rho_{adim} = 1$ and $U_{\infty_{adim}} = 1$ (the free-stream values are the same ρ and U_∞ values). The Reynolds reference length is for all the cases $c = 1$, since the nondimensionalized profile coordinates are used. The nondimensionalization allows to input the dynamic viscosity as the reciprocal of the Reynolds number $\mu = 1/Re$, simplifying the configuration file set-up. In addition to this, the free-stream velocity can now be simply inputted as the cosine and the sine of the simulated angle of attack.
The considered angles of attack are related to the simulation of a complete 2D polar curve, that is: $\alpha = -4.4°$, $\alpha = -2°$, $\alpha = -0.3°$, $\alpha = 0.9°$, $\alpha = 2.4°$, $\alpha = 4°$, $\alpha = 5.4°$, $\alpha = 7.1°$, $\alpha = 8.8°$, $\alpha = 10.2°$, $\alpha = 12.6°$, $\alpha = 14.4°$, $\alpha = 16.4°$, and $\alpha = 18.6°$.
Regarding the numerical schemes adopted for the flow numerical method set-up, it was decided to use the following:

- the JST model for the discretization of convective fluxes terms [60],
- the MUSCL scheme for the spatial discretization (2nd order scheme), and
- the Euler Implicit scheme for the time discretization.

As for the numerical schemes regarding the turbulent equation discretization, the following were chosen:

- a scalar upwind discretization for the convective fluxes terms,
- a 1st order scheme for the spatial discretization, and
- an Euler Implicit scheme for the time discretization.

In addition to the set-up described so far, the Multigrid algorithm implemented in the solver is used to accelerate the convergence of the simulation. This is adapted as follows:

- the Multigrid cycle type "W" was chosen;
- a total of 3 multigrid coarsening levels were chosen;
- the damping restriction factor value is 0.65;
- the damping prolongation factor value is 0.65;
- the pre-smooth number of cycles for each coarsening level is chosen as follows (1,1,1,1) (the first number refers to the original grid provided in input, to which apply the pre-smoothing cycles);
- the post-smooth number of cycles for each coarsening level is chosen as follows (1,1,1,1) (the first number refers to the original grid provided in input, to which apply the post-smoothing cycles);

The boundary conditions used for the simulations are:

- *wall boundary condition*, used for the airfoil profile, and
- *farfield boundary condition*, used for the external boundary delimiting the O-Grid mesh created.

The Courant-Friedrichs-Lewy (CFL) condition of the finest computational grid (the original grid provided in input) is ensured to be $CFL = 1$.
The convergence criterion for all the simulations was a reduction of the residuals order of magnitude 10^{-14}. The residuals are calculated as the log_{10} of the L-2 norm of original residuals for the entire computational domain. A High Performance Computing facility is used to run the aforementioned cases, and each simulated case is run on a single node consisting of 24 cores. All the simulations were run for a total of 150.000 iterations, corresponding to approximately 8 hours of computational time.

4.3.3 Results

With the simulations' set-up described in 4.3.2, the results for the two considered turbulence models are compared in terms of their lift and drag coefficients.
The values of the lift and drag coefficients are obtained from the *log.txt* file resulting from the SU2 simulations, and are shown in Figure 4.3 and Figure 4.4.
From Figure 4.3, it can be seen that the SA model with the B-C transition model is able to capture the linear portion of the lift curve with a very good accuracy, from an angle of attack of $\alpha = -4.4°$ to $\alpha = 7.1°$. When approaching stall conditions for the considered airfoil section, that can be evinced from the experimental curve shown, it can be seen that the simulation values of the lift coefficient start to deviate from the experimental curve considerably. The critical angle of attack and the corresponding lift coefficient value are overpredicted. The critical conditions are identifiable from the experimental values at an angle of attack of $\alpha = 10.2°$, with a corresponding lift coefficient value of $C_L = 1.37$, whereas the simulations show a critical condition at an angle of attack of $\alpha = 14.4°$, with a lift coefficient value of $C_L = 1.67$.
When considering the SST model without transition, in the linear portion of the lift coefficient curve, it can be seen that the lift coefficient values are underpredicted, with respect to the experimental reference values. This is in agreement with the fact that the SST turbulence model considered refers to fully turbulent flow conditions, being a transition model not implemented at the moment of writing this thesis. The flow conditions that are being simulated are only comparable with experimental values that are related to not fully developed turbulent flow conditions, such as the values considered in this comparison. These flow conditions require a flow-transition detection, since the airfoil experiences laminar flow conditions in the initial portion of the airfoil surface. Therefore, a turbulence model without a suitable transition model is not able to represent the flow conditions investigated for the *Smooth* case presented in the reference paper.
Regarding the stalled flow conditions, it can be seen that the simulations results are closer to the experimental values in terms of lift coefficient. From a qualitative point of view, this portion of the lift curve is better captured than the curve resulting from the simulations with the SA Turbulence model with the B-C transition model implementation. It can be seen, in fact, that with the SST turbulence model, the critical condition is identifiable at an angle of attack of $\alpha = 12.6°$, with a lift coefficient value of $C_L = 1.39$. Therefore, this condition is still overpredicted but with less difference from the experimental reference.
Regarding the comparison of the turbulence models related to the drag coefficient values obtained, shown in Figure 4.4, in the region where the drag coefficient is characterized typically by a constant value, the simulations considering the SA model with the B-C transition model show a very close prediction with the experimental reference values. The critical condition from the simulations is again identifiable at an angle of attack of $\alpha = 14.4°$, confirming what was obtained from the figure of the lift coefficient comparison.
The SST model shows a general overprediction in the constant-value portion of the drag coefficient curve. Under stalled flow conditions, the drag coefficient's results obtained with this model are closer to the experimental values, as seen in the lift coefficient values as well.

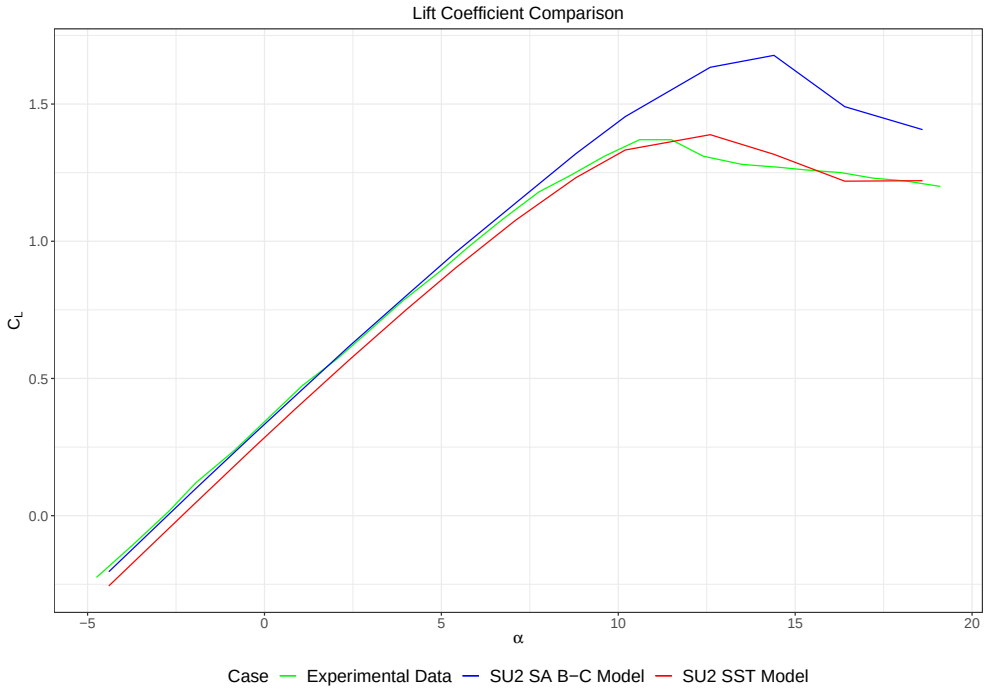

Figure 4.3: Turbulence models comparison by means of the resulting lift coefficient

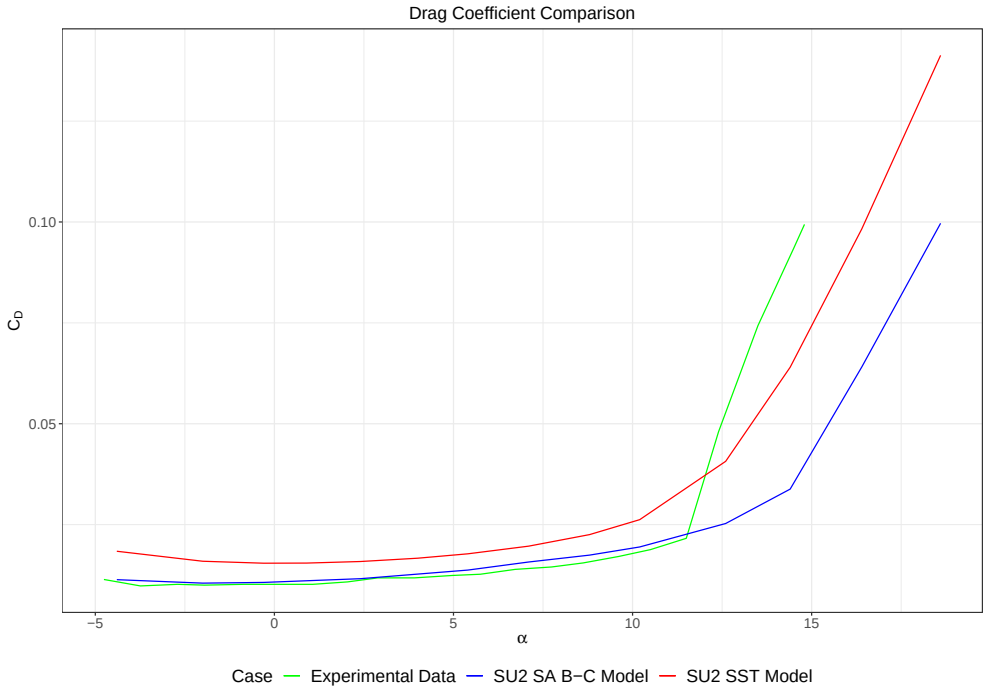

Figure 4.4: Turbulence models comparison by means of the resulting drag coefficient

From the simulations run, the results in terms of pressure coefficient values are compared as well, as can be seen in Figure 4.5 and Figure 4.6.
The pressure coefficient values are obtained directly from the *surface_flow.csv* file resulting from the SU2 simulations. The cases considered are related to an angle of attack $\alpha = 8.8°$, characterizing an incipient stalled flow condition, and to an angle of attack of $\alpha = 16.4°$, describing a developed stalled flow condition.
From Figure 4.5 describing the case at $\alpha = 8.8°$, it can be seen that at the suction side, the results using the SA with the B-C transition model show a general overprediction of the data until the $x/c = 0.7$ location. Around the leading edge and trailing edge location, at the suction side, these simulation values are close to the experimental data. As for the pressure side, it can be seen that at the leading edge, the results provided by the simulations are close to the experimental values, whereas at the trailing edge they are considerably distant from the experiments curve.
Regarding the pressure coefficient values obtained with the SST model, these are overall closer to the experimental values. Around the leading edge location at the suction side, it can be seen that the SST model overpredicts the pressure coefficient values. Therefore, it can be stated that the SST model is predicting the pressure coefficient distribution better than the SA with the B-C transition model, as was highlighted from the previous lift and drag coefficient figures.

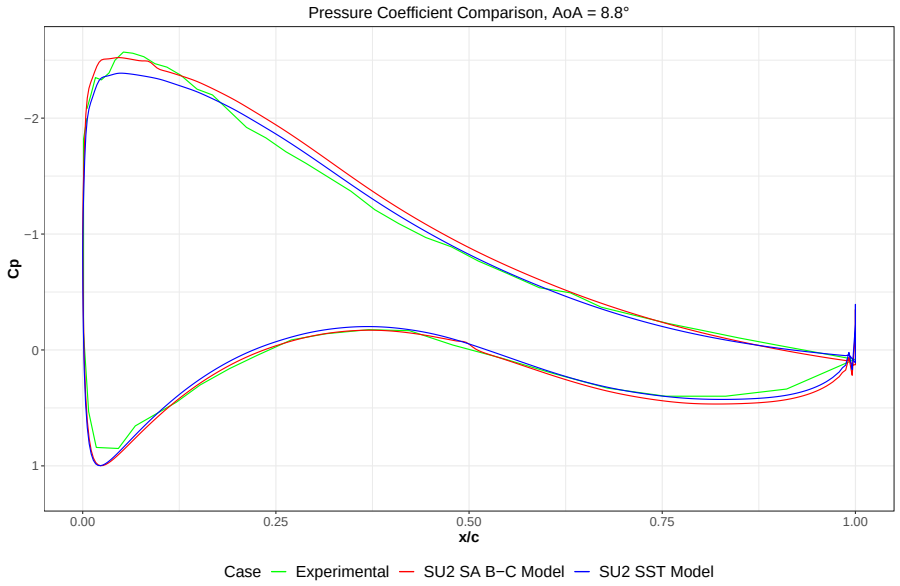

Figure 4.5: Turbulence models comparison by means of the resulting pressure coefficient, for the angle of attack of $\alpha = 8.8°$

In Figure 4.6, it can be seen that the pressure coefficient values at the pressure side are close to the experimental values. At the suction side, the pressure coefficient distribution shows a general overprediction in the first half of the airfoil profile, up to $x/c = 0.4$. For the remaining portion of the airfoil profile, the simulation values are underpredicting the experiments. This figure is representative of a developed stalled flow condition, in which the separation point at the suction side can be clearly identified with the location after which the pressure coefficient curve becomes flat. From the leading edge to the separation point, the figure shows that both the SST model and the SA with the B-C transition model are distant from the experimental reference curve. After the separation point, the SST model slightly overpredicts the experimental pressure coefficient curve at the suction side, whereas the SA with the B-C model underpredicts considerably the reference values.

From the evaluation of the pressure coefficient for the $\alpha = 16.4°$ case, it can be concluded that the curve behaviours described confirm what was stated from the comparison of the two turbulence models by means of the lift and drag coefficient curves. The SST model is able to better describe stalled flow conditions than the SA with the B-C transition model.

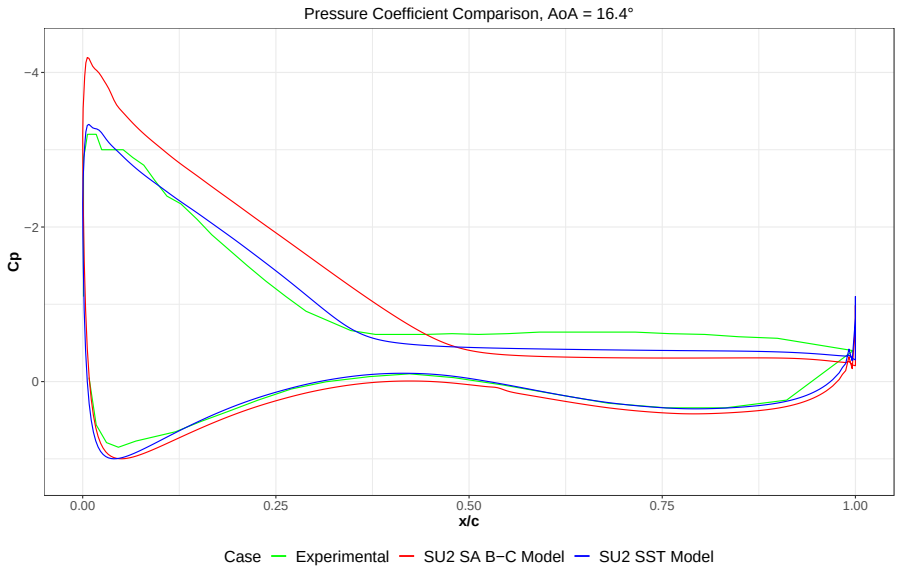

Figure 4.6: Turbulence models comparison by means of the resulting pressure coefficient, for the angle of attack of $\alpha = 16.4°$

4.3.4 Mesh dependency

To validate the 2D results obtained, a mesh dependency study was performed for two flow conditions, at an angle of attack $\alpha = 4°$ and $\alpha = 8.8°$. The turbulence model considered is the SA with the B-C transition model. Four different mesh grids were created, following the procedure described in 4.3.1. These mesh grids were generated with a progressively increasing number of cells, changing only the Growth Rate parameter of the Hyperbolic Normal Extrusion as reported in Table 4.1.

Total number of cells	**Growth Rate of the Hyperbolic Normal Extrusion**
95500	1.088
177000	1.04
274500	1.02
333000	1.01

Table 4.1: Computational grids created for the mesh dependency study

The results are presented in terms of pressure coefficient curves in Figure 4.7. It can be seen from both plots that the pressure coefficient curves for the four cases considered coincide. The results from the simulations are, therefore, independent from the mesh provided as an input, confirming that the simulations using the coarsest mesh of 95500 cells provide accurate results.

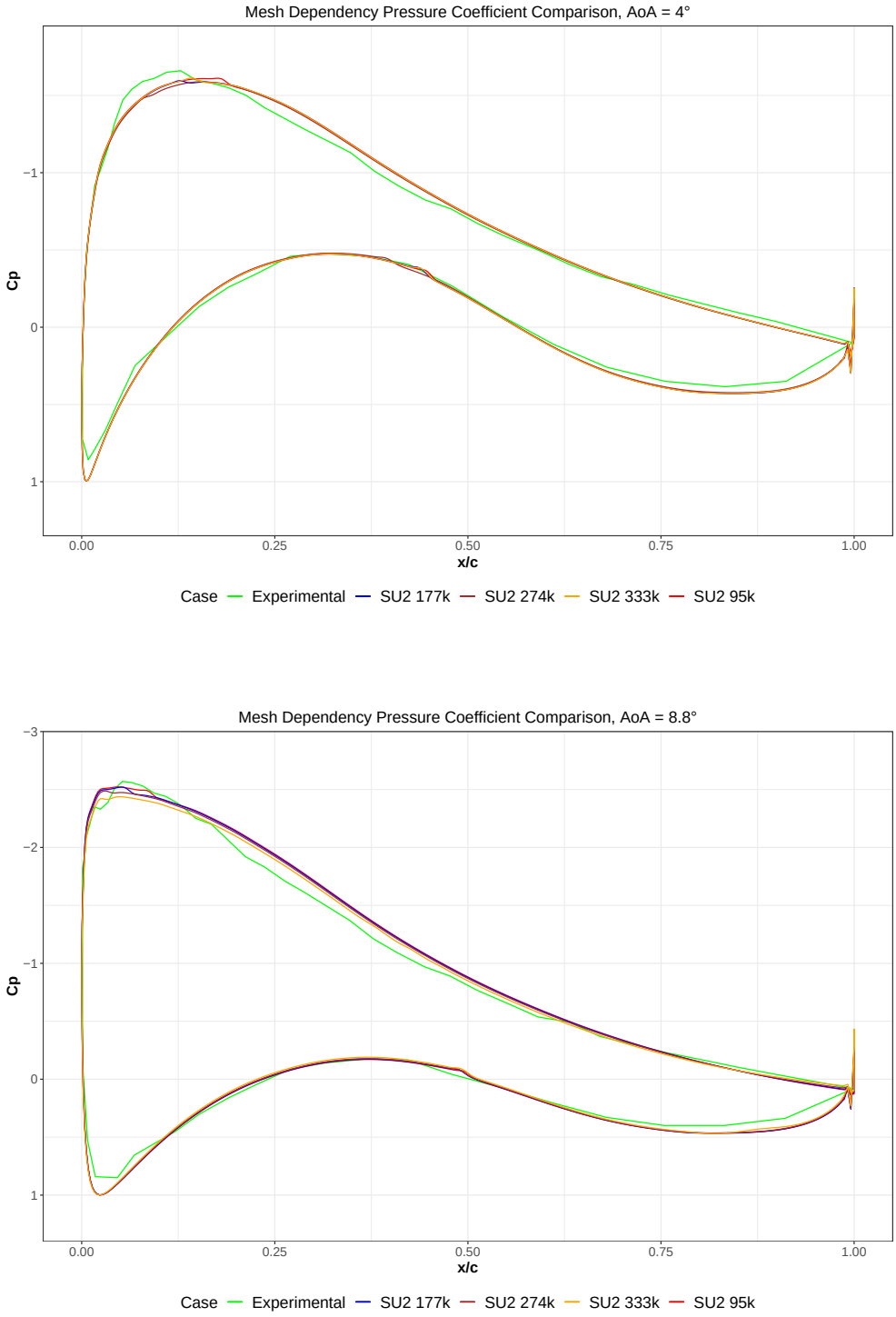

Figure 4.7: Mesh dependency results in terms of pressure coefficient values. The top image refers to the $\alpha = 4°$ flow condition. The bottom image refers to the $\alpha = 8.8°$ flow condition.

4.4 Farfield Boundary Condition Test Case

As a final test case, it was decided to verify the farfield boundary condition implementation present in SU2, to test its influence on the solutions obtained from the solver. Therefore, in this test case the lift and drag coefficients values are considered, for the FFA-W3-241 airfoil section at an angle of attack of $\alpha = 4°$. 2D simulations were run, comparing the values from the simulations with the experimental reference ones.

4.4.1 Pre-Processing

The CAD model creation and the mesh-grid generation procedure are the same as the ones described in 4.3.1. The only difference is the *Stop Conditions: Total Height* parameter, that is changed accordingly with the desired farfield distance to investigate.
A total of 8 different farfield distances were considered, from a distance of $500c$ to a distance of $20c$, with c being the airfoil chord.
Mantaining the same settings of the previous cases in 4.3.1 ensured a constant grid resolving of the boundary layer region, so that the influence of the farfield boundary condition regarding the lift and drag coefficients values could be evaluated without considering the effect of a different grid refinement.

4.4.2 CFD Simulations Set-Up

All the configuration settings reported in 4.3.2 were used in these test cases as well. The computational time and convergence criteria were approximately the same too. In the cases were the farfield distance was lower, this resulted in less computational cells created, therefore allowing a slight computational time saving.

4.4.3 Results

The results from this test case are reported in Table 4.2 and Figure 4.8.
Regarding the lift coefficient values, it can be seen from Figure 4.8 that decreasing the farfield distance from the airfoil profile decreases progressively the lift coefficient values. When considering the influence on the drag coefficient, lowering the farfield distance is seen to increase the drag. Comparing the different lift coefficient values with the experimental reference data, it can be seen that from a farfield distance of $300c$ on to lower distances, the lift computed from the simulations results in underpredicted values. As for the drag, it is seen that generally the increased farfield distance causes larger overprediction of the corresponding computed values.

Farfield Distance	Lift Coefficient	Drag Coefficient
500*c	0.800619	0.012736
400*c	0.798316	0.012938
300*c	0.792990	0.013427
200*c	0.794651	0.013296
100*c	0.790585	0.013717
60*c	0.788235	0.013999
40*c	0.784383	0.014434
20*c	0.773285	0.015655

Table 4.2: Farfield test case results in terms of lift and drag coefficient. The airfoil considered is the FFA-W3-241 at an angle of attack of $\alpha = 4°$.

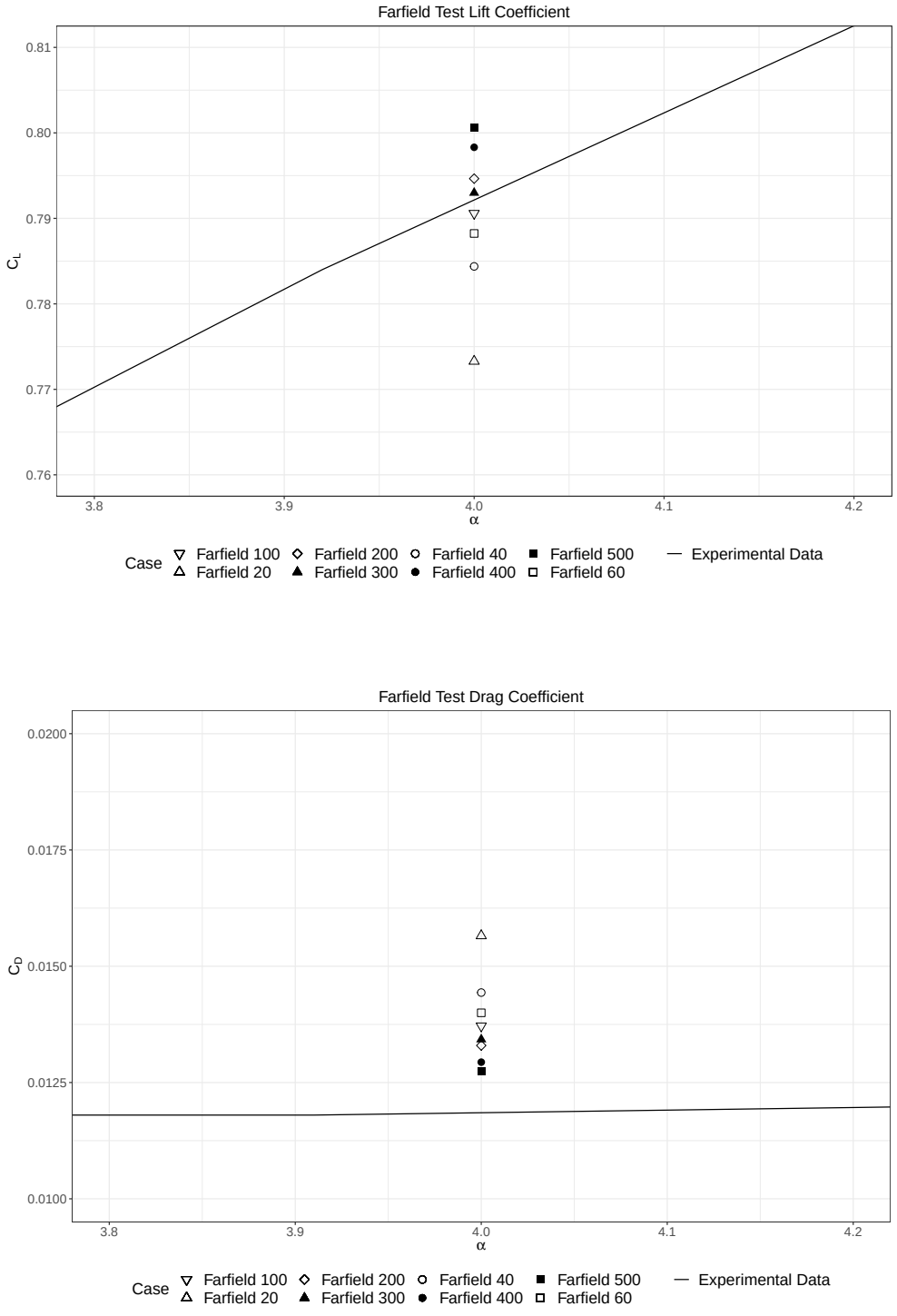

Figure 4.8: Farfield test case results in terms of lift and drag coefficient. The airfoil considered is the FFA-W3-241 at an angle of attack of $\alpha = 4°$. The top image shows the lift coefficient results. The bottom image shows the drag coefficient resulting values.

4.5 Conclusions

In this chapter the initial test-cases phase of this thesis is presented. The reference paper for the experimental data to test is first introduced, describing briefly how the data were obtained.
The SU2 incompressible solver is then described, highlighting its set-up complications due to the particular solver formulation.
Then the test cases conducted are reported. Two main test cases were considered, one testing the turbulence models' accuracy in terms of lift, drag and pressure coefficient values, and another verifying the influence of the farfield boundary condition regarding the lift and drag coefficient values obtained.
The test cases run for the turbulence models show that the SA turbulence model with the B-C transition model is able to reproduce better the experimental results, when considering flow conditions characterizing the linear portion of the lift coefficient curve, that is non stalled flow conditions. The SST model implemented is instead able to capture more accurately the flow features of stalled flow conditions. These results will be used when setting up the final simulations, differentiating the set-up with regards to the flow condition considered. The main interest of this thesis is demonstrating the SU2 solver capabilities in resolving properly the flow conditions investigated with respect to the experimental reference data, thus a suitable choice of turbulence models is necessary in light of these results.
The test case run verifying the influence of the farfield boundary condition shows that, when considering a distance from the airfoil profile not far enough, the lift coefficient values decrease progressively as shorter distances are used, with a corresponding increase in the drag coefficient values. With this information, the choice of the farfield distance from the airfoil profile will be maintained at a value of 500 times the airfoil chord length, since this value is regarded to be far enough for the simulations to not be influenced by it.

Chapter 5

Methodology

In this chapter the methodology followed in the Pre-Processing, in the CFD Simulations Set-Up and in the Post-Processing phases is presented.
First, the experimental reference is introduced, providing the geometrical parameters to recreate the experimental configurations for the simulations.
Then, the Pre-Processing phase is briefly described. This phase involves the CAD model creation and the computational mesh generation process.
In the CFD Simulations Set-Up section, the numerical models and the set-up of the configuration files that are used to run the simulations are reported.
In the final part of the methodology, the Post-Processing phase is described in detail, indicating the procedures used to create each figure presented in the Results chapter.

5.1 Experimental Reference

The reference paper is [23]. In this paper, the airfoils are tested both as simple extruded airfoils shape and as extruded airfoils with vortex generators placed on the top surface.
The vortex generators tested experimentally are the typical triangular vanes, placed orthogonally to the airfoil surface. They are arranged in a common-flow-down configuration, that is, an arrangement in pairs with equal and opposite angles, calculated relatively to the airfoil chord. Their height increases towards the airfoil trailing edge.
The Reynolds number used is $Re = 1.6 * 10^6$, for all the experiments conducted, and the turbulence intensity at the inlet of the test section is 1%.
The VG design configurations considered in the reference paper are the ones depicted in Figure 5.1, where the corresponding geometrical dimensions are displayed.
In the simulations performed in this thesis, only the FFA-W3-241 and the FFA-W3-301 airfoil profiles are considered.
Out of all the configurations presented in the paper, the ones simulated are:

- For the FFA-W3-301 airfoil profile:
  - *Smooth*, the configuration without VGs mounted on top of the suction side surface,
  - *VG x/c=0.2 h=6mm*, the configuration with a VG strip placed at a normalized streamwise position of *x/c=0.2*, characterized by VGs with a height of *h=6mm*
  - *VG x/c=0.3 h=6mm*, the configuration with a VG strip placed at a normalized streamwise position of *x/c=0.3*, characterized by VGs with a height of *h=6mm*

- For the FFA-W3-241 airfoil profile:
  - *Smooth*, the configuration without VGs mounted on the top surface,
  - *VG x/c=0.2 h=4mm*, the configuration with a VG strip placed at a normalized streamwise position of *x/c=0.2*, characterized by VGs with a height of *h=4mm*
  - *VG x/c=0.2 h=6mm*, the configuration with a VG strip placed at a normalized streamwise position of *x/c=0.2*, characterized by VGs with a height of *h=6mm*
  - *VG x/c=0.3 h=6mm*, the configuration with a VG strip placed at a normalized streamwise position of *x/c=0.3*, characterized by VGs with a height of *h=6mm*

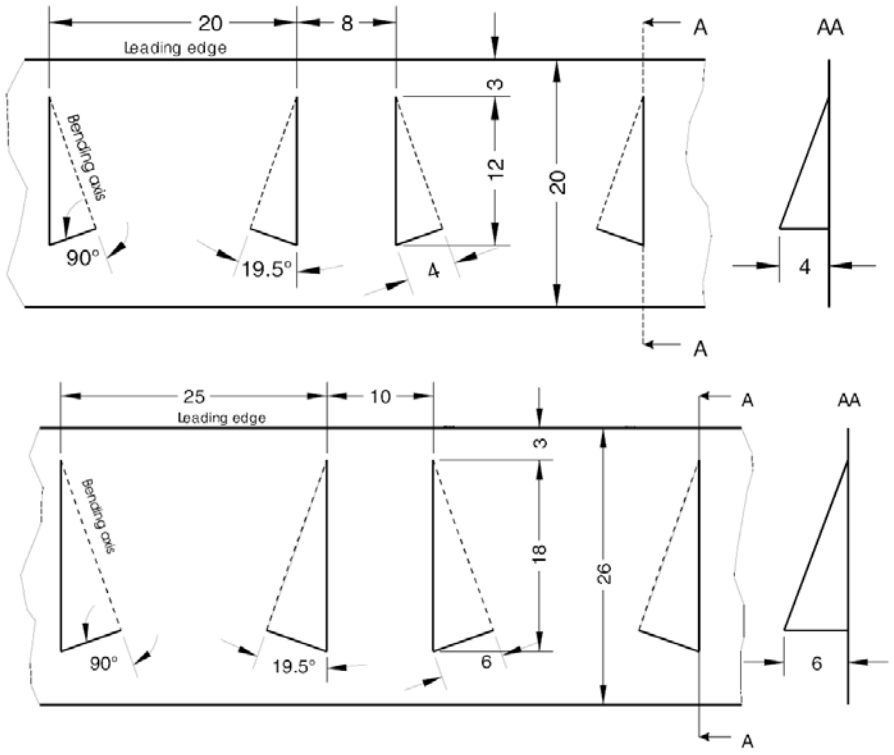

Figure 5.1: Original VG geometrical dimensions from [23]. In the top image the dimensions for the VG with height *h=4mm* are shown. In the bottom image the dimensions for the VG with height *h=6mm* are instead displayed. The dimensions reported are in millimeters.

The airfoil chord considered was the unitary chord $c = 1$, enabling the original normalized airfoil coordinates to be used. Following this choice, the VG dimensions were appropriately changed as shown in Figure 5.2. It was decided to reduce the computational domain to half the original VG pair domain, for reasons related to the boundary conditions available in the solver, as explained in Section §5.3.

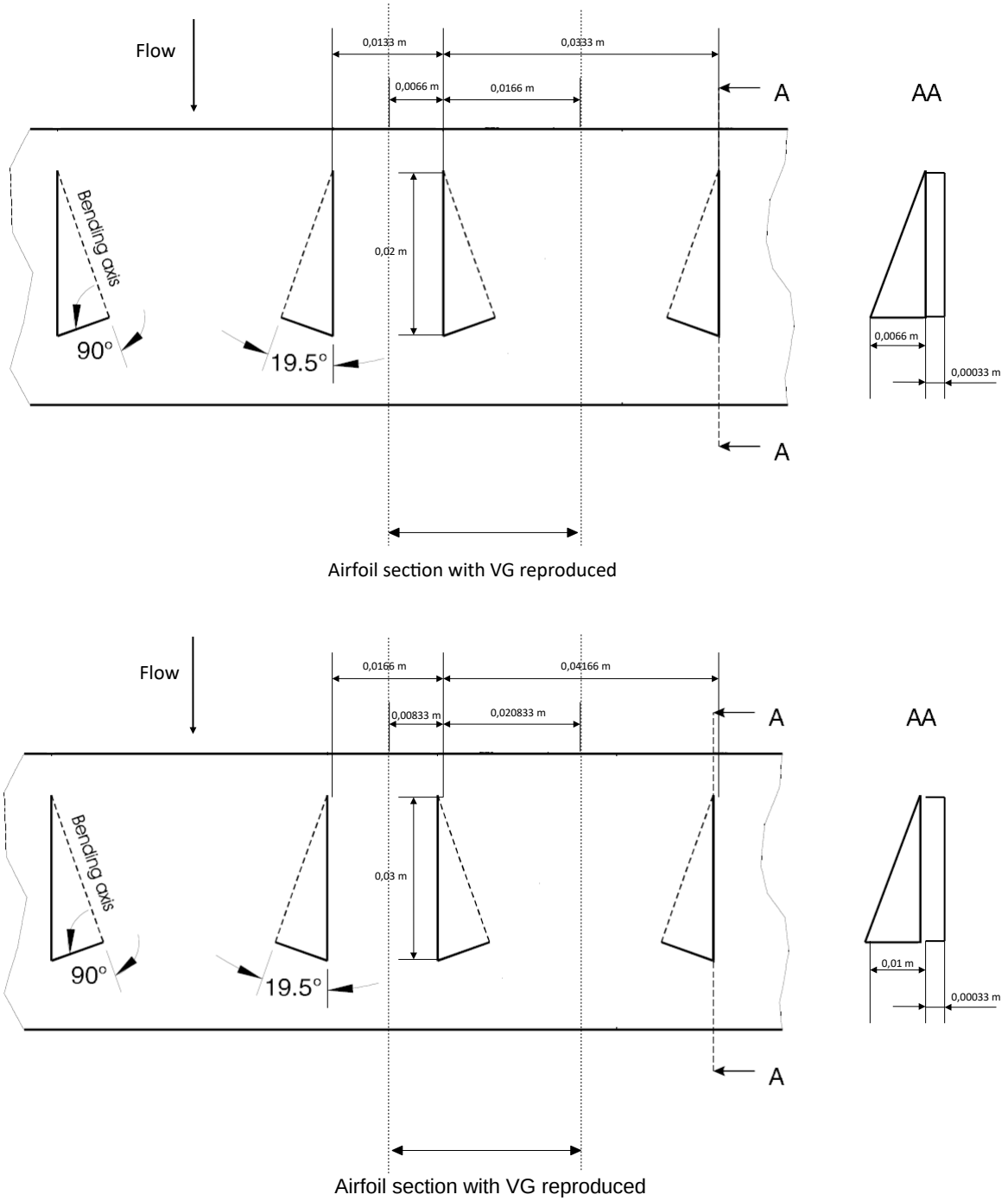

Figure 5.2: Scaled dimensions for the airfoil sections with VG reproduced. In the top image the dimensions used for the VG cases with height h=*4mm* are displayed. In the bottom image the dimensions used for the VG cases with height h=*6mm* are instead shown.

5.2 Pre-Processing

In this section the CAD model creation and the mesh generation process are presented. For the CAD model creation, only a brief explanation is provided, since this step of the Pre-Processing phase is easily reproducible without the need for a detailed description. As for the mesh generation process, this is only summarized, since the complete mesh generation process is reported in Appendix C and Appendix D.

5.2.1 CAD Model Creation

Prior to executing the simulations, a 3D CAD model needs to be created to reproduce the half section depicted in Figure 5.2.
The 3D CAD model is generated using the commercial software *SolidWorks*. The steps to create the 3D CAD model, for both the Smooth and the VG simulations, can be summarized in the following steps:

1. Import the airfoil profile coordinates from the corresponding text file (in Solidworks this could be achieved using the *Curve Through XYZ Points* feature)

2. Create 2 planes parallel to the airfoil profile imported in step 1. These 2 planes are positioned at an equal and opposite distance from the airfoil profile. On these planes project the airfoil profile. Then, from the 2 projected profiles, create the extruded airfoil section using a Loft-like function. This produces a better 3D model of the airfoil section, as can be seen in Figure 5.3. In *SolidWorks* this was achieved using the *Loft* function.

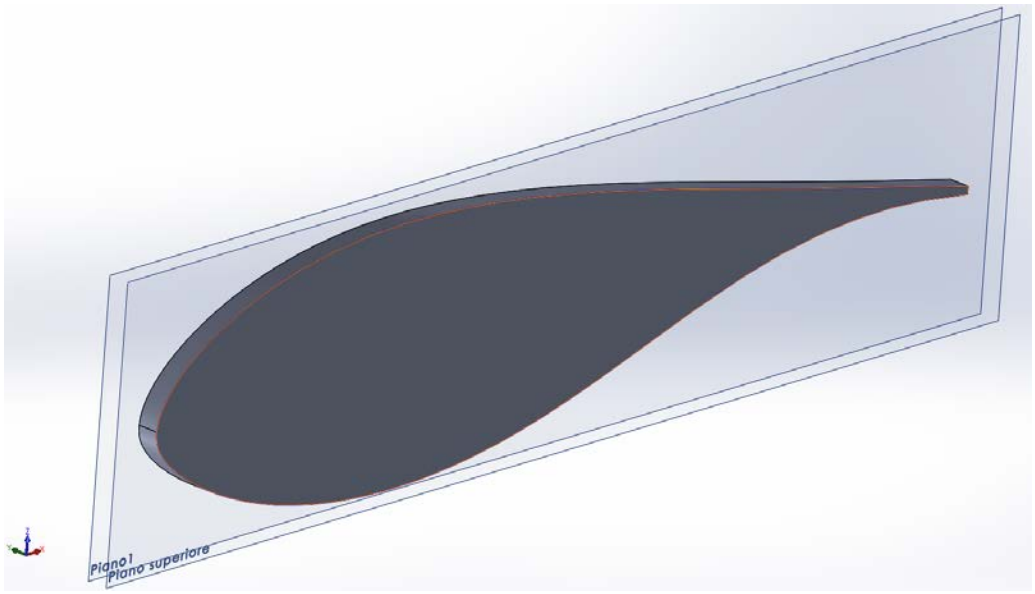

Figure 5.3: Smooth airfoil section extruded

3. In case an additional VG CAD model has to be created for the corresponding simulations:

   (a) Create a plane parallel to the airfoil profile imported in step 1, at a specified distance from the minimum-spanwise-coordinate plane created in step 2. On this plane, a vertical line is drawn at the VG leading edge streamwise position, intersecting the suction side surface of the airfoil section, as seen in Figure 5.4.

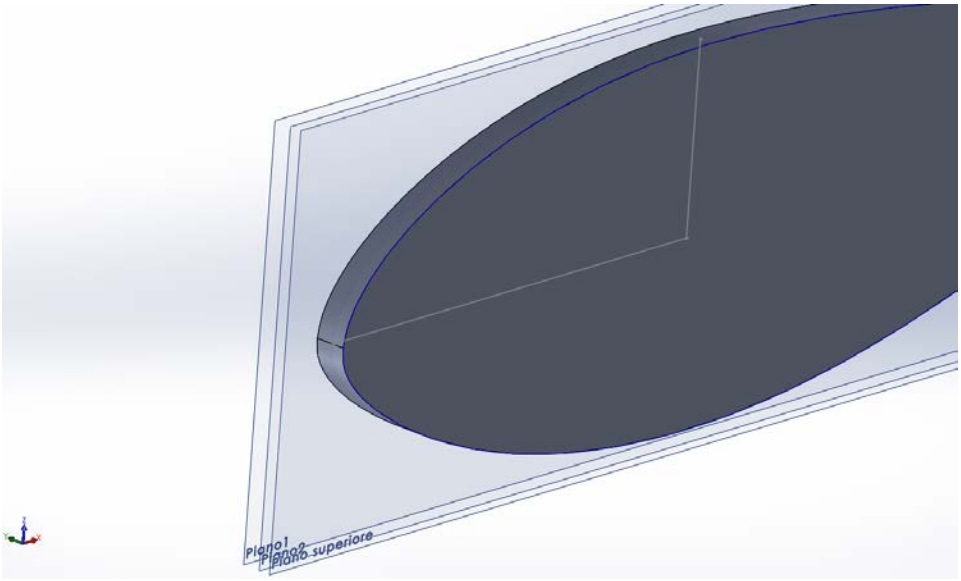

Figure 5.4: Plane created to position the VG at the given streamwise coordinate location

   (b) Create a plane using the vertical line as reference, and specifying an inclination angle equal to the VG inclination angle, as shown in Figure 5.5. On this plane, the trapezoidal sketch of the VG is created.

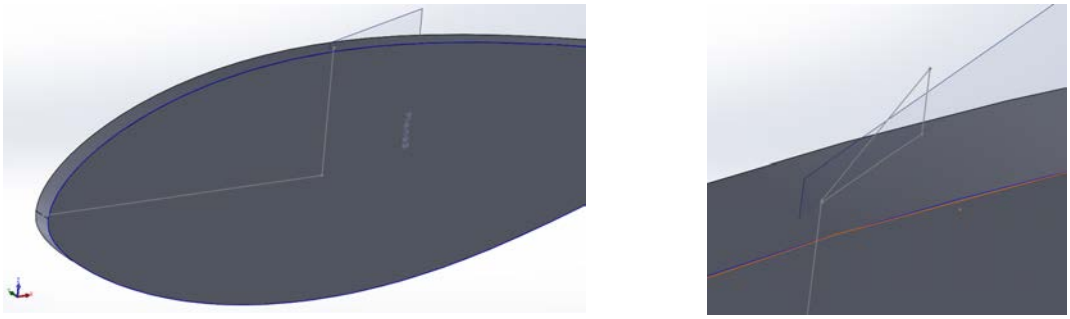

Figure 5.5: The plane created for the VG sketch is shown in the left figure. The trapezoidal VG sketch is shown in the right figure.

(c) Project this sketch on the two extreme planes delimiting the airfoil section, that were created in step 2, as shown in Figure 5.6.

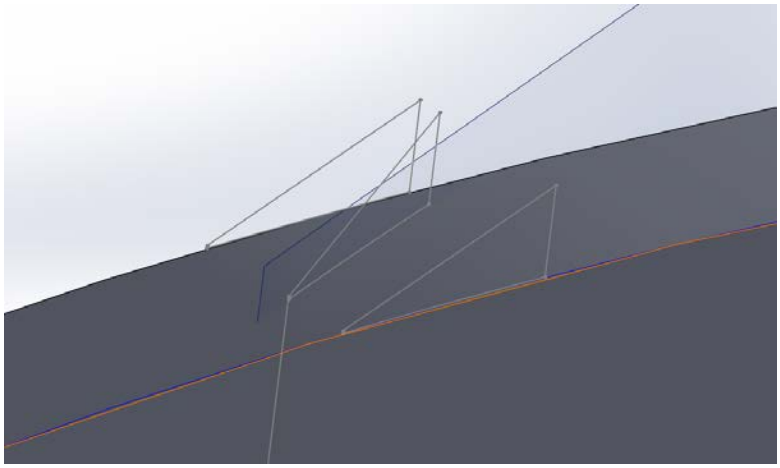

Figure 5.6: VG sketch projected on the side planes.

(d) Create 2 extruded lofts, from the VG sketch to both opposite projected sketches created in (c). These lofts are representative of the mesh blocking strategy used to create the computational grid for the simulations, as it can be seen in Figure 5.7.

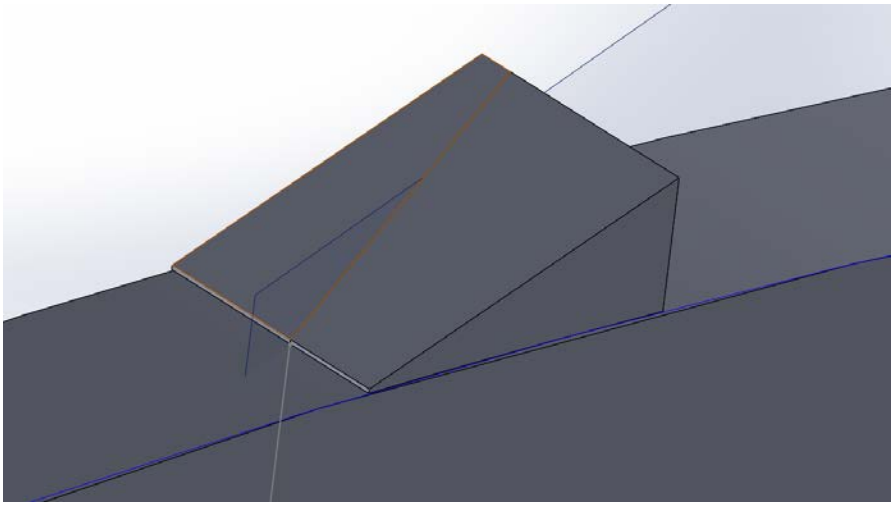

Figure 5.7: VG blocks for the mesh blocking strategy.

The VG was modeled as a 2D surface of zero thickness that is shared between the two lofts created in (d). It was determined to create a trapezoidal profile for the VG, considering the base band thickness together with the triangular shape of the actual VG. The resulting trapezoidal sketch allows an easier mesh creation on the VG surface.

5.2.2 Mesh Generation Process

After the CAD model design phase, the computational grid is created using the commercial software *Pointwise*. The main steps for the creation of the 3D grid representing the flow domain are the following:

1. Import the CAD model and create connectors on the database entities imported, as shown in Figure 5.8.

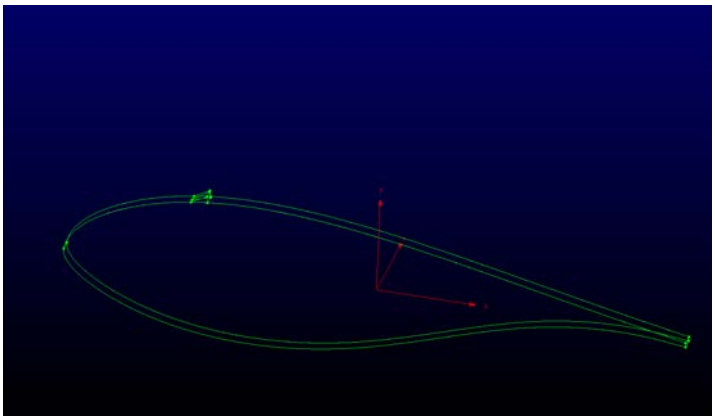

Figure 5.8: CAD model imported

2. When a VG case is considered:
   (a) Mirror the trapezoid blocks as in Figure 5.9.

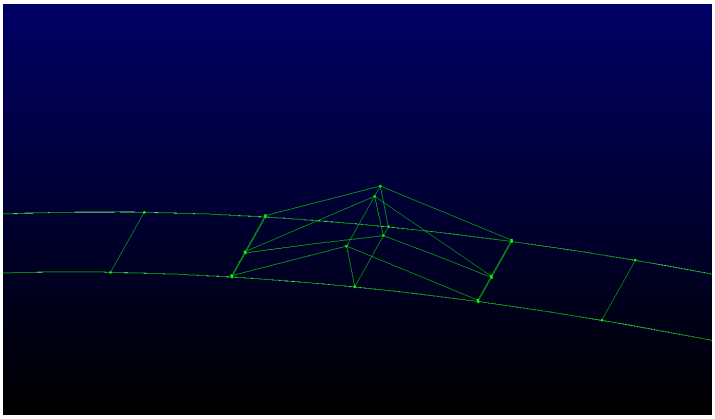

Figure 5.9: VG trapezoid blocks mirrored

   (b) Create a 2D mesh for each surface of the original and mirrored VG blocks.

(c) Create the 3D mesh blocks from the mesh surfaces generated in (b), as shown in Figure 5.10.

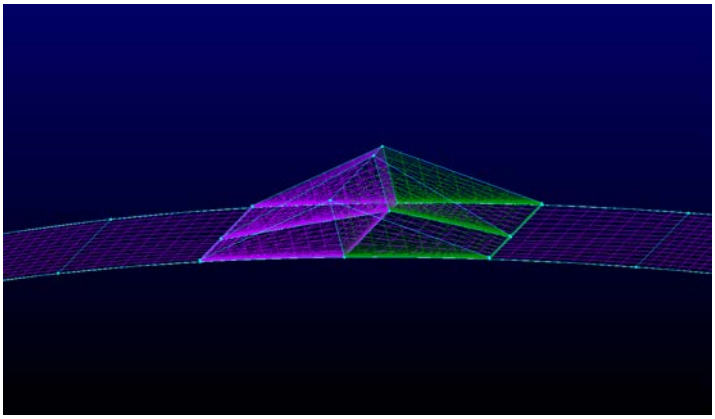

Figure 5.10: Mesh surfaces for the VG trapezoid blocks.

3. Generate the airfoil surface mesh. When a VG case is considered, the surface mesh for the portion of the surface not occupied by the presence of the original and mirrored VG blocks is generated.

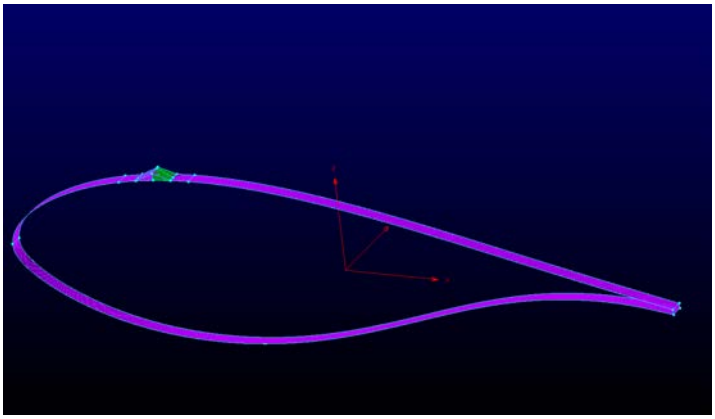

Figure 5.11: Airfoil surface mesh.

4. Generate the 3D grid for the flow domain, using the hyperbolic normal extrusion feature as follows:

   (a) If a Smooth case is considered, generate directly the whole flow domain grid extruding from the airfoil surface, as it can be seen in Figure 5.12.

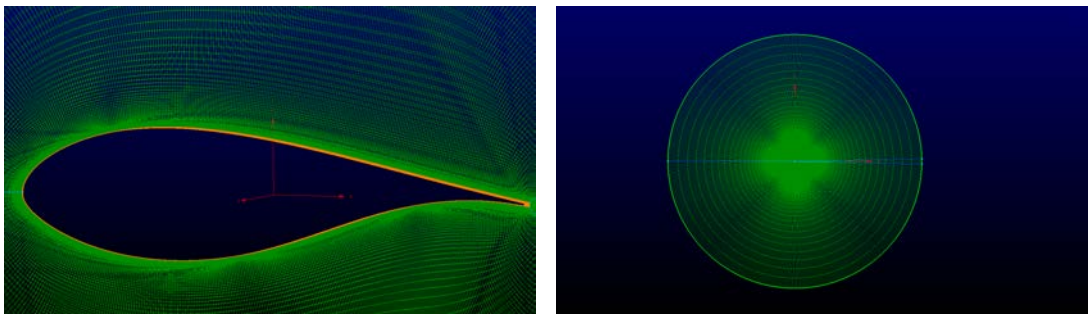

Figure 5.12: Generated 3D flow domain mesh for the Smooth airfoil case.

   (b) If a VG case is considered, an extrusion from the airfoil surface is first generated, to match the mesh surfaces of the VG base band. Subsequently, select all the outer spanwise mesh surfaces generated, and extrude them to create the final flow domain. This can be seen in Figure 5.13 and Figure 5.14.

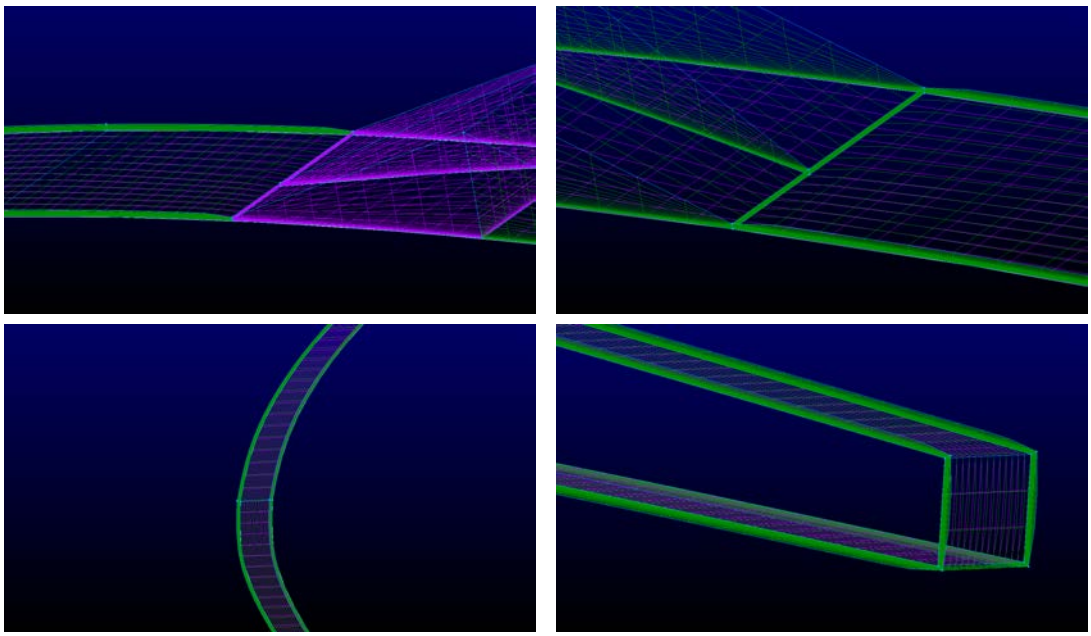

Figure 5.13: First boundary layer normal hyperbolic extrusion

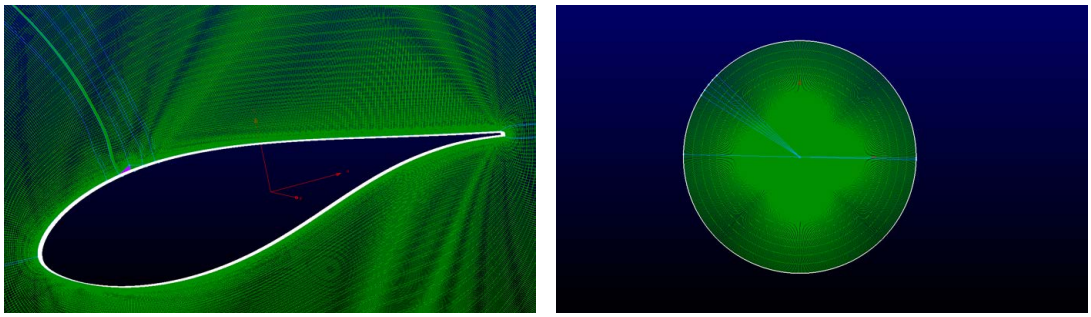

Figure 5.14: Generated 3D flow domain mesh for VG airfoil cases.

The blocking strategy, used for resolving the flow domain near the VG, is chosen in order to create a more uniform cell distribution in the vicinity of the VG surface modeled. If the VG blocks are not mirrored, the trapezoidal shape introduced will cause an excessive cell stretching in the region immediately downstream of the VG.
In the hyperbolic normal extrusion phase, the initial grid spacing of the first cells adjacent to the airfoil surface and the growth ratio of the subsequent extruded cells have a fundamental importance in properly resolving the boundary layer.
The initial grid spacing value Δs is derived from the flat plate boundary layer theory as presented in [14]:

$$Re_x = \frac{\rho U_\infty c}{\mu} \quad \Rightarrow \quad C_f = \frac{0.026}{Re_x^{1/7}} \quad \Rightarrow \quad \tau_{wall} = \frac{C_f \rho U_\infty^2}{2} \quad \Rightarrow \quad U_{fric} = \sqrt{\frac{\tau_{wall}}{\rho}} \quad \Rightarrow \quad \Delta s = \frac{y^+ \mu}{U_{fric} \rho}$$

where ρ is the air density, U_∞ the free-stream velocity, c the airfoil chord, μ the dynamic viscosity, Re_x the Reynolds number related to the airfoil chord length, C_f the skin friction coefficient, τ_{wall} the shear stress at the wall, U_{fric} the friction velocity, and y^+ the dimensionless wall distance.
To calculate the Δs spacing, the values of ρ, U_∞, c, μ have to be provided together with the desired y^+. For all the cases simulated, a $y^+ = 1$ is specified.
For the whole hyperbolic normal extrusion, a growth factor of less than 10%, with respect to the previous cell progressively generated, is ensured. This provides an adequate number of cells in the boundary layer region. The maximum extrusion distance was guaranteed to be 500 times the chord length, to avoid any possible influence of the farfield boundary condition, as highlighted in Chapter 4.
The mesh generated is of the O-Grid type, with approximately 2.5 million cells in the VG cases, and 1.5 million cells for the Smooth cases.
The cells created have a hexahedral shape throughout the whole computational domain.
The mesh quality metrics Equiangular Skewness and Aspect Ratio indicate that the grids created are of appropriate quality. An Equiangular Skewness maximum value of 0.63 is ensured for both the Smooth and the VG cases. As for the Aspect Ratio, this metric presents large values in the boundary layer region, expecially in the very first cells adjacent to the airfoil surface with Aspect Ratio values of 24000. This is due to the very thin spanwise distance considered in choosing the geometrical boundaries of the flow domain to be simulated. These boundaries choice follows from the geometrical parameters of the original VG configuration tested in the reference paper, and therefore can not be avoided. Since all the cells on the airfoil surface are of the hexahedral type, normal to the surface and following the airfoil profile curvature, it is possible to conclude that even with these high Aspect-Ratio-values the cells created are of acceptable quality. The constraint imposed of cells normal to the airfoil profile introduces more computational benefits than disadvantages.

5.3 CFD Simulations Set-Up

After creating the grids for all the configurations, the simulations can be run.
It was determined to run the configurations mentioned previously at angles of attack that hypothetically would refer to stalled conditions, or near-stalled conditions. These angles of attack are chosen by visually inspecting the lift coefficient and drag coefficient curves, identifying the flow conditions around the maximum lift coefficient value after which the airfoils are proved to stall.
In addition to this selection of angles of attack conditions, the test-cases run in Chapter 4 are used to select the turbulence model that allows the best flow results. The difference in turbulence models employed is due to the fact that the current SU2 implementation does not provide full set of turbulence models yet. The models implemented are the Spalart–Allmaras (SA) [61] and the Menter's Shear Stress Transport (SST) [58]. For the SA model, the transition is considered using the Bas-Cakmakcioglu (B-C) transition model [59], whereas for the SST model no transition model implementation is present so far.
From the test cases, it is seen that the SA model, with the transition phenomena described by the B-C model, predicts the flow in the boundary layer, up to the expected maximum lift coefficient, with good accuracy. The linear portion of the lift coefficient matches the experimental results. When approaching stalled conditions, this model departs from the experimental results considerably. Therefore, being the SST model known to capture best the flow features under developed turbulent conditions like the ones in deep stall, from the expected point of maximum lift coefficient on, the SST model is chosen instead of the SA B-C used previously. In the following simulations the SA B-C model is used for most of the cases, to try to capture the transition flow region inevitably experienced by the airfoils considered.
The complete list of choices for the turbulence models is reported in Table 5.1 for the FFA-W3-241 airfoil section, and in Table 5.2 for the FFA-W3-301 section:

Angle of Attack	**Smooth**	**VG x/c=0.2 h=4mm**	**VG x/c=0.2 h=6mm**	**VG x/c=0.3 h=6mm**
8.8°	SA B-C Model	SA B-C Model	SA B-C Model	SA B-C Model
10.2°	SST Model	SST Model	SST Model	SST Model
12.6°	SST Model	SST Model	SST Model	SST Model
14.4°	SST Model	SST Model	SST Model	SST Model

Table 5.1: Turbulence models-choice for the FFA-W3-241 simulated cases

Angle of Attack	**Smooth**	**VG x/c=0.2 h=6mm**	**VG x/c=0.3 h=6mm**
9°	SA B-C Model	SA B-C Model	SA B-C Model
11.2°	SA B-C Model	SA B-C Model	SA B-C Model
12.9°	SA B-C Model	SA B-C Model	SA B-C Model
14.6°	SA B-C Model	SA B-C Model	SA B-C Model

Table 5.2: Turbulence models-choice for the FFA-W3-301 simulated cases

The SU2 solver is set-up through a configuration text file for each case considered.
In this text file the initial conditions specified are the free-stream flow properties, that is:

- the free-stream density ρ and the dynamic viscosity μ, and
- the free-stream velocity components as $(u, v, w) = U_\infty(cos(\alpha), sin(\alpha), 0)$.

In addition to these conditions, the Reynolds reference length c, corresponding to the airfoil chord, is specified as well.

These values are introduced as an input in nondimensionalized quantities, allowing an easier set-up for each case.
Considering the free-stream density ρ and the free-stream velocity magnitude U_∞, nondimensionalizing these values by the free-stream flow conditions results in unitary values $\rho_{adim} = 1$ and $U_{\infty_{adim}} = 1$ (the free-stream values are the same ρ and U_∞ values). The nondimensionalization, together with the Reynolds reference length, that is for all the cases $c = 1$ since the nondimensionalized profile coordinates are used, allows to input the dynamic viscosity as the reciprocal of the Reynolds number $\mu = 1/Re$, simplifying the configuration file setup. In addition to this, the free-stream velocity can now be simply inputted as the cosine and the sine of the simulated angle of attack.
Regarding the numerical schemes adopted for the flow numerical method set-up it was decided to use the following:

- the JST model for the discretization of convective fluxes terms [60],
- the MUSCL scheme for the spatial discretization (2nd order scheme), and
- the Euler Implicit scheme for the time discretization.

As for the numerical schemes regarding the turbulent equation discretization, the following were chosen:

- a scalar upwind discretization for the convective fluxes terms,
- a 1st order scheme for the spatial discretization, and
- an Euler Implicit scheme for the time discretization.

In addition to the set-up described so far, the Multigrid algorithm implemented in the solver is used to accelerate the convergence of the simulation. This is adapted as follows:

- the Multigrid cycle type "W" was chosen;
- a total of 2 multigrid coarsening levels were chosen;
- the damping restriction factor value is 0.65;
- the damping prolongation factor value is 0.65;
- the pre-smooth number of cycles for each coarsening level is chosen as follows (1,1,0) (the first number refers to the original grid provided in input, to which apply the pre-smoothing cycles);
- the post-smooth number of cycles for each coarsening level is chosen as follows (1,1,1) (the first number refers to the original grid provided in input, to which apply the post-smoothing cycles);

The boundary conditions used for the simulations are:

- *wall boundary condition*, used for the airfoil and VG surfaces,
- *farfield boundary condition*, used for the most external grids delimiting the O-Grid mesh created, in the spanwise direction,
- *symmetry boundary condition*, used for the lateral grid surfaces delimiting the O-Grid mesh.

The choice to reproduce half of the original strip section with the VG pair is considered to reduce the size and the number of grid cells of the computational mesh. At the lateral boundaries of the flow domain, the *symmetry boundary condition* ensures that the VG pair effect is reproduced correctly.
The Courant-Friedrichs-Lewy (CFL) condition of the finest computational grid (the original grid provided in input) is ensured to be $CFL = 1$.

The convergence criteria for all the simulations was a reduction of the residuals order of magnitude of 10^{-8}. The residuals are calculated as the log_{10} of the L-2 norm of original residuals of the entire computational domain.
A High Performance Computing facility is used to run the aforementioned cases, and each case simulated is run on a single node consisting of 24 cores. All the simulations were run for a total of 80.000 iterations, corresponding to approximately 5 days of computational time. This time constraint was quite prohibitive, and therefore a mesh dependency study was not performed, since it would have required an excessive amount of time for each case considered. The mesh dependency performed in Chapter 4, for the 2D airfoil profile, was considered to validate the grid refinement chosen for the final 3D cases run. Therefore, the same boundary layer grid refinement was ensured at each spanwise position, in order to validate the simulations to run.

5.4 Post Processing

In the Post Processing phase, the data was extracted from the simulations to produce the figures displayed in Chapter 6. In the extraction phase, the open-source software *Paraview* is used, exploiting the *Python* scripting capabilities provided with this software. The plots were created using both the *R* language and the *Python* language. The extraction phase and the subsequent figure creation step are therefore fully automated. An example of the scripts created can be found in Appendix E and Appendix F.
In the following subsections, the data extraction procedures and the consequent post-processing steps for the figures created are explained.

Figure 6.1

In this figure, the lift coefficient and drag coefficient data are shown, comparing the experimental values and the simulations results for the FFA-W3-301 airfoil section.

Experimental Data

The experimental data displayed are obtained from the reference paper [23], digitizing Figure 10-3 and Figure 10-4 from the mentioned document.

Simulations Data

The simulation data are obtained directly from the log file output of the SU2 simulations.

Figure Creation

The figure is created by combining all the single plots for the *Smooth*, the *VG x/c=0.2 h=6mm* and the *VG x/c=0.3 h=6mm* configurations in a unique figure.

Figure 6.2

In this figure, the lift coefficient and drag coefficient data are shown, comparing the experimental values and the simulations results for the FFA-W3-241 airfoil section.

Experimental Data

The experimental data displayed are obtained from the reference paper [23], digitizing Figure 5-3 and Figure 5-4 from the mentioned document.

Simulations Data

The simulation data are obtained directly from the log file output of the SU2 simulations.

Figure Creation

The figure is created by combining all the single plots for the *Smooth*, the *VG x/c=0.2 h=4mm*, the *VG x/c=0.2 h=6mm* and the *VG x/c=0.3 h=6mm* configurations in a unique figure.

Figure 6.3

In this figure, the pressure coefficient data are shown, comparing the experimental values and the simulations results for the FFA-W3-241 airfoil section.

Experimental Data

The experimental data displayed are obtained from the reference paper [23], digitizing the following figures from the mentioned document:

- Figure 4-1 for the *Smooth* case experimental values, considering the angles of attack $\alpha = 8.8^{\circ}$, $\alpha = 10.2^{\circ}$, $\alpha = 12.6^{\circ}$, $\alpha = 14.4^{\circ}$;
- Figure 5-1 for the experimental values of the *VG x/c=0.2 h=4mm*, the *VG x/c=0.2 h=6mm* and the *VG x/c=0.3 h=6mm* cases, at an angle of attack of $\alpha = 10.2^{\circ}$;
- Figure 5-2 for the experimental values of the *VG x/c=0.3 h=6mm* at an angle of attack $\alpha = 14.4^{\circ}$.

For the *VG x/c=0.2 h=4mm* case in Figure 5-1, the original angle of attack reported in [23] is $\alpha = 10.1^{\circ}$. For consistency with the simulations data obtained at an angle of attack of $\alpha = 10.2^{\circ}$, in the remainder of the thesis, these experimental values are referred to as related to the $\alpha = 10.2^{\circ}$ angle of attack. This choice was made to be able to compare different VG configurations at the same angle of attack, since both the *Smooth* and the VG cases remaining are reported for $\alpha = 10.2^{\circ}$.
It is believed that the difference between the angle of attack actually tested in the experiments ($\alpha = 10.1^{\circ}$), and the one considered for the simulations to compare the experiments with ($\alpha = 10.2^{\circ}$), will not add a considerable error to the qualitative discussion related to the *VG x/c=0.2 h=4mm* plot.
The same reasoning applies to the *VG x/c=0.3 h=6mm* case in Figure 5-2, where the original angle of attack is $\alpha = 14.0^{\circ}$. This experimental case will be referred to as the $\alpha = 14.4^{\circ}$, hypothesizing again not an appreciable qualitative difference with the simulations considered. The angle of attack $\alpha = 14.4^{\circ}$ chosen for the simulations allows a comparison with the corresponding *Smooth* case.

Simulations Data

The simulation data are obtained extracting the pressure coefficient values already present in the *surface_flow.vtk* files, created during the SU2 simulations.
If a VG solution is considered, first the VG surface mesh coordinates are extracted from the corresponding *.pw* file. This is achieved selecting the grid surface interactively in *Pointwise*, exporting it in the *.cgns* file format. Obtaining the VG coordinates allows, in the following data extraction phase, to skip points too close to the VG surface. In this way points in the computational cells immediately adjacent to the VG surface are not extracted, avoiding unwanted interpolation errors due to the underlying *Paraview* functions used.
The data extraction phase is described in the following steps:

1. Import data of interest. These are contained in the *surface_flow.vtk* file and in the *VG_ GridPoints.cgns* file. The last file is imported only if a VG simulation case is considered.

2. Input the variable string name to extract, in this case the corresponding pressure coefficient string in the *surface_flow.vtk* file. All the variables present in this file are first displayed in the standard output, to allow the user to choose the proper string name.

3. Input whether the streamwise and spanwise locations, from which to extract the data, are to be created linearly spaced, or are user-specified.

   (a) In case they are to be created linearly spaced, input first the number of points in the streamwise direction to consider, and then the number of points in the spanwise direction for each streamwise location. These linearly spaced coordinates are created between the streamwise and spanwise airfoil surface boundaries, automatically obtained from the *surface_flow.vtk* solution.

   (b) In case the locations are user-specified, input first the streamwise locations and then the spanwise ones for each streamwise position.

4. If the simulation results, from which to obtain the pressure coeffcient data, are of a VG case simulated, then store the coordinates near the VG surface to avoid. These coordinates are selected from the ones created in Step 3.

5. Extract the data, avoiding in the extraction loop the coordinates stored in Step 4:

   (a) First slice the *surface_flow.vtk* solution with a plane normal to the streamwise axis.

   (b) Then slice the extracted data from (a) with a plane normal to the spanwise axis.

   (c) From the extracted data in (b), get the coordinates of the point in the upper and the one in the lower airfoil surface (that is respectively suction side and pressure side)

   (d) Find the unique indices of the points from (c), in the complete *surface_flow.vtk* solution

   (e) Extract the flow variable of interest, in this case the pressure coefficient, from the complete *surface_flow.vtk* solution. This is done using the unique indices from (d).

6. Store the extracted pressure coefficient data, together with the coordinates of the locations considered, in the corresponding *.csv* files for the upper and lower airfoil surface

Figure Creation

The figure is created by combining all the single plots for the configurations mentioned in the Experimental Data subsection in a unique figure.

Figure 6.4

In this figure, the pressure coefficient data are shown, comparing the experimental values and the simulations results for the FFA-W3-301 airfoil section.

Experimental Data

The experimental data displayed were obtained from the reference paper [23], digitizing the following figures from the mentioned document:

- Figure 9-1 for the *Smooth* case experimental values, considering the angles of attack $\alpha = 9^{\circ}$, $\alpha = 11.2^{\circ}$, $\alpha = 12.9^{\circ}$, $\alpha = 14.6^{\circ}$;
- Figure 10-1 for the experimental values of the *VG x/c=0.2 h=6mm* and the *VG x/c=0.3 h=6mm* cases, at an angle of attack of $\alpha = 9^{\circ}$;
- Figure 5-2 for the experimental values of the *VG x/c=0.3 h=6mm* at an angle of attack $\alpha = 12.9^{\circ}$.

The data from Figure 10-1 are originally referred to $\alpha = 9.4^{\circ}$ for the *VG x/c=0.2 h=6mm* case, and to $\alpha = 9.5^{\circ}$ for the *VG x/c=0.2 h=6mm* case.
The data from Figure 5-2 are also referred to a slightly different condition, that is $\alpha = 12.9^{\circ}$ for the *VG x/c=0.3 h=6mm*.
For analogous reasons as the ones stated for the previous cases in the Experimental Data subsection of Figure 6.3, the data will be referred to the angle of attack of the SU2 simulations, since a negligible difference regarding the qualitative behaviour of the curves displayed can be assumed.

Simulations Data

The simulation data are obtained extracting the pressure coefficient values already present in the *surface_flow.vtk* files, created during the SU2 simulations. The same extraction process described in the Simulations Data subsection of Figure 6.3 is also applied in this case.

Figure Creation

The figure is created by combining all the single plots for the configurations mentioned in the Experimental Data subsection in a unique figure.

Figure 6.5

In this figure, the pressure coefficient values from the simulations of the Smooth and the VG configurations are compared. The results displayed are related to the FFA-W3-241 airfoil at an angle of attack of $\alpha = 10.2^{\circ}$, and to the FFA-W3-301 airfoil at an angle of attack of $\alpha = 11.2^{\circ}$.

Simulations Data

The simulation data considered for the FFA-W3-241 plot are related to the *Smooth*, *VG x/c=0.2 h=4mm*, *VG x/c=0.2 h=6mm* and the *VG x/c=0.3 h=6mm* cases, for the angle of attack $\alpha = 10.2^{\circ}$.
Instead, the simulation data used for the FFA-W3-301 plot are related to the *Smooth*, *VG x/c=0.2 h=6mm* and the *VG x/c=0.3 h=6mm* cases, for the angle of attack $\alpha = 11.2^{\circ}$.
The simulation data are obtained extracting the pressure coefficient values already present in the *surface_flow.vtk* files, created during the SU2 simulations.
The same extraction process described in the Simulations Data subsection of Figure 6.3 is also applied in this case.

Figure Creation

The plots are created importing the data stored in the *.csv* files produced in the Simulations Data subsection. The data in each of the dataframes, for the configurations considered, are averaged for each streamwise location, calculating the arithmetic mean of all the spanwise locations extracted.
The figure is created by combining the plots for the configurations mentioned in the Simulations Data subsection in a unique figure.

Figure 6.6

In this figure, the pressure coefficient values from the simulations of the Smooth and the VG configurations are compared. The results displayed are related to the FFA-W3-241 airfoil at an angle of attack of $\alpha = 14.4°$, and to the FFA-W3-301 airfoil at an angle of attack of $\alpha = 12.9°$.

Simulations Data

The simulation data considered for the FFA-W3-241 plot are related to the *Smooth*, *VG x/c=0.2 h=4mm*, *VG x/c=0.2 h=6mm* and the *VG x/c=0.3 h=6mm* cases, for the angle of attack $\alpha = 14.4°$.
Instead, the simulation data used for the FFA-W3-301 plot are related to the *Smooth*, *VG x/c=0.2 h=6mm* and the *VG x/c=0.3 h=6mm* cases, for the angle of attack $\alpha = 12.9°$.
The simulation data are obtained extracting the pressure coefficient values already present in the *surface_flow.vtk* files, created during the SU2 simulations.
The same extraction process described in the Simulations Data subsection of Figure 6.3 is also applied in this case.

Figure Creation

The plots are created importing the data stored in the *.csv* files produced in the Simulations Data subsection. The data in each of the dataframes, for the configurations considered, are averaged for each streamwise location, calculating the arithmetic mean of all the spanwise locations extracted.
The figure is created by combining the plots for the configurations mentioned in the Simulations Data subsection in a unique figure.

Figure 6.7

In this figure, the skin friction coefficient magnitude values from the simulations of the Smooth and the VG configurations are compared. The results displayed are related to the FFA-W3-241 airfoil at an angle of attack of $\alpha = 10.2°$, and to the FFA-W3-301 airfoil at an angle of attack of $\alpha = 11.2°$.

Simulations Data

The simulation data considered for the FFA-W3-241 plot are related to the *Smooth*, *VG x/c=0.2 h=4mm*, *VG x/c=0.2 h=6mm* and the *VG x/c=0.3 h=6mm* cases, for the angle of attack $\alpha = 10.2°$.
Instead, the simulation data used for the FFA-W3-301 plot are related to the *Smooth*, *VG x/c=0.2 h=6mm* and the *VG x/c=0.3 h=6mm* cases, for the angle of attack $\alpha = 11.2°$.
The simulation data are obtained extracting the skin friction coefficient values already present in the *surface_flow.vtk* files, created during the SU2 simulations.
The same extraction process described in the Simulations Data subsection of Figure 6.3 is also applied in this case, with two main differences:

- Only values at the suction side of the airfoil are extracted, since this is the surface where VGs are applied, and therefore where the favourable effects of VGs are better appreciated.

- From the SU2 simulations, values of skin friction along the 3D directions are provided. Since in the plots considered the skin friction magnitude is displayed, the extraction of all the three components is required. These skin friction values are subsequently used for calculating the skin friction magnitude when generating the plots.

Figure Creation

The plots are created importing the data stored in the *.csv* files produced in the Simulations Data subsection. The data in each dataframe are averaged for each streamwise location, calculating the arithmetic mean of all the spanwise locations extracted.
The skin friction coefficient magnitude is then computed as the square root of the three skin friction components extracted for each configuration.
The figure is created by combining the plots for the configurations mentioned in the Simulations Data subsection in a unique figure.

Figure 6.8

In this figure, the skin friction coefficient magnitude values from the simulations of the Smooth and the VG configurations are compared. The results displayed are related to the FFA-W3-241 airfoil at an angle of attack of $\alpha = 10.2°$, and to the FFA-W3-301 airfoil at an angle of attack of $\alpha = 11.2°$.

Simulations Data

The simulation data considered for the FFA-W3-241 plot are related to the *Smooth*, *VG x/c=0.2 h=4mm*, *VG x/c=0.2 h=6mm* and the *VG x/c=0.3 h=6mm* cases, for the angle of attack $\alpha = 10.2°$.
Instead, the simulation data used for the FFA-W3-301 plot are related to the *Smooth*, *VG x/c=0.2 h=6mm* and the *VG x/c=0.3 h=6mm* cases, for the angle of attack $\alpha = 11.2°$.
The simulation data displayed are obtained extracting the skin friction coefficient values already present in the *surface_flow.vtk* files, created during the SU2 simulations.
The same extraction process described in the Simulations Data subsection of Figure 6.3 is also applied in this case.

Figure Creation

The plots are created importing the data stored in the *.csv* files produced in the Simulations Data subsection. The data in each dataframe are averaged for each streamwise location, calculating the arithmetic mean of all the spanwise locations extracted.
The skin friction coefficient magnitude is then computed as the square root of the three skin friction components extracted for each configuration.
The figure is created by combining the plots for the configurations mentioned in the Simulations Data subsection in a unique figure.

Figure 6.9 and Figure 6.10

In these figures, the vorticity magnitude is displayed in contour plots for different streamwise locations. The results displayed are related to the FFA-W3-301 airfoil at an angle of attack of $\alpha = 12.9°$, for the *Smooth* and the *VG x/c=0.2 h=6mm* cases.

Simulations Data

The simulation data displayed are obtained extracting slices normal to the airfoil streamwise direction axis, from the *Results.vtk* files created during the SU2 simulations.
If a VG solution is considered, first the VG surface mesh coordinates are extracted from the corresponding *.pw* file. This is achieved by selecting the grid surface interactively in *Pointwise*, exporting it in the *.cgns* file format. Obtaining the VG coordinates allows, in the following data extraction phase, to skip locations too close to the VG surface. With this approach, points in the computational cells immediately adjacent to the VG surface are not considered, thus avoiding unwanted interpolation errors due to the underlying *Paraview* functions used.
The data extraction phase is described by the following steps:

1. Import data of interest. These are contained in the *Results.vtk*, in the *surface_flow.vtk* file and in the *VG_GridPoints.cgns* file. The last file is imported only if a VG simulation case is considered.

2. Compute the vorticity magnitude from the data provided by the SU2 simulation:

   (a) The first step is to create a vector quantity in Paraview, corresponding to the velocity field. This is performed using the Calculator function, creating a vector variable *Vel_Field* from all the velocity components already present in the *Results.vtk* file.

   (b) In the second step the Python Calculator function is used, computing the curl of the velocity field created in (a). This produces the vorticity field.

   (c) In the third step, the vorticity magnitude is calculated from the vorticity field using the Calculator function

3. The resulting flow domain from 2.(c) is mirrored with respect to the global minimum spanwise location ('Y Min' option), using the function Reflect. This produces the flow domain for the VG pair.

4. Input the variables string names to extract, that is the corresponding vorticity magnitude string. All the variables present in this file are first displayed in the standard output, to allow the user to choose the proper string name.

5. Compute the normal vectors of the grid nodes in the airfoil surface solution *surface_flow.vtk*. This is done first using the ExtractSurface function on the *surface_flow.vtk* data, in order to produce a PolyData dataset. This PolyData dataset is subsequently given in input to the function GenerateSurfaceNormals, producing the resulting surface data together with the computed normals.

6. Input whether the streamwise and spanwise locations from which to extract the data, are to be created linearly spaced, or are user-specified.

   (a) In case they are to be created linearly spaced, input first the number of points in the streamwise direction to consider, and then the number of points in the spanwise direction for each streamwise location. These linearly spaced coordinates are created between the streamwise and spanwise airfoil surface boundaries, automatically obtained from the *surface_flow.vtk* solution.

   (b) In case the locations are user-specified, input first the streamwise locations and then the spanwise ones for each streamwise position.

7. If the simulation results are of a VG case simulated, then store the coordinates near the VG surface to avoid. These coordinates are selected from the ones created in Step 3.

8. Extract the data, avoiding in the extraction loop the coordinates stored in Step 4:

   (a) First, slice the results from 5. with a plane normal to the streamwise axis.

   (b) Then, slice the extracted data from (a) with a plane normal to the spanwise axis.

   (c) From the extracted data in (b), get the coordinates of the point in the upper airfoil surface (that is the suction side), find its unique index in the global solution, and extract the corresponding normal vector using this unique index.

   (d) Calculate the perpendicular normal to the one found from (c), and slice the flow domain from 2.(c) with this perpendicular normal computed, at the point location given from (c).

   (e) Resize the slice from (d), selecting only the solution in the airfoil suction side region. Resize further this result, selecting solution points up to a given distance specified by the user (this distance is selected in order to consider only the flow region affcted by the VG). The resizing process is done using the SelectPoints and ExtractSelection functions with the proper boolean expression

   (f) Extract the flow variable of interest, in this case the vorticity magnitude, from the resulting domain from (e).

   (g) Store the extracted vorticity magnitude data, together with the coordinates of the points considered, in the corresponding *.csv* files.

Figure Creation

The data stored in the *.csv* files produced in the Simulations Data subsection are imported, and the contour plots are created with equally spaced contour levels.
The figure is created by combining the plots for the configurations mentioned in the Simulations Data subsection in a unique figure.

Figure 6.11 and Figure 6.12

In these figures, the velocity components u, v and w, related to the corresponding coordinates directions x, y and z, are displayed in contour plots for different airfoil streamwise locations.
The results displayed are related to the FFA-W3-301 airfoil at an angle of attack of $\alpha = 12.9°$, for the *Smooth* and the *VG x/c=0.2 h=6mm* cases.

Simulations Data

The simulation data displayed are obtained extracting slices normal to the airfoil streamwise direction axis, from the *Results.vtk* files created during the SU2 simulations.
The extraction process is the same as described in the Simulations Data subsection of Figure 6.9 and Figure 6.10.

Figure Creation

The data stored in the *.csv* files produced in the Simulations Data subsection are imported, and the contour plots are created with equally spaced contour levels.
The figure is created by combining the plots for the configurations mentioned in the beginning of this subsection in a unique figure, with three columns: the first related to the u component, the second to the v component, and the third to the w component.

Figure 6.13

In this figure, the vorticity magnitude profiles at different streamwise locations are displayed, together with the boundary layer thickness evolution along the streamwise direction.
The results are related to the FFA-W3-241 airfoil at an angle of attack of $\alpha = 8.8°$, for the *Smooth* and the *VG x/c=0.2 h=6mm* cases.

Simulations Data

The simulation data displayed are obtained extracting lines normal to the airfoil streamwise direction axis, from the *Results.vtk* files created during the SU2 simulations.
If a VG solution is considered, first the VG surface mesh coordinates are extracted from the corresponding *.pw* file. This is done selecting the grid surface interactively in *Pointwise*, exporting it in the *.cgns* file format. Obtaining the VG coordinates allows, in the following data extraction phase, to skip locations too close to the VG surface. In this way points in the computational cells immediately adjacent to the VG surface are not extracted, avoiding unwanted interpolation errors due to the underlying *Paraview* functions used.
The data extraction phase is described by the following steps:

1. Import data of interest. These are contained in the *Results.vtk*, in the *surface_flow.vtk* file and in the *VG_GridPoints.cgns* file. The last file is imported only if a VG simulation case is considered.

2. Compute the vorticity magnitude from the data provided by the SU2 simulation:

   (a) The first step is to create a vector quantity in *Paraview*, corresponding to the velocity field. This is performed using the Calculator function, creating a vector variable *Vel_Field* from all the velocity components already present in the *Results.vtk* file.

   (b) In the second step the Python Calculator function is used, computing the curl of the velocity field created in (a). This produces the vorticity field.

   (c) In the third step, the vorticity magnitude is calculated from the vorticity field using the Calculator function

3. Input the variables string names to extract, in this case the corresponding vorticity magnitude string. All the variables present in this file are first displayed in the standard output, to allow the user to choose the proper string name.

4. Compute the normal vectors of the grid nodes in the airfoil surface solution *surface_flow.vtk*. This is done first using the ExtractSurface function on the *surface_flow.vtk* data, in order to produce a PolyData dataset. This PolyData dataset is subsequently given in input to the function GenerateSurfaceNormals, producing the resulting surface data together with the computed normals.

5. Input whether the streamwise and spanwise locations, from which to extract the data, are to be created linearly spaced, or are user-specified.

   (a) In case they are to be created linearly spaced, input first the number of points in the streamwise direction to consider, and then the number of points in the spanwise direction for each streamwise location. These linearly spaced coordinates are created between the streamwise and spanwise airfoil surface boundaries, automatically obtained from the *surface_flow.vtk* solution.

   (b) In case the locations are user-specified, input first the streamwise locations and then the spanwise ones for each streamwise position.

6. If the simulation results are of a VG case simulated, then store the coordinates near the VG surface to avoid. These coordinates are selected from the ones created in Step 3.

7. Extract the data, avoiding in the extraction loop the coordinates stored in Step 4:
   (a) First, slice the results from 4. with a plane normal to the streamwise axis.
   (b) Then, slice the extracted data from (a) with a plane normal to the spanwise axis.
   (c) From the extracted data in (b), get the coordinates of the point in the upper airfoil surface (that is the suction side), find its unique index in the global solution, and extract the corresponding normal vector using this unique index.
   (d) Create the normal polyline source, corresponding to the normal line to extract. This is done using the normal vector and the point coordinates on the airfoil surface obtained from (c)
   (e) Resample the flow solution calculated in 2.(c) with the normal line created in (d), using the function ResampleWithDataset.
   (f) Extract the flow variable of interest, in this case the vorticity magnitude, from the resulting domain from (e).
   (g) Store the extracted vorticity magnitude data, together with the coordinates of the points considered, in the corresponding *.csv* files

Figure Creation

The data stored in the *.csv* files produced in the Simulations Data subsection are imported.
The data for each streamwise location are averaged computing the arithmetic mean of the corresponding spanwise positions.
The resulting spanwise averaged data for each streamwise location are subset according to the value of the vorticity magnitude. A user-defined threshold is used in order to first select the solution data with a value of the vorticity magnitude equal or greater than the threshold specified.
From this subset of each streamwise location, the minimum vorticity magnitude value is detected, identifying the boundary layer thickness for that streamwise position.
In the end, all the streamwise vorticity magnitude profiles are grouped in plots displaying 5 profiles each, with the corresponding boundary layer thicknesses.
In each plot, both the Smooth and the VG case considered are shown.
The figure is created by combining these plots in a unique figure.

Figure 6.14

In this figure, the u velocity profiles at different streamwise locations are displayed, together with the boundary layer thickness evolution along the streamwise direction.
The results are related to the FFA-W3-301 airfoil at an angle of attack of $\alpha = 12.9°$, for the *VG x/c=0.3 h=6mm* configuration.

Simulations Data

The simulation data displayed are obtained extracting lines normal to the airfoil streamwise direction axis, from the *Results.vtk* files created during the SU2 simulations.
The extraction process is the same as described in the Simulations Data subsection of Figure 6.13.

Figure Creation

The data stored in the *.csv* files produced in the Simulations Data subsection are imported.
The data for each streamwise location are averaged computing the arithmetic mean of the corresponding spanwise positions.
The resulting spanwise averaged u components are plotted along the streamwise direction, grouped in plots displaying 5 profiles each.
In each plot, both the Smooth and the VG case considered are shown.

Figure 6.15, Figure 6.16 and Figure 6.17

In these figures, the integral boundary layer quantities evolution in the streamwise direction is displayed, that is the displacement thickness δ^*, the momentum thickness θ and the energy thickness θ^*.
The results are related to the FFA-W3-241 airfoil for all the angles of attack simulated, that is $\alpha = 8.8°$, $\alpha = 10.2°$, $\alpha = 12.6°$ and $\alpha = 14.4°$. The curves shown are related to all the previous angles of attack mentioned, and to all the configurations considered, i.e the *Smooth*, the *VG x/c=0.2 h=4mm,* the *VG x/c=0.2 h=6mm* and the *VG x/c=0.3 h=6mm*.

Simulations Data

The simulation data displayed are obtained extracting lines normal to the airfoil streamwise direction axis, from the *Results.vtk* files created during the SU2 simulations.
If a VG solution is considered, first the VG surface mesh coordinates are extracted from the corresponding *.pw* file. This is done selecting the grid surface interactively in *Pointwise*, exporting it in the *.cgns* file format. Obtaining the VG coordinates allows, in the following data extraction phase, to skip locations too close to the VG surface. In this way points in the computational cells immediately adjacent to the VG surface are not extracted, avoiding unwanted interpolation errors due to the underlying *Paraview* functions used.
The data extraction phase is described by the following steps:

1. Import data of interest. These are contained in the *Results.vtk*, in the *surface_flow.vtk* file and in the *VG_GridPoints.cgns* file. The last file is imported only if a VG simulation case is considered.
2. Compute the vorticity magnitude from the data provided by the SU2 simulation:
   (a) The first step is to create a vector quantity in *Paraview*, corresponding to the velocity field. This is performed using the Calculator function, creating a vector variable *Vel_Field* from all the velocity components already present in the *Results.vtk* file.
   (b) In the second step the *Python* Calculator function is used, computing the curl of the velocity field created in (a). This produces the vorticity field.

(c) In the third step, the vorticity magnitude is calculated from the vorticity field using the Calculator function

3. Input the variables string names to extract, in this case the u velocity component and the vorticity magnitude string. All the variables present in this file are first displayed in the standard output, to allow the user to choose the proper string name.

4. Compute the normal vectors of the grid nodes in the airfoil surface solution *surface_flow.vtk*. This is done first using the ExtractSurface function on the *surface_flow.vtk* data, in order to produce a PolyData dataset. This PolyData dataset is subsequently given in input to the function GenerateSurfaceNormals, producing the resulting surface data together with the computed normals.

5. Input whether the streamwise and spanwise locations, from which to extract the data, are to be created linearly spaced, or are user-specified.

   (a) In case they are to be created linearly spaced, input first the number of points in the streamwise direction to consider, and then the number of points in the spanwise direction for each streamwise location. These linearly spaced coordinates are created between the streamwise and spanwise airfoil surface boundaries, automatically obtained from the *surface_flow.vtk* solution.

   (b) In case the locations are user-specified, input first the streamwise locations and then the spanwise ones for each streamwise position.

6. If the simulation results are of a VG case simulated, then store the coordinates near the VG surface to avoid. These coordinates are selected from the ones created in Step 3.

7. Extract the data, avoiding in the extraction loop the coordinates stored in Step 4:

   (a) First, slice the results from 4. with a plane normal to the streamwise axis.

   (b) Then, slice the extracted data from (a) with a plane normal to the spanwise axis.

   (c) From the extracted data in (b), get the coordinates of the point in the upper airfoil surface (that is the suction side), find its unique index in the global solution, and extract the corresponding normal vector using this unique index.

   (d) Create the normal polyline source, corresponding to the normal line to extract. This is done using the normal vector and the point coordinates on the airfoil surface obtained from (c).

   (e) Resample the flow solution calculated in 2.(c) with the normal line created in (d), using the function ResampleWithDataset.

   (f) Extract the flow variables of interest, in this case the u velocity component and the vorticity magnitude, from the resulting domain from (e).

   (g) Store the extracted data, together with the coordinates of the points considered, in the corresponding *.csv* files.

Figure Creation

The data stored in the *.csv* files produced in the Simulations Data subsection are imported.
The data for each streamwise location are averaged computing the arithmetic mean of the corresponding spanwise positions.
The resulting spanwise averaged data for each streamwise location are subset according to the value of the vorticity magnitude. A user-defined threshold is used in order to first select the solution data with a value of the vorticity magnitude equal or greater than the threshold specified.

From this subset of each streamwise location, the minimum vorticity magnitude value is detected, identifying the boundary layer thickness for that streamwise position.
Identified the boundary layer thickness, the values of δ^*, θ and θ^* can be integrated between the wall airfoil surface and the boundary layer thickness found.
Each plot displays the computed displacement, momentum or energy thickness for the specified streamwise coordinates.

Figure 6.18, Figure 6.19 and Figure 6.20

In these figures, the integral boundary layer quantities evolution in the streamwise direction is displayed, that is the displacement thickness δ^*, the momentum thickness θ and the energy thickness θ^*.
The results are related to the FFA-W3-301 airfoil for all the angles of attack simulated, that is $\alpha = 9°$, $\alpha = 11.2°$, $\alpha = 12.9°$ and $\alpha = 14.6°$. The curves shown are related to all the previous angles of attack mentioned, and to all the configurations considered, i.e the *Smooth*, the *VG x/c=0.2 h=6mm* and the *VG x/c=0.3 h=6mm*.

Simulations Data

The simulation data displayed are obtained extracting lines normal to the airfoil streamwise direction axis, from the *Results.vtk* files created during the SU2 simulations.
The extraction process is the same as described in the Simulations Data subsection of Figure 6.15, Figure 6.16 and Figure 6.17.

Figure Creation

The data stored in the *.csv* files produced in the Simulations Data subsection are imported.
The plots creation process is the same one reported in the Figure Creation subsection of Figure 6.15, Figure 6.16 and Figure 6.17.
Each plot displays the computed displacement, momentum or energy thickness for the specified streamwise coordinates.

Figure 6.21

In this figure the vortex core line is displayed together with the velocity profiles, for the FFA-W3-301 airfoil at an angle of attack of $\alpha = 12.9°$, in the *VG x/c=0.3 h=6mm* configuration.

Simulations Data

The simulation data displayed are obtained extracting lines normal to the airfoil streamwise direction axis, from the *Results.vtk* files created during the SU2 simulations.
The extraction process is the same as described in the Simulations Data subsection of Figure 6.13.
The vortex core lines are instead extracted using the Vortex Core Plugin of Paraview [62].
The steps to reproduce the vortex core lines extracted are:

1. Create the velocity field vector from the velocity components provided in output in the SU2 simulations
2. Use the VCGVortexCores with input the velocity field vector just created

The parameters that have been set in the VCGVortexCores filter are the following:

- Method = Sujudi-Haimes;
- Min Num of vertices = 100;

- Max Num of Exceptions = 1;
- Min Strength = 100;
- Max Angle = 30;

The algorithm used to identify the vortex core points is the one proposed by Sujudi and Hames in [63]. This metod of identifying vortex cores lines relies upon the critical-point theory, which states that the eigenvalues and eigenvectors of the velocity gradient tensor, when evaluated at a critical point, describe the local flow about that point. A critical point in general is a point where the vector field vanishes and different vector field trajectories converge or intersect. Critical points are considered to be part of the vortex core line, therefore to identify such a line, the algorithm can be briefly summarized as follows:

1. Compute the velocity gradient tensor J;
2. Compute the three eigenvalues of J;
3. If two of the eigenvalues computed in step 2 are complex conjugate:
   (a) Compute the eigenvector for the remaining real eigenvalue from 2.
   (b) Project the velocity vectors on the plane normal to the eigenvector calculated in (a)
   (c) If one of the projected velocity vectors from (b) is zero, the point considered is part of the vortex core line.

To be able to plot the vortex core line on the corresponding velocity profiles plot, the distance of the vortex core points from the airfoil surface has to be computed.
To do so, the vortex core line extracted is projected on the airfoil surface. This is performed using the SliceAlongPolyline filter, subsetting the sliced data selecting only line on the suction side. The sliced line is the actual projected line on the airfoil surface, so that a point-to-point subtraction can be executed between the original vortex core line and the one projected on the surface of the airfoil, obtaining the vortex core line distance from the airfoil.

Figure Creation

The plot creation process for the streamwise velocity profiles is the same as the one described in the Figure Creation subsection of Figure 6.13.
At this point, the vortex core line along the streamwise direction can be displayed in the corresponding plots. Following the procedure mentioned in the Simulations Data subsection, this line is the 2D projection of the 3D line obtained from the VCGVortexCores filter. The plane onto which this line is projected is the streamwise plane of the airfoil section. To plot this line, only the x coordinate of the extracted vortex core line is displayed, together with the distance of the line from the surface computed in the Simulations Data subsection.

Figure 6.22

This figure displays the vortex tube evolution for the FFA-W3-301 *VG x/c=0.3 h=6mm* case at an angle of attack of $\alpha = 12.9°$.

Simulations Data and Figure Creation

The vortex tube displayed is obtained using the Q-Criterion feature of the GradientOfUnstructuredDataset filter. To use this filter, first the velocity field has to be created from the velocity components of the SU2 simulation result *Results.vtk*. Subsequently with the filter, it is possible to compute the divergence of the velocity field, the vorticity, and the Q-Criterion.
The Q-Criterion is based on the velocity gradient tensor $D_{ij} = \nabla u = \frac{\partial u_i}{\partial x_j}$ [64].
This is a second order tensor, therefore it can be decomposed into a symmetric and a skew-symmetric part, i. e. $D_{ij} = S_{ij} + \Omega_{ij}$. The symmetric part S_{ij} is also known as the rate-of-strain tensor, and it is expressed as $S_{ij} = 1/2 * (\frac{\partial u_i}{\partial x_j} + \frac{\partial u_j}{\partial x_i})$. The skew-symmetric part is the vorticity tensor expressed by $\Omega_{ij} = 1/2 * (\frac{\partial u_i}{\partial x_j} - \frac{\partial u_j}{\partial x_i})$.
The characteristic equation for D_{ij} results in:

$$\lambda^3 + P\lambda^2 + Q\lambda + R = 0$$

where P, Q and R are the three invariants, that is the quantities that remain unchanged when transformations are applied to them. With the definitions of S_{ij} and Ω_{ij}, the invariants can be expressed as:

$$P = -tr(D_{ij})$$

$$Q = 1/2 * tr[(D_{ij})^2 - tr(D_{ij}^2)] = 1/2 * \parallel \Omega_{ij} \parallel^2 - \parallel S_{ij} \parallel^2$$

$$R = -det(D_{ij})$$

The Q-Criterion defines a vortex as the connected fluid region where $Q > 0$. The invariant Q represents the balance between the shear-strain-rate magnitude $\parallel S_{ij} \parallel^2$ and the vorticity magnitude $\parallel \Omega_{ij} \parallel^2$, so the condition $Q > 0$ defines a vortex as the fluid area where the vorticity magnitude is greater than the shear-strain-rate magnitude.
The vortex core line displayed is extracted with the procedure mentioned in the Simulations Data subsection of Figure 6.21.

Figure 6.23

These figures display the skin friction lines on the airfoil surface. The configurations considered are the Smooth and the *VG x/c=0.2 h=6mm* ones, for the FFA-W3-301 airfoil section at an angle of attack of $\alpha = 12.9°$.

Simulations Data and Figure Creation

To create these figures, first the skin friction coefficient vector is created from the skin friction components provided in the SU2 simulation result *surface_flow.vtk*.
Then a Surface Line Integral Convolution representation of this vector is applied, loading the SurfaceLIC Paraview plugin, and selecting the SurfaceLIC option in the representation panel in the left side of the GUI. Line Integral Convolution (LIC) is a visualization technique for representing dense streamlines in a vector field, that takes in input a vector field and a white noise texture [65]. This texture is smoothed locally along the streamlines of the vector field, performing a convolution integral of the resulting smoothed texture with a filter kernel. The neighbouring pixels along streamlines present a high correlation between grey-scale values, whereas the pixels perpendicular to the streamlines have little to no correlation with this grey-scale values.

5.5 Conclusions

In this chapter, the methodology followed to set up and run the simulations is described, considering all the main phases typical of a CFD simulation process.
The Pre-Processing phase, consisting of the CAD model creation and the mesh generation procedure, is summarized. A detailed mesh description can be found in Appendix C and Appendix D. The CFD's configuration-files set-up is described in detail, with all the relevant numerical models and all the values of the parameters used. The Post-Processing phase is subsequently described in more detail, presenting all the procedures for the data extraction and the figures creation. This allows to recreate all the figures displayed in Chapter 6.

Chapter 6

Results

This chapter presents the results obtained from the simulations. The results are introduced by discussing each research question through the use of line plots, contour plots and 3D visualization figures.
The four research questions introduced in Section §1.2 are:

1. Is the current SU2's incompressible solver implementation able to reproduce vortex generators' experimental results up to a reasonable degree of accuracy?
2. Are the results obtained from the simulations qualitatively describing the relevant flow modifications?
3. Is a 2D boundary layer analysis showing the expected essential qualitative aspects?
4. Is a 3D qualitative flow visualization analysis displaying the important flow features?

6.1 Question 1

In this section the results related to the first research question proposed are discussed, comparing the simulations data with the corresponding experimental values.
This comparison is performed through the analysis of lift coefficient, drag coefficient and pressure coefficient values, for both the FFA-W3-241 and the FFA-W3-301 airfoils sections.
In Figure 6.1 the FFA-W3-301 experimental and simulated values of the lift and drag coefficients are shown, for the angles of attack simulated, i.e $\alpha = 9°$, $\alpha = 11.2°$, $\alpha = 12.9°$, $\alpha = 14.6°$. The configurations displayed are: *Smooth* (e.g without VGs), *VG x/c=0.2 h=6mm* and *VG x/c=0.3 h=6mm*. The values of the lift and drag coefficients are obtained from the log files resulting from the SU2 simulations. These plots were resized to display only the region of interest of the polar curve, allowing a better comparison of the experimental values with the simulation results.
It can be seen that the values obtained from the simulations are significantly different from the results presented in the reference paper [23].
In some cases, it is possible to see that the simulations somehow capture the curve shape behaviour, as in the *Smooth* and *VG x/c=0.2 h=6mm* cases.
In the *Smooth* case, the lift shows a peak in values as displayed also in the corresponding experimental data, after which the curve has initially a slight decrease, followed by a further increase. The peak from the simulations results is likely to be related to the experimental value at the bottom left of the plot considered, thus corresponding to an overestimation of both the maximum lift value and of the corresponding angle of attack. This means that the critical angle of attack from the simulations can be identified as $\alpha = 11.2°$, whereas the angle from experiments as $\alpha = 9°$.

Considering also the other plots' lift curves behaviours, it can be stated that the simulations for the *Smooth* case predict stall conditions later than what is indicated from experiments.
In the *VG x/c=0.2 h=6mm*, the overestimation of the stall conditions is not easily recognizable, since both the experimental and simulations values are increasing, without a clear decrease after a certain peak value.
In the *VG x/c=0.3 h=6mm* plot, the overestimation of the critical conditions is instead clearly visible, since the simulations still show a rising and almost linear curve shape. From the wind tunnel results, the airfoil would be expected to stall earlier than what the simulations results display, with the lift values already decreasing for angles of attack $\alpha = 13°$.
As for the drag coefficient, the results generally underpredict the corresponding experimental ones.
In the *Smooth* case, the drag curve shape is well captured, even if the difference in values with the experiments is quite noticeable. From this curve it is possible to identify the stall angle of attack as $\alpha = 9°$, confirming the value hypothesized from the *Smooth* lift curve.
In the other two cases, the difference in values for the drag coefficient is substantial, with curves that depart significantly from the expected values.
In Figure 6.2, the experimental and simulated values of the lift and drag coefficients for the FFA-W3-241 airfoil are shown. The angles of attack simulated are $\alpha = 8.8°$, $\alpha = 10.2°$, $\alpha = 12.6°$, and $\alpha = 14.4°$. The configurations displayed are: *Smooth* (e.g without VGs), *VG x/c=0.2 h=4mm*, *VG x/c=0.2 h=6mm,* and *VG x/c=0.3 h=6mm*. The values of the lift and drag coefficients are again obtained from the log files from the SU2 simulations. The plots were resized as in Figure 6.1.
Regarding the *Smooth* case, the lift coefficient shows an overpredicted maximum value when compared to the reference values from [23]. The drag coefficient shows overestimated values for angles of attack below the stall angle, in contrast with what described for the FFA-W3-301 airfoil. When considering stall flow condition, the general underprediction behaviour of the previous FFA-W3-241 cases is instead confirmed. From the curves plotted, the critical angle of attack can be identified around $\alpha = 12.4°$.
As for the *VG x/c=0.2 h=4mm* case, it can be seen that the lift curve shape is well described in comparison with the experimental values. In this case, the lift critical value is not displayed, since it lies outside the range plotted for the angles of attack, for both the simulations and the experimental values. The drag coefficient curve for this case has values closer to the experimental reference, although observing the plot, it can not be stated that the simulations' curve shape is representative of the corresponding experimental values.
For the remaining two cases, that is *VG x/c=0.2 h=6mm* and *VG x/c=0.3 h=6mm*, the drag coefficient values are overpredicted in the angles of attack range before stall. Nothing can be said about the stall region, since it is not clearly identifiable the critical angle of attack after which the curve departures from a previous nearly linear behaviour.
Regarding the lift coefficient behaviour, the *VG x/c=0.2 h=6mm* case shows an unexplicable peak for the $\alpha = 10.2°$ simulation, when compared to the other simulation values: this could be due to an improper mesh refinement in some regions of the flow domain, or to some hardly identifiable numerical bugs in the code.
In the *VG x/c=0.3 h=6mm* case, the simulations curve shape seems to agree with the increasing trend of the corresponding experimental reference values. The stall peak is not captured, but in accordance with the previous cases, where generally the maximum lift coefficient in the simulations was overpredicted, it could be stated that also in this case the critical lift is likely to be overpredicted.

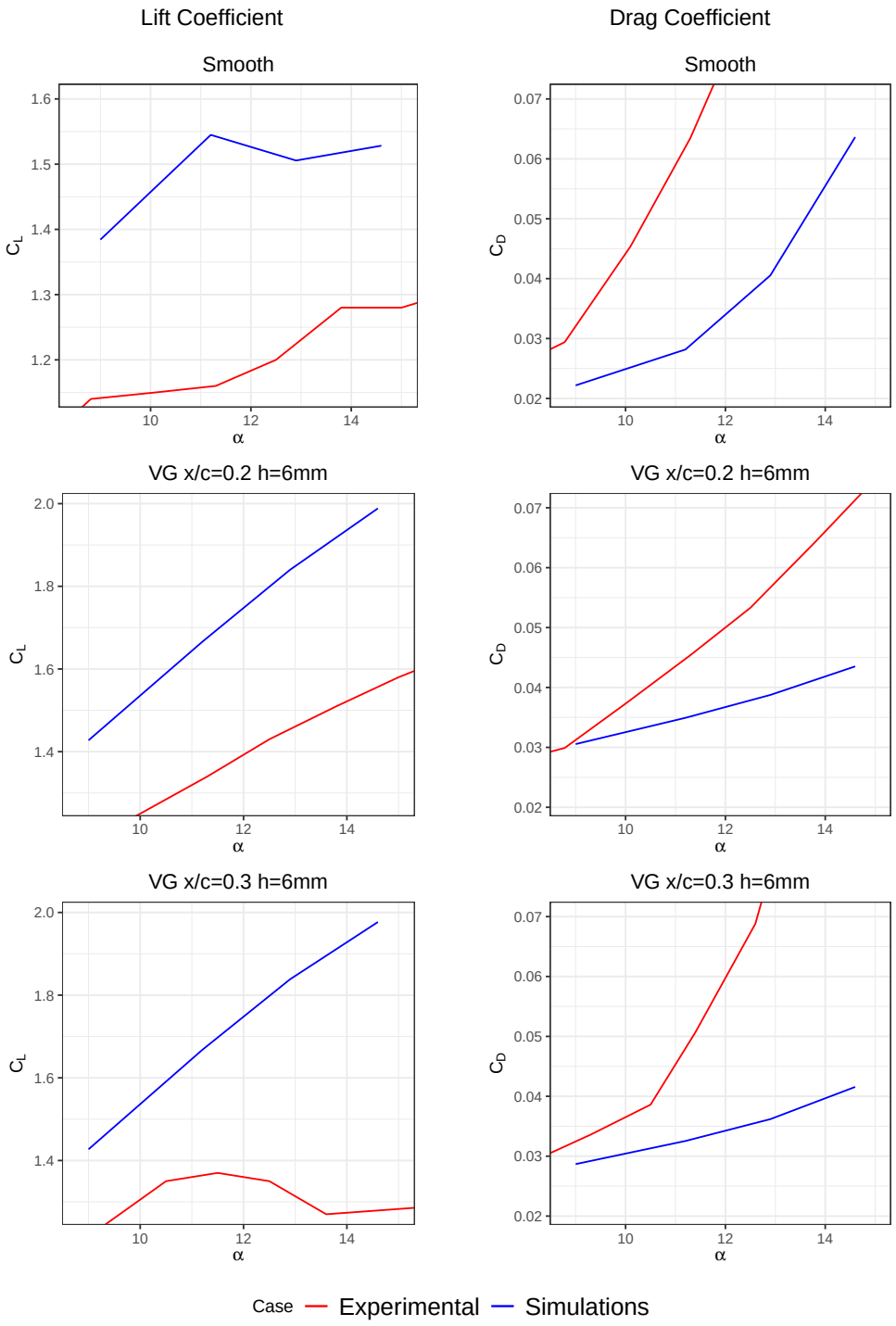

Figure 6.1: Comparison between experimental and simulated values of lift and drag coefficient, for the FFA-W3-301 airfoil

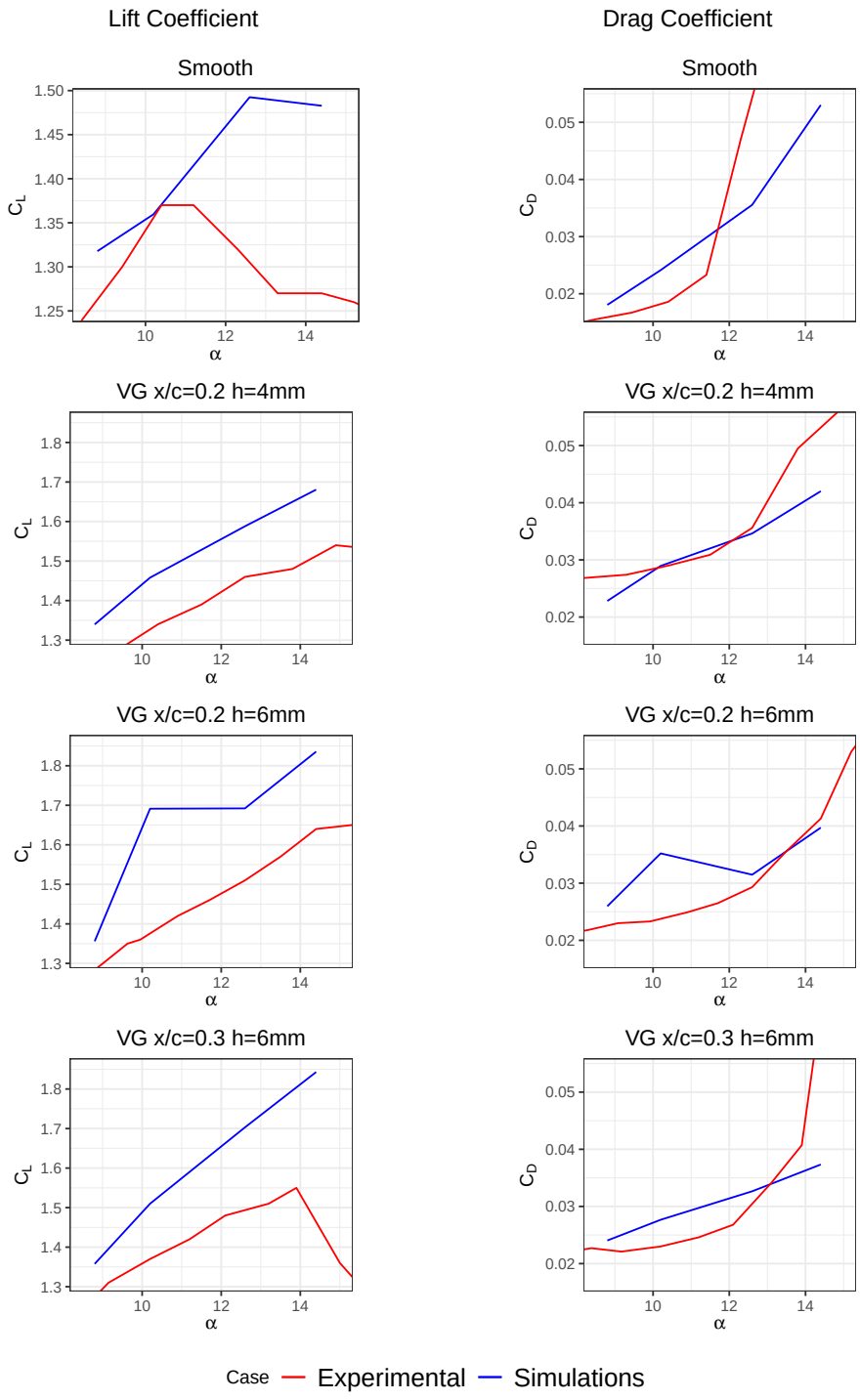

Figure 6.2: Comparison between experimental and simulated values of lift and drag coefficient, for the FFA-W3-241 airfoil

In Figure 6.3, the pressure coefficient for the FFA-W3-241 airfoil is displayed, comparing the simulations results with the corresponding experimental values.
The configurations displayed are:

- *Smooth* (e.g without VGs) for the angles of attack $\alpha = 8.8°$, $\alpha = 10.2°$, $\alpha = 12.6°$, $\alpha = 14.4°$,
- *VG x/c=0.2 h=4mm*, *VG x/c=0.2 h=6mm* and *VG x/c=0.3 h=6mm* for the angle of attack $\alpha = 10.2°$, and
- *VG x/c=0.3 h=6mm* for the angle of attack $\alpha = 14.4°$.

The y-axis has been inverted, in order to show the suction side on the upper part and the pressure side on the lower part of each plot. This is in accordance with the typical airfoil sections representation.
Regarding the *Smooth* simulations, for the $\alpha = 8.8°$ and the $\alpha = 10.2°$ case, a good agreement between experimental and simulated data is shown. The streamwise locations where the simulations depart from the experimental reference are detectable near the leading edge and trailing edge location of the airfoil profile, both for the pressure and suction side. In the remaining streamwise locations, at the suction side a slight underestimation of the values from the simulations is noticeable, whereas, at the pressure side, a close agreement between the two curves is identifiable.
For the stalled cases, i.e the $\alpha = 12.6°$ and the $\alpha = 14.4°$ angles of attack, a considerable difference between values from the simulations and the experiments can be seen at the suction side. At the leading edge streamwise location there is a substantial underprediction in the pressure values resulting from simulations, when compared to the experimental reference. In the following adverse-pressure-gradient portion of the airfoil, the values are therefore underestimated, leading to a displacement of the separation point towards greater streamwise positions than the experimentally predicted results. For the $\alpha = 12.6°$ case, the separation point is predicted to be at approximately $x/c = 0.5$ from the experimental results, whereas, from the simulation results, it is calculated at around $x/c = 0.75$. For the $\alpha = 14.4°$ case, the separation point is expected at approximately $x/c = 0.4$ from the experimental results; from the simulation values it is instead predicted at $x/c = 0.55$.
At the pressure side, a good agreement between experiments and simulations can instead be found for the cases so far investigated.
For the VG cases, the simulations predict reasonably well the pressure coefficient for the three cases at $\alpha = 10.2°$, that is the *VG x/c=0.2 h=4mm*, *VG x/c=0.2 h=6mm,* and *VG x/c=0.3 h=6mm* cases. At the suction side, there is a minimal overall underprediction of the simulated values, whereas, at the pressure side, the simulation results reasonably agree with the experiments. At the leading edge, the largest differences can be found. It is also noticeable the characteristic decreasing peak in pressure corresponding to the VG location considered.
In the *VG x/c=0.3 h=6mm* case at $\alpha = 14.4°$, the simulation results at the suction side of the airfoil, when compared with the corresponding experimental values, deviate considerably in the first portion of the airfoil, from the leading edge to half the normalized chord $x/c = 0.5$; in the remaining part of the airfoil chord, the simulations instead agree with the experiments. At the pressure side, a negligible difference between the results and the simulations can be seen.
For all the cases displayed in Figure 6.3, at the trailing edge streamwise position an outlier peak can be seen, probably due to some numerical errors during the calculations.

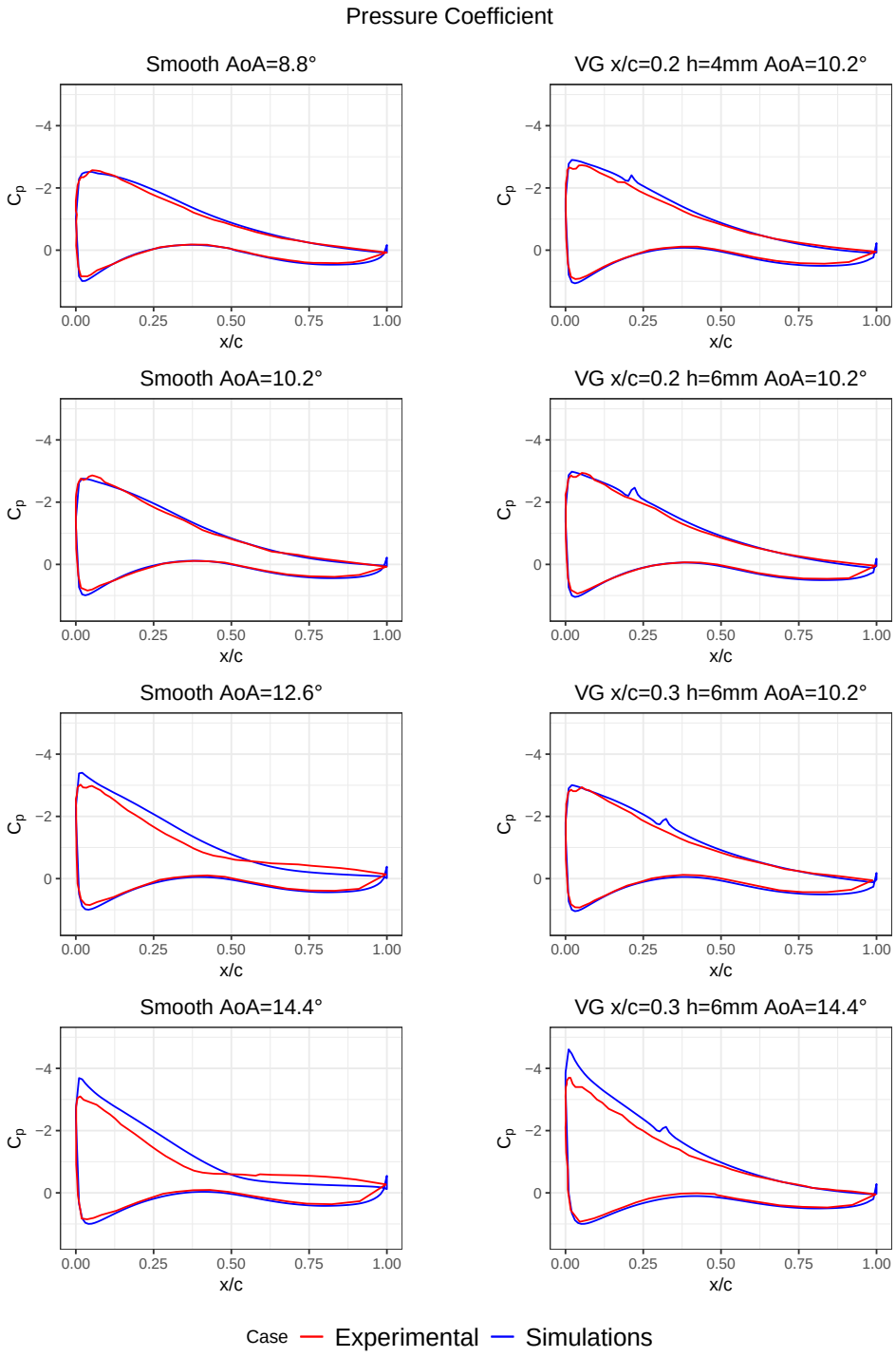

Figure 6.3: Comparison between experimental and simulated values of the pressure coefficient, for the FFA-W3-241 airfoil

In Figure 6.4, the pressure coefficient comparison between the simulation results and the corresponding experimental values is displayed, for the FFA-W3-301 airfoil section.
For the *Smooth* simulations considered, an overall underprediction of the simulated values with respect to the experimentally obtained results is noticeable at the suction side.
In the $\alpha = 9°$ case, from the leading edge location to approximately $x/c = 0.6$, at the suction side the resulting values are generally lower than the corresponding experimental results. At the pressure side the values are overpredicted, in contrast to what generally found for the FFA-W3-241 airfoil.
For the $\alpha = 11.2°$ and the $\alpha = 12.9°$ cases, in addition to the substantial difference of the simulated values with the reference ones, it can be seen that the separation point location is generally overestimated. In the $\alpha = 11.2°$ case, from experiments separation is expected to occur after approximately $x/c = 0.5$, however in the simulations, it is predicted around $x/c = 0.8$. In the $\alpha = 12.9°$, the flow separation is expected experimentally from $x/c = 0.45$ on, whereas, in the simulations, it occurs at $x/c = 0.65$.
In the $\alpha = 14.6°$ case, the results from the simulations completely fail to predict the pressure values, with an initial overestimation at the leading edge location at the suction side, followed by an oscillatory curve behaviour both at the suction and pressure side.
Regarding the VG cases, for the *VG x/c=0.2 h=6mm* and *VG x/c=0.3 h=6mm* ones, at $\alpha = 9°$, it can be seen that experimental values are well predicted by simulations at the pressure side of the airfoil, whereas, at the suction side, the general underprediction mentioned previously is again noticeable. At the suction side near the leading edge locations, the pressure values from the simulation results are initially lower than the corresponding results obtained experimentally; approaching the trailing edge positions, the values gradually increase, matching the experiments.
For the remaining VG case displayed, i.e the *VG x/c=0.3 h=6mm* at $\alpha = 12.9°$, the pressure values at the pressure side are again well predicted, with a slightly more pronounced overestimation in the central streamwise positions. At the suction side, from the leading edge up to approximately $x/c = 0.6$, the values obtained from the simulations are quite underpredicted.
For all the cases displayed, as noticed also in Figure 6.3, at the trailing edge streamwise position an outlier peak is again seen, possibly due to some numerical errors during the calculations.

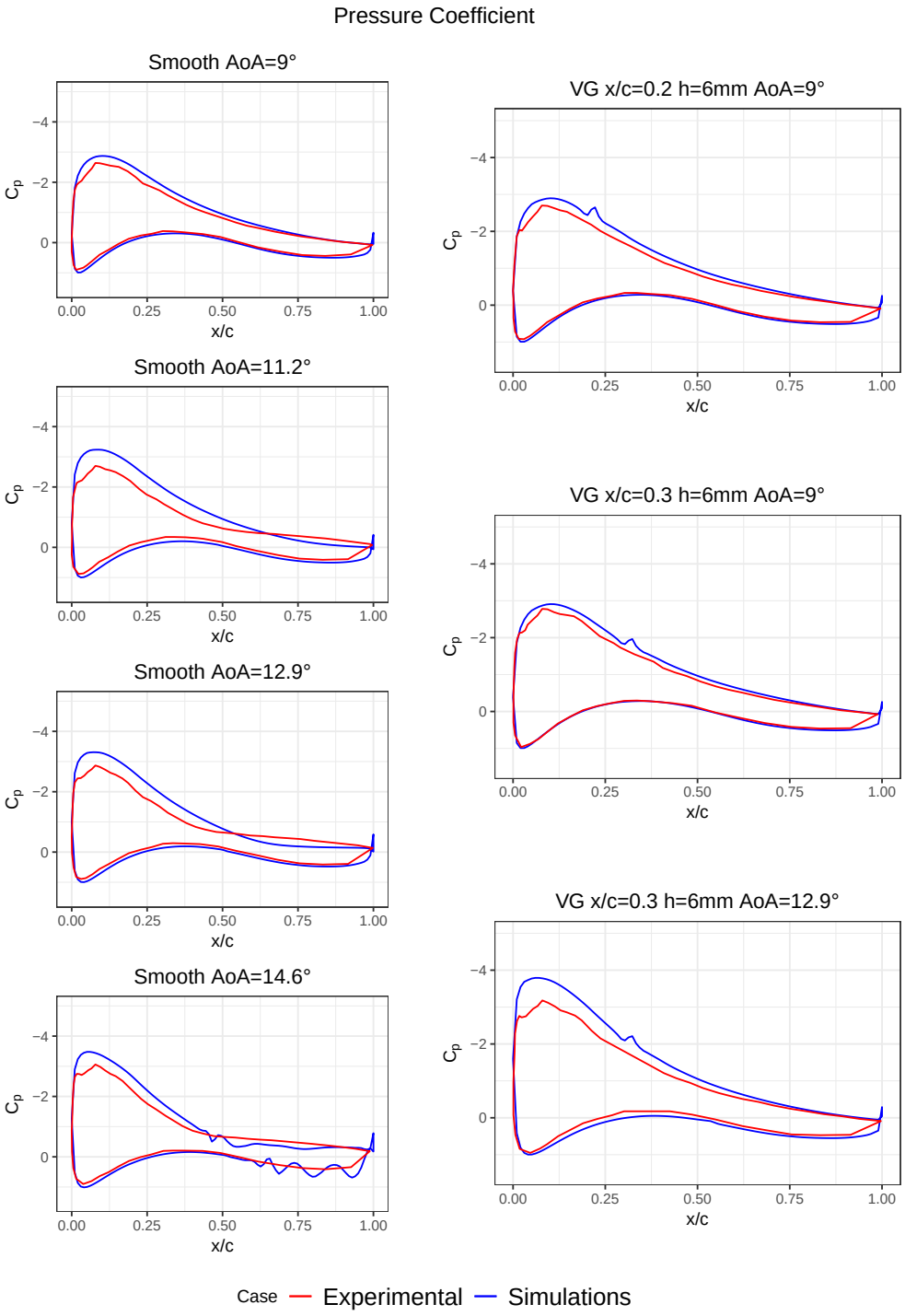

Figure 6.4: Comparison between experimental and simulated values of the pressure coefficient, for the FFA-W3-301 airfoil

6.2 Question 2

To answer the second question, the simulations data are analyzed from a qualitative point of view. This is performed through a comparison, in terms of pressure coefficient and skin friction magnitude values, of all the cases simulated for the FFA-W3-241 and the FFA-W3-301 airfoil sections. In addition to that, the contour plots of the vorticity magnitude and the u, v, w velocity components are displayed, investigating the flow features from a 2D perspective.

6.2.1 Pressure Coefficient Plots

In Figure 6.5, the pressure coefficient is plotted against the normalized streamwise coordinate x/c of the airfoil section, for both the FFA-W3-241 and FFA-W3-301 profiles.
These two plots are obtained slicing the original 3D solution at 100 different linearly spaced streamwise locations, and, for each one of these, 20 different linearly spaced spanwise positions are extracted. The data obtained are then averaged in the spanwise direction, for each streamwise location considered.
The FFA-W3-241 plot is obtained for all the *Smooth* and VG cases at the same $\alpha = 10.2°$ angle of attack, while the FFA-W3-301 plot is obtained for all the related *Smooth* and VG cases at $\alpha = 11.2°$.
In the FFA-W3-241 plot, it can be seen that all the VG cases are characterized by a lower pressure on the suction side of the airfoil, and a slightly higher value on the pressure side, when compared to the corresponding *Smooth* case. This results in an increase of the lift coefficient, as would be expected from the use of Vortex Generators.
The position of the VGs is displayed clearly with the corresponding peaks of low pressure. These peaks can be explained considering that the pressure data are obtained from numerical simulations in which the VGs are modeled only through a 2D surface object, in order to simplify the meshing generation process. Therefore, slicing a 3D solution with a plane produces sharp discontinuities in the values extracted.
For the VG cases, the pressure decrease and departure from the distribution of the *Smooth* airfoil configuration occurs almost immediately after the leading edge, whereupon the pressure increases smoothly as it approaches the trailing edge (apart from the peaks due to the presence of the VG). As for the pressure distribution at the trailing edge, the *Smooth* case shows a slight lower pressure than the VG cases.
Overall, it can be seen that the pressure recovery in the streamwise direction is increased with the use of VGs, when compared to the *Smooth* reference configuration. This pressure recovery is supported by the increase of flow mixing in the downstream region of the VG, which prevents flow in the boundary layer from experiencing strong negative effects of the adverse pressure gradient.
In the FFA-W3-301 plot, the lower pressure on the suction side of the airfoil due to the VG presence is even more evident. This causes, for this particular airfoil at the given angle of attack, a higher lift than what would be experienced under the *Smooth* case circumstances. The flow conditions considered at $\alpha = 10.2°$ are in fact close to the stalled values, characterized in the *Smooth* case by a decrease in lift capability.
For this airfoil, it can also be noted that near the trailing edge, the previous airfoil behaviour, regarding a slight lower pressure present in the clean case when compared with the VG cases, is not that pronounced.
All the other considerations made for the FFA-W3-241 plot are valid for the FFA-W3-301 as well.

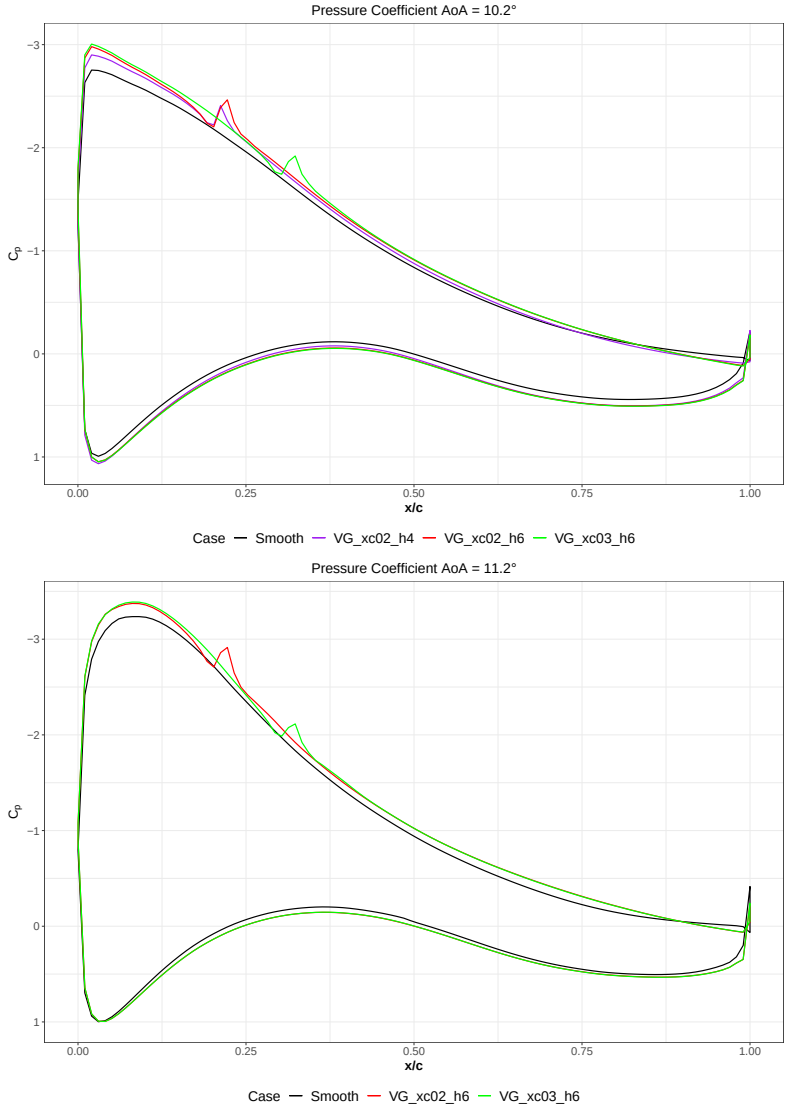

Figure 6.5: Pressure coefficient comparison of all the simulated configurations. On the top plot, the FFA-W3-241 airfoil case at an angle of attack of $\alpha = 10.2°$ is shown, displaying the *Smooth, VG x/c=0.2 h=4mm, VG x/c=0.2 h=6mm* and the *VG x/c=0.3 h=6mm* configurations. On the bottom plot, the FFA-W3-301 airfoil case at an angle of attack of $\alpha = 11.2°$ is shown, displaying the *Smooth, VG x/c=0.2 h=6mm* and the *VG x/c=0.3 h=6mm* configurations.

In Figure 6.6, the pressure coefficient of a flow condition characterized by developed stall is considered. These two plots were obtained in the same way as what done in Figure 6.5, regarding the spanwise and streamwise locations considered. The FFA-W3-241 plot is obtained for all the cases at the same $\alpha = 14.4°$ angle of attack, while the FFA-W3-301 plot is obtained for all the related cases at $\alpha = 12.9°$.
In these plots, it is possible to distinguish clearly the occurring separation, characterized by a flat portion of the pressure coefficient curve. For the FFA-W3-241 case, there is a separation from $x/c = 0.55$, whereas, for the FFA-W3-301, a separation occurs from $x/c = 0.65$.

In both cases it is therefore possible to detect the aerodynamic performance enhancement of the VGs, by simply looking at the curve behaviour for all the VG cases. The curve does not present the flat portion anymore, and overall, the low pressure on the suction side decreases, causing a raise in the lift capability of the airfoil.
For the FFA-W3-241, there seems to be a higher improvement on the lift for the *VG x/c=0.2 h=6mm* and the *VG x/c=0.3 h=6mm* cases, probably due to the fact that higher-height VGs are able to break the growth of the boundary layer and energize it more efficiently when stalled flow conditions arise.
For the FFA-W3-301, there seems to be little to no difference regarding lift improvement between the two VG cases considered. This is likely due to the fact that both VGs configurations have the same height, thus increasing performance similarly under stalled flow conditions.

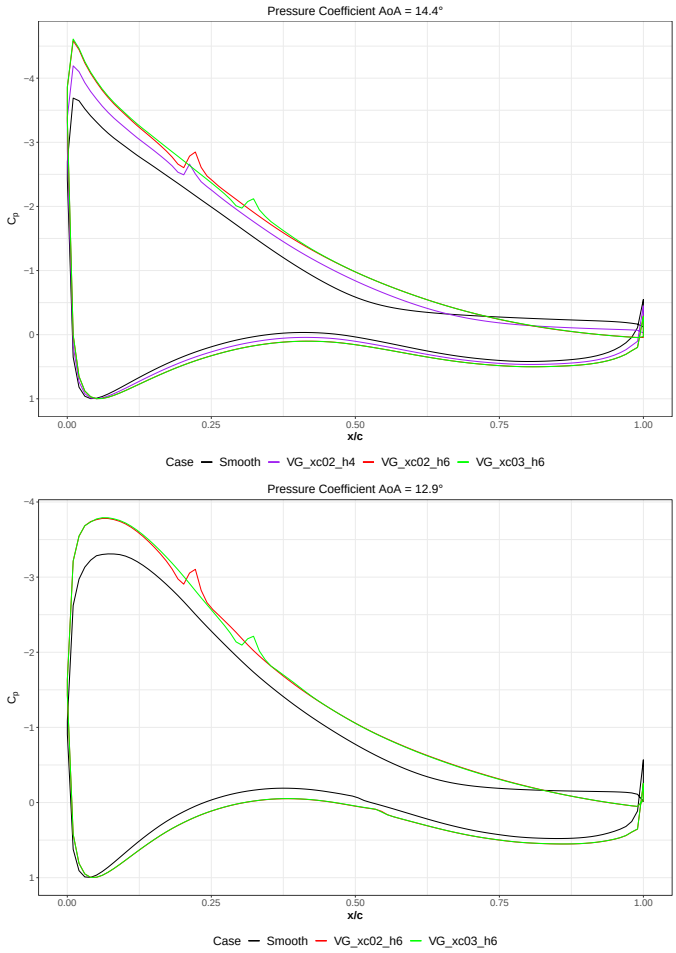

Figure 6.6: Pressure coefficient comparison of all the simulated configurations. On the top plot, the FFA-W3-241 airfoil case at an angle of attack of $\alpha = 14.4°$ is shown, displaying the *Smooth, VG x/c=0.2 h=4mm, VG x/c=0.2 h=6mm,* and the *VG x/c=0.3 h=6mm* configurations. On the bottom plot, the FFA-W3-301 airfoil case at an angle of attack of $\alpha = 12.9°$ is shown, displaying the *Smooth, VG x/c=0.2 h=6mm,* and the *VG x/c=0.3 h=6mm* configurations.

6.2.2 Skin Friction Coefficient Plots

In Figure 6.7, the magnitude of the skin friction coefficient is plotted against the normalized streamwise coordinate x/c of the FFA-W3-241 and FFA-W3-301 airfoil sections.
These two plots are obtained slicing the original 3D solution in the same manner as Figure 6.5: 100 different streamwise locations, and, for each one of these, 20 different spanwise positions are extracted. The data obtained are then averaged in the spanwise direction, for each streamwise location considered.
The FFA-W3-241 plot is obtained for all the cases at the same $\alpha = 10.2^{\circ}$ angle of attack, while the FFA-W3-301 plot is obtained for all the related cases at $\alpha = 11.2^{\circ}$.
In both plots, the favourable effect of the VG presence regarding prevention of flow separation can be easily noticed.
In fact, the large peaks occurring in the plots at the related VG locations on the airfoil surface are the sign of enhanced flow-mixing, that causes a sudden increase in the skin friction values as expected.
The transition to turbulent flow conditions for the angles of attack considered, is seen to always occur before the VG location.
Increasing the skin friction coefficient, donwstream of the VG, allows still an attached flow at the airfoil wall surface, although this results in increased energy dissipation due to the greater friction in the same boundary layer region. This attached flow situation will not occur in the case of separated flow, in which the skin friction coefficient would reach a zero value, increasing then slightly for the remaining portion of the surface.
In the FFA-W3-241 plot, it can be seen that the airfoil without VG does not experience considerable flow separation yet, even if the angle of attack $\alpha = 10.2^{\circ}$ could be related to incipient stall conditions, based on the evaluation of the lift coefficient for the airfoil considered. In fact, the skin friction coefficient zero value is at a streamwise coordinate very close to the trailing edge.
For the VG cases, a noticeable increase of the skin friction values can be seen, with a fast decay of these values for the remaining portion of the airfoil surface, downstream of the VG. This behaviour could be explained with the fact that, immediately after the VG, the flow mixing is considerable and energizes the flow at the cost of an increase in friction due to the vortex arising from the mixing. As already confirmed in [18], for a counter-rotating pair of VG as the ones considered, this vortex, after an initial direction towards the surface, tends to move away from it, carrying with itself the fluid that has been subject to mixing. With this flow movement, less fluid affects the airfoil surface, thus causing a rapid decrease in skin friction compared to the initial values.
It can be seen also that for the same VG position, its height has an influence on the length of the favourable mixing.
Looking at the decrease of skin friction for the two cases *VG x/c=0.2 h=4mm* and *VG x/c=0.2 h=6mm*, in the case with VG height *h=6mm,* the skin friction rises to almost the same value of the *h=4mm* case, but it decays slower than it.
In the area near the trailing edge, the airfoil will consequently experience a higher skin friction. This is an indication of a more effective mixing of the flow, regarding prevention of detachment and separation from the surface.
In the case of the VG placed at *x/c=0.3*, the peak of skin friction is less pronounced than the other cases, and after a short path the values almost approach the ones from the *VG x/c=0.2 h=6mm* case.
Summarizing, it can be seen that for the purposes of separation and stall prevention, the cases *VG x/c=0.2 h=6mm* and *VG x/c=0.3 h=6mm* are the most effective, causing a higher value of the skin friction coefficient in the zone where the flow is expected to be separating, that is, near the trailing edge.
In the FFA-W3-301 plot, a different flow condition than the previous is displayed. The data displayed were extracted from a case with an angle of attack $\alpha = 11.2^{\circ}$ of the ones in the stalled conditions for this airfoil. It is therefore possible to detect the separating flow region and the even clearer positive effect of the presence of VGs.
For the *Smooth* case, the flow condition considered is characterized by a fast decay of the skin friction coefficient in the initial portion of the airfoil near the leading edge. This behaviour most probably corresponds

to the laminar flow region.
Very close to the leading edge, at the position of $x/c = 0.06$, the flow already transitions to turbulent conditions, and the skin friction coefficient decays downstream of this position, reaching a zero value at $x/c = 0.76$.
At this location, the flow separates leading to detachment from the surface, as it can be seen by the skin friction coefficient values of the remaining portion until the trailing edge. These values are slowly increasing after the flow separation point, but with very low values, indicating that there is a small fluid fraction which is still in contact with the airfoil surface.
The use of VGs in this case clearly prevents flow separation, as it can be evinced from the skin friction curves behaviour for both the *VG x/c=0.2 h=6mm* and the *VG x/c =0.3 h=6mm*.
Both VG configurations cause a higher skin friction downstream of them, not reaching a zero value in the airfoil portion which otherwise would experience flow separation.
It can also be noticed that the presence of VGs triggers transition to turbulent conditions earlier than the *Smooth* case, in the upstream portion of the airfoil.
Regarding this airfoil application, it could be stated that the *VG x/c=0.3 h=6mm* configuration is the most favourable regarding aerodynamic efficiency, with lower skin friction values than the other VG case, and therefore, less drag force.
In Figure 6.8, the magnitude of the skin friction coefficient for a deep stalled flow condition is shown.
These two plots are obtained using the same method as for what done in Figure 6.7, regarding the spanwise and streamwise locations considered.
The FFA-W3-241 plot is obtained for all the cases at the same $\alpha = 14.4°$ angle of attack, while the FFA-W3-301 plot is obtained for all the related cases at $\alpha = 12.9°$.
In the FFA-W3-241 plot, it is shown that the *VG h=4mm* configuration helps to delay separation, but not completely prevent it, since the separation point is only moved further from $x/c = 0.55$ to $x/c = 0.75$. The other two VG cases are able to prevent separation completely, since the skin friction coefficient values never reach the separated condition denoted by a zero value.
In the FFA-W3-301 plot, the trend observed for the previous corresponding case at an angle of attack of $\alpha = 10.2°$ is confirmed. The only difference is in the separation point position, that is displaced before than the previous case mentioned, since the flow is characterized by a stronger adverse pressure gradient.

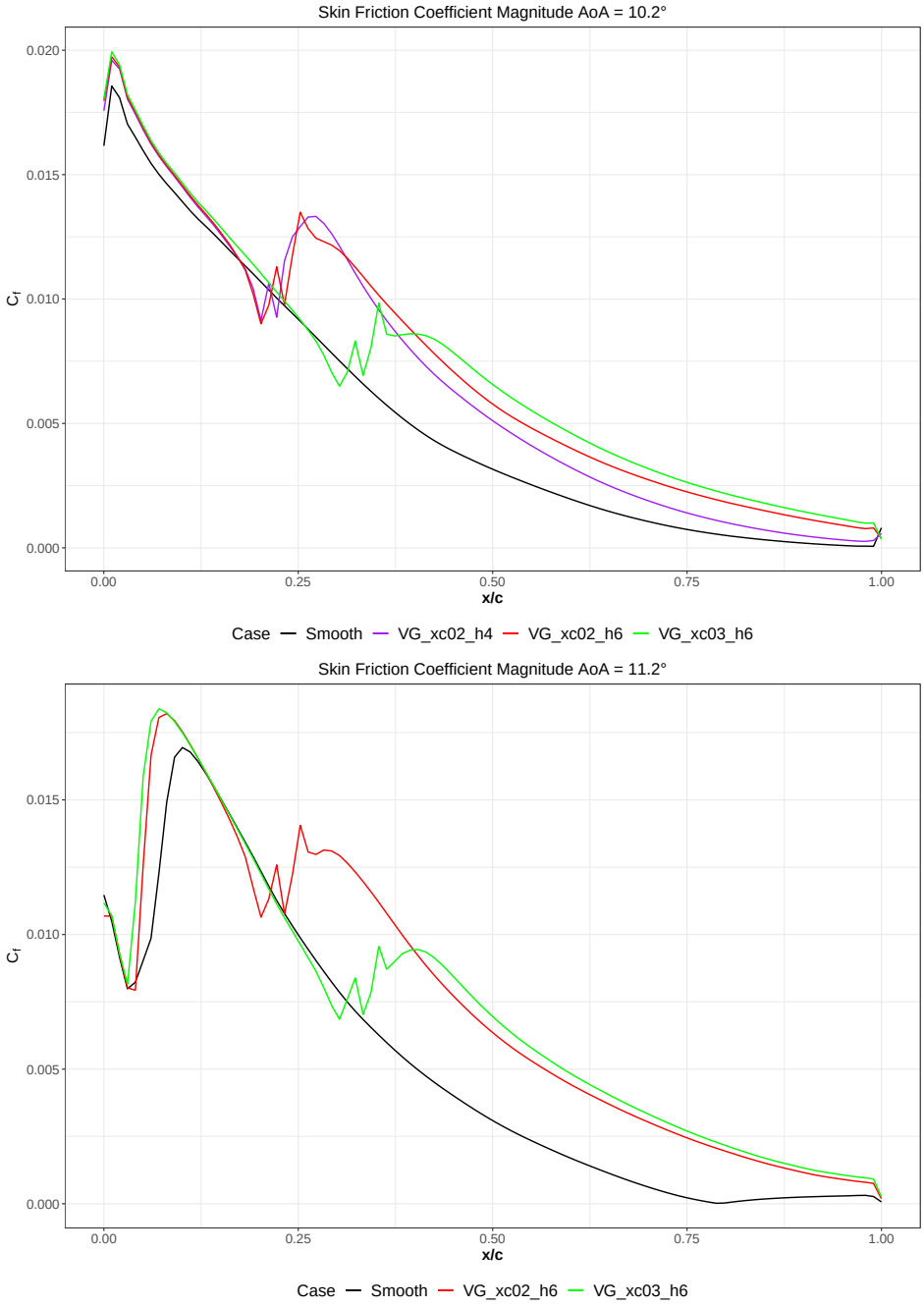

Figure 6.7: Skin friction magnitude coefficient comparison of all the simulated configurations. On the top plot, the FFA-W3-241 airfoil case at an angle of attack of $\alpha = 10.2°$ is shown, displaying the *Smooth, VG x/c=0.2 h=4mm, VG x/c=0.2 h=6mm,* and the *VG x/c=0.3 h=6mm* configurations. On the bottom plot, the FFA-W3-301 airfoil case at an angle of attack of $\alpha = 11.2°$ is shown, displaying the *Smooth, VG x/c=0.2 h=6mm* and the *VG x/c=0.3 h=6mm* configurations.

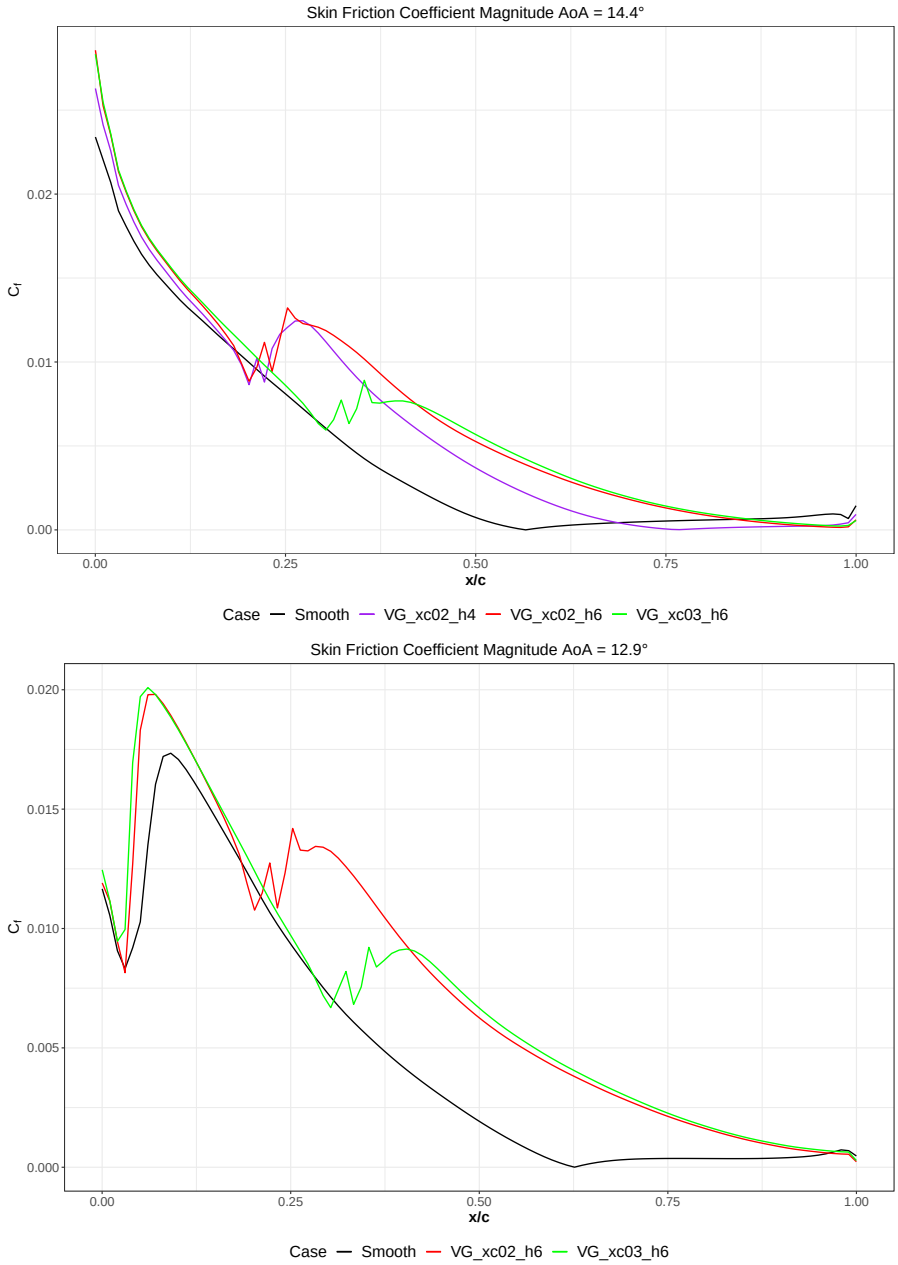

Figure 6.8: Skin friction magnitude coefficient comparison of all the simulated configurations. On the top plot, the FFA-W3-241 airfoil case at an angle of attack of $\alpha = 14.4°$ is shown, displaying the *Smooth, VG x/c=0.2 h=4mm, VG x/c=0.2 h=6mm,* and the *VG x/c=0.3 h=6mm* configurations. On the bottom plot, the FFA-W3-301 airfoil case at an angle of attack of $\alpha = 12.9°$ is shown, displaying the *Smooth, VG x/c=0.2 h=6mm* and the *VG x/c=0.3 h=6mm* configurations.

6.2.3 Contour Plots

In Figure 6.9 and Figure 6.10, the vorticity magnitude evolution in the streamwise direction of the FFA-W3-301 airfoil it is displayed, for both the *Smooth* case and the *VG x/c=0.2 h=6mm* configuration, at an angle of attack of $\alpha = 12.9°$.
The streamwise locations considered are $x/c = 0.1054$, $x/c = 0.2106$, $x/c = 0.26$, $x/c = 0.3159$, $x/c = 0.36$, $x/c = 0.4211$, $x/c = 0.6316$, $x/c = 0.8421$.
In each contour plot, 20 equally spaced levels are shown, from a vorticity magnitude value of 0 to a value of 150.
The domain from the CFD simulations was reflected with respect to the minimum spanwise coordinate (y-coordinate), to reproduce the VG pair simulated. In the y-axis, the normal distance from the airfoil surface is considered.
The plots present the boundary layer region at the suction side, where the VG is positioned.
It was chosen to display the vorticity magnitude, since this is a quantity that allows a clear qualitative evaluation of the intensity of the vortical structures arising due to the influence of VGs.
Looking at the VG figure, it can be seen that immediately donwstream of the VG location, at $x/c = 0.2106$, small turbulent structures appear in the boundary layer region. This increased turbulence is the direct effect of the VG presence, and together with the primary vortices helps in energizing the boundary layer, mantaining it attached to the wall.
These turbulent structures soon grow in radius, as shown in the $x/c = 0.26$ streamwise position: the two primary vortices identified by Velte, that where introduced in Section §3.1, become, therefore, identifiable.
Proceeding downstream, the two vortices gradually lose their intensity: this is due to the energy dissipation from larger to smaller turbulent scales, as explained in 2.3.2. As a consequence of this, the vortices tend to increase more their radius, thus progressively converging on each other.
The counter-rotating vortical movement of the VG pair's vortices can be easily evinced from the smoothed contours. This movement is causing the flow in the boundary layer to be forced closer to the wall, as can be seen from the $x/c = 0.36$ location on. Moreover, in the middle region between the two vortices a slight increase in the boundary layer thickness is also noticeable, when compared to the extreme spanwise positions of the plot being considered.
The situation depicted is typical of the common-flow-down category for a counter-rotating VG pair, where the outer flow is entrained near the wall in the middle-spanwise area between the VGs.
From the comparison between the smooth and the VG case of interest, it can be seen that starting from $x/c = 0.26$, the boundary layer is considerably thinned in the VG case, as it would be expected using this type of passive flow control device. The flow separation that would otherwise occur for some streamwise location after $x/c = 0.6316$, is clearly prevented. This can be seen in particular for the $x/c = 0.8421$ position considered, where the flow leaving the airfoil surface is identified by lighter blue regions surrounded by darker blue areas. For the VG case in the same position, only the dissipating vortical movement of the vortices induced by the VG is identifiable in the same flow area, with a lower boundary layer region still presenting enough vorticity to sustain the adverse pressure gradient.

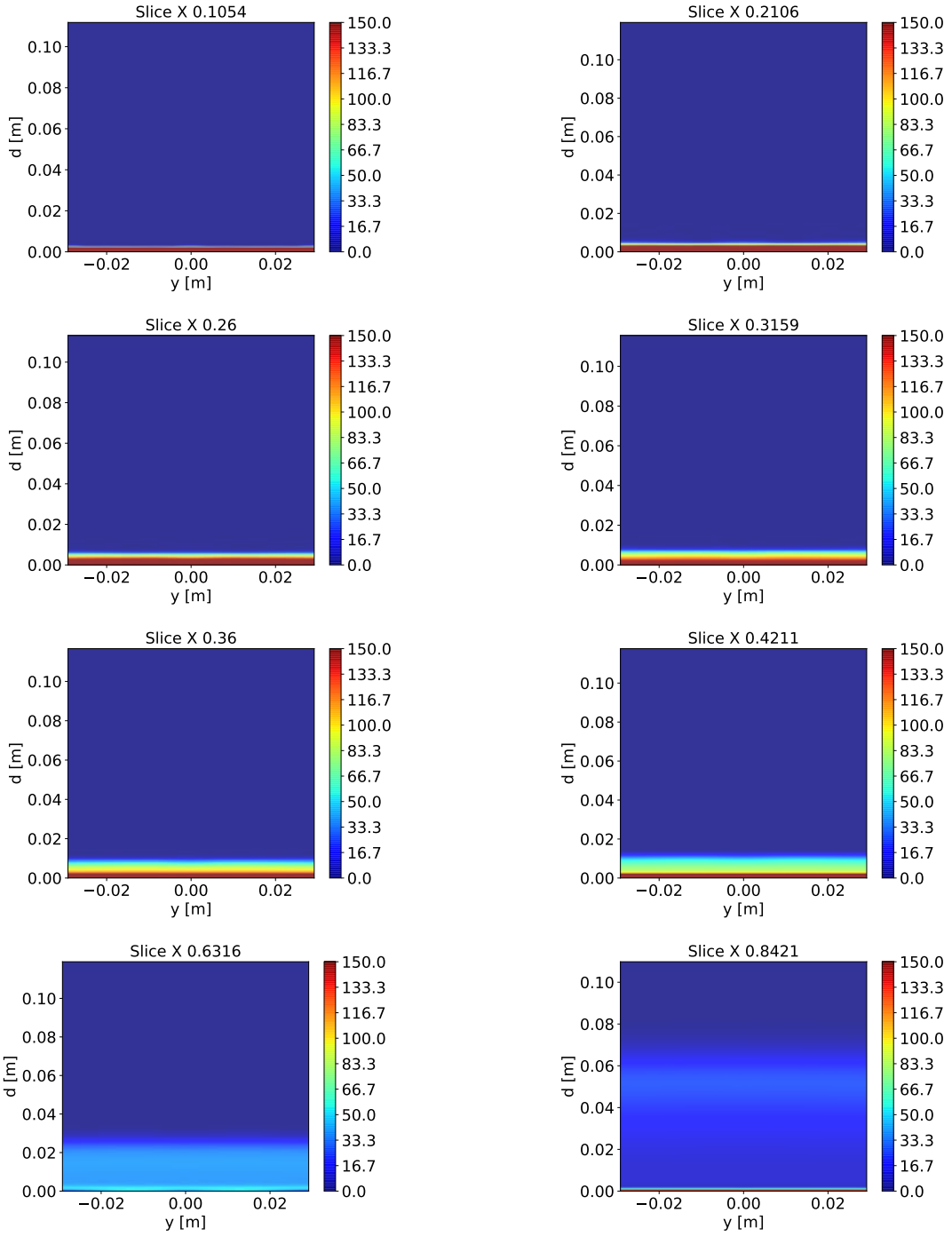

Figure 6.9: Vorticity magnitude contour plots for the FFA-W3-301 airfoil at an angle of attack of $\alpha = 12.9°$ for the *Smooth* case.

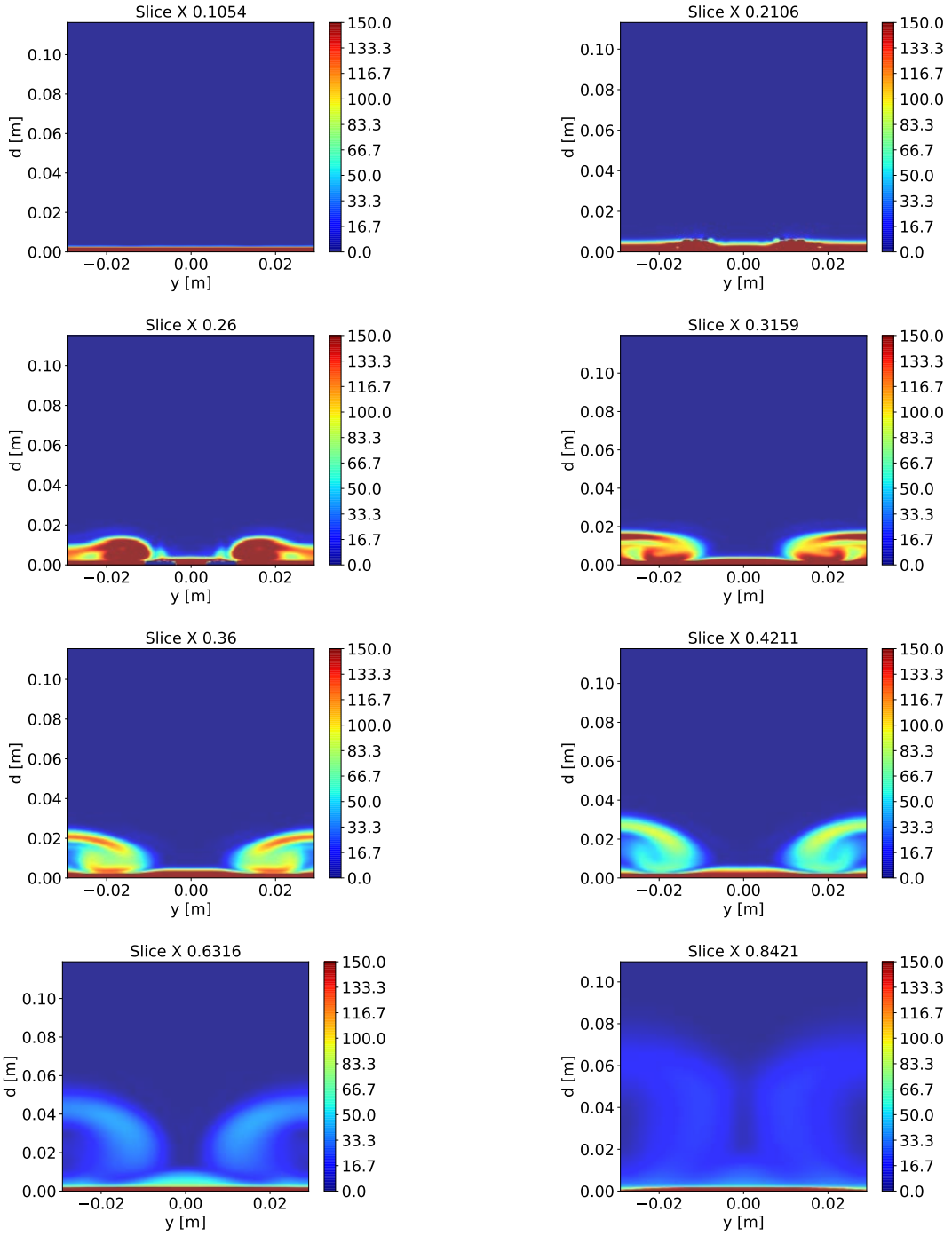

Figure 6.10: Vorticity magnitude contour plots for the FFA-W3-301 airfoil at an angle of attack of $\alpha = 12.9°$ for the *VG x/c=0.2 h=6mm* case.

In Figure 6.11 and Figure 6.12, the FFA-W3-301 is again considered, at an angle of attack of $\alpha = 12.9°$, displaying the velocity components for different streamwise positions using smoothed contour plots. Since the VG is positioned at the suction side of the airfoil, where the flow would experience the greater separation, in the plots the boundary layer region is presented for this side of the airfoil. From left to right, the columns show to the u, v and w velocity components, respectively, related to the corresponding x, y and z geometrical axis.
The velocity components u, v and w resulting from the SU2 simulations are nondimensionalized internally in the solver with respect to the freestream velocity. A value greater than 1 represents therefore a local increased velocity compared to the undisturbed freestream velocity value, whereas a value lower than 1 indicates a local decrease in velocity.
The contour levels chosen for each plot are determined by a sequence of 20 linearly spaced values. The levels vary from the minimum to the maximum value displayed in each plot, thus changing for every streamwise position considered.
The domain from the CFD simulations was reflected with respect to the minimum spanwise coordinate (y-coordinate), to reproduce the simulated VG pair. In the y-axis, the normal distance from the airfoil surface is considered.
Regarding the smooth case, in the left column the acceleration that the u component is subject to is clearly seen. This is displayed by the red range of values resulting in values up to $u = 1.8$, from the streamwise location at $x/c = 0.1054$ to the position at $x/c = 0.4211$. These higher velocities are the effect of the highly-cambered FFA-W3-301 airfoil shape, characterized by a 30% thickness at the point of maximum lift at $x/c = 0.3$. The curvature introduced in the flow field by the presence of the airfoil solid object is what induces the described local acceleration. At the $x/c = 0.6316$ position, the initial flow reversal at the wall can be noticed by the appearance of a very small negative u value in the scale of the contour levels.
The v velocity component in the *Smooth* case, presented in the middle column, allows the identification of the vortical movements in the boundary layer. These are displayed by the blue and red contour regions appearing in the plots. From the contour level bar at the side of the plot, it can be evinced that the red regions are related to a positive v component, whereas, the blue regions indicate a negative v component. Relative to each plot-coordinates frame-of reference, that could be evinced by the axis values for each plot, a positive v value characterizes a velocity vector in the right direction of the plot considered, and a negative v value denotes instead a velocity vector pointing in the left direction of the plot.
With this information, the growing vortices inside the boundary layer can be qualitatively evaluated.
These vortices present stronger velocity components in the first streamwise positions, i.e $x/c = 0.1054$ and $x/c = 0.2106$. Two stronger vortices in the middle region of the flow domain are identifiable, with weaker vortices at the two sides of the plot. The vortices in the middle are initially characterized by a larger radius, when compared to the vortical structures at the sides.
Proceeding downstream, the spanwise v velocity values decrease in both the minimum and maximum values. The vortices in the middle are seen to grow in radius slower than the vortices at the side, which become predominant from $x/c = 0.4211$ on. In the last contour plot shown at $x/c = 0.6316$, it can be seen that the vortices at the sides prevail over the vortical structures in the middle, and that two main diverging flow directions are noticeable, pointing to the sides of the flow domain.
The w velocity component, in the right column of the *Smooth* case figure, does not add any meaningful information. In fact, it shows that, in the first locations until the point of maximum lift, i.e from $x/c = 0.1054$ to before the $x/c = 0.36$ position, the velocity points in the upward direction due to the curvature of the airfoil. From the point of maximum lift at $x/c = 0.3$ on, the velocity is characterized mainly by a downward movement, trying to follow the airfoil shape curvature. It can be noted that in the $x/c = 0.6316$ location, in the region closer to the wall, the flow is characterized by a growing upward w velocity component, indicating the start of separating flow phenomena.
From the evaluation of Figure 6.11, it can be stated that the separation occurring for the considered flow situation is mainly due to the combined effect of the streamwise u velocity component and the spanwise

v velocity component. The w component only shows the expected behaviour, following the airfoil shape curvature, with the indication of a growing upward velocity direction after $x/c = 0.6316$.
It is possible at this point to compare the flow velocity behaviour described for the *Smooth* case with the VG pair case.
Related to the u component in the left column, the main effect of the VG pair is to introduce a deceleration at the sides of the flow domain. This deceleration corresponds to the vortical regions of the two induced vortices, inside of which u decreases due to the viscous dissipation becoming predominant. Regarding the maximum u values, an overall increase can be seen in the boundary layer middle region, when compared to the *Smooth* case. This is a clear indication of the energization of the boundary layer, since the flow presenting a higher streamwise velocity component, is able to resist the adverse pressure gradient experienced after the point of maximum lift.
The v component in the middle column shows the disappearence of the vortical movement that was noticed for the *Smooth* case in the middle region of the boundary layer.
At the $x/c = 0.1054$ location, with respect to the *Smooth* case, smaller and weaker vortices are present, spread on the airfoil surface.
Right after the VG location, the disappearance of the two vortices in the middle region mentioned before is visible. With the considerations introduced for the *Smooth* case, related to the colours displayed in the contour plots and the corresponding signs of the v component, the two counter-rotating vortices introduced by the VG presence in the flow field can be identified.
These are the two main vortical structures that are present in the flow field downstream of the VG. In the middle region of the boundary layer, the energization by the mixing induced by the vortices creates a mainly streamwise velocity direction that helps in preventing flow separation reducing flow lateral movements.
The w component in the right column indicates, at the sides of the flow domain, a flow movement away from the wall. This confirms what has been seen in the vorticity magnitude contour plots in Figure 6.10, where the vortices tend to lift away from the wall, increasing their radiuses and consequently lowering their intensity due to the viscous dissipation. In the middle region of the boundary layer, a strong tendency of the flow to move towards the wall is seen, that explains the persistence of an attached flow condition downstream of the VG. This behaviour is expected from a common-flow-down counter-rotating VG configuration.
From the evaluation of Figure 6.12, a typical flow behaviour for the VG configuration investigated is noticed, thus confirming that, from a qualitative point of view, the simulations are able to capture the relevant 3D flow features. In fact, it is shown that the flow remains attached to the airfoil surface in the boundary layer, due to the combination of the increasing streamwise u velocity component and the strong downward movement of the w component. The middle vortices in the boundary layer, that were present in the *Smooth* case, disappear. This can be considered one of the causes for the delay of the streamwise separation location, since the two main vortices, arising after the VG location, mix with each other later than what would occur in the *Smooth* case. In this situation, in fact, an earlier mixing of the two main vortical structures in the boundary layer, the middle and the lateral ones, is seen to create a strong flow divergence that is likely to contribute to the 3D flow separation phenomenon.

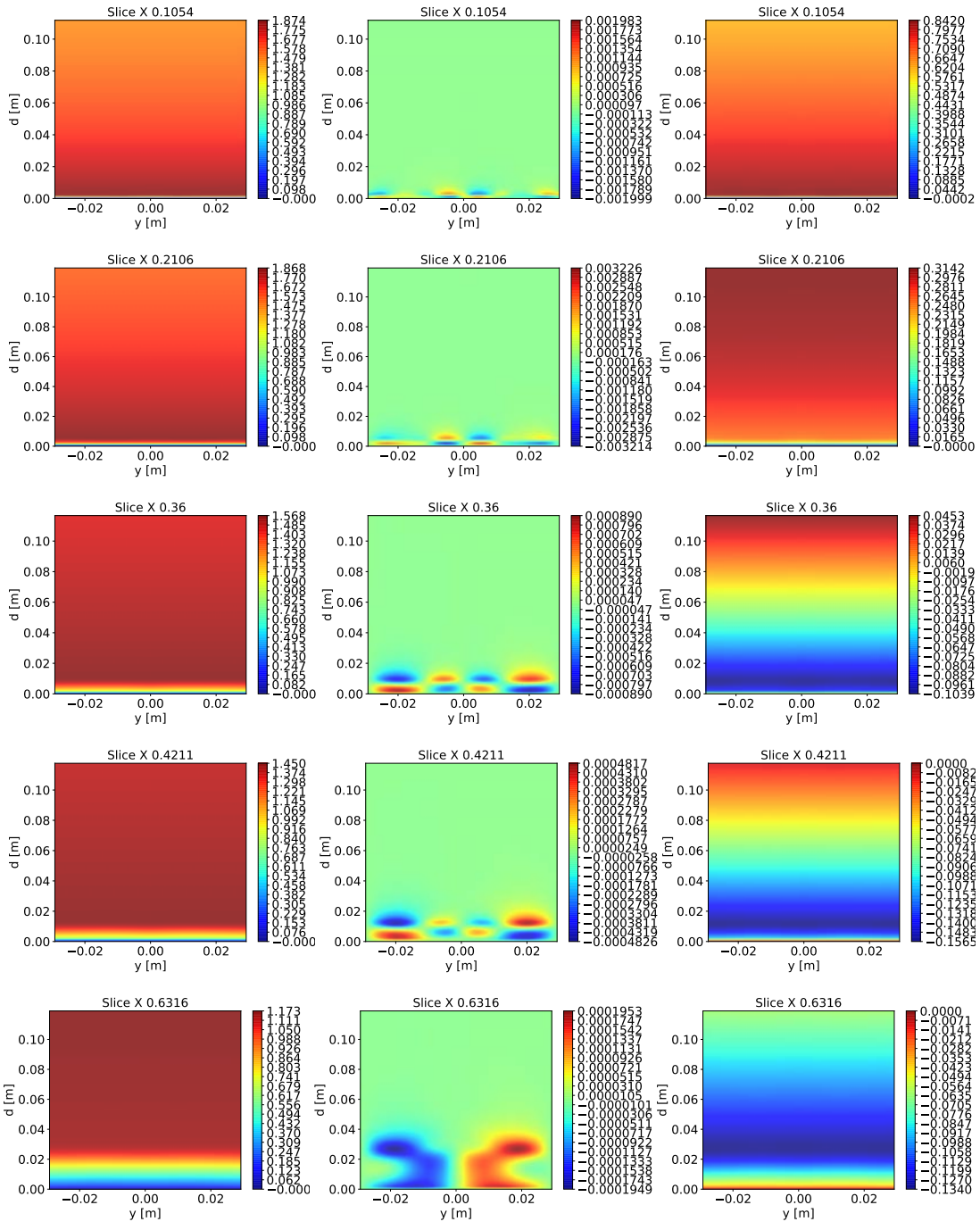

Figure 6.11: Velocity components contour plots for the FFA-W3-301 airfoil at an angle of attack of $\alpha = 12.9°$ for the *Smooth* case. The left column shows the u component in the x direction (airfoil streamwise direction). The middle column shows the v component in the y direction (airfoil spanwise direction). The right column shows the w component in the z direction (direction normal to the airfoil).

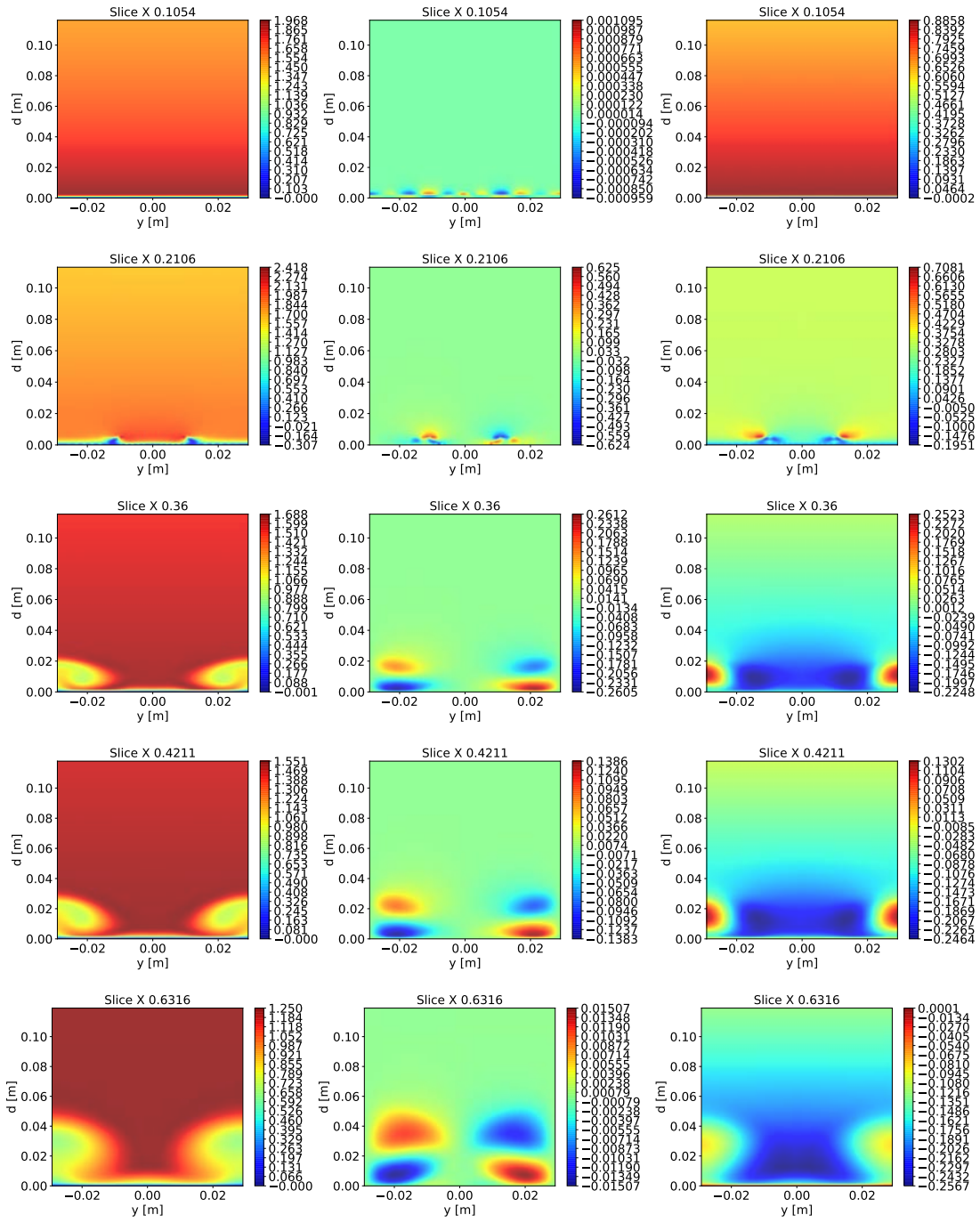

Figure 6.12: Velocity components contour plots for the FFA-W3-301 airfoil at an angle of attack of $\alpha = 12.9°$ for the *VG x/c=0.2 h=6mm* case. The left column shows the u component in the x direction (airfoil streamwise direction). The middle column shows the v component in the y direction (airfoil spanwise direction). The right column shows the w component in the z direction (direction normal to the airfoil).

6.3 Question 3

The third question is discussed considering the boundary layer from an averaged 2D point of view. This is performed through the evaluation of the 2D vorticity magnitude and the u velocity profiles, together with the boundary layer thickness for the cases considered. In addition to these figures, the three integral boundary layer thicknesses introduced in Section §2.4 are calculated, showing the results through cumulative plots of all the *Smooth* and VG configurations tested, for all the simulated angles of attack.

6.3.1 Boundary Layer Profiles Analysis

In Figure 6.13, the vorticity magnitude evolution at the suction side of the FFA-W3-241 airfoil is shown along with the boundary layer thickness, for an angle of attack of $\alpha = 8.8°$.
This plot was obtained extracting the solution along lines normal to the airfoil surface, up to a distance of $d = 0.08 * c$, with c being the airfoil chord. A total of 30 linearly spaced streamwise locations was considered, and for each streamwise position, 20 spanwise locations lines were extracted. The profiles corresponding to a given streamwise location are obtained averaging all the corresponding extracted lines in the spanwise direction.
The vorticity magnitude is obtained from the vorticity field, computed as the curl of the velocity field resulting from the simulations.
The boundary layer thickness evolution line is obtained considering that the vorticity magnitude tipically decays exponentially from the airfoil surface to the outside of the boundary layer, where it reaches a zero value.
It is therefore possible to detect the edge of the boundary layer by filtering the vorticity magnitude values, from the maximum value down to a minimum value threshold specified by the user (usually as a percent value threshold, typically in the order of magnitude of 10^{-2}).
In this plot, the increase in the boundary layer thickness due to the presence of the VG can immediately be seen. This is due to the induced vortex inside the boundary layer, causing a greater vorticity and thus a shift in the boundary layer edge.
In the position upstream of the VG, the vorticity magnitude profiles of the *Smooth* and VG case almost match. As the flow is approaching the obstacle caused by the VG, its presence is detected by the flow, causing a slight increase in vorticity, when compared to the *Smooth* case.
Immediately after the VG position, for the case taken into consideration ($x/c = 0.2m$), the vorticity magnitude profiles of the VG solution show an increase in vorticity in the region near the airfoil surface. A peak in the vorticity magnitude profiles starts to arise.
This peak is most probably corresponding to the peak that would be expected in the region of maximum vorticity inside the vortex generated.
Proceeding downstream, the vorticity profiles reveal that initially the vortex stays closer to the wall, with a greater vorticity in this area. The vorticity peak denoted before decreases in magnitude, and the cross-section of the ideal vortex tube starts to diverge, as denoted by the stretching of the profiles. This is the cause of the greater boundary layer thickness.
The profiles are more and more stretched in the normal direction as the trailing edge is approached, and this denotes the lift-off of the vortex from the surface. In this region, the boundary layer thickness increases, but the vorticity near the airfoil surface decreases in magnitude when compared to the *Smooth* case.

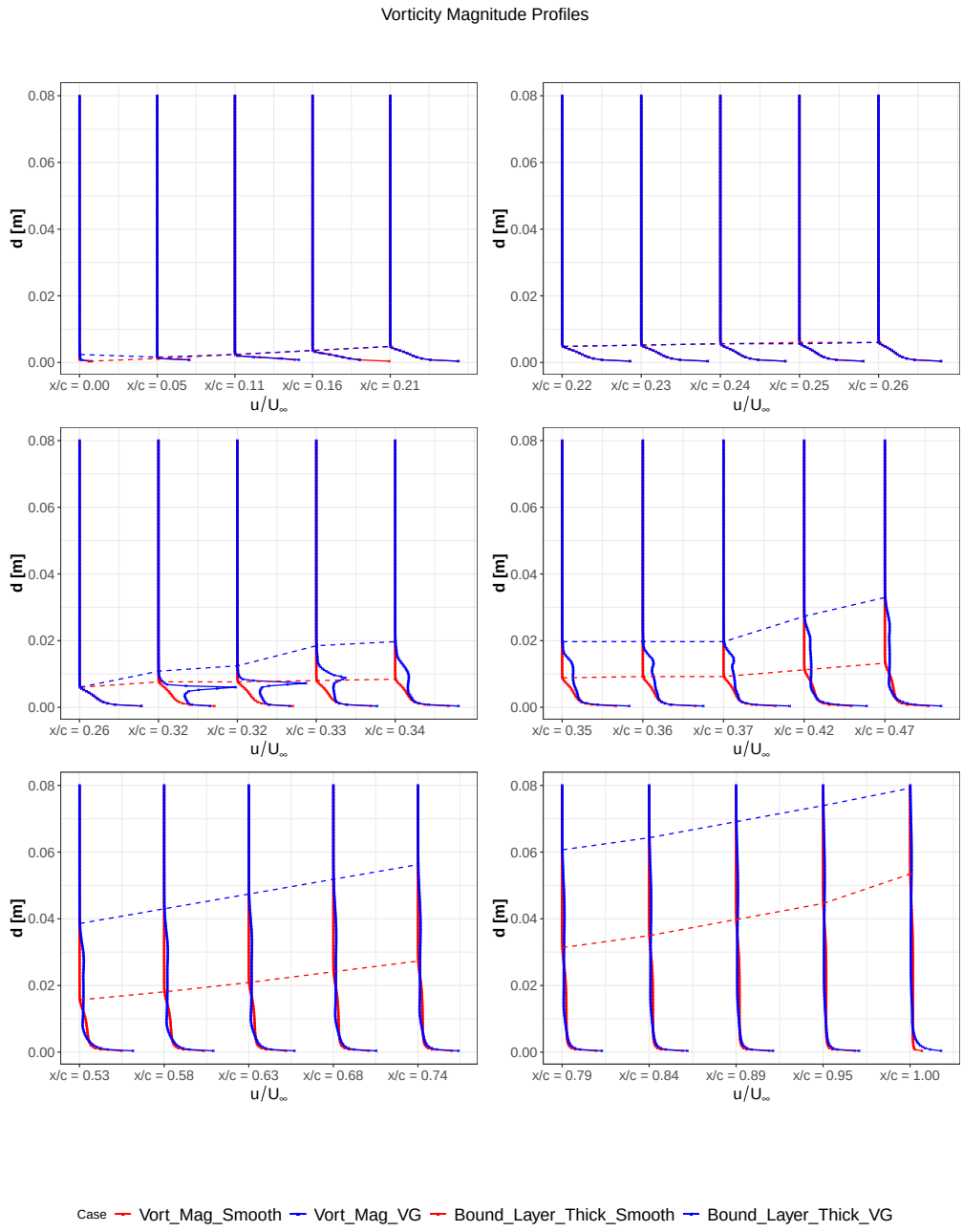

Figure 6.13: Vorticity magnitude 2D profiles in the streamwise direction, with the boundary layer thickness evolution. The airfoil considered is the FFA-W3-241 at an angle of attack of $\alpha = 8.8°$. The configurations displayed are the *Smooth* and the *VG x/c=0.3 h=6mm*.

In Figure 6.14, the streamwise-component velocity profiles development in the streamwise direction, for the FFA W3 301 airfoil, is shown, at an angle of attack $\alpha = 12.9°$. The VG configuration considered is the *VG x/c=0.3 h=6mm*.
The profiles were obtained extracting lines normal to the airfoil surface, up to a distance of $d = 0.08 * c$, with c the airfoil chord. The lines are considered at 30 different streamwise locations and 20 different spanwise locations. The plots show the u values for each streamwise locations, averaged with respect to the spanwise direction.
From the figure, it can be seen how the streamwise-component u evolves on the airfoil surface.
Before the location where the VG is positioned, the profiles of the Smooth and the VG case are nearly identical. They show the characteristic turbulent profiles shape, with very large velocity gradients near the wall, followed by the distinguishable slope change, up to the freestream constant value, that identifies the turbulent mixing region.
Right after the VG, from the analysis of the profiles shape, it can be seen that the flow modification induced is resembling one similar to the presence of an obstacle in the flow, as it is actually experienced by the streamwise flow developing near the airfol surface. In the very first two locations after the VG, that is the two $x/c = 0.32$ locations (coordinates were rounded for displaying purposes), two distinct flow regions can be identified in the boundary layer, one characterized by an almost zero velocity, and the other identified by the freestream U_∞ velocity value.
As the flow proceeds downstream, the region characterized by a zero velocity regains a higher u value already at the $x/c = 0.42$ location. The velocity profiles at nearly zero distances values, that is close to the airfoil surface, show a shape similar to the one shown in 2.3.2.
Due to the vortex arising in the flow, caused by the VG presence, flow mixing occurs in a shear layer at a certain distance from the wall. From the velocity profiles shape, this shear layer region can be identified by the slope change of the curves between the turbulent velocity profile near the airfoil wall surface, and the outer free stream constant profile.
Starting from the $x/c = 0.42$ streamwise position, the effect of the adverse pressure gradient can be qualitatively evaluated by the considerable deceleration that the *Smooth* case velocity profiles are experiencing. The position of the velocity profile inflection that can be regarded as the beginning of flow separation is identifiable at $x/c = 0.68$, after which a flow reversal appears and aerodynamic stalled conditions develop. From this location on, the positive effect of the VG in the flow is clearly visible. The corresponding velocity profiles do not show the inflection and flow reversal behaviour that characterizes separated flow conditions. The flow can therefore be considered staying attached on the whole airfoil surface.

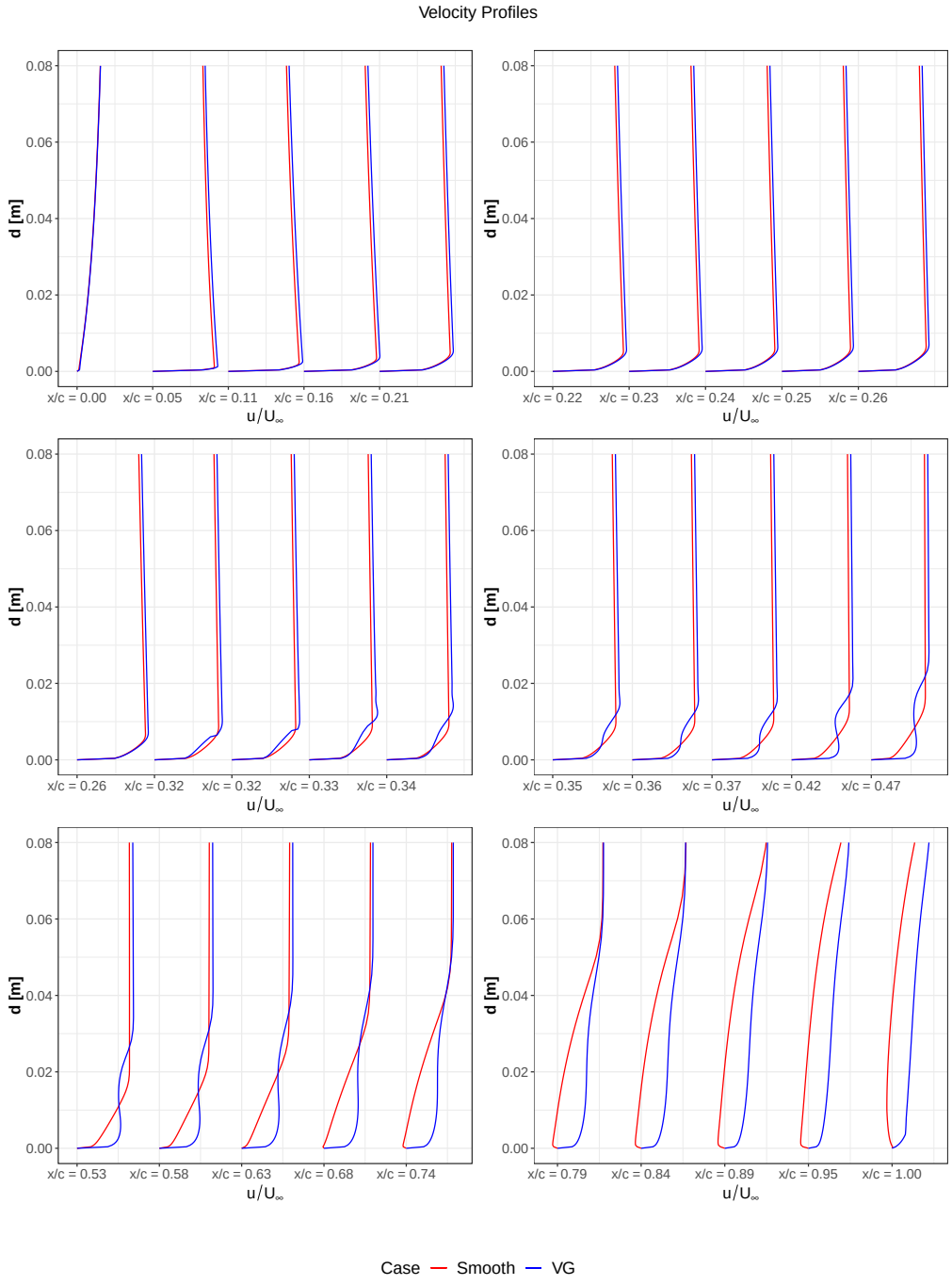

Figure 6.14: 2D profiles of the u velocity component in the streamwise direction, with the boundary layer thickness evolution. The airfoil considered is the FFA-W3-301 at an angle of attack of $\alpha = 12.9°$. The configurations displayed are the *Smooth* and the *VG* x/c=*0.3* h=*6mm*.

6.3.2 Integral Boundary Layer Analysis

In the following figures, from Figure 6.15 to Figure 6.17, the integral boundary layer quantities displacement thickness δ^*, momentum thickness θ, and energy thickness θ^* are displayed, for all the configurations and angles of attack simulated for the FFA-W3-241 airfoil.
These figures were obtained extracting lines normal to the airfoil surface, from 30 different streamwise locations and 20 different spanwise locations. The plots show the calculated thicknesses values for each streamwise locations, averaged with respect to the spanwise direction.
In Figure 6.15 the calculated displacement thickness δ^* is displayed.
It can be seen that at angles of attack near stall, for example $\alpha = 8.8°$, the presence of VGs in the flowfield induces a higher displacement thickness when compared with the *Smooth* case.
The highest δ^* values at the trailing edge are obtained in the *VG x/c=0.2 h=6mm* case. Recalling 2.4.3, it was said that the displacement thickness could be interpreted as the height of the free-shear-layer centerline for separated flow conditions. In this case, since the VG introduces an additional mixing in the flow, an associated free-shear-layer can be considered forming, therefore allowing the use of the mentioned interpretation. It can then be stated that a VG of an elevated height, placed at an early streamwise location under flow conditions close to the stalled ones, causes a free shear layer at a higher distance from the airfoil surface than the other configurations investigated. Being δ^* also the mass defect of the real flow compared to a theoretically Equivalent Inviscid Flow (see 2.4.3), a higher displacement thickness value implies, from an integral boundary layer point of view, less energy in the boundary layer donwstream of the VG, caused by this higher shear layer.
When considering more developed stalled flow conditions, occurring at higher angles of attack, the effect of VGs is to decrease progressively the growth of δ^* along the streamwise direction. With the information reintroduced before in 2.4.3, this indicates a lower mass defect and therefore an increased energy in the boundary layer. The beneficial effect of VGs in terms of aerodynamic performance can be clearly evaluated when considering deep stall flow conditions such as the ones at $\alpha = 14.4°$. The displacement thicknesses of the VG cases maintain much lower values along the streamwise direction than the corresponding *Smooth* case. The lowest δ^* values for high angles of attack are obtained in the *VG x/c=0.3 h=6mm* case. This indicates that, in order for wind turbines to withstand more severe operating conditions, a single strip of VGs of an elevated height, placed at a farther streamwise location from the leading edge, can be employed, allowing attached flow conditions for a longer streamwise distance.
In Figure 6.16, the momentum thickness θ is displayed.
From this figure, an increase in the momentum thickness is seen for all the VG cases considered, when compared to the *Smooth* reference. The highest θ values are obtained with the *VG x/c=0.2 h=6mm* case.
Recalling the physical explanation of the momentum thickness θ introduced in 2.4.3, related to the momentum defect due to the drag force, from the curves plotted it can evinced that using a VG with an elevated height at an early streamwise position causes a detrimental effect on the airfoil performance. In fact, the *VG x/c=0.2 h=6mm* case highlighted before shows an increase in the momentum thickness, implying an increase in drag. In this VG configuration the displacement thickness δ^* is also high with respect to other VGs configurations. Being the mass defect δ^* related to less energy in the flow, as stated previously, the information from θ, together with the behaviour of δ^*, explains the detrimental effect on the airfoil performance for the VG configuration mentioned previously.
From the momentum thickness curves, the transition from laminar to turbulent flow conditions can be evinced more easily than from the behaviour of the displacement thickness curves. The typical slope change can be detected more clearly, and it can be seen that it occurs at the VG location of the configuration considered.

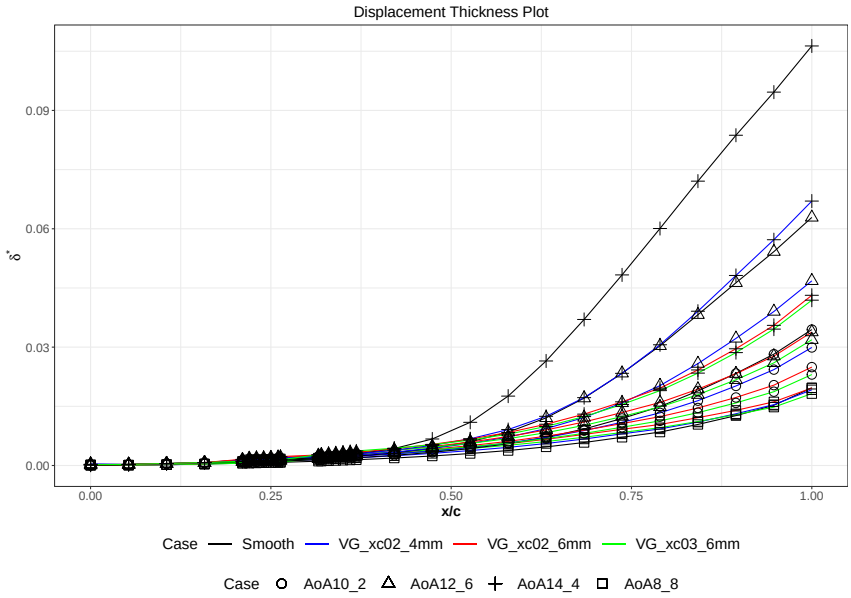

Figure 6.15: Displacement thickness calculated for the FFA-W3-241 airfoil. The angles of attack considered are $\alpha = 8.8°$, $\alpha = 10.2°$, $\alpha = 12.6°$, and $\alpha = 14.4°$. The configurations displayed are *Smooth*, *VG x/c=0.2 h=4mm*, *VG x/c=0.2 h=6mm*, and *VG x/c=0.3 h=6mm*.

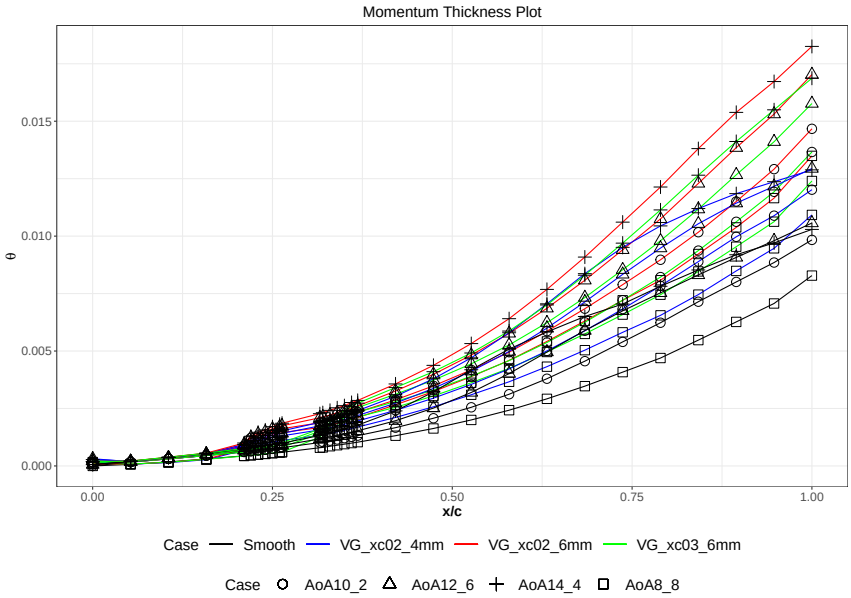

Figure 6.16: Momentum thickness calculated for the FFA-W3-241 airfoil. The angles of attack considered are $\alpha = 8.8°$, $\alpha = 10.2°$, $\alpha = 12.6°$, and $\alpha = 14.4°$. The configurations displayed are *Smooth*, *VG x/c=0.2 h=4mm*, *VG x/c=0.2 h=6mm*, and *VG x/c=0.3 h=6mm*.

In Figure 6.17, the energy thickness θ^* is displayed.
In 2.4.3, it was seen that the physical interpretation of the energy thickness was related to the combined action of the drag and the viscous forces. Being the integral boundary layer thicknesses generally related to a defect of a certain physical quantity, in the case of the energy thickness, this is related to an energy defect of the real boundary layer compared to an inviscid ideal flow (EIF). Since the vortices induced in the flowfield by VGs introduce viscous dissipation in the flow through a shear layer, with the physical interpretation cited previously, it can be stated that the use of VGs increases the energy defect donwstream of the VG location, thus increasing the energy dissipated in the boundary layer.
This would seem in contrast with what said in previous considerations, where the enhanced mixing of VGs in the flow was said to cause an energization, allowing attached flow conditions. The explanation for the increased energy thickness is to be found in the averaging processing of the 3D data, that smooths the local flow behaviour. This smoothing is then subject to an additional integration to derive the integral boundary layer quantities. The resulting values are due to the averaged sum of regions where the flow is not energized, that is near the vortices, and of regions where the flow is effectively mantained closer to the wall, through the entrainment from the vortices of the outer high energy flow.
The energy thickness curves show a behaviour similar to the momentum thickness ones. This follows from the definition of the two thicknesses, being in fact the energy thickness proportional to the momentum thickness through a factor $(1 + \overline{u}/U_\infty)$. Hence, it is displayed that, for all the angles of attack considered, the *VG x/c=0.2 h=4mm* configuration causes the highest energy thickness; for the momentum thickness the same VG configuration shows analogously the maximum values. Similarly to the previous explanation, this is related to an increase in drag, but also for this particular case to an increased vicous dissipation. This dissipation develops earlier than what would instead happen with a VG positioned at greater streamwise locations, causing therefore more disadvantages than benefits.

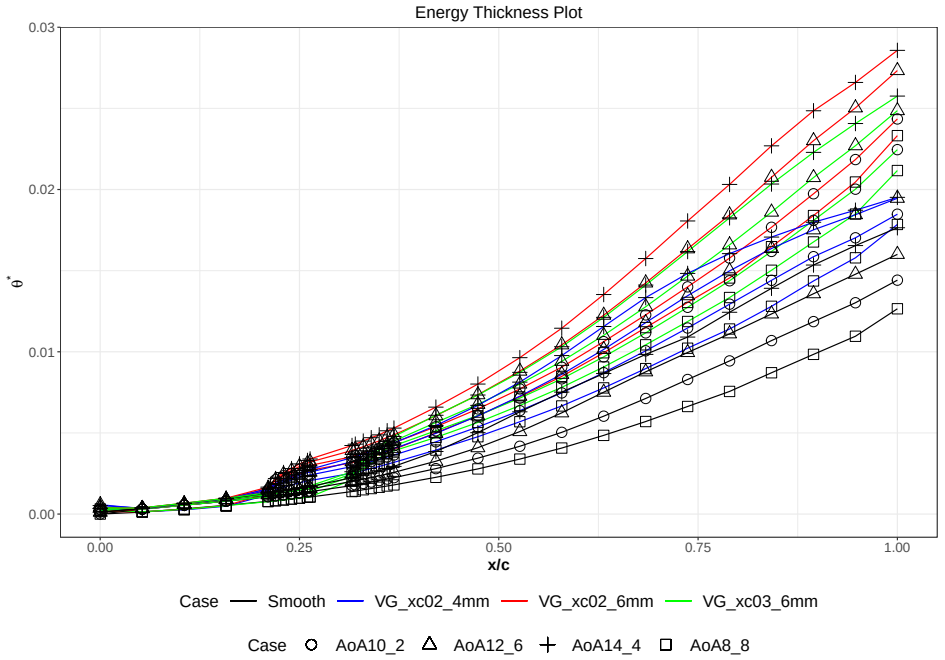

Figure 6.17: Energy thickness calculated for the FFA-W3-241 airfoil. The angles of attack considered are $\alpha = 8.8°$, $\alpha = 10.2°$, $\alpha = 12.6°$, and $\alpha = 14.4°$. The configurations displayed are *Smooth*, *VG x/c=0.2 h=4mm*, *VG x/c=0.2 h=6mm*, and *VG x/c=0.3 h=6mm*.

In Figure 6.18 to Figure 6.20, the displacement thickness, momentum thickness and energy thickness for the FFA-W3-301 airfoil are displayed, for all the configurations and simulated angles of attack.
These figures were obtained extracting lines normal to the airfoil surface as done for the FFA-W3-241 case; 30 different streamwise locations and 20 different spanwise locations were considered. The plots show the calculated thicknesses values for each streamwise locations, averaged with respect to the spanwise direction.
In all the three figures, relatively to each integral boundary layer thickness, similar considerations to the ones presented for the FFA-W3-241 airfoil can be stated.
For the FFA-W3-301, the decrease of δ^* and the increase of θ and θ^* when using VGs are more pronounced than the FFA-W3-241 case.
The same physical interpetations stated for the FFA-W3-241 integral thicknesses can be applied too, with the addition that the change of slope due to the transition from laminar to turbulent is even more visible from the energy and momentum thicknesses plots. The order of magnitude of the calculated δ^*, θ, and θ^* is comparable with the values obtained for the FFA-W3-241 airfoil.

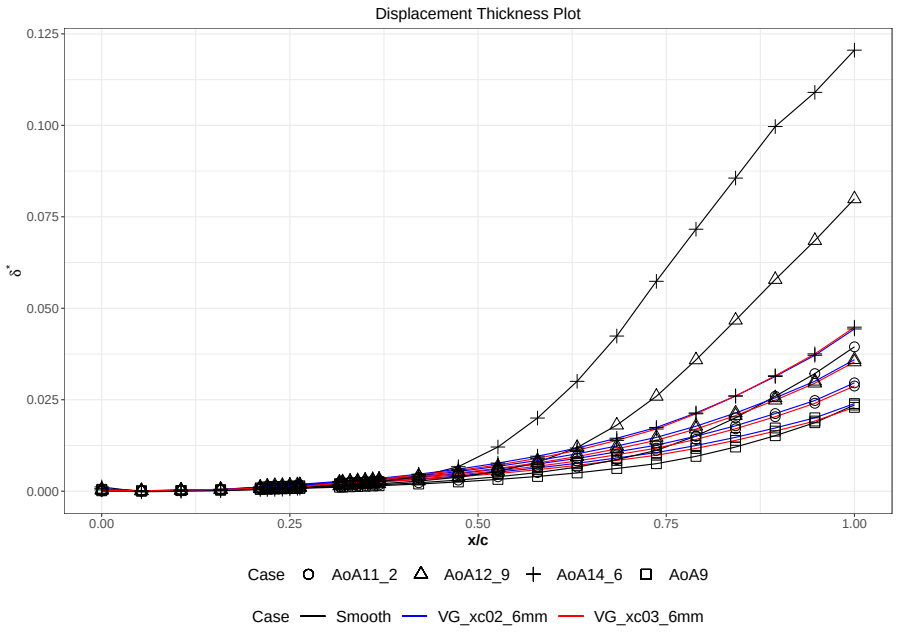

Figure 6.18: Displacement thickness calculated for the FFA-W3-301 airfoil. The angles of attack considered are $\alpha = 9°$, $\alpha = 11.2°$, $\alpha = 12.9°$, and $\alpha = 14.6°$. The configurations displayed are *Smooth*, *VG x/c=0.2 h=6mm*, and *VG x/c=0.3 h=6mm*.

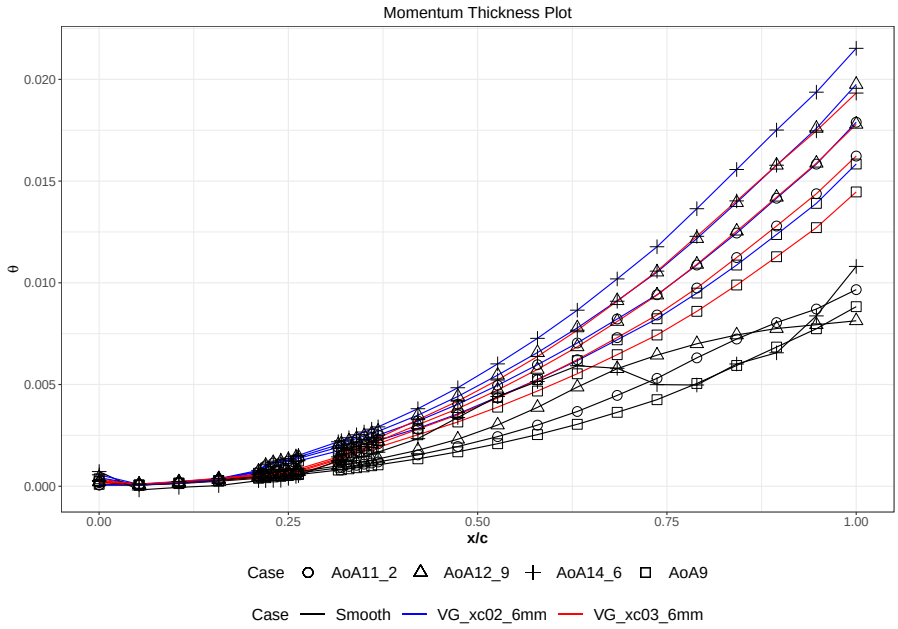

Figure 6.19: Momentum thickness calculated for the FFA-W3-301 airfoil. The angles of attack considered are $\alpha = 9°$, $\alpha = 11.2°$, $\alpha = 12.9°$, and $\alpha = 14.6°$. The configurations displayed are *Smooth*, *VG x/c=0.2 h=6mm*, and *VG x/c=0.3 h=6mm*.

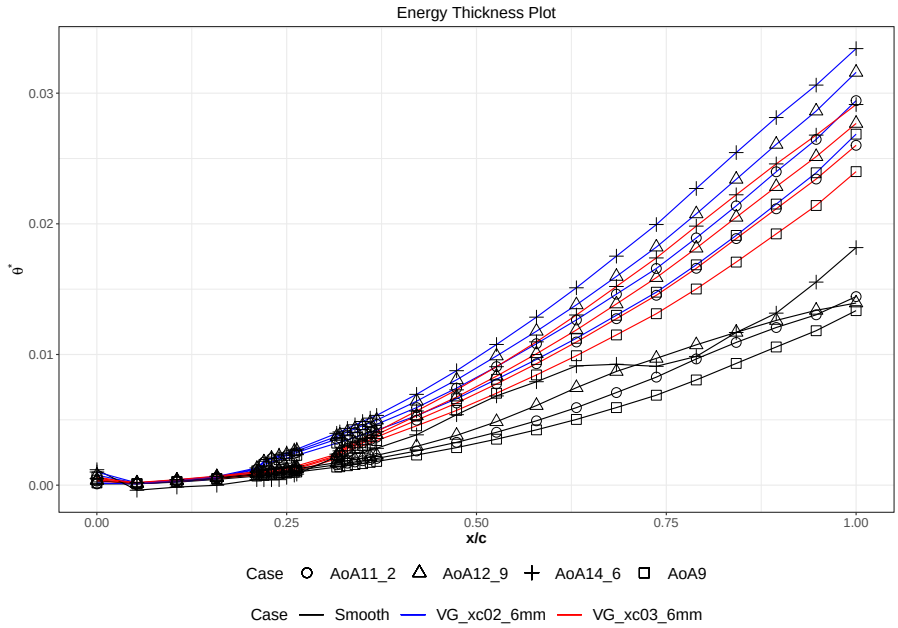

Figure 6.20: Energy thickness calculated for the FFA-W3-301 airfoil. The angles of attack considered are $\alpha = 9°$, $\alpha = 11.2°$, $\alpha = 12.9°$, and $\alpha = 14.6°$. The configurations displayed are *Smooth*, *VG x/c=0.2 h=6mm*, and *VG x/c=0.3 h=6mm*.

6.4 Question 4

The fourth question is discussed considering 3D visualization techniques. This is performed using Vortex Cores Line detection, Q-Criterion calculations and Surface Line Integral Convolution visualizations.

6.4.1 Vortex Cores Line

In Figure 6.21, it is shown the vortex core line extracted from the simulation results, together with the u velocity component profiles. This line is representative of the presumed vortex core centre as it evolves in the streamwise direction. The airfoil configuration considered is the FFA-W3-301 *VG x/c=0.3 h=6mm* at an angle of attack of $\alpha = 12.9°$.
Recalling what said in Figure 6.14, it can be seen that the vortex core line extracted from the data is in agreement with the considerations about the change of slope. This change of slope occurrs outside the viscous sublayer, in the outer region of the turbulent boundary layer. Outside the viscous sublayer, as can be seen in the figure, the effect of the VG regarding the slope of the profiles is to introduce a local minimum for each profile. These local minima can be physically interpreted as describing the locations near to the vortex core. This seems to be in contrast with intuitive physical considerations regarding ideal irrotational vortices. These are known to be characterized by a minimum pressure region near the vortex core, and therefore, a higher velocity. The real vortices evolution is instead influenced by a dissipation phenomena due to viscosity; inside the vortex region this affects considerably the velocity, decreasing it if compared to the region outside the vortex. For this reason, lower velocities are identifiable in the vortices region.
Therefore, it can be seen that the vortex core line extracted is close to the ideal line that would connect the local minima in the velocity profile, confirming this interpretation.
In the vortex core line extraction process, the parameters tuning procedure of the model is of fundamental importance, since it affects the number of points on the vortex core line extracted. As for the line obtained, various parameters combinations were tested, and the final set-up reported in Section §5.4 allowed to attain a qualitatively representative line of the VG vortex centre path. However, the number of points of the line extracted is not sufficient to describe the vortex propagation until the trailing edge of the airfoil. It is believed that the reason for this incomplete point detection is related to the progressive vortex dissipation and mixing with the outer flow, that prevents a proper detection of the vortex centre evolution.

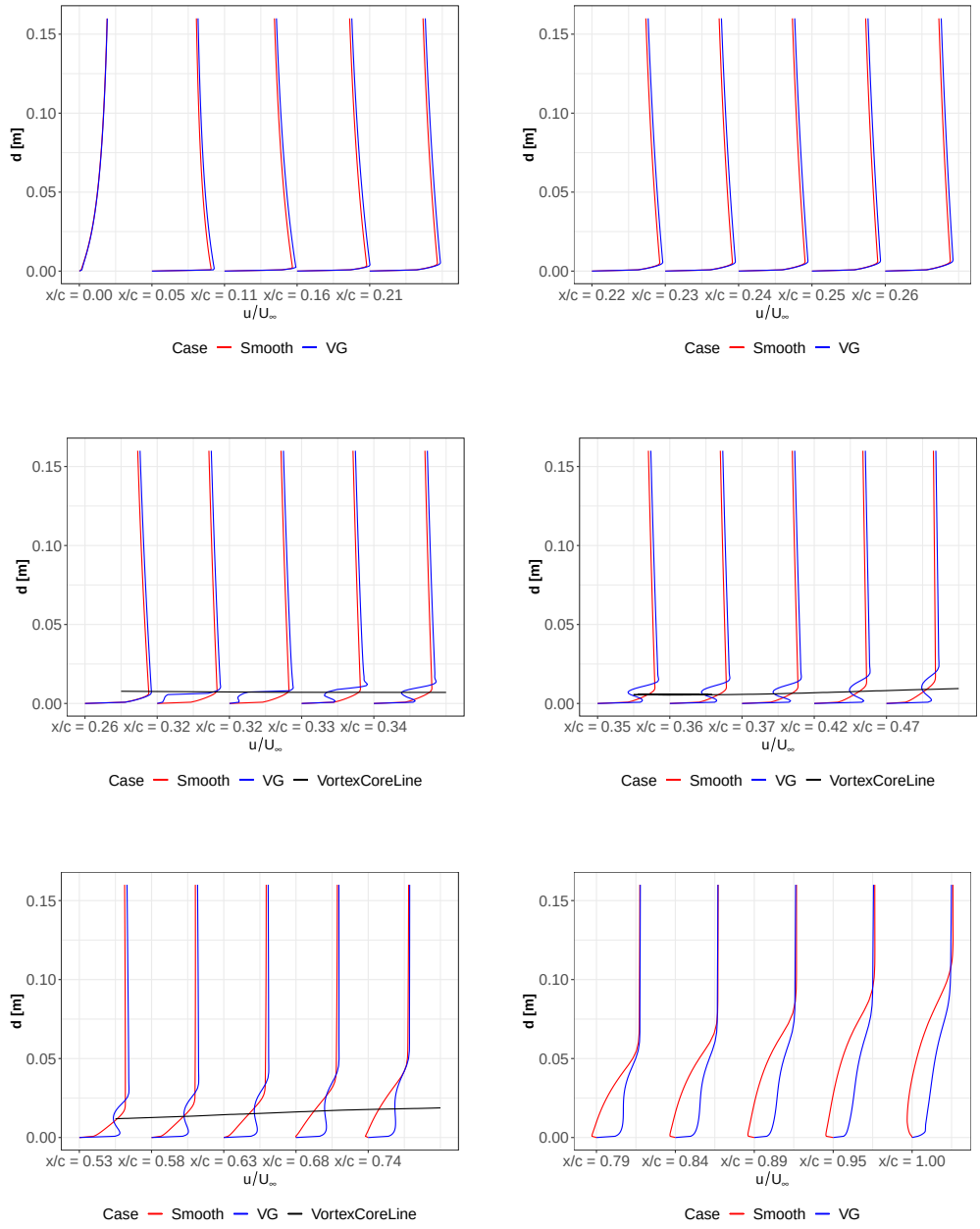

Figure 6.21: Profiles evolution of the u velocity component, together with the vortex core line extracted. The configuration considered is the FFA-W3-301 *VG x/c=0.3 h=6mm* at an angle of attack of $\alpha = 12.9°$.

6.4.2 Q-Criterion

From the top image in Figure 6.22, the vortex tube evolution is shown for the FFA-W3-301 *VG x/c=0.3 h=6mm* case, at an angle of attack of $\alpha = 12.9°$. This figure is created from the Q-Criterion calculation, displaying the contour level value of 30. It can be seen that it is possible from the simulation performed to capture the evolution of the vortex tube arising from the VG. The vortex tube was coloured by the corresponding vorticity magnitude values, showing the decay of the strength of the vortex as it proceeds downstream the VG location.
From the bottom image in Figure 6.22, is shown the vortex tube evolution, together with the vortex core line extracted. The case considered is the same FFA-W3-301 *VG x/c=0.3 h=6mm*, at an angle of attack of $\alpha = 12.9°$. It is clearly shown in this image that the vortex core line is indeed representative of the vortex tube that describes the induced vortex due to the VG presence on the flow field.

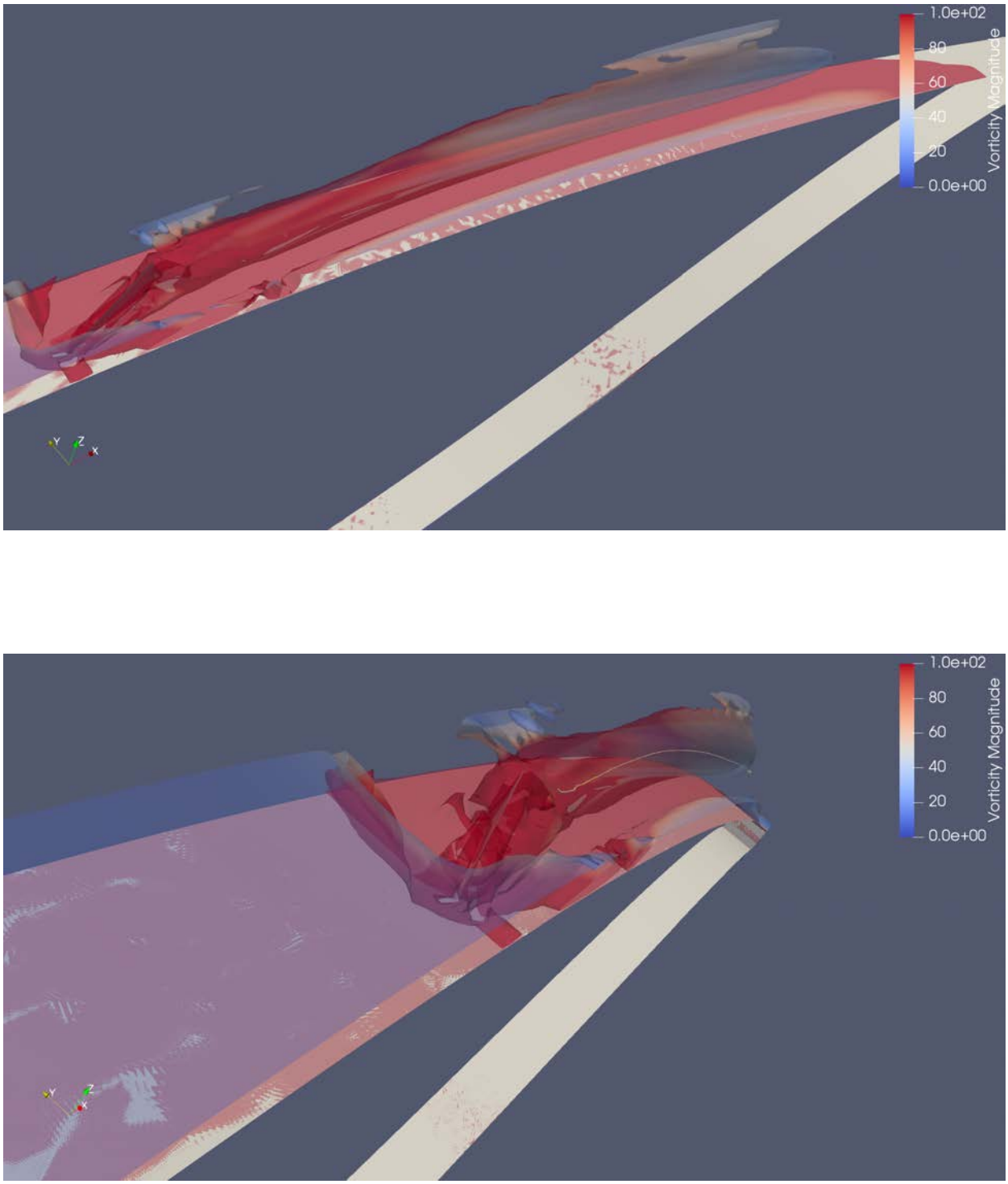

Figure 6.22: Q-Criterion visualization for the FFA-W3-301 *VG x/c=0.3 h=6mm* configuration, at an angle of attack of $\alpha = 12.9°$. The top image shows a contour level value of 100 for the Q-Criterion calculated. The bottom image shows the same case as the top image, together with the vortex core line extracted.

6.4.3 Surface Line Integral Convolution

In Figure 6.23, the skin friction coefficient lines are displayed on the airfoil surface. This image was obtained using a surface Line Integral Convolution representation of the skin friction coefficient vector created with the skin friction coefficient components present in the SU2 simulations results. In this picture, the VG pair is recreated mirroring the surface flow solution with respect to the minimum spanwise coordinate.
In the *VG x/c=0.2 h=6mm* case, the two vortices arising from the VG pair can be easily noticed by the skin friction lines pointing to the sides of the flow domain. These skin friction lines show a curved behaviour that resembles the vortical movement of the flow near the airfoil surface. In the middle region, the skin friction lines are mainly oriented in the streamwise direction, identifying an attached flow condition. For this VG configuration, no flow separation is experienced, and this can be observed by the absence of clear converging skin friction lines on the airfoil surface.
In the *Smooth* case, the skin friction lines show a main streamwise direction. Flow separation in this case is expected to occur at around x/c=0.6 from the 2D skin friction magnitude figure in Figure 6.8. From a qualitative evaluation of this 3D image, the visual inspection of the skin friction lines shows a strange behaviour of the lines around the x/c=0.6 streamwise location, although it is not the converging behaviour expected from the theoretical explanations of flow separation for 3D flows presented in Section §2.5.

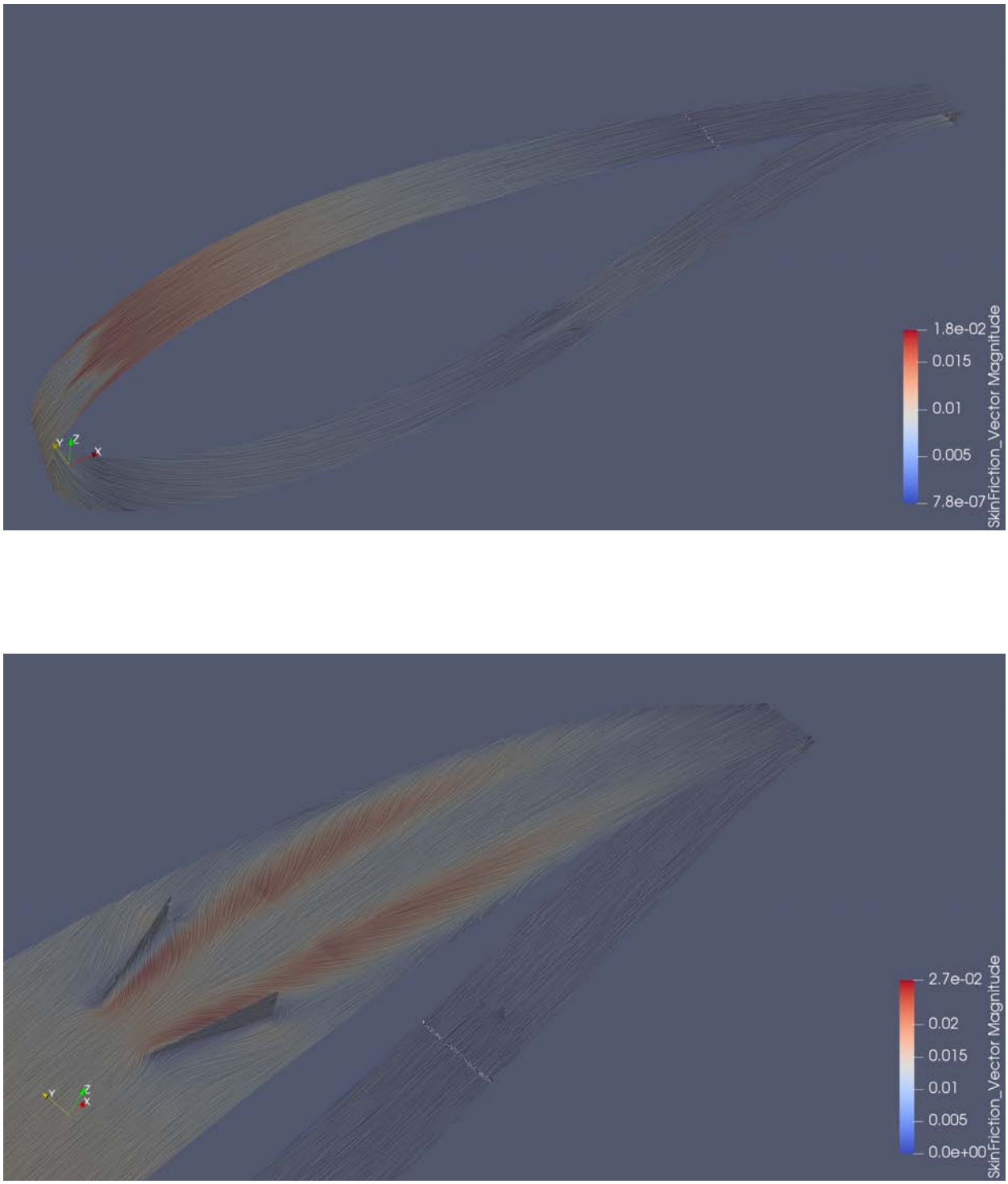

Figure 6.23: Surface Line Integral Convolution visualization of the skin friction vector, for the FFA-W3-301 *Smooth* and *VG x/c=0.2 h=6mm* configurations. The angle of attack is $\alpha = 12.9°$. The top image shows the *Smooth* configuration. The bottom image shows the *VG x/c=0.2 h=6mm* configuration.

6.5 Conclusions

In this chapter, the simulation results were discussed for each research question proposed. In the following chapter, the conclusions of this analysis are presented, answering the research questions together with future work recommendations.

Chapter 7

Conclusions

In this thesis, a numerical investigation of the effect of vortex generators placed at the suction side of various wind turbine airfoil sections was conducted.
The airfoil sections and configurations are reported in [23]. From this paper, it was decided to analyze the FFA-W3-301 and the FFA-W3-241 sections, considering angles of attack in near-stalled flow conditions. This choice was motivated by the visual inspection of the values of the lift and drag coefficients from the experimental data: in these flow conditions a qualitative analysis could show clearly the benefits of such devices regarding flow separation prevention. The configurations analyzed from the paper consider two different VG heights, *h=4mm* and *h=6mm*, and two different airfoil sections streamwise positions, *x/c=0.2* and *x/c=0.3*.
CAD models of the geometrical configurations of the airfoil sections, with and without the VGs strips, were created, simulating only a single VG instead of the original VG pair. This allowed a reduction in the number of grid cells generated during the subsequent mesh creation process, reducing the computational time. The simulations were run using the current SU2's incompressible solver, investigating its capabilities. The result were investigated discussing four research questions introduced in Section §1.2, to which an answer is provided as follows:

Question 1

The first question proposed was:

Is the current SU2's incompressible solver implementation able to reproduce vortex generators' experimental results up to a reasonable degree of accuracy?

From the analysis of Figure 6.1 to Figure 6.4, it can be concluded that the results obtained from the simulations generally do not match the experimental values of reference. This becomes clear when considering the comparison between the lift and drag coefficient for the cases simulated, but it is less obvious when examining the pressure coefficient plots. In fact, when considering the FFA-W3-241 airfoil in the *Smooth* configuration case at an angle of attack of $\alpha = 8.8°$, together with the $\alpha = 10.2°$ case in the *Smooth*, *VG x/c=0.2 h=4mm*, *VG x/c=0.2 h=6mm* and *VG x/c=0.3 h=6mm* configuration, it seems that the simulations do not mispredict excessively the reference values from the experiments in [23]. In the remaining cases, for both the FFA-W3-241 and the FFA-W3-301 airfoils, the results from the simulations are clearly different from the experimental values. The substantial deviation, with respect to the experiments, of the values of lift and drag coefficient obtained numerically with SU2, could be explained considering that, even if in some cases the pressure qualitatively seems predicted reasonably well, the small differences still contribute significantly during the integration to obtain the lift and drag forces and the related coefficients.

Question 2

The second question proposed was:

Are the results obtained from the simulations qualitatively describing the relevant flow modifications?

From the analysis of Figure 6.5 to Figure 6.12, it can be stated that the relevant flow features are captured qualitatively.
Regarding the pressure coefficient, Figure 6.6 show that the flow mixing induced by the VGs is delaying flow separation. Overall, the VG presence is seen to decrease the pressure at the suction side more than the corresponding *Smooth* cases, as it would be expected from the use of such devices. The decrease in pressure at the suction side causes an increase in lift, confirming what was seen also in the reference paper.
As for the skin friction coefficient magnitude, it is shown clearly from both Figure 6.7 and Figure 6.8 how the VGs increase the skin friction because of the vortical mixing. This favourable effect with regard to flow separation mantains a skin friction value high enough to be able to withstand the adverse pressure gradient, thus mantaining the flow attached until the trailing edge.
From the contour plots of the vorticity magnitude in Figure 6.10, the primary vortices described in [18] are captured. Regarding the secondary vortical movements, these are not captured in the simulations results, in accordance to what would be generally expected from Reynolds Averaged Navier Stokes CFD simulations.
In the contour plots of the velocity components in Figure 6.12, the flow generally tends to stay closer to the wall, as indicated by the downward w velocity component (velocity in the z direction). This confirms the benefits of VGs in mantaining the flow attached to the airfoil surface. In these plots, the dissipation occurring in the vortices is also displayed: in fact, this is indicated by the lower u velocity component inside the vortical structures.

Question 3

The third question proposed was:

Is a 2D boundary layer analysis showing the expected essential qualitative aspects?

From the analysis of Figure 6.13 to Figure 6.20, the main 2D boundary layer features are captured, as can be seen from the vorticity magnitude profiles in Figure 6.13 and from the u velocity profiles in Figure 6.14.
The vorticity magnitude profiles have the typical shape showing an exponential decay, with a distinguishable peak in correspondence of the vortex. The vortex dissipation along the streamwise direction is depicted by the decrease in magnitude of the peak.
The u velocity profiles show clearly how the flow is decelerated in the streamwise direction by the presence of the VG. The profiles show an inflection in correspondence of the vortex core, and near the airfoil surface the typical turbulent profile shape can be noticed. When comparing the *Smooth* and a VG case, the prevention of separation is highlighted by the disappearance of the flow reversal typical shape, characterized by negative streamwise u velocity component values.
Regarding the integral boundary layer analysis from Figure 6.15 to Figure 6.20, the displacement thicknesses δ^* show an increase in values for the VG cases when compared to the Smooth ones, conferming the increased drag force caused by the shear layer forming. The momentum thicknesses θ show the characteristic change of slope in correspondence of the transition from laminar to turbulent flow conditions, that occurs at the VG location. In accordance with the displacement thickness behaviour, θ shows an increase caused by the drag force as well. The energy thicknesses θ^* tend to also increase when considering the use of VGs, due to the combined action of drag forces and viscous dissipation.

Question 4

The fourth question proposed was:

Is a 3D qualitative flow visualization analysis displaying the important flow features?

From the analysis of Figure 6.21 to Figure 6.23, it can be stated that the results are able to partially capture 3D flow features.
From the representation of the vortex core line, together with the velocity profiles, it can be seen that the vortex core line extracted is representative of the inflection points of the velocity profiles. This is expected, since this low-velocity region is the one where the highest dissipation occurs, that is, at the core of the vortex.
As for the vortex tube detection, the Q-Criterion is able to capture the vortex evolution up to a certain streamwise location, after which the dissipation occuring and the consequent increase in the vortex tube radius prevent a distinguishable visualization.
The skin friction lines' visualization, using a Surface Line Integral Convolution representation, shows that the skin friction lines characterizing the flow separation from the surface are not clearly identifiable. The converging behaviour of the lines towards an asymptote is not detectable. However, the lines computed describe the vortices movements on the surface with reasonable accuracy, when compared to the vortices development shown in Figure 6.10.

Future Work

From the numerical analysis conducted, it is therefore possible to conclude that the current SU2's solver implementation is capable to resolve the main flow features. During the course of this thesis work, an important aspect of the Pre-Processing phase was identified in the mesh generation process. From Chapter 4 and from the final simulations' set-up in Chapter 5, a proper resolving of key flow regions to investigate has shown a considerable improvement in the resulting data obtained. However, this step of the Pre-Processing phase is quite time-consuming, and even with an acceptable mesh resolution, the final results are still far from the corresponding experimental data obtained. Therefore, it is believed that a further investigation on different mesh generation strategies could lead to an improved accuracy in the results.
Nevertheless, the results obtained are considered to be accurate enough to be used for modelling purposes, especially in Integral Boundary Layer codes. In fact, from Figure 6.15 to Figure 6.20, it was shown that the integral quantities computed already describe qualitatively the expected thicknesses curves' trends. From these data, a suitable model for the 2D VG influence in the flow field could be derived.
An attempt in this direction was presented in [66], where an integral boundary layer model for the effect of VGs mounted on flat plates is introduced, with promising results.

Bibliography

[1] EIA. EIA International Energy Outlook 2017. *U.S. Energy Information Administration*, IEO2017(2017):143, 2017.

[2] B. Wehrmann. German onshore wind power - output, business and perspectives. `www.cleanenergywire.org.`, 2018.

[3] Suhaib Salah El-Tayeb Awad. *Numerical simulation of vortex trapped Airfoil*. PhD thesis, 2015.

[4] S. A. Prince, V. Khodagolian, C. Singh, and T. Kokkalis. Aerodynamic Stall Suppression on Aerofoil Sections Using Passive Air-Jet Vortex Generators. *AIAA Journal*, 47(9):2232–2242, 2009.

[5] Raymond Chow and C. van Dam. Inboard Stall and Separation Mitigation Techniques on Wind Turbine Rotors. (January):1–11, 2014.

[6] Michael Cavanaugh, Paul Robertson, and William Mason. Wind Tunnel Test of Gurney Flaps and T-Strips on an NACA 23012 Wing. (June):1–18, 2012.

[7] D. W. Bechert, M. Bruse, W. Hage, J. G.T. Van Der Hoeven, and G. Hoppe. Experiments on drag-reducing surfaces and their optimization with an adjustable geometry. *Journal of Fluid Mechanics*, 338:59–87, 1997.

[8] Peter M. Hartwich. United States Patent (19) 54. 1992.

[9] WindTurbine Rotor Winglets unmounted. `https://commons.wikimedia.org/wiki/File:WindTurbine{\_}Rotor{\_}Winglets{\_}unmounted.jpg`.

[10] J.C.Lin. *Review of research on low-profile vortex generators to control boundary-layer separation*, volume 38. 2002.

[11] Martin O.L Hansen. *Aerodynamics of Wind Turbines*. 2008.

[12] J. F. Manwell, J. G. McGowan, and A. L. Rogers. *Wind Energy Explained*. 2009.

[13] Doug McLean. *Understanding Aerodynamics*. 2013.

[14] Frank M. White. *Viscous Fluid Flow*. 1992.

[15] Mark Drela. *Flight Vehicle Aerodynamics*. MIT Press, 2013.

[16] A. E. P. Veldman. Boundary Layers in Fluids Lecture Notes in Applied Mathematics. *Boundary Layers in Fluids*, 2008.

[17] Frank K. Lu, Qin Li, and Chaoqun Liu. Microvortex generators in high-speed flow. *Progress in Aerospace Sciences*, 53:30–45, 2012.

[18] Clara Marika Velte. *Generator Induced Flow PhD Thesis*. PhD thesis, 2009.

[19] Benoiit Gardarin and Laurent Jacquin. On The Physics Of Vortex Generators For Flow Separation Control. *Sixth International Symposium on Turbulence and Shear Flow Phenomena*, 2009.

[20] Wayne R. Pauley and John K. Eaton. Experimental study of the development of longitudinal vortex pairs embedded in a turbulent boundary layer. *AIAA Journal*, 26(7):816–823, 2008.

[21] Nic Sharpley. Increasing wind turbine efficiency with vortex generators. `www.windpowerengineering.com`, 2015.

[22] Haipeng Wang, Bo Zhang, Qinggang Qiu, and Xiang Xu. Flow control on the NREL S809 wind turbine airfoil using vortex generators. *Energy*, 118:1210–1221, 2017.

[23] Peter L. Fuglsang, Ioannis Antoniou, K.S. S Dahl, and H Aa Madsen. *Wind tunnel tests of the FFA-W3-241, FFA-W3-301 and NACA 63-430 airfoils*, volume 1041. 1998.

[24] A. van Wingerde. Special report: Developments in rotor design. Technical report, Fraunhofer IWES, 2012.

[25] Fabrizio De Gregorio and Giuseppe Fraioli. Flow control on a high thickness airfoil by a trapped vortex cavity. *14th Int Symp on Applications of Laser Techniques to Fluid Mechanics*, (October):7–10, 2008.

[26] Demeter G. Fertis. New Airfoil Design Concept with Improved Aerodynamic Characteristics. 7(3):328–339, 1994.

[27] Jeppe Johansen and Niels N. Sørensen. Aerodynamic investigation of Winglets on Wind Turbine Blades using CFD. *Risø National Laboratory*, 1543(February):1–17, 2006.

[28] Ron Barrett and Saeed Farokhi. Subsonic aerodynamics and performance of a smart vortex generator system. *Journal of Aircraft*, 33(2):393–398, 2008.

[29] Juan J. Alonso, Sean R. Copeland, Francisco Palacios, Trent W. Lukaczyk, and Thomas D. Economon. SU2: An Open-Source Suite for Multiphysics Simulation and Design. *AIAA Journal*, 54(3):828–846, 2015.

[30] J. A. D. Ackroyd, B. P. Axcell, and A. I. Ruban. *Early Developments of Modern Aerodynamics*. 2001.

[31] H. K. Moffat. A Brief Introduction To Vortex Dynamics And Turbulence. 2011.

[32] A. D. Cutler and P. Bradshaw. Strong vortex/boundary layer interactions: Part I. Vortices high. *Experiments in Fluids: Experimental Methods and their Applications to Fluid Flow*, 14(5):321–332, 1993.

[33] A.D. Cutler and P. Bradshaw. Strong Vortex / Boundary Layer Interactions. Part II. Vortex Low. *Experiments in Fluids*, 14:393–401, 1993.

[34] H.H. Pearcey. *Introduction To Shock-Induced Separation and Its Prevention By Design and Boundary Layer Control*. PERGAMON PRESS LTD, 2014.

[35] T. Shizawa and J. K. Eaton. Interaction of a longitudinal vortex with a three-dimensional, turbulent boundary layer. *AIAA Journal*, 30(5):1180–1181, 2008.

[36] W.J. Kim and V.C. Patel. Influence Of Streamwise Curvature On Longitudinal Vortices Imbedded In Turbulent Boundary Layers. 1993.

[37] H. Babinsky, Y. Li, and C. W. Pitt Ford. Microramp Control of Supersonic Oblique Shock-Wave/Boundary-Layer Interactions. *AIAA Journal*, 47(3):668–675, 2009.

[38] P Ashill, J Fulker, and K Hackett. Research at DERA on sub boundary layer vortex generators. (January), 2001.

[39] Julianne C. Dudek. Modeling Vortex Generators in a Navier-Stokes Code. *AIAA Journal*, 49(4):748–759, 2011.

[40] Christopher D. Booker, Xin Zhang, and Sergei I. Chernyshenko. Large-Scale Vortex Generation Modeling. *Journal of Fluids Engineering*, 133(12):121201, 2011.

[41] Florian Von Stillfried, Stefan Wallin, and Arne V. Johansson. Evaluation of a Vortex Generator Model in Adverse Pressure Gradient Boundary Layers. *AIAA Journal*, 49(5):982–993, 2011.

[42] Florian Von Stillfried, Stefan Wallin, and Arne V. Johansson. Vortex-Generator Models for Zero- and Adverse-Pressure-Gradient Flows. *AIAA Journal*, 50(4):855–866, 2012.

[43] Adam Jirasek. Vortex-Generator Model and Its Application to Flow Control. *Journal of Aircraft*, 42(6):1486–1491, 2005.

[44] Kenrick A Waithe. Source Term Model for an Array of Vortex Generator Vanes. (March), 2003.

[45] S. Lee, E. Loth, and H. Babinsky. Normal shock boundary layer control with various vortex generator geometries. *Computers and Fluids*, 49(1):233–246, 2011.

[46] Akshoy Ranjan Paul, Pritanshu Ranjan, Vivek Kumar Patel, and Anuj Jain. Comparative studies on flow control in rectangular S-duct diffuser using submerged-vortex generators. *Aerospace Science and Technology*, 28(1):332–343, 2013.

[47] J. M. Wu and W. Q. Tao. Impact of delta winglet vortex generators on the performance of a novel fin-tube surfaces with two rows of tubes in different diameters. *Energy Conversion and Management*, 52(8-9):2895–2901, 2011.

[48] Linyue Gao, Hui Zhang, Yongqian Liu, and Shuang Han. Effects of vortex generators on a blunt trailing-edge airfoil for wind turbines. *Renewable Energy*, 76:303–311, 2015.

[49] Lei Zhang, Xingxing Li, Ke Yang, and Dingyun Xue. Effects of vortex generators on aerodynamic performance of thick wind turbine airfoils. *Journal of Wind Engineering and Industrial Aerodynamics*, 156:84–92, 2016.

[50] Niels N. Sørensen, F. Zahle, C. Bak, and T. Vronsky. Prediction of the effect of vortex generators on airfoil performance. *Journal of Physics: Conference Series*, 524(1), 2014.

[51] U Fernández-Gamiz, P.-E. Réthoré, N N Sørensen, C M Velte, F Zahle, and E Egusquiza. Comparison of four different models of vortex generators. *In Proceedings of EWEA 2012 - European Wind Energy Conference & Exhibition European Wind Energy Association (EWEA)*, 2012.

[52] Delphine De Tavernier, Daniel Baldacchino, and Carlos Ferreira. An integral boundary layer engineering model for vortex generators implemented in XFOIL. *Wind Energy*, 21(10):906–921, 2018.

[53] Anders Bjorck. Coordinates and Calculations for the FFA-Wl-xxx, FFA-W2-xxx, FFA-W2-xxx and FFA-W3-xxx Series of Airfoils for Horizontal Axis Wind Turbines. *Technical Report FFA Tn 1990-15, Stockholm, Sweden*, 1990.

[54] Francisco Palacios, Michael Colonno, Thomas Economon, Sean Copeland, Aniket Aranake, Thomas Taylor, Trent Lukaczyk, Amrita Lonkar, Juan Alonso, and Alejandro Campos. Stanford University Unstructured (SU2): An open-source integrated computational environment for multi-physics simulation and design. (January):1–60, 2013.

[55] Alexandre Joel Chorin. A Numerical Method for Solving Incompressible Viscous Flow Problems. *Journal of Computational Physics*, pages 12–26, 1967.

[56] D. Choi and C. L. Merkle. Application of time-iterative schemes to incompressible flow. *AIAA Journal*, 23(10):1518–1524, 2008.

[57] Dochan Kwak, James L C Changt, Samuel P Shankst, and Sukumar R Chakravarthyj. A Three-Dimensional Incompressible Navier-Stokes. 24(3):390–396, 1986.

[58] F. R. Menter. Two-equation eddy-viscosity turbulence models for engineering applications. *AIAA Journal*, 32(8):1598–1605, 2008.

[59] Samet Caka Cakmakcioglu, Onur Bas, and Unver Kaynak. A correlation-based algebraic transition model. *Proceedings of the Institution of Mechanical Engineers, Part C: Journal of Mechanical Engineering Science*, 232(21):3915–3929, 2018.

[60] Antony Jameson, Wolfgang Schmidt, and Eli Turkel. AIAA 1981-1259 Numerical Solution of the Euler Equations by Finite Volume Methods Schemes AIAA 14th Fluid and Plasma Dynamic Conference Palo Alto , California. *Convergence*, M(AIAA 81-1259):1–19, 1981.

[61] P R Spalart, S R Allmaras, and January Reno. One-Equatlon Turbulence Model for Aerodynamic Flows Boeing. *AIAA*, page 23, 1992.

[62] Martin Roth, Ronald Peikert, and Filip Sadlo. Vcg vortex cores. `https://vcg.iwr.uni-heidelberg.de/plugins/vortexcores`.

[63] David Sujudi and Robert Haimes. Identification of swirling flow in 3-D vector fields. pages 1–8, 2013.

[64] J. C. R. Hunt, A. A. Wray, and Parviz Moin. Eddies, streams, and convergence zones in turbulent flows. *Center for Turbulence Research, Proceedings of the Summer Program*, (August):193–208, 1988.

[65] Charles D. Hansen and Chris R. Johnson. *The Visualization Handbook*. 2005.

[66] Akshay Koodly Ravishankara, Huseyin Ozdemir, and Andrea Franco. Towards a Vortex Generator Model for Integral Boundary Layer Methods. (January):1–16, 2019.

[67] L. F. Crabtree, G. E. Gadd, N. Gregory, C. R. Illingworth, C. W. Jones, D. Küchemann, M. J. Lighthill, R. C. Pankhurst, L. Rosenhead, L. Sowerby, J. T. Stuart, E. J. Watson, and G. B. Whitham. *Laminar Boundary Layers*. 1988.

Appendix A

Boundary Layer Equations

A.1 Boundary Layer Equations

Following is the approach of Veldman [16] to derive the laminar boundary layer equations.
First an order of magnitude analysis is performed, to determine the corresponding factors by which to nondimensionalize the 2D Navier-Stokes equations:
The relations are presented in Equation (A.1):

$$u \sim U_\infty, \quad x \sim c, \quad y \sim \delta, \quad p \sim \rho U_\infty^2 \tag{A.1}$$

where U_∞ is the boundary layer edge velocity (the velocity that corresponds to the outer inviscid irrotational fluid), x and y are the coordinates respectively in the tangential and normal direction to the surface, and δ is the boundary layer thickness measured along the y direction here defined.
From the terms in Equation (A.2) it could be derived an expression for the velocity v, expressed in Equation (A.3):

$$\frac{\partial u}{\partial x} + \frac{\partial v}{\partial y} = 0 \tag{A.2}$$

$$(\frac{U_\infty}{c}) + (\frac{v}{\delta}) = 0 \quad \Rightarrow \quad v \sim \frac{U_\infty \delta}{c} \tag{A.3}$$

The analysis for the x-momentum equation in Equation (A.4) provides for all the terms the relations in Equation (A.5):

$$u\frac{\partial u}{\partial x} + v\frac{\partial u}{\partial y} = -\frac{1}{\rho}\frac{\partial p}{\partial x} + \nu\,(\frac{\partial^2 u}{\partial x^2} + \frac{\partial^2 u}{\partial y^2}) \tag{A.4}$$

$$(\frac{U_\infty^2}{c}) + (\frac{U_\infty^2}{c}) = (\frac{U_\infty^2}{c}) + (\nu\frac{U_\infty}{c^2}) + (\nu\frac{U_\infty}{\delta^2}) \tag{A.5}$$

Recalling the hypothesis of the boundary layer model stated in Equation (2.7), the viscous term $\nu\frac{\partial^2 u}{\partial x^2}$ can be neglected, and from the remaining terms in Equation (A.6), the relation in Equation (A.7) can be obtained:

$$(\frac{U_\infty^2}{c}) + (\frac{U_\infty^2}{c}) = (\frac{U_\infty^2}{c}) + (\nu\frac{U_\infty}{\delta^2}) \tag{A.6}$$

$$\frac{\delta}{c} \sim \sqrt{\frac{\nu}{U_\infty c}} \sim \frac{1}{\sqrt{Re}} \tag{A.7}$$

where $Re = \frac{U_\infty c}{\nu}$ is the Reynolds number, the nondimensional parameter that represents the ratio between inertia and viscous forces.
Using Equation (A.7) in the expression for the velocity component v obtained in Equation (A.3), it is possible to derive the final expression for this velocity component, shown in Equation (A.8):

$$v \sim \frac{U_\infty \delta}{c} \sim \frac{U_\infty}{\sqrt{Re}} \tag{A.8}$$

Having performed this order of magnitude analysis, at this point it is possible to derive the nondimensional boundary layer equations, applying the nondimensionalization to the original variables with the estimated quantities just obtained, as expressed in Equation (A.9):

$$u \sim U_\infty, \quad x \sim c, \quad y \sim \delta, \quad p \sim \rho U_\infty^2, \quad v \sim \frac{U_\infty \delta}{c} \tag{A.9}$$

The nondimensional variables are the following ones in Equation (A.10), with the prime sign identifying them:

$$x' = \frac{x}{c}, \quad y' = \frac{y}{\delta} = \frac{y}{c}\sqrt{Re}, \quad u' = \frac{u}{U_\infty}, \quad v' = \frac{v}{\frac{U_\infty \delta}{c}} = \frac{v}{U_\infty}\sqrt{Re}, \quad p' = \frac{p}{\rho U_\infty^2} \tag{A.10}$$

The incompressible Navier-Stokes equations nondimensionalized are provided in Equation (A.11), Equation (A.12) and Equation (A.13):

$$\frac{U_\infty}{c}\frac{\partial u'}{\partial x'} + \frac{U_\infty}{c}\frac{\partial v'}{\partial y'} = 0 \tag{A.11}$$

$$\frac{U_\infty^2}{c}u'\frac{\partial u'}{\partial x'} + \frac{U_\infty^2}{c}v'\frac{\partial u'}{\partial y'} = -\frac{U_\infty^2}{c}\frac{\partial p'}{\partial x'} + \nu\frac{U_\infty}{c^2}\frac{\partial^2 u'}{\partial x'^2} + \nu Re\frac{U_\infty}{c^2}\frac{\partial^2 u'}{\partial y'^2} \tag{A.12}$$

$$\frac{U_\infty^2}{c}\frac{1}{\sqrt{Re}}(u'\frac{\partial v'}{\partial x'} + v'\frac{\partial v'}{\partial y'}) = -\sqrt{Re}\frac{U_\infty^2}{c}\frac{\partial p'}{\partial y'} + \frac{1}{\sqrt{Re}}\nu\frac{U_\infty}{c^2}\frac{\partial^2 v'}{\partial x'^2} + \sqrt{Re}\nu\frac{U_\infty}{c^2}\frac{\partial^2 v'}{\partial y'^2} \tag{A.13}$$

These equations can be simplified, if Equation (A.11) is divided by $\frac{U_\infty}{c}$ and if Equation (A.12) and Equation (A.13) are divided by the corresponding factor in front of the pressure term.
The resulting equations are shown in Equation (A.14), Equation (A.15) and Equation (A.16):

$$\frac{\partial u'}{\partial x'} + \frac{\partial v'}{\partial y'} = 0 \tag{A.14}$$

$$u'\frac{\partial u'}{\partial x'} + v'\frac{\partial u'}{\partial y'} = -\frac{\partial p'}{\partial x'} + \frac{1}{Re}\frac{\partial^2 u'}{\partial x'^2} + \frac{\partial^2 u'}{\partial y'^2} \tag{A.15}$$

$$\frac{1}{Re}(u'\frac{\partial v'}{\partial x'} + v'\frac{\partial v'}{\partial y'}) = -\frac{\partial p'}{\partial y'} + \frac{1}{Re^2}\frac{\partial^2 v'}{\partial x'^2} + \frac{1}{Re}\frac{\partial^2 v'}{\partial y'^2} \tag{A.16}$$

The final step is to take the limit for large Reynolds number, since this is the assumption for the viscous forces to be neglected, obtaining in the end the final nondimensionalized boundary layer equations, reported in Equation (A.17), Equation (A.18) and Equation (A.19):

$$\frac{\partial u'}{\partial x'} + \frac{\partial v'}{\partial y'} = 0 \tag{A.17}$$

$$u'\frac{\partial u'}{\partial x'} + v'\frac{\partial u'}{\partial y'} = -\frac{\partial p'}{\partial x'} + \frac{\partial^2 u'}{\partial y'^2} \tag{A.18}$$

$$0 = \frac{\partial p'}{\partial y'} \tag{A.19}$$

A.2 Von Kàrmàn Integral Momentum Equation

For the derivation of the Von Kàrmàn integral momentum equation, Equation (2.27) is considered. This equation can be first modified, according to [14], as shown in Equation (A.20):

$$\overline{u}\frac{\partial \overline{u}}{\partial x} + \overline{v}\frac{\partial \overline{u}}{\partial y} = \frac{1}{\rho}\frac{\partial \tau}{\partial y} + U_\infty \frac{\partial U_\infty}{\partial x}, \quad \Rightarrow \quad \rho\overline{u}\frac{\partial \overline{u}}{\partial x} + \rho\overline{v}\frac{\partial \overline{u}}{\partial y} = \frac{\partial \tau}{\partial y} + \rho U_\infty \frac{\partial U_\infty}{\partial x} \tag{A.20}$$

It is then possible to add and subtract to the LHS of Equation (A.20) the following quantity $\rho u \frac{\partial U_\infty}{\partial x}$, obtaining Equation (A.21), that can be further simplified as in Equation (A.22):

$$\begin{gathered}\rho\overline{u}\frac{\partial \overline{u}}{\partial x} + \rho\overline{v}\frac{\partial \overline{u}}{\partial y} + \rho\overline{u}\frac{\partial U_\infty}{\partial x} - \rho\overline{u}\frac{\partial U_\infty}{\partial x} = \frac{\partial \tau}{\partial y} + \rho U_\infty \frac{\partial U_\infty}{\partial x}, \quad \Rightarrow \\ \rho\overline{u}\frac{\partial U_\infty}{\partial x} - \rho\overline{u}\frac{\partial \overline{u}}{\partial x} - \rho\overline{v}\frac{\partial \overline{u}}{\partial y} - \rho\overline{u}\frac{\partial U_\infty}{\partial x} + \rho U_\infty \frac{\partial U_\infty}{\partial x} = -\frac{\partial \tau}{\partial y}\end{gathered} \tag{A.21}$$

$$\rho\overline{u}\frac{\partial}{\partial x}(U_\infty - \overline{u}) - \rho\overline{v}\frac{\partial \overline{u}}{\partial y} + \rho(U_\infty - \overline{u})\frac{\partial U_\infty}{\partial x} = -\frac{\partial \tau}{\partial y} \tag{A.22}$$

The term $-\rho\overline{v}\frac{\partial \overline{u}}{\partial y}$ can be further rewritten as in Equation (A.23):

$$-\rho\overline{v}\frac{\partial \overline{u}}{\partial y} = -\rho\overline{v}\frac{\partial[U_\infty - (U_\infty - \overline{u})]}{\partial y} = -\rho\overline{v}\frac{\partial(U_\infty)}{\partial y} + \rho\overline{v}\frac{\partial(U_\infty - \overline{u})}{\partial y} = \rho\overline{v}\frac{\partial(U_\infty - \overline{u})}{\partial y} \tag{A.23}$$

considering that $\frac{\partial(U_\infty)}{\partial y} \to 0$ inside the boundary layer.
Equation (A.22) therefore results in Equation (A.24):

$$\rho\overline{u}\frac{\partial}{\partial x}(U_\infty - \overline{u}) + \rho\overline{v}\frac{\partial(U_\infty - \overline{u})}{\partial y} + \rho(U_\infty - \overline{u})\frac{\partial U_\infty}{\partial x} = -\frac{\partial \tau}{\partial y} \tag{A.24}$$

Integrating Equation (A.22) term by term, from $y = 0$ (y coordinate corresponding to the airfoil surface) to $y = \delta$ (y coordinate corresponding to the edge of the boundary layer), yields for each term Equation (A.25), Equation (A.26) and Equation (A.27):

$$\int_0^\delta \rho(U_\infty - \overline{u})\frac{\partial U_\infty}{\partial x}dy = \rho U_\infty \frac{\partial U_\infty}{\partial x}\int_0^\delta (1 - \frac{\overline{u}}{U_\infty})dy = \rho U_\infty \frac{\partial U_\infty}{\partial x}\delta^* \tag{A.25}$$

$$\int_0^\delta \rho\overline{v}\frac{\partial(U_\infty-\overline{u})}{\partial y}dy = \rho\overline{v}(U_\infty-\overline{u})\mid_0^\delta -\rho\int_0^\delta (U_\infty-\overline{u})\frac{\partial\overline{v}}{\partial y}dy = 0+\rho\int_0^\delta (U_\infty-\overline{u})\frac{\partial\overline{u}}{\partial x}dy \tag{A.26}$$

$$\int_0^\delta -\frac{\partial\tau}{\partial y}dy = -\tau\mid_0^\delta = \tau_w \tag{A.27}$$

Substituting Equation (A.25), Equation (A.26) and Equation (A.27) in Equation (A.24), an intermediate integral equation is obtained in Equation (A.28):

$$\begin{aligned}\int_0^\delta \rho\overline{u}\frac{\partial}{\partial x}(U_\infty-\overline{u})dy+\rho\int_0^\delta (U_\infty-\overline{u})\frac{\partial\overline{u}}{\partial x}dy+\rho U_\infty\frac{\partial U_\infty}{\partial x}\delta^* = \tau_w, \quad \Rightarrow \\ \int_0^\delta [\rho\overline{u}\frac{\partial}{\partial x}(U_\infty-\overline{u})+\rho(U_\infty-\overline{u})\frac{\partial\overline{u}}{\partial x}]dy+\rho U_\infty\frac{\partial U_\infty}{\partial x}\delta^* = \tau_w\end{aligned} \tag{A.28}$$

As a last step, the remaining integral in Equation (A.28) can be rewritten as shown in Equation (A.29):

$$\begin{aligned}\int_0^\delta [\rho\overline{u}\frac{\partial}{\partial x}(U_\infty-\overline{u})+\rho(U_\infty-\overline{u})\frac{\partial\overline{u}}{\partial x}]dy = \int_0^\delta [\rho\frac{\partial}{\partial x}\overline{u}(U_\infty-\overline{u})]dy = \frac{\partial}{\partial x}\int_0^\delta \rho[\overline{u}(U_\infty-\overline{u})]dy = \\ \frac{\partial}{\partial x}\int_0^\delta \rho[\overline{u}U_\infty(1-\frac{\overline{u}}{U_\infty})]dy = \frac{\partial}{\partial x}\rho U_\infty^2\int_0^\delta [\frac{\overline{u}}{U_\infty}(1-\frac{\overline{u}}{U_\infty})]dy = \frac{\partial}{\partial x}(\rho U_\infty^2\theta)\end{aligned} \tag{A.29}$$

Substituting Equation (A.29) in Equation (A.28), the Von Kàrmàn integral momentum equation in dimensional form results in Equation (A.30):

$$\frac{\partial}{\partial x}(\rho U_\infty^2\theta) = \tau_w - \rho U_\infty\frac{\partial U_\infty}{\partial x}\delta^* \tag{A.30}$$

A.3 Integral Kinetic Energy Equation

For the derivation of the integral kinetic energy equation, both Equation (2.26) and Equation (2.27) will be considered. These equations are modified following the approach in [67], that initially considers Equation (A.31) and Equation (A.32):

$$\frac{\partial\overline{u}}{\partial x}+\frac{\partial\overline{v}}{\partial y} = 0, \quad \Rightarrow \quad 0 = \rho(U_\infty^2-\overline{u}^2)[\frac{\partial\overline{u}}{\partial x}+\frac{\partial\overline{v}}{\partial y}] \tag{A.31}$$

$$\overline{u}\frac{\partial\overline{u}}{\partial x}+\overline{v}\frac{\partial\overline{u}}{\partial y} = \frac{1}{\rho}\frac{\partial\tau}{\partial y}+U_\infty\frac{\partial U_\infty}{\partial x}, \quad \Rightarrow \quad -2\overline{u}\frac{\partial\tau}{\partial y} = 2\overline{u}\rho U_\infty\frac{\partial U_\infty}{\partial x}-2\overline{u}\rho\overline{u}\frac{\partial\overline{u}}{\partial x}-2\overline{u}\rho\overline{v}\frac{\partial\overline{u}}{\partial y} \tag{A.32}$$

Equation (A.31) and Equation (A.32) are summed together, yielding Equation (A.33):

$$-2\overline{u}\frac{\partial\tau}{\partial y} = 2\overline{u}\rho U_\infty\frac{\partial U_\infty}{\partial x}-2\overline{u}\rho\overline{u}\frac{\partial\overline{u}}{\partial x}-2\overline{u}\rho\overline{v}\frac{\partial\overline{u}}{\partial y}+\rho U_\infty^2\frac{\partial\overline{u}}{\partial x}-\rho\overline{u}^2\frac{\partial\overline{u}}{\partial x}+\rho U_\infty^2\frac{\partial\overline{v}}{\partial y}-\rho\overline{u}^2\frac{\partial\overline{v}}{\partial y} \tag{A.33}$$

From Equation (A.33) the shear stress term, the derivatives in the x and the y direction are considered separately, as in Equation (A.34), Equation (A.35) and Equation (A.36) respectively:

$$-2\overline{u}\frac{\partial\tau}{\partial y} = -2[\frac{\partial(\tau\overline{u})}{\partial y}-\tau\frac{\partial\overline{u}}{\partial y}] = -2\frac{\partial(\tau\overline{u})}{\partial y}+2\tau\frac{\partial\overline{u}}{\partial y} \tag{A.34}$$

$$2\overline{u}\rho U_\infty \frac{\partial U_\infty}{\partial x} - 2\overline{u}\rho\overline{u}\frac{\partial \overline{u}}{\partial x} + \rho U_\infty^2 \frac{\partial \overline{u}}{\partial x} - \rho\overline{u}^2\frac{\partial \overline{u}}{\partial x} = \overline{u}\rho 2U_\infty \frac{\partial U_\infty}{\partial x} + \rho U_\infty^2 \frac{\partial \overline{u}}{\partial x} - 3\rho\overline{u}^2\frac{\partial \overline{u}}{\partial x} =$$
$$\rho[\overline{u}\frac{\partial U_\infty^2}{\partial x} + U_\infty^2\frac{\partial \overline{u}}{\partial x} - \frac{\partial \overline{u}^3}{\partial x}] = \rho[\frac{\partial(U_\infty^2\overline{u})}{\partial x} - \frac{\partial \overline{u}^3}{\partial x}] = \rho\frac{\partial(U_\infty^2\overline{u} - \overline{u}^3)}{\partial x} \tag{A.35}$$

$$-2\overline{u}\rho\overline{v}\frac{\partial \overline{u}}{\partial y} + \rho U_\infty^2\frac{\partial \overline{v}}{\partial y} - \rho\overline{u}^2\frac{\partial \overline{v}}{\partial y} = \rho[-\overline{v}\frac{\partial \overline{u}^2}{\partial y} + U_\infty^2\frac{\partial \overline{v}}{\partial y} - \overline{u}^2\frac{\partial \overline{v}}{\partial y}]$$
$$= \rho[-\frac{\partial(\overline{v}\overline{u}^2)}{\partial y} + \frac{\partial(U_\infty^2\overline{v})}{\partial y}] = \rho\frac{\partial(U_\infty^2\overline{v} - \overline{v}\overline{u}^2)}{\partial y} \tag{A.36}$$

After the rearranging, the differential equation results in Equation (A.37):

$$-2\frac{\partial(\tau\overline{u})}{\partial y} + 2\tau\frac{\partial \overline{u}}{\partial y} = \rho\frac{\partial(U_\infty^2\overline{u} - \overline{u}^3)}{\partial x} + \rho\frac{\partial(U_\infty^2\overline{v} - \overline{v}\overline{u}^2)}{\partial y} \tag{A.37}$$

Equation (A.37) can be integrated term by term, from $y = 0$ (y coordinate corresponding to the airfoil surface) to $y = \delta$ (y coordinate corresponding to the edge of the boundary layer), yielding Equation (A.38), Equation (A.39) and Equation (A.40):

$$\int_0^\delta [-2\frac{\partial(\tau\overline{u})}{\partial y} + 2\tau\frac{\partial \overline{u}}{\partial y}]dy = \int_0^\delta -2\frac{\partial(\tau\overline{u})}{\partial y}dy + \int_0^\delta 2\tau\frac{\partial \overline{u}}{\partial y}dy = 0 + 2D \tag{A.38}$$

$$\int_0^\delta \rho\frac{\partial(U_\infty^2\overline{u} - \overline{u}^3)}{\partial x}dy = \frac{\partial}{\partial x}[\rho\int_0^\delta (U_\infty^2\overline{u} - \overline{u}^3)dy] = \frac{\partial}{\partial x}[\rho\int_0^\delta U_\infty^2\overline{u}(1 - \frac{\overline{u}^2}{U_\infty^2})dy] =$$
$$\frac{\partial}{\partial x}[\rho U_\infty^3\int_0^\delta \frac{\overline{u}}{U_\infty}(1 - \frac{\overline{u}^2}{U_\infty^2})dy] = \frac{\partial(\rho U_\infty^3\theta^*)}{\partial x} \tag{A.39}$$

$$\int_0^\delta \rho\frac{\partial(U_\infty^2\overline{v} - \overline{v}\overline{u}^2)}{\partial y} = \rho[(U_\infty^2\overline{v} - \overline{v}\overline{u}^2)\ |_0^\delta] = 0 \tag{A.40}$$

The integral kinetic energy equation in its dimensional form follows in Equation (A.41):

$$2D = \frac{\partial(\rho U_\infty^3\theta^*)}{\partial x} \tag{A.41}$$

Appendix B

Mesh Description 2D

1. Import the 2D CAD Model, as follows:

   1.1 Go to File -> Properties, and in the Tolerances Frame set Model Size = 10 (following *Pointwise* Guidelines, this value has to be 1 Order of Magnitude greater than the largest dimension of the CAD Model (in this case airfoil chord=1), to allow the software to detect the edges of the 2D CAD Model correctly. A value too large may cause wrong edges creation from the Database entities imported)

   1.2 Go to File -> Import -> Database, and from the Browser Window that appears select the CAD file containing the 2D Model

   1.3 In the Import Database Panel that appears, choose Metric in the Units Frame, and Use Format Specific Conversion Settings in the File Conversion Frame, and click OK

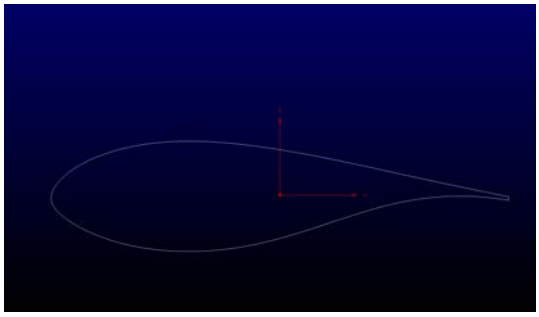

Figure B.1: CAD Model imported

2. Create Connectors from the 2D Model imported as follows

   2.1 Select all Database Entities and create Connectors on Database Entities

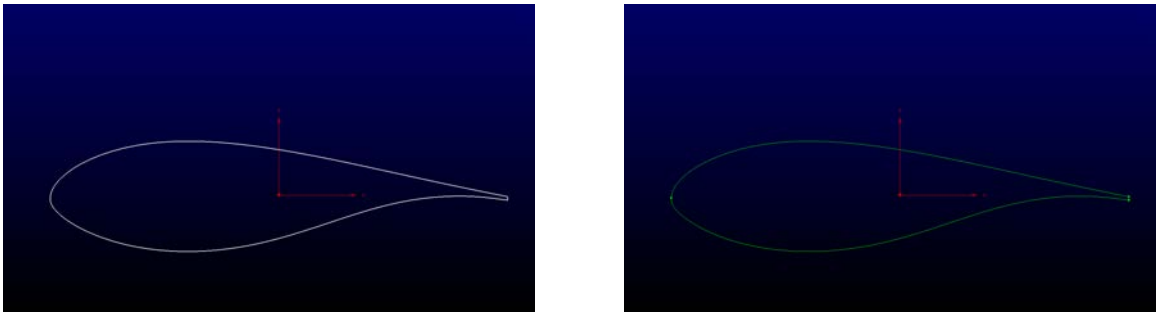

Figure B.2: Create connectors on database entities

3. Assign number of nodes on connectors

   3.1 Assign 250 nodes to connectors along airfoil surface (Suction and Pressure Side)

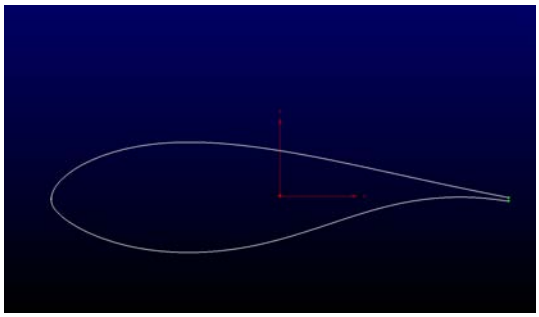

Figure B.3: Connectors along airfoil surface

   3.2 Assign 4 nodes to connectors along blunt Trailing Edge

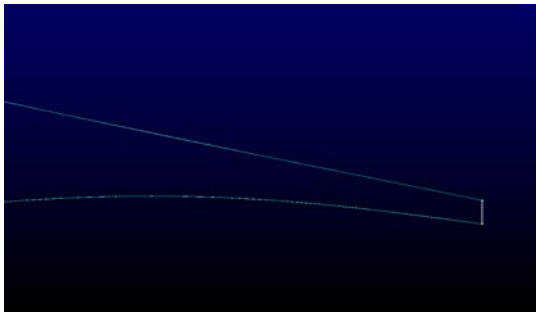

Figure B.4: Connectors along blunt Trailing Edge

4. Create Normal Extrusion Domain as follows:

   4.1 Select Connectors to extrude from

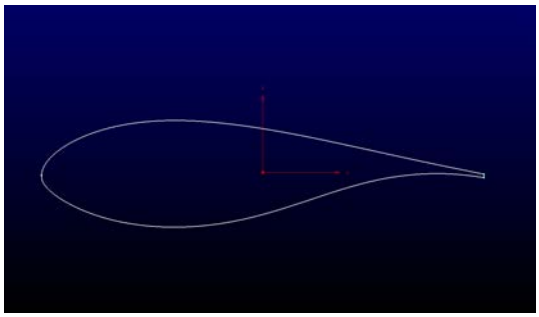

Figure B.5: Connectors to extrude from

   4.2 Go to Create -> Extrude -> Normal

   4.3 In the Assemble frame accept the proposed assembling choice and click Done

   4.4 Set the parameters of the Normal Extrusion in the Attributes tab

      4.4.1 In the Step Size frame set:
      - $Initial\Delta s = 4.56e-6$
      - $GrowthRate = 1.088$

      4.4.2 In the Orientation frame click on Flip, if the normals are not pointing out

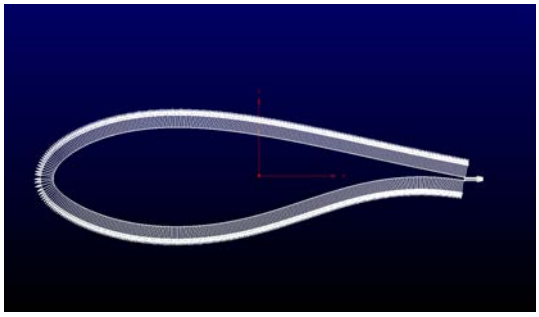

Figure B.6: Normals pointing out

      4.4.3 In the Stop Conditions frame set Total Height = 500 (it defines the maximum limit of the extrusion distance from the connectors, to extrude from)

   4.6 In the Run tab, in the Extrude frame, set the number of extrusion steps to a large arbitrary number (e.g Steps=500), and click Run. The Stop Condition Total Height will stop the extrusion when the desired distance from the surface has reached the value 500.

4.7 Click OK to accept the resulting extrusion

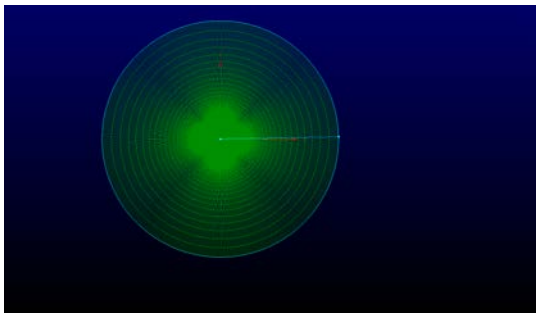

Figure B.7: Total Normal Extrusion

5. Define Boundary Conditions and Output format of the Mesh created

5.1 Go to CAE -> Select Solver -> Stanford ADL/SU2 and click OK

5.2 Go to CAE -> Set Dimension -> 2D

5.3 Go to CAE -> Set Boundary Conditions, and define the boundary conditions as follows:

5.3.1 Create with the New Button 2 Boundary Conditions, named “airfoil”,”farfield”

5.3.2 Select Domains for the “airfoil” Boundary Condition

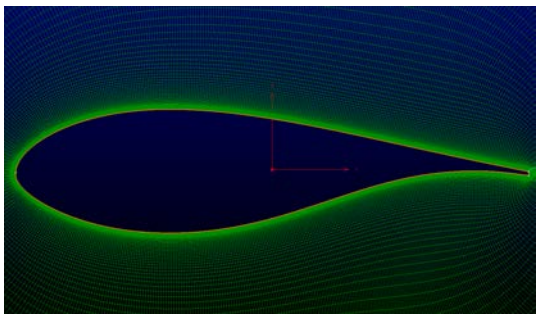

Figure B.8: Airfoil Boundary Condition

5.3.3 Click on the tick box near the “airfoil” Boundary Condition name, to assign the connectors selected to the corresponding Boundary Condition

5.3.4 Select Domains for the “farfield” Boundary Condition

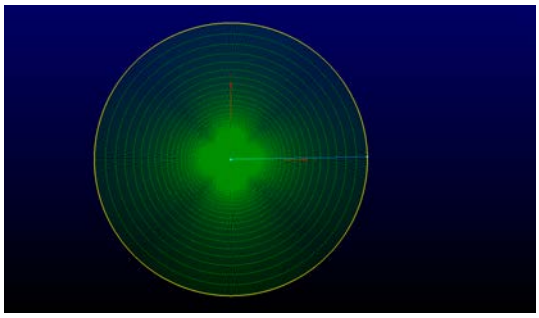

Figure B.9: Farfield Boundary Condition

5.3.5 Click on the tick box near the “farfield” Boundary Condition name, to assign the connectors selected to the corresponding Boundary Condition

6. Export the 2D Mesh created in the SU2 format

6.1 Select all the domains created

6.2 Go to File -> Export -> CAE

6.3 Specify name of the *.su2 file to be created

6.4 In the frame Data Precision specify Double for Double Precision

6.5 Click OK to generate the Mesh

Appendix C

Mesh Description 3D Smooth

1. Import the 3D CAD Model, as follows:

   1.1 Go to File -> Properties, and in the Tolerances Frame set Model Size = 10 (following *Pointwise* Guidelines, this value has to be 1 Order of Magnitude greater than the largest dimension of the CAD Model (in this case airfoil chord=1), to allow the software to detect the edges of the 3D CAD Model correctly. A value too large may cause wrong edges creation from the Database entities imported)

   1.2 Go to File -> Import -> Database, and from the Browser Window that appears select the CAD file containing the 3D Model

   1.3 In the Import Database Panel that appears, choose Metric in the Units Frame, and Use Format Specific Conversion Settings in the File Conversion Frame, and click OK

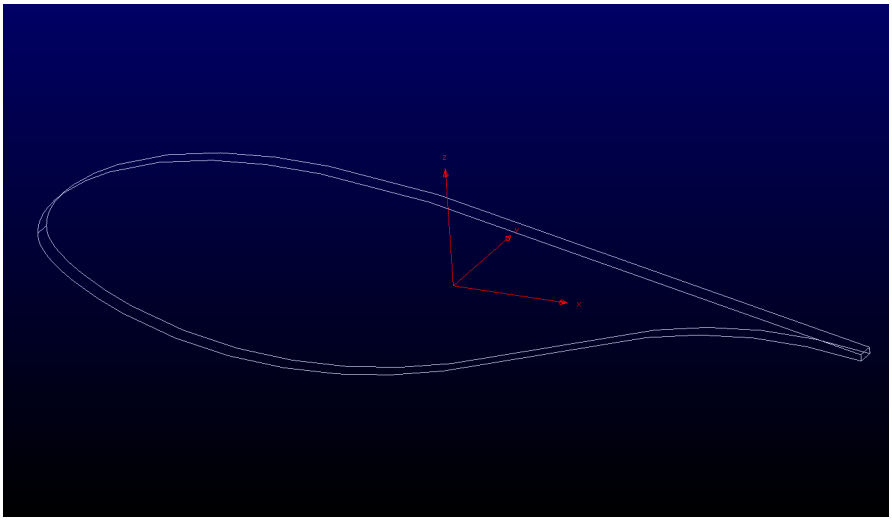

Figure C.1: CAD Model imported

2. Create Connectors from the 3D Model imported as follows:

   2.1 Delete the 2 redundant lateral surfaces created after the import, to avoid wrong connector creation

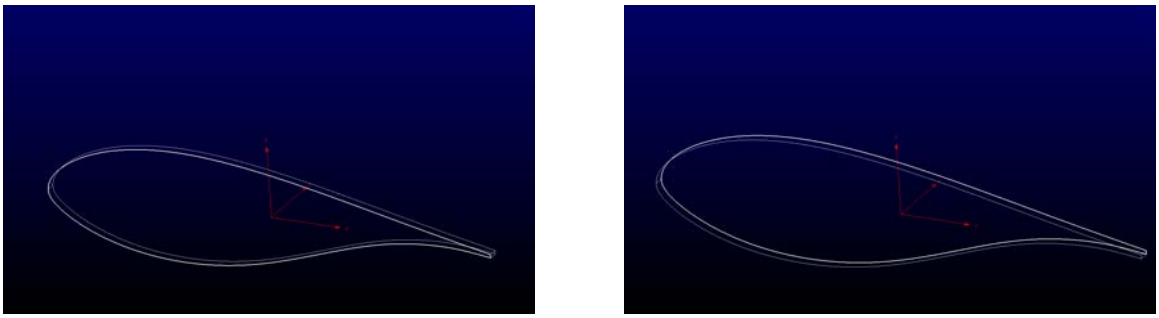

Figure C.2: Lateral surfaces to delete

   2.2 Select all Database Entities and create Connectors on Database Entities

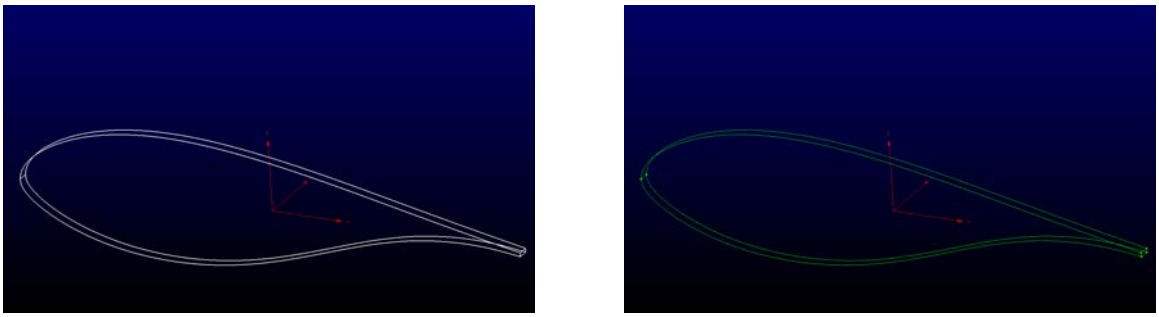

Figure C.3: Create connectors on database entities

3. Assign number of nodes on connectors

   3.1 Assign 250 nodes to connectors along airfoil surface (Suction and Pressure Side)

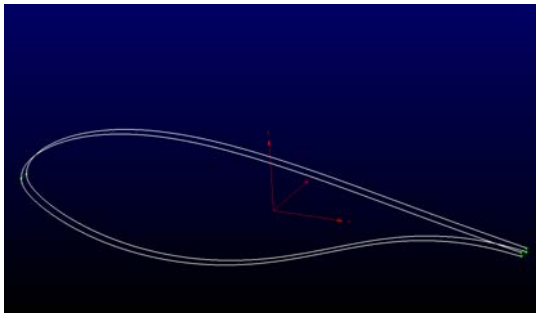

Figure C.4: Connectors along airfoil surface

3.2 Assign 15 nodes along third direction

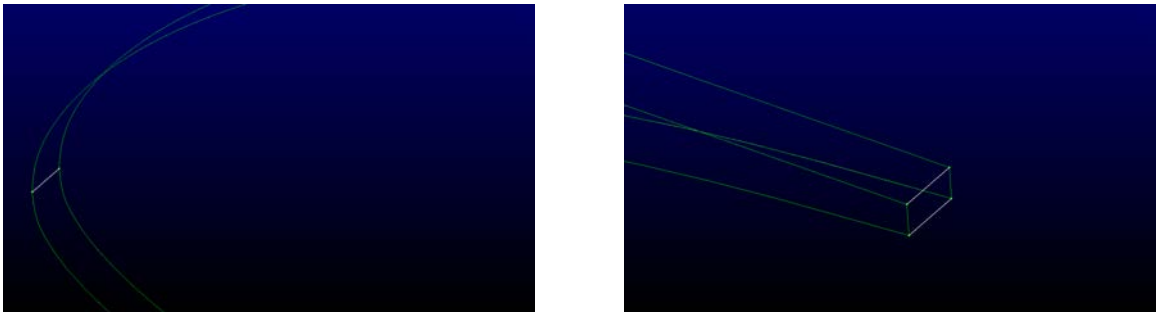

Figure C.5: Connectors along third direction

3.3 Assign 4 nodes to connectors along blunt Trailing Edge

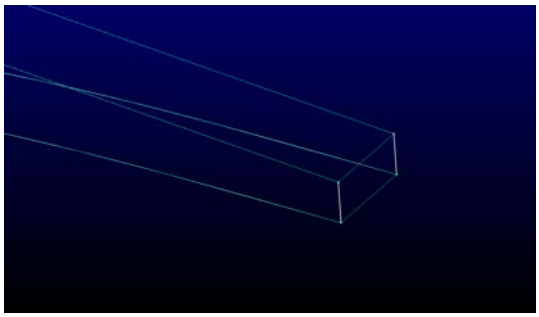

Figure C.6: Connectors along blunt Trailing Edge

4. Assemble Domains from connectors created and defined. All domains will have quadrilateral cells ("structured" according to *Pointwise* definition). In order to do so, for every domain to be created, select a closed loop of connectors (ensuring that opposite sides have the same number of nodes) and go to Create -> Assemble Special -> Domain

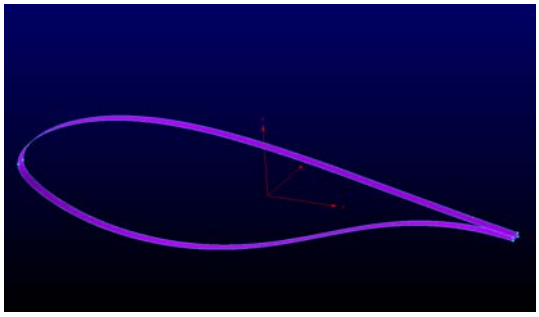

Figure C.7: Assembled domains

5. Create Normal Extrusion Block as follows:

   5.1 Select Domains to extrude from

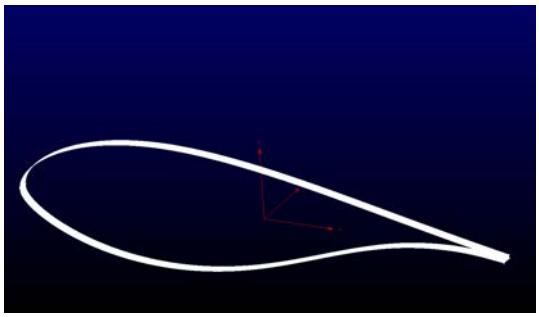

Figure C.8: Domains to extrude from

   5.2 Go to Create -> Extrude -> Normal

   5.3 In the Assemble frame accept the proposed assembling choice and click Done

   5.4 Set the parameters of the Normal Extrusion in the Attributes tab

      5.4.1 In the Step Size frame set:
      - $Initial\Delta s = 4.56e-6$
      - $GrowthRate = 1.088$

      5.4.2 In the Orientation frame click on Flip, if the normals are not pointing out

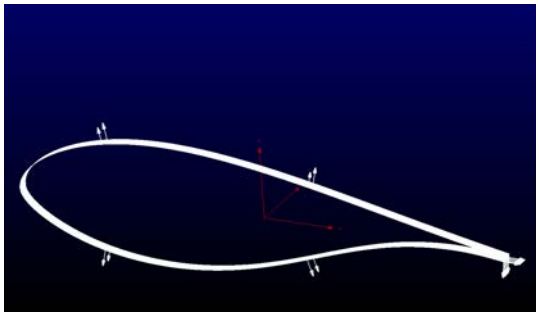

Figure C.9: Normals pointing out

      5.4.3 In the Stop Conditions frame set Total Height = 500 (it defines the maximum limit of the extrusion distance, from the surface to extrude from)

5.5 In the Boundary Condition tab define the boundary conditions of the Normal Extrusion:

5.5.1 All the connectors will be set to the Boundary Condition Type=Symmetry Y

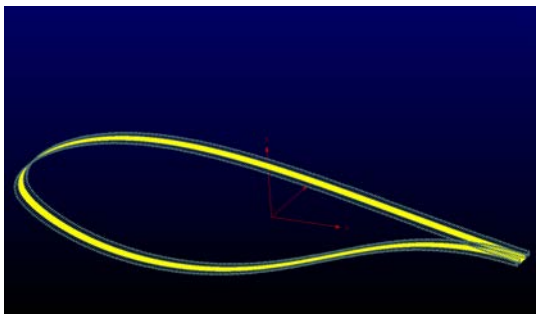

Figure C.10: Symmetry Y Boundary Condition for the Last Normal Extrusion

5.6 In the Run tab, in the Extrude frame, set the number of extrusion steps to a large arbitrary number (e.g Steps=500), and click Run. The Stop Condition Total Height will stop the extrusion when the desired distance from the surface has reached the value 500.

5.7 Click OK to accept the resulting extrusion

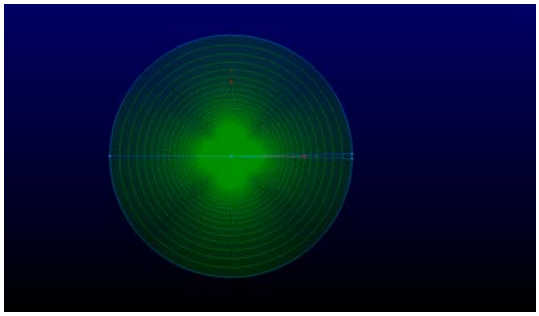

Figure C.11: Total Normal Extrusion

6. Define Boundary Conditions and Output format of the Mesh created

   6.1 Go to CAE -> Select Solver -> Stanford ADL/SU2 and click OK

   6.2 Go to CAE -> Set Dimension -> 3D

   6.3 Go to CAE -> Set Boundary Conditions, and define the boundary conditions as follows:

      6.3.1 Create with the New Button 3 Boundary Conditions, named “airfoil”,”symmetry”,”farfield”

      6.3.2 Select Domains for the “airfoil” Boundary Condition

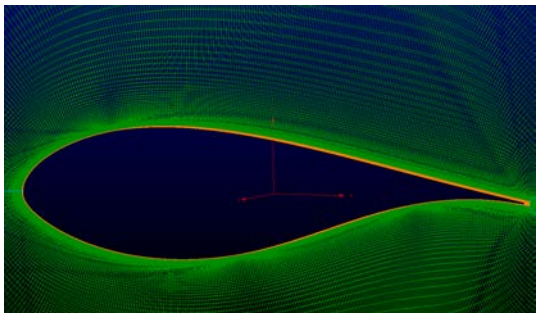

Figure C.12: Airfoil Boundary Condition

      6.3.3 Click on the tick box near the “airfoil” Boundary Condition name, to assign the Domains selected to the corresponding Boundary Condition

      6.3.4 Select Domains for the “farfield” Boundary Condition

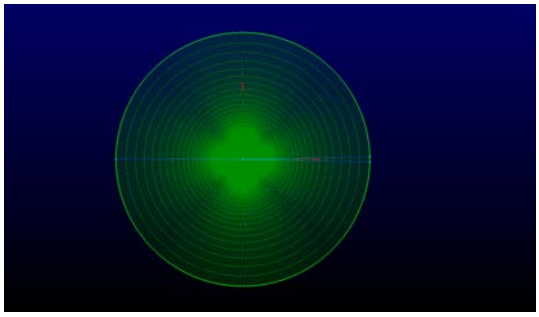

Figure C.13: Farfield Boundary Condition

      6.3.5 Click on the tick box near the “farfield” Boundary Condition name, to assign the Domains selected to the corresponding Boundary Condition

6.3.6 Select Domains for the "symmetry" Boundary Condition (all the Domains with the normal to the domain pointing in the y-direction)

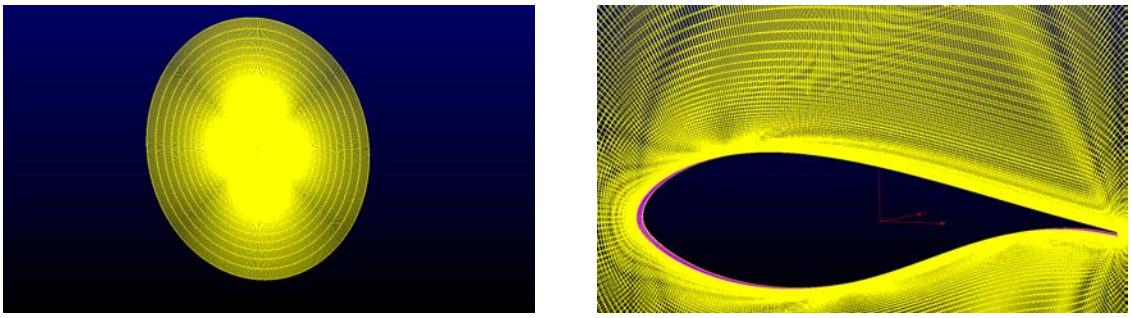

Figure C.14: Symmetry Boundary Condition

6.3.7 Click on the tick box near the "symmetry" Boundary Condition name, to assign the Domains selected to the corresponding Boundary Condition

7. Export the 3D Mesh created in the SU2 format

7.1 Select all the blocks created

7.2 Go to File -> Export -> CAE

7.3 Specify name of the *.su2 file to be created

7.4 In the frame Data Precision specify Double for Double Precision

7.5 Click OK to generate the Mesh

Appendix D

Mesh Description 3D VG

1. Import the 3D CAD Model, as follows:

   1.1. Go to File -> Properties, and in the Tolerances Frame set Model Size = 10 (following *Pointwise* Guidelines, this value has to be 1 Order of Magnitude greater than the largest dimension of the CAD Model (in this case airfoil chord=1), to allow the software to detect the edges of the 3D CAD Model correctly. A value too large may cause wrong edges creation from the Database entities imported)

   1.2. Go to File -> Import -> Database, and from the Browser Window that appears select the CAD file containing the 3D Model

   1.3. In the Import Database Panel that appears, choose Metric in the Units Frame, and Use Format Specific Conversion Settings in the File Conversion Frame, and click OK

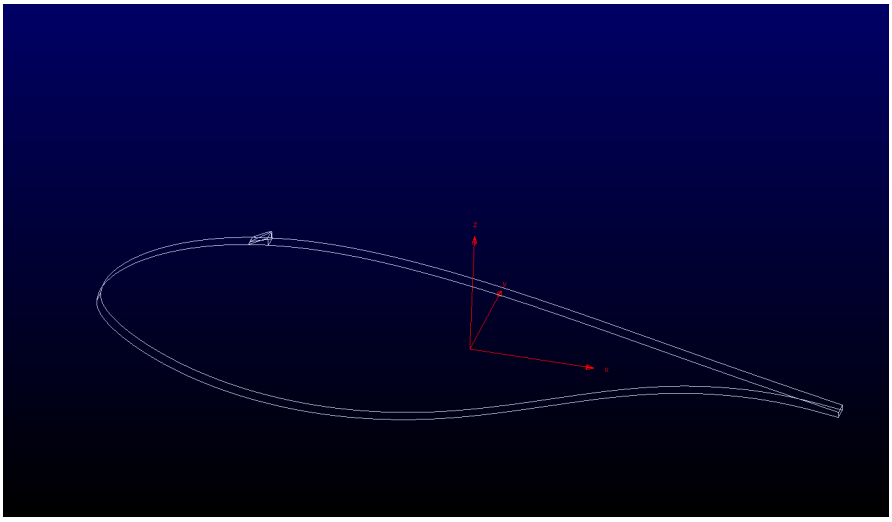

Figure D.1: CAD Model imported

2. Create Connectors from the 3D Model imported as follows:

   2.1. Delete the 2 redundant lateral surfaces created after the import, to avoid wrong connector creation

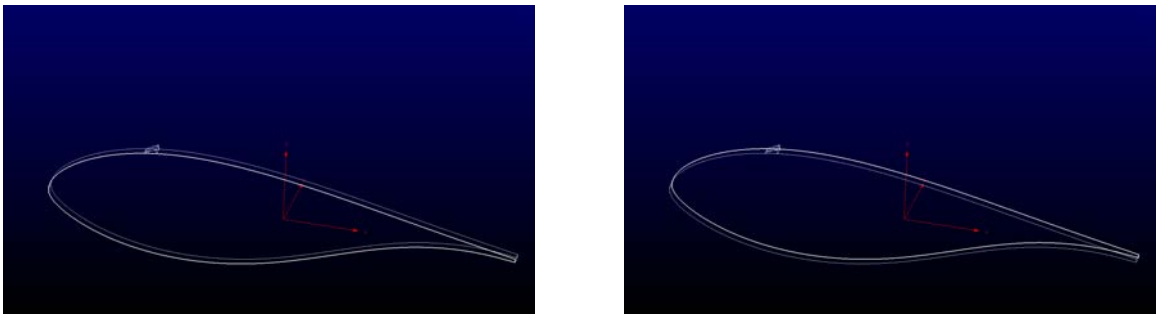

Figure D.2: Lateral edges to delete

   2.2. Select all Database Entities and create Connectors on Database Entities

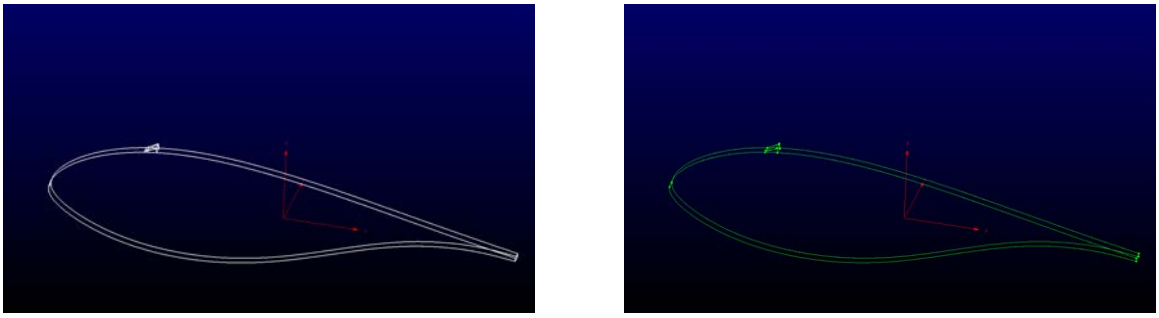

Figure D.3: Create connectors on database entities

3. Starting from the 3D CAD model, the VG blocking already created in it is now mirrored as follows:

   3.1. Copy and Translate lateral edges of the VG Blocking

      3.1.1. Select lateral Edge VG Blocking

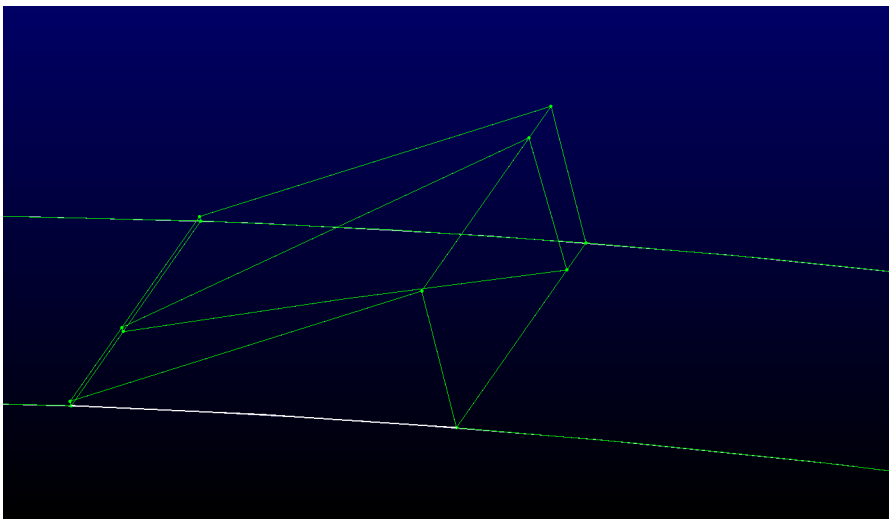

Figure D.4: Lateral edge VG Blocking

      3.1.2. Go to Edit -> Copy

      3.1.3. Go to Edit -> Paste -> Translate

      3.1.4. Click on Clear Translation Vector (only if previous translation vectors are already defined)

      3.1.5. Define Points of the Translation Vector

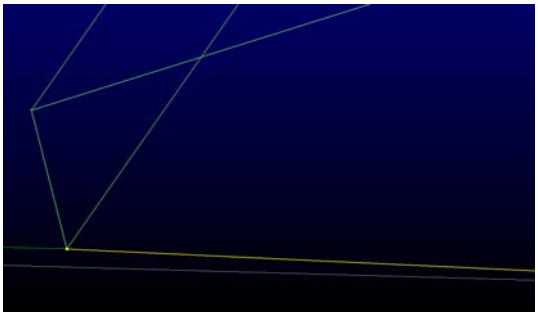

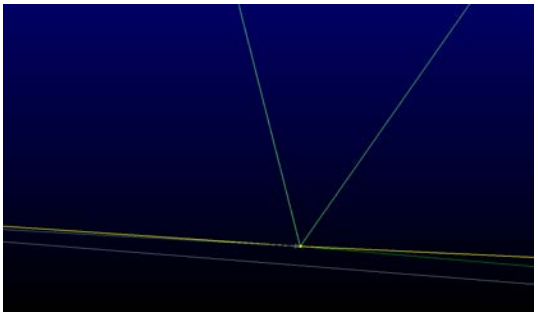

Figure D.5: Define points of the translation vector

3.1.6. Click OK to confirm the procedure

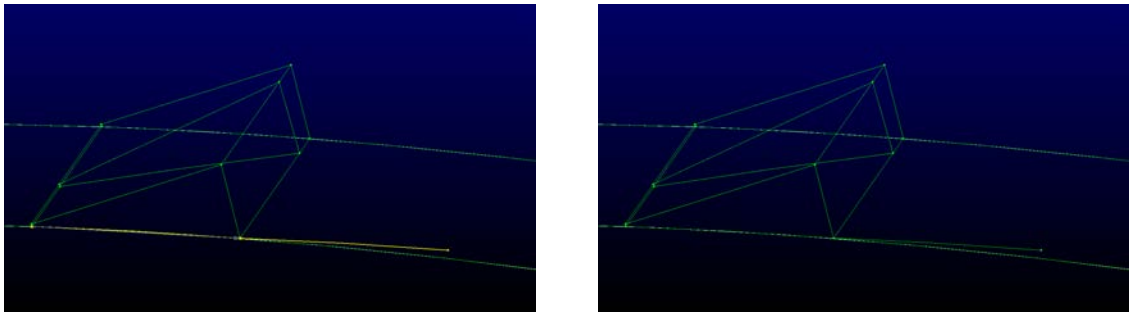

Figure D.6: Translated edge

3.1.7. Repeat from 3.1.1 to 3.1.6 for the other lateral edge

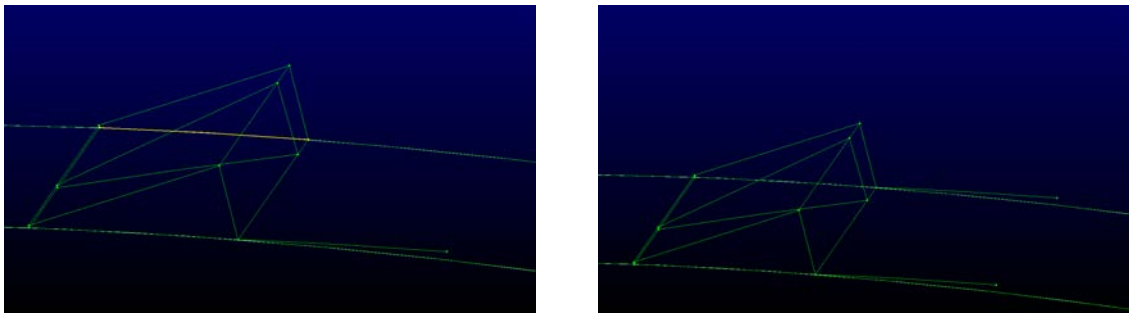

Figure D.7: Other translated edge

3.2. Split airfoil connectors selecting end point of the connectors just translated

3.2.1. Select airfoil connector

3.2.2. Go to Edit -> Split

3.2.3. Select end point of the connector translated at point 3.1, and click OK

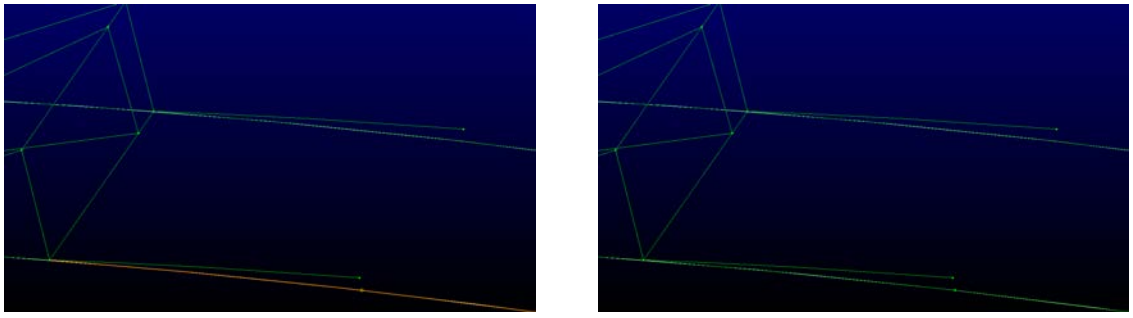

Figure D.8: Split airfoil connector

3.2.4. Repeat from point 3.2.1 to 3.2.3 for the other connector on the opposite side

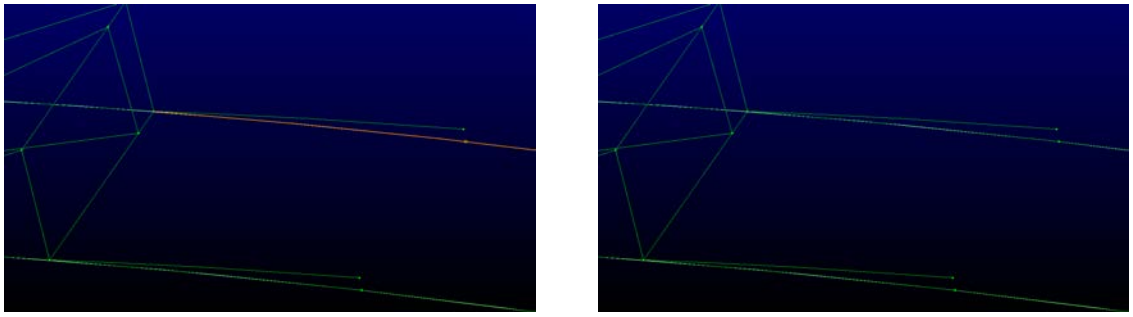

Figure D.9: Other Airfoil connector split

3.3. Delete connectors translated at point 3.1

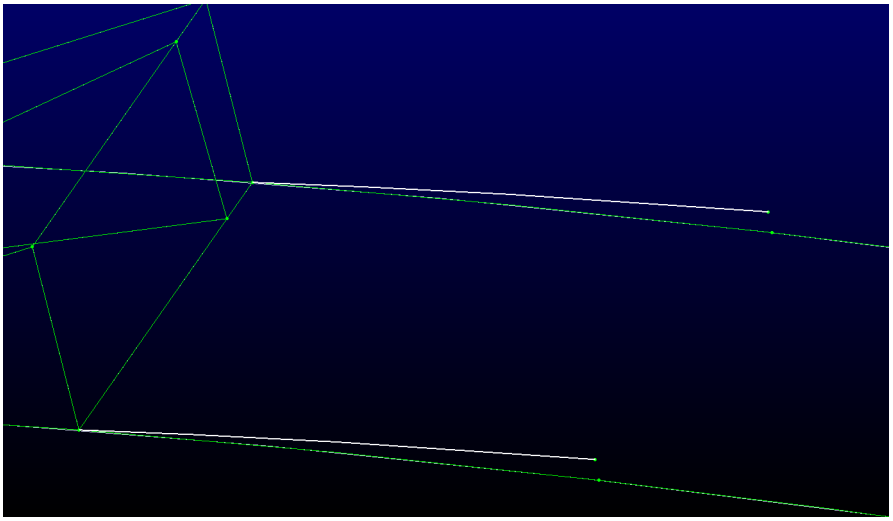

Figure D.10: Delete previously translated connectors

3.4. Copy and Translate connectors corresponding to VG base band thickness

3.4.1. Select connector

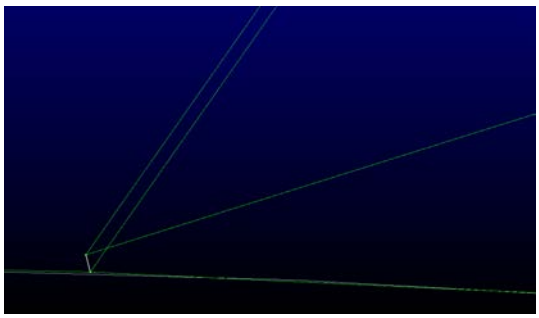

Figure D.11: Connector of the VG Base Band Thickness

3.4.2. Go to Edit -> Copy

3.4.3. Go to Edit -> Paste -> Translate

3.4.4. Click on Clear Translation Vector (only if previous translation vectors are already defined)

3.4.5. Define Points of the Translation Vector

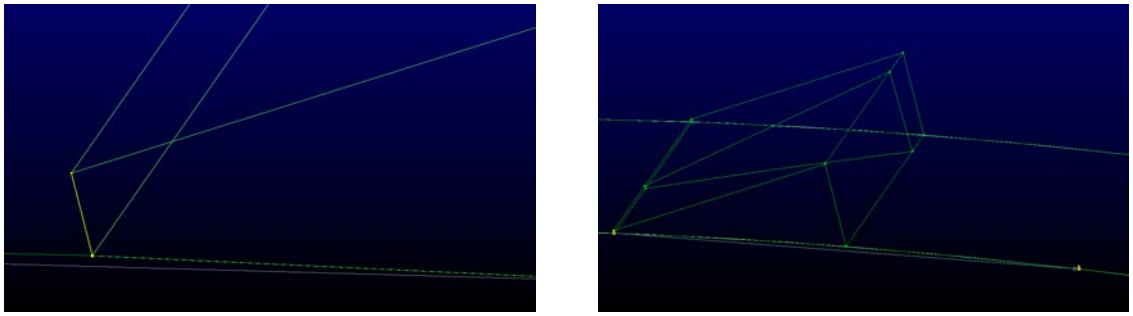

Figure D.12: Translation vector of the connector corresponding to the VG Base Band Thickness

3.4.6. Click OK to confirm the procedure

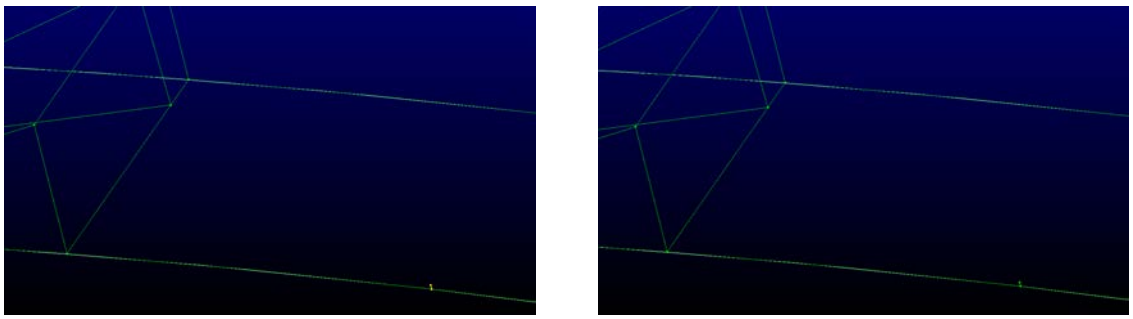

Figure D.13: VG Base Band Thickness connector translated

3.4.7. Repeat from 3.4.1 to 3.4.6 for the other connector

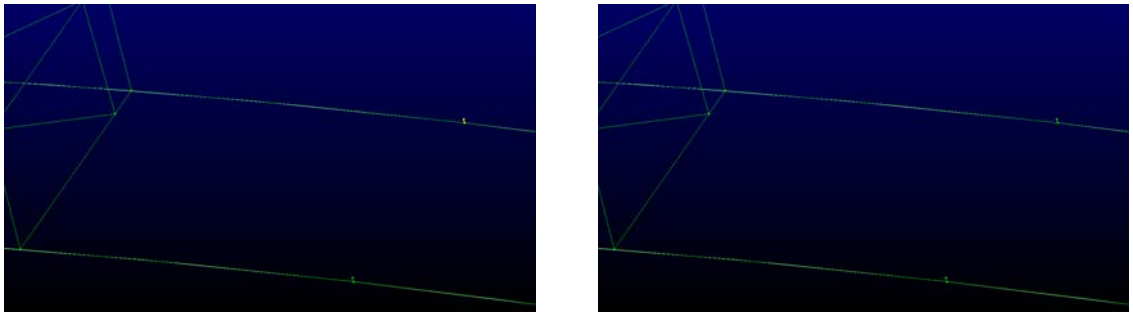

Figure D.14: Other VG Base Band thickness connector translated

3.5. Create connector on the airfoil surface connecting the 2 VG base band thickness connectors just created

3.5.1. Go to Create -> Draw Curves -> Line on Database

3.5.2. In the On Database Options frame click Begin

3.5.3. Select Database corresponding to the airfoil surface

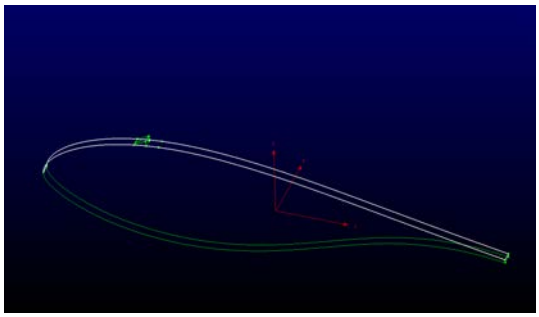

Figure D.15: Database to draw line on

3.5.4. Click End

3.5.5. Create connector selecting the 2 points on opposite sides

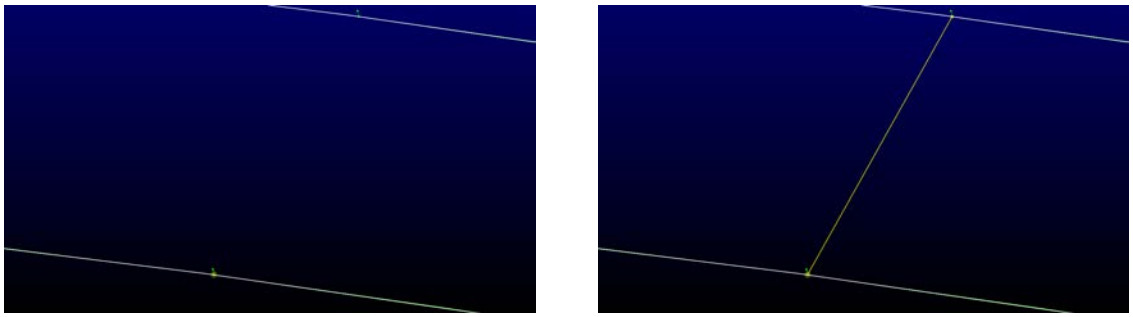

Figure D.16: Select connector start and end points

3.5.6. Click Apply

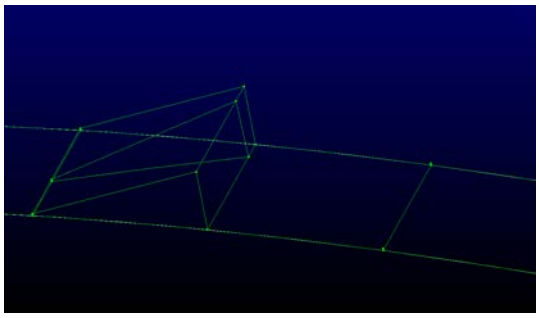

Figure D.17: Line on database created

3.6. Copy and Translate VG Base Band Edge of the Blocking

3.6.1. Select VG Base Band Edge of the Blocking

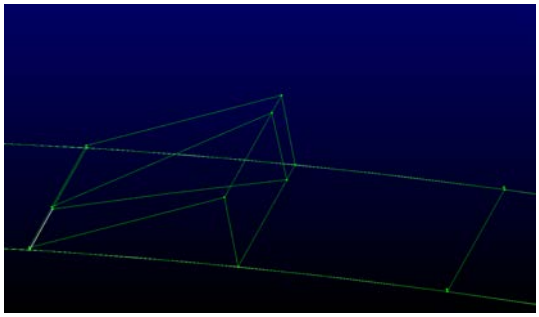

Figure D.18: VG Base Band Edge of the Blocking

3.6.2. Go to Edit -> Copy

3.6.3. Go to Edit -> Paste -> Translate

3.6.4. Click on Clear Translation Vector (only if previous translation vectors are already defined)

3.6.5. Define Points of the Translation Vector

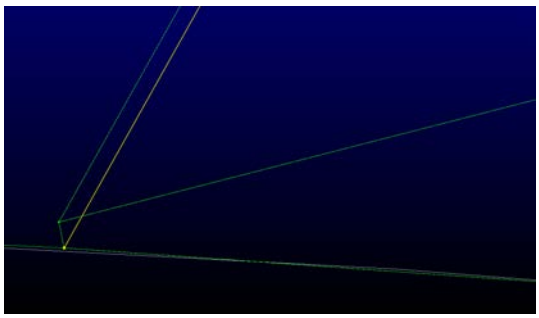

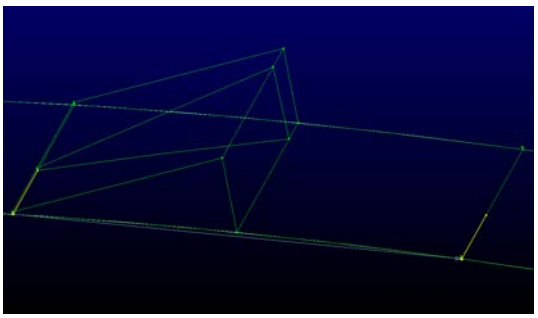

Figure D.19: Translation Base Band Edge connector

3.6.6. Click OK to confirm the procedure

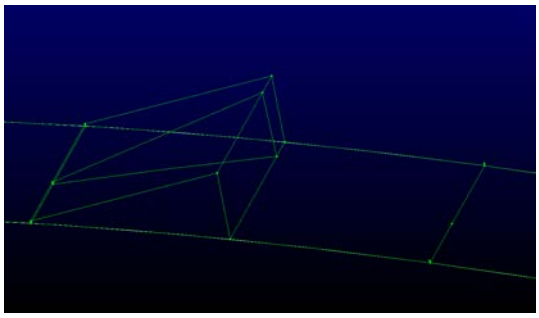

Figure D.20: Base Band Edge Translated

3.7. Split connector created at point 3.5, selecting the end point of the VG Base Band Edge just created

3.7.1. Select connector created at point 3.5

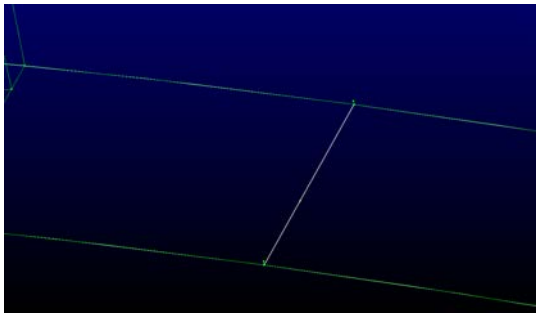

Figure D.21: Select connector created at point 3.5

3.7.2. Go to Edit -> Split

3.7.3. Select end point of the VG Base Band Edge created at point 3.6, and click OK

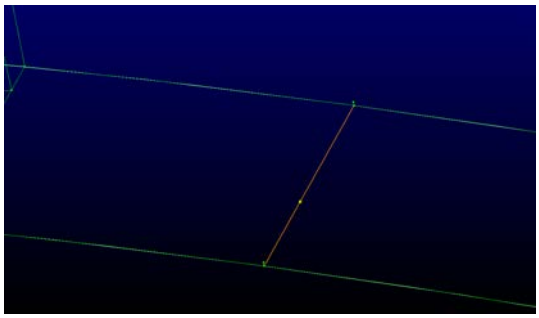

Figure D.22: Split connector created at point 3.5

3.8. Copy and Translate connector normal to VG Base Band Edge of the Blocking

3.8.1. Select connector from point 3.4

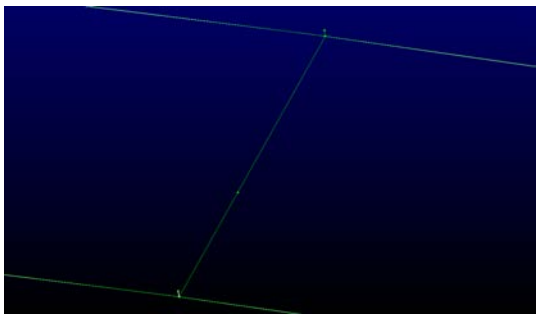

Figure D.23: Select connector to translate

3.8.2. Go to Edit -> Copy

3.8.3. Go to Edit -> Paste -> Translate

3.8.4. Click on Clear Translation Vector (only if previous translation vectors are already defined)

3.8.5. Define Points of the Translation Vector

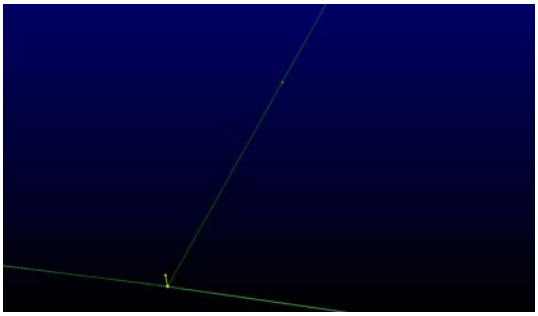

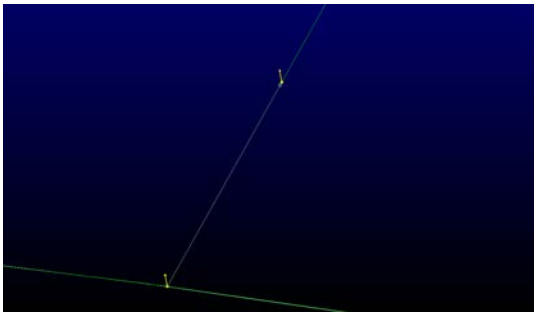

Figure D.24: Define Translation Vector

3.8.6. Click OK to confirm the procedure

3.9. Create remaining connectors to complete the VG Blocking Mirroring, with Create -> 2 Point Curves and Create -> Line on Database

4. Create additional edges on the airfoil surface, to avoid not regular mesh lines on the remaining part of the surface

   4.1. Copy and Translate lateral edges of the VG Blocking, to translate it before the VG

      4.1.1. Select lateral Edge VG Blocking

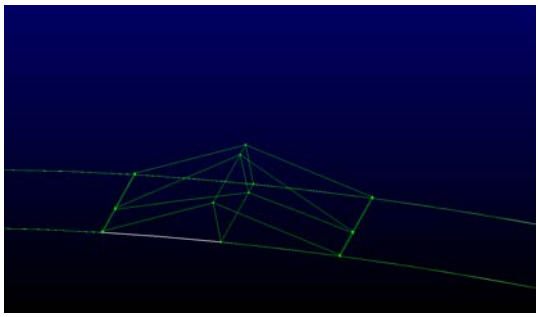

Figure D.25: Additional edge on airfoil surface, before the VG

      4.1.2. Go to Edit -> Copy

      4.1.3. Go to Edit -> Paste -> Translate

      4.1.4. Click on Clear Translation Vector (only if previous translation vectors are already defined)

      4.1.5. Define Points of the Translation Vector

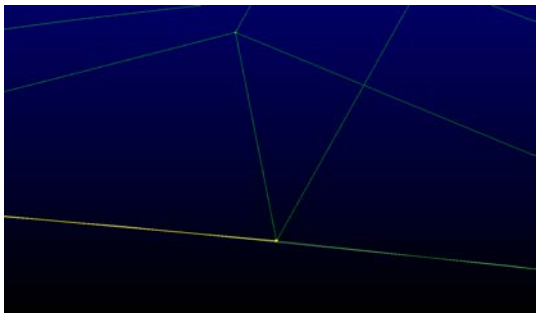

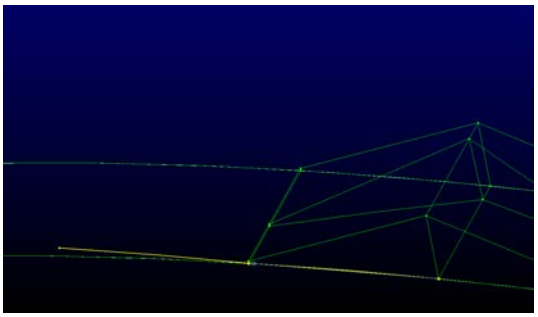

Figure D.26: Define Translation Vector

      4.1.6. Click OK to confirm the procedure

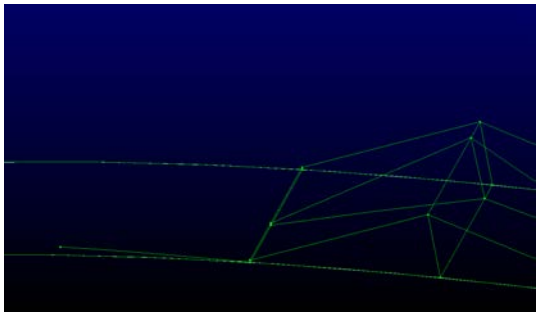

Figure D.27: Translated additional edge

4.1.7. Repeat from 4.1.1 to 4.1.6 for the other additional edge

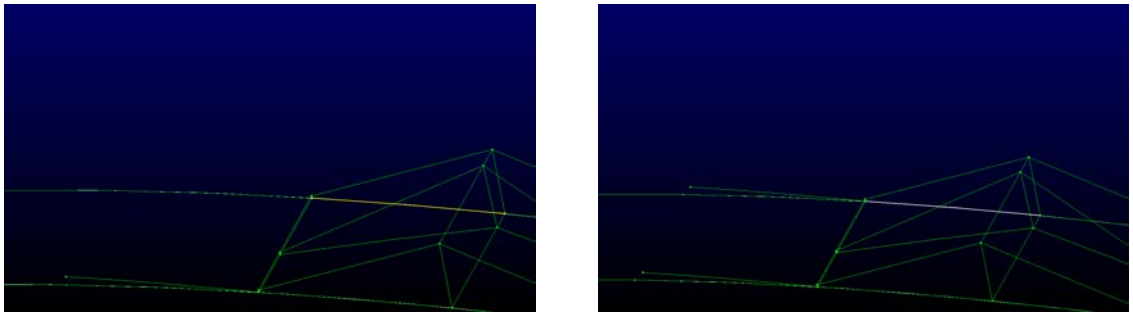

Figure D.28: Other additional edge before the VG

4.2. Copy and Translate lateral edges of the VG Blocking, to translate it after the VG

4.2.1. Select lateral Edge VG Blocking

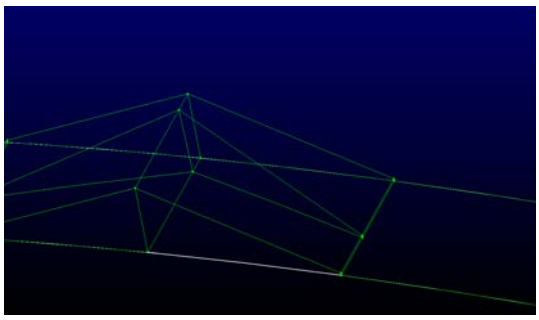

Figure D.29: Additional edge on airfoil surface, after the VG

4.2.2. Go to Edit -> Copy

4.2.3. Go to Edit -> Paste -> Translate

4.2.4. Click on Clear Translation Vector (only if previous translation vectors are already defined)

4.2.5. Define Points of the Translation Vector

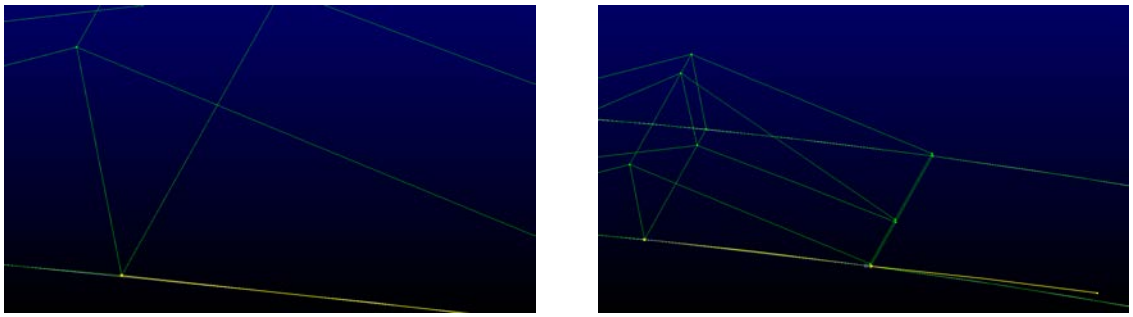

Figure D.30: Define Translation vector

4.2.6. Click OK to confirm the procedure

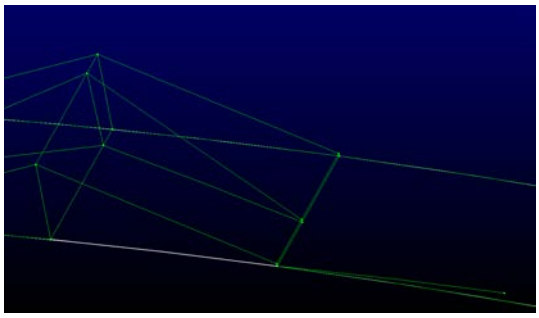

Figure D.31: Translated additional edge

4.2.7. Repeat from 4.2.1 to 4.2.6 for the other additional edge

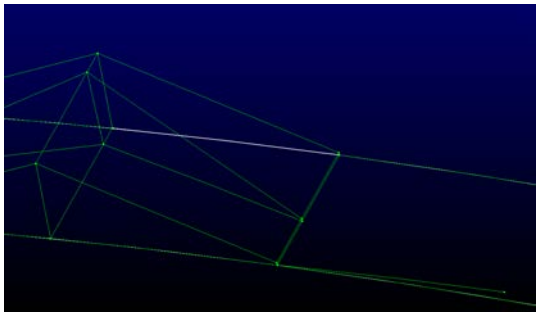

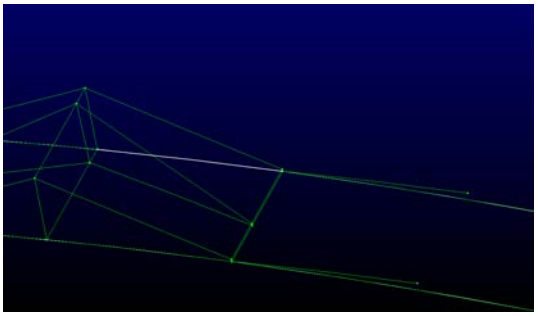

Figure D.32: Other additional edge before the VG

5. Split the airfoil surface connectors, following the procedure at point 3.2, considering the end point of the connectors created at point 4. Create then the connectors on the airfoil surface as in point 3.5

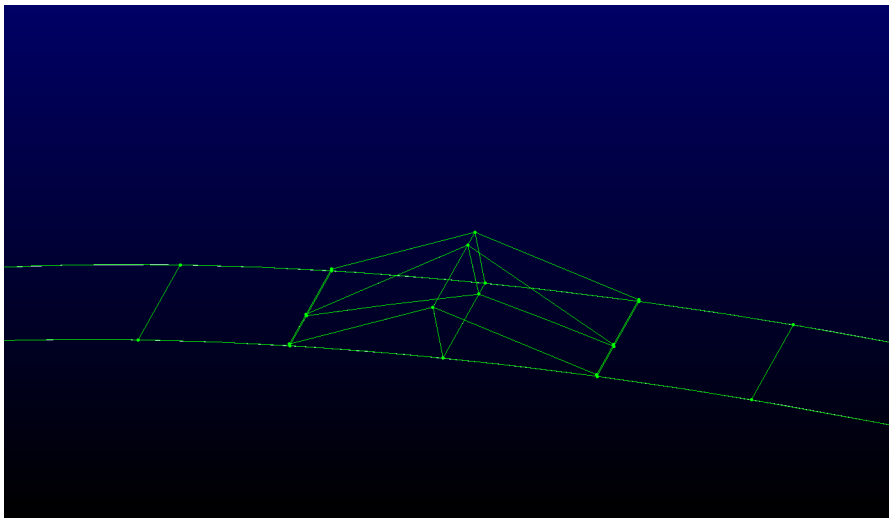

Figure D.33: Additional connectors created

6. Assign number of nodes on connectors

   6.1. Assign 34 nodes to connectors normal to airfoil surface (to resolve properly Boundary Layer in the regions away from the VG)

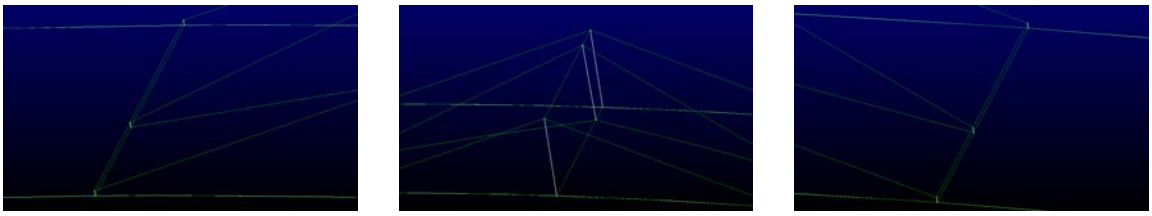

Figure D.34: Connectors normal to airfoil surface

6.2. Assign 10 nodes to connectors along airfoil surface (not too many nodes since it's not necessary to resolve too fine the region near the VG. It's important to resolve properly the region after the VG)

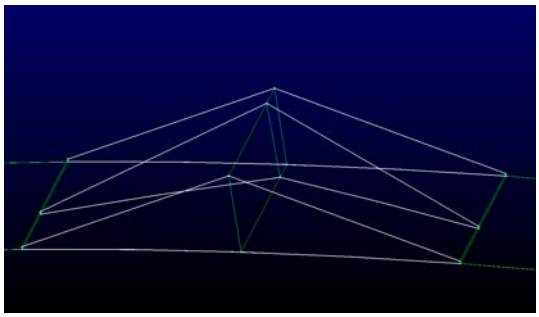

Figure D.35: Connectors along airfoil surface

6.3. Assign 8 nodes to connectors along third dimension (extruding direction of the airfoil profile)

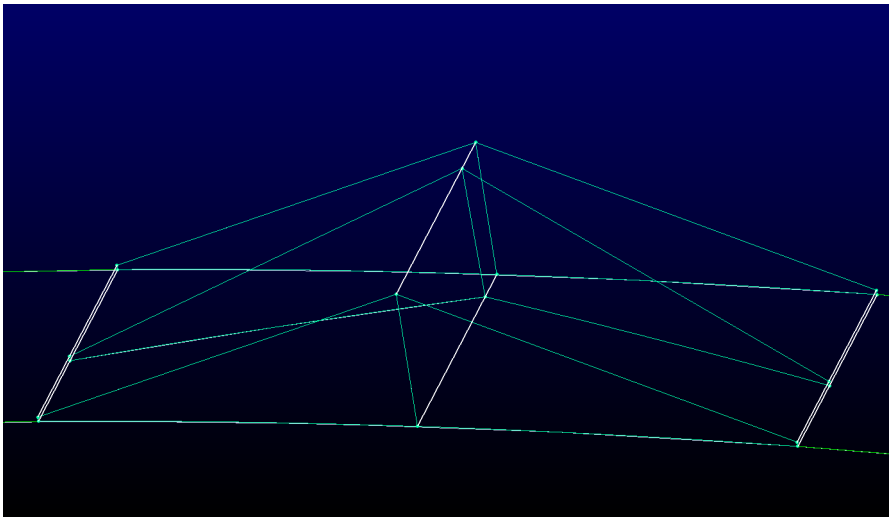

Figure D.36: Connectors along extruding direction of the airfoil profile

6.4. Assign 10 nodes to additional edges along airfoil surface

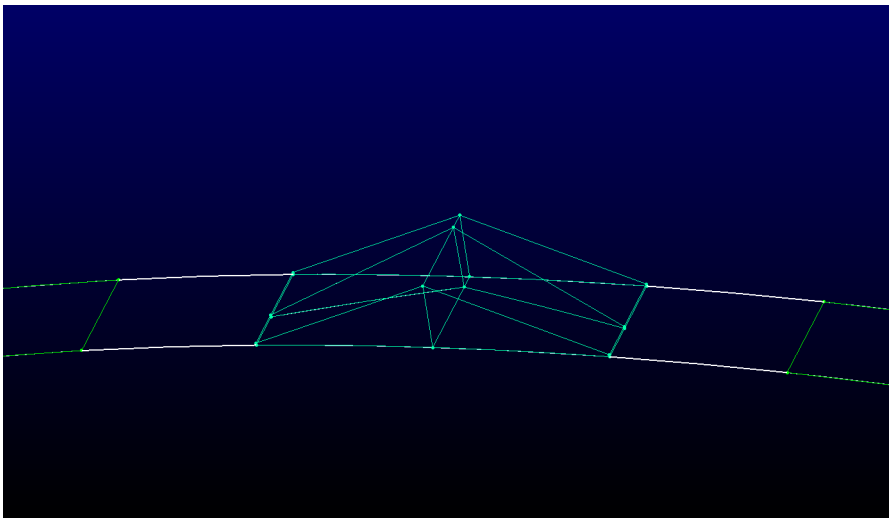

Figure D.37: Additional connectors along airfoil surface

6.5. Assign 15 nodes along third direction

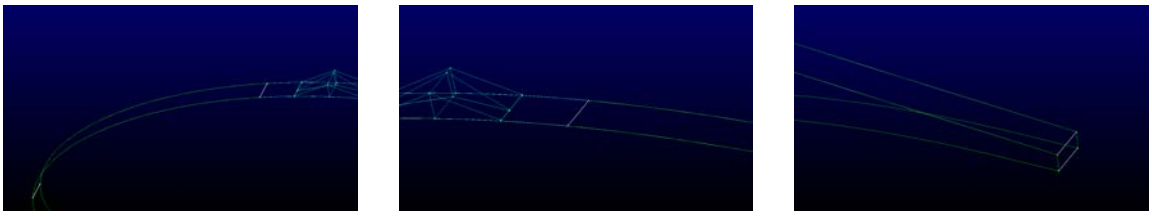

Figure D.38: Connectors along third direction

6.6. Assign 90 nodes to connectors along airfoil surface, before the VG

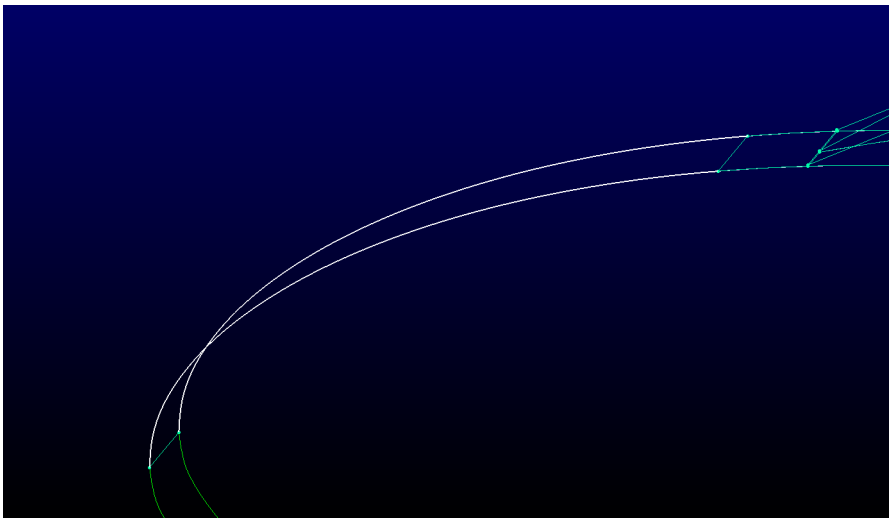

Figure D.39: Connectors along airfoil surface, before the VG

6.7. Assign 393 nodes to connectors along airfoil surface, after the VG

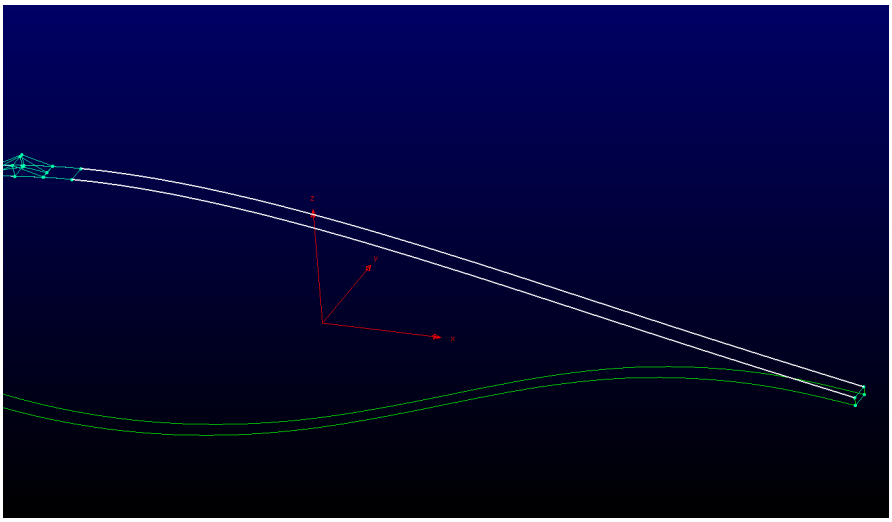

Figure D.40: Connectors along airfoil surface, after the VG

6.8. Assign 520 nodes to connectors along airfoil surface, on the pressure side

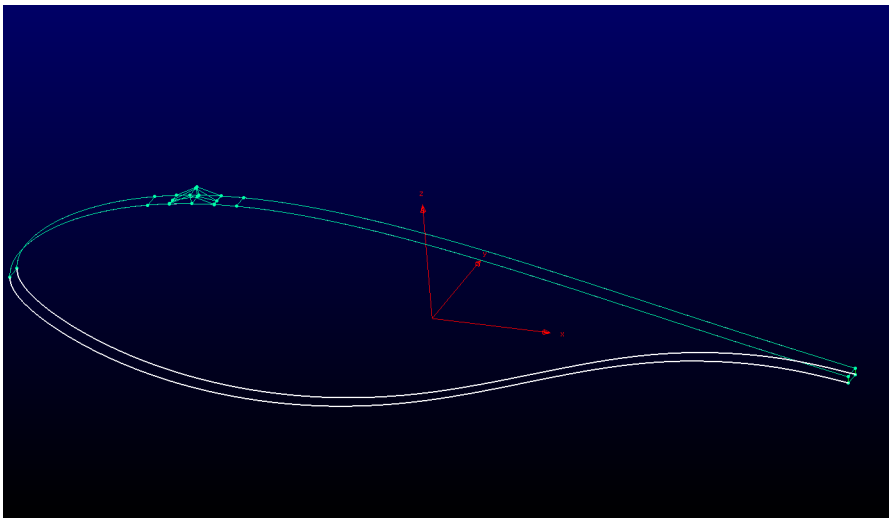

Figure D.41: Connectors along airfoil surface, on the pressure side

6.9. Assign 4 nodes to connectors along blunt Trailing Edge

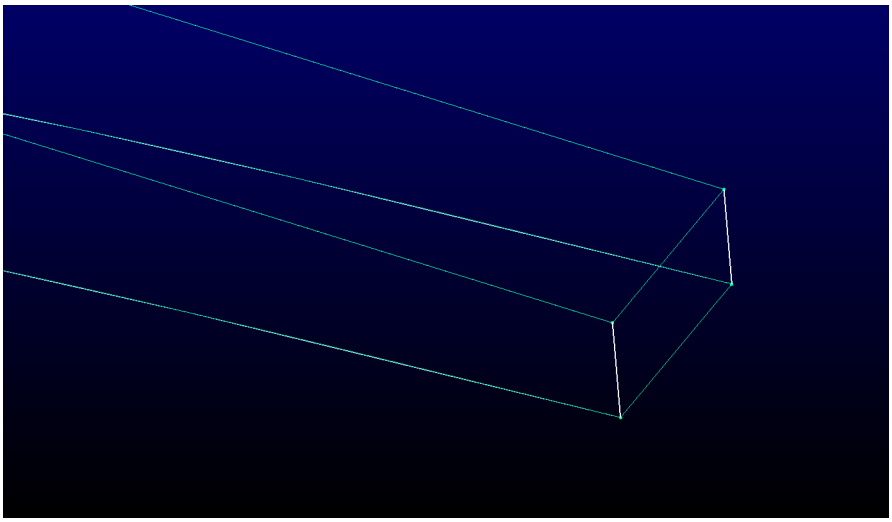

Figure D.42: Connectors along blunt Trailing Edge

7. Define end spacing of connectors normal to the airfoil surface, setting it to the value 4.56e-6 (half of the spacing necessary to obtain a $y^+ = 1$, to ensure a good y^+ value at the end of the simulation)

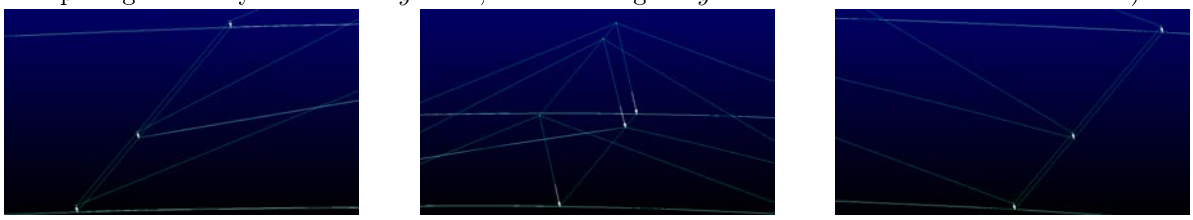

Figure D.43: End Spacing of connectors normal to the airfoil surface

8. Assemble Domains from connectors created and defined. All domains will have quadrilateral cells ("structured" according to *Pointwise* definition). In order to do so, for every domain to be created, select a closed loop of connectors (ensuring that opposite sides have the same number of nodes) and go to Create -> Assemble Special -> Domain

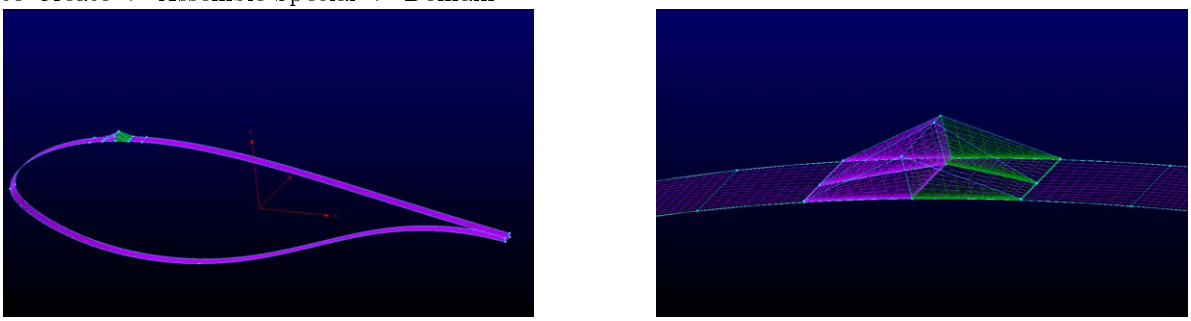

Figure D.44: Assembled domains

9. Create Blocks out of the domains created for the VG Blocking. In order to do so, to construct a "structured block" according to *Pointwise* definition, select for each block 6 domains and go to Create -> Assemble Special -> Block.

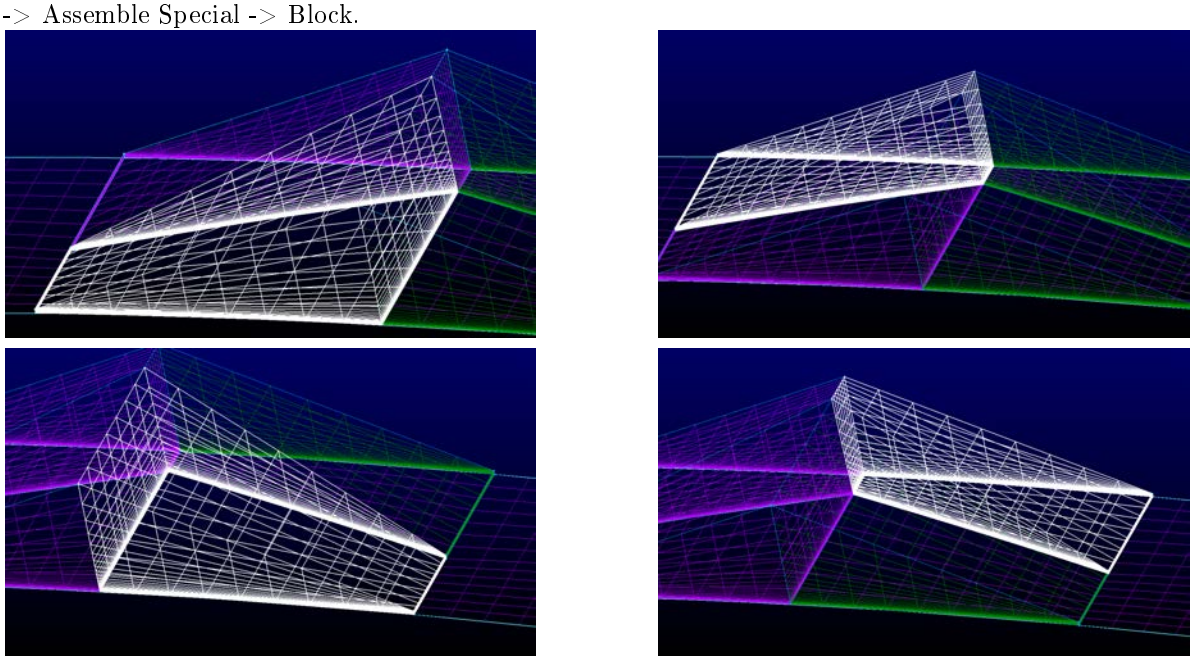

Figure D.45: VG Blocking

10. Create First Extrusion Block, relative to the Boundary Layer, as follows:

    10.1. Select Domains to extrude from

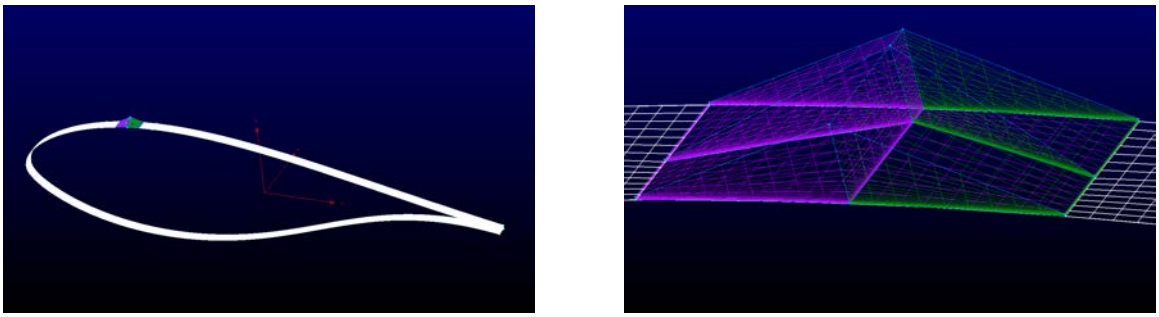

Figure D.46: Domains to extrude from

    10.2. Go to Create -> Extrude -> Normal

    10.3. In the Assemble frame accept the proposed assembling choice and click Done

    10.4. Set the parameters of the Normal Extrusion in the Attributes tab

        10.4.1. In the Step Size frame set:
        - $Initial\Delta s = 4.56e-6$
        - $GrowthRate = 1.088$

10.4.2. In the Orientation frame click on Flip, if the normals are not pointing out

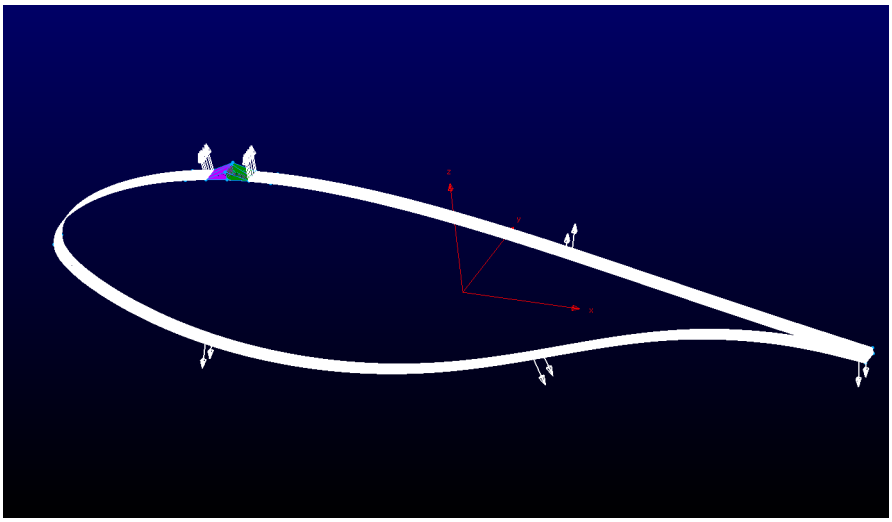

Figure D.47: Normals pointing out

10.4.3. In the Stop Conditions frame set Total Height = 500 (it define the maximum limit of the extrusion distance, from the surface to extrude from)

10.5. In the Boundary Condition tab define the boundary conditions of the Normal Extrusion:

10.5.1. In the Boundary Conditions frame select Type=Adjacent Grid

10.5.2. Select the connector adjacent to the Domain representing the VG Band Thickness

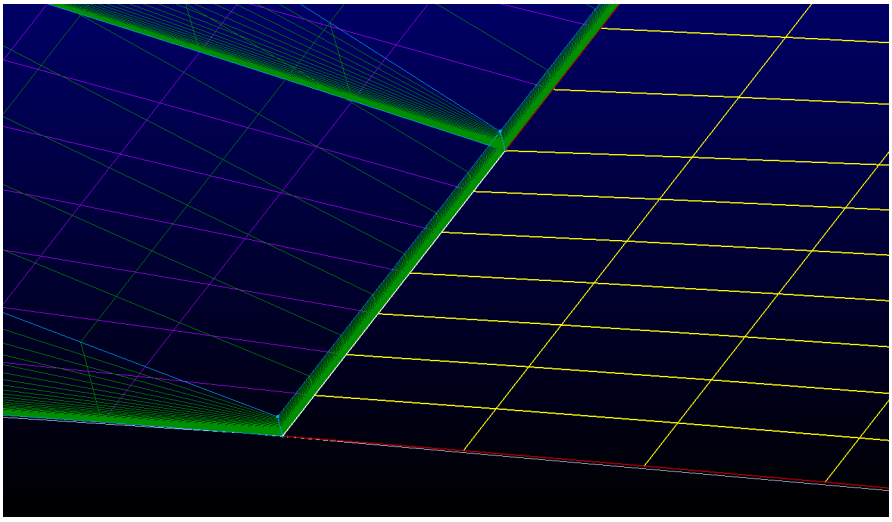

Figure D.48: Connector adjacent to VG Band Thickness

10.5.3. In the Adjacent Grid Selection frame click Begin

10.5.4. Select the Adjacent Grid that will provide the spacing that the Normal Extrusion algorithm will follow

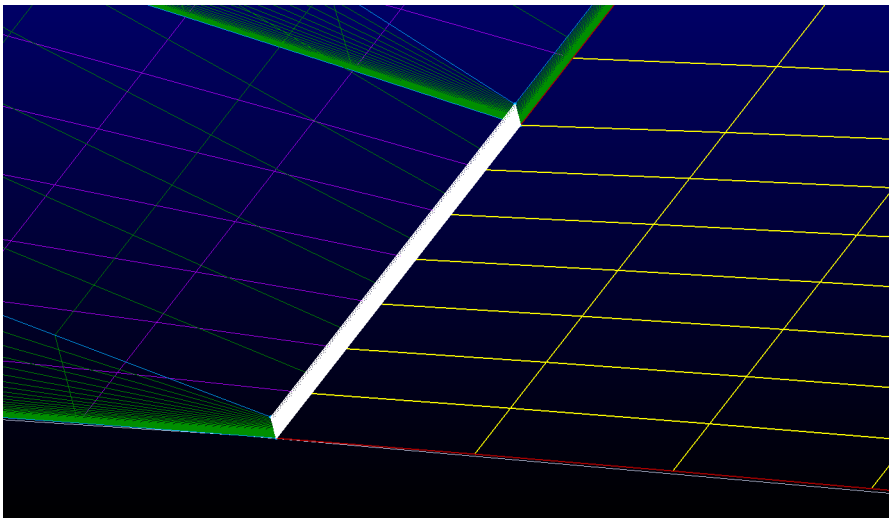

Figure D.49: Select Adjacent Grid

10.5.5. In the Adjacent Grid Selection frame click End

10.5.6. In the Boundary Conditions frame click Set Boundary Condition

10.5.7. Repeat points 10.5.1 to 10.5.6 for the other connectors adjacent to the Domains representing the VG Band Thickness

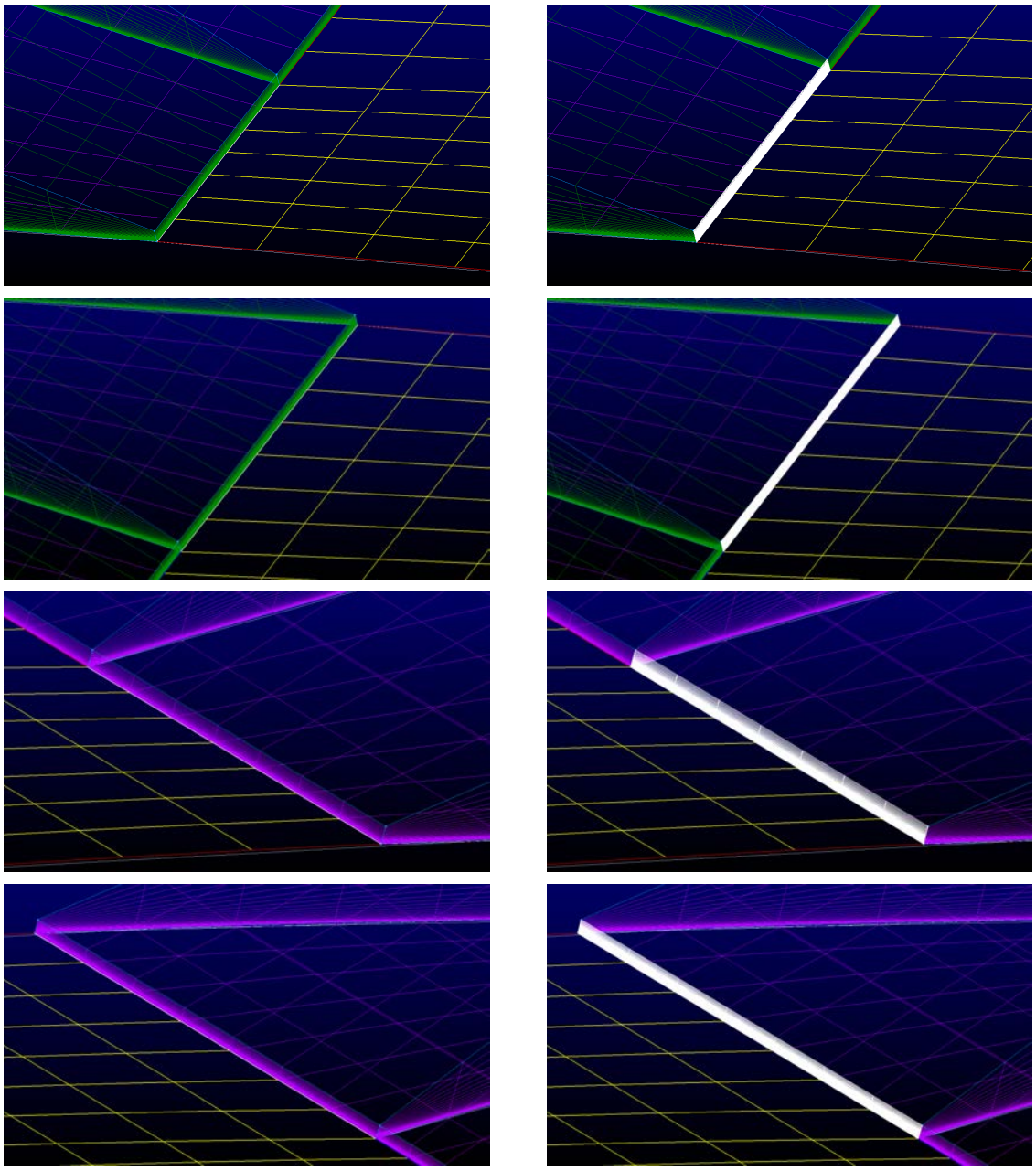

Figure D.50: Other connectors adjacent to the Domains representing the VG Band Thickness

10.5.8. All the other connectors will be set to the Boundary Condition Type=Symmetry Y

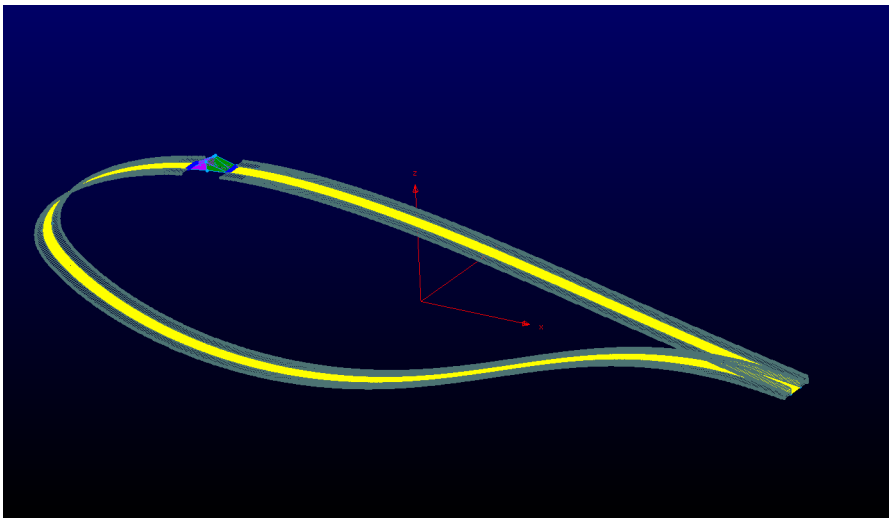

Figure D.51: Symmetry Y Boundary Condition for the Normal Extrusion of the region in the Boundary Layer

10.6. In the Run tab, in the Extrude frame, set the number of extrusion steps Steps=33, and click Run

10.7. Click OK to accept the resulting extrusion

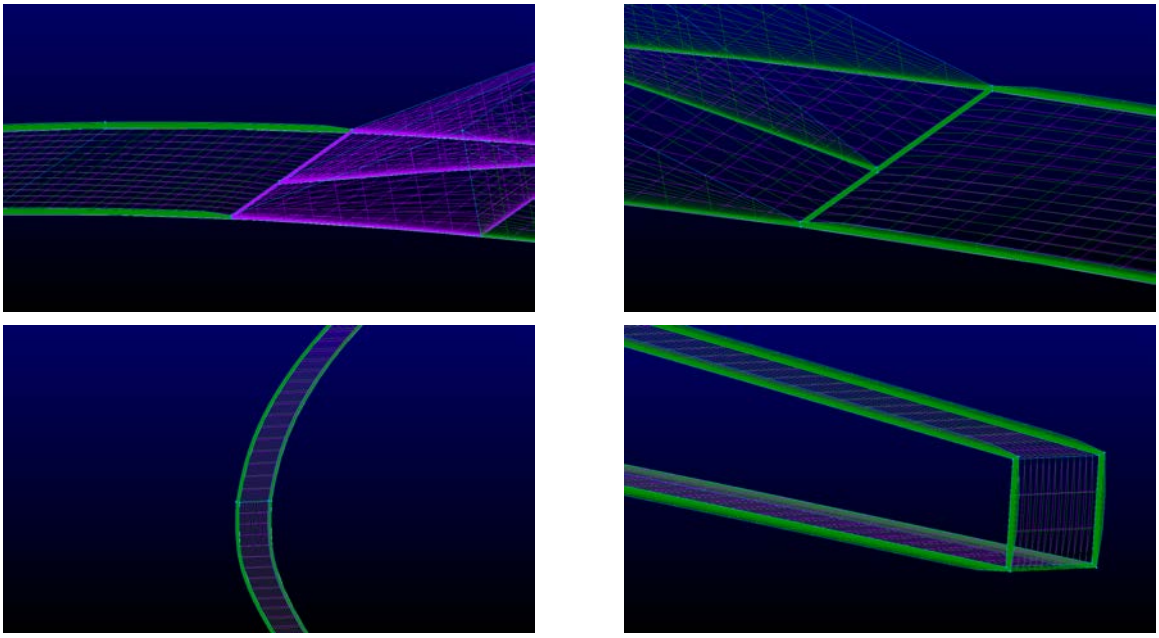

Figure D.52: Boundary Layer Normal Extrusion

11. Create Last Extrusion Block as follows:

11.1. Select Domains to extrude from

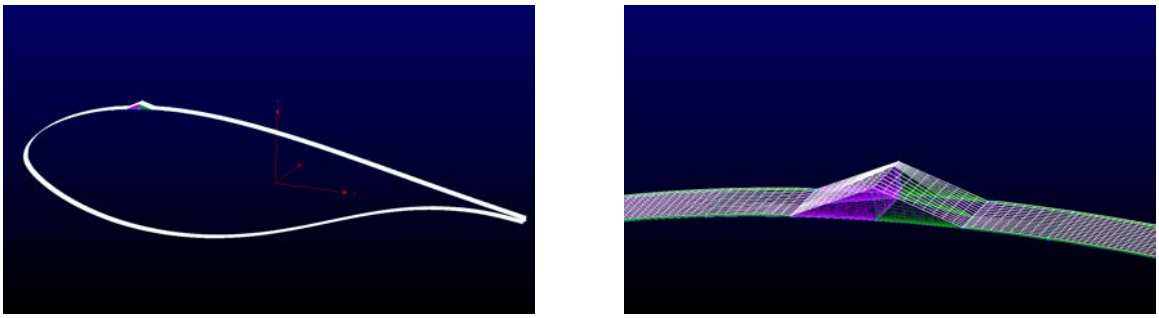

Figure D.53: Domains to extrude from

11.2. Go to Create -> Extrude -> Normal

11.3. In the Assemble frame accept the proposed assembling choice and click Done

11.4. Set the parameters of the Normal Extrusion in the Attributes tab

11.4.1. In the Step Size frame set:
- $Initial\Delta s = 1/10 * MinimumSurfaceSpacing$ (MinimumSurfaceSpacing is specified by *Pointwise* right above the box $Initial\Delta s$. This ensures a good growth of the cells during the extrusion)
- $GrowthRate = 1.088$

11.4.2. In the Orientation frame click on Flip, if the normals are not pointing out

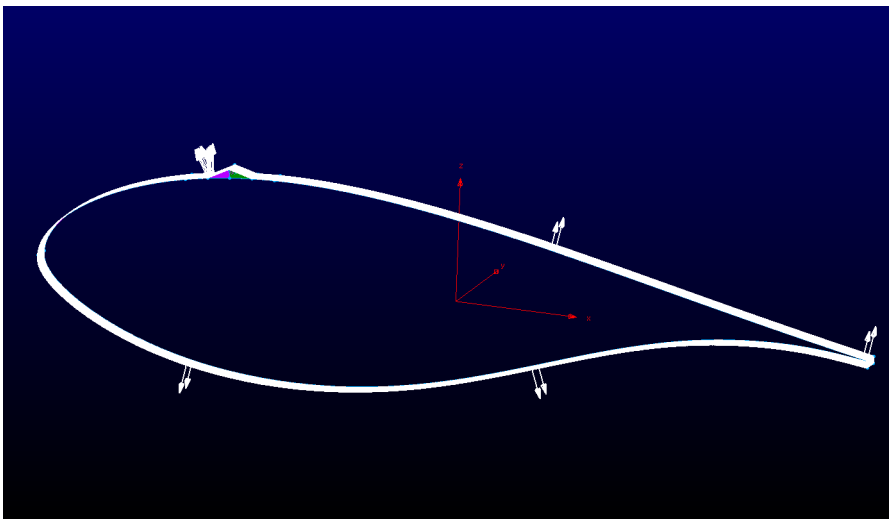

Figure D.54: Normals pointing out

11.4.3. In the Stop Conditions frame set Total Height = 500 (it defines the maximum limit of the extrusion distance, from the surface to extrude from)

11.5. In the Boundary Condition tab define the boundary conditions of the Normal Extrusion:

11.5.1. All the connectors will be set to the Boundary Condition Type=Symmetry Y

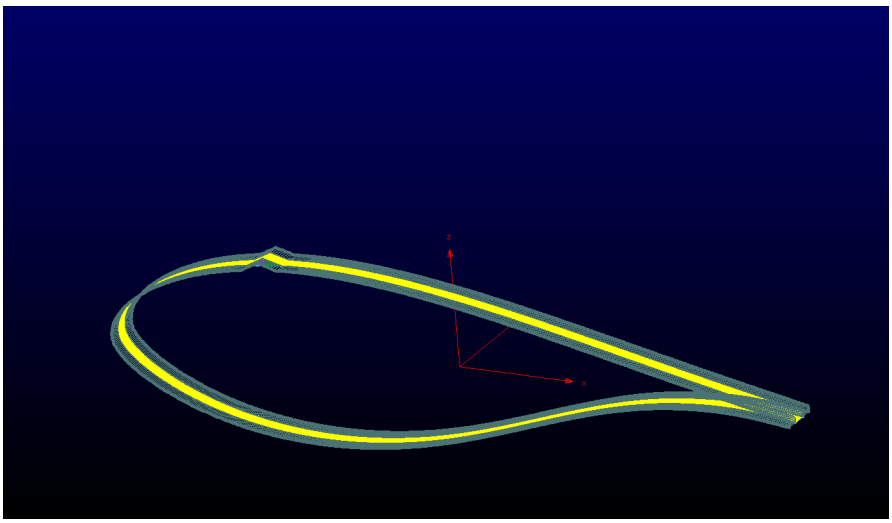

Figure D.55: Symmetry Y Boundary Condition for the Last Normal Extrusion

11.6. In the Run tab, in the Extrude frame, set the number of extrusion steps to a large arbitrary number (e.g Steps=500), and click Run. The Stop Condition Total Height will stop the extrusion when the desired distance from the surface has reached the value 500.

11.7. Click OK to accept the resulting extrusion

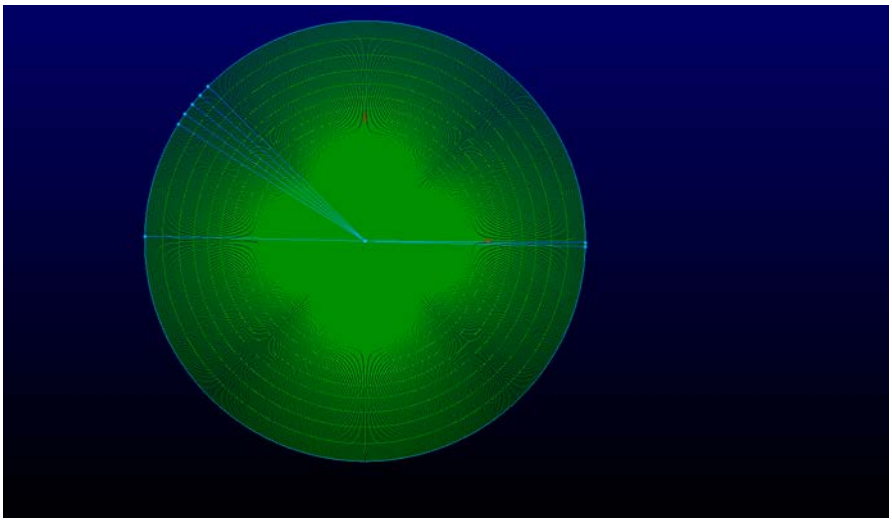

Figure D.56: Total Normal Extrusion

12. Define Boundary Conditions and Output format of the Mesh created

    12.1. Go to CAE -> Select Solver -> Stanford ADL/SU2 and click OK

    12.2. Go to CAE -> Set Dimension -> 3D

    12.3. Go to CAE -> Set Boundary Conditions, and define the boundary conditions as follows:

        12.3.1. Create with the New Button 4 Boundary Conditions, named “airfoil”,”symmetry”,”farfield”,”vg”

        12.3.2. Select Domains for the “airfoil” Boundary Condition

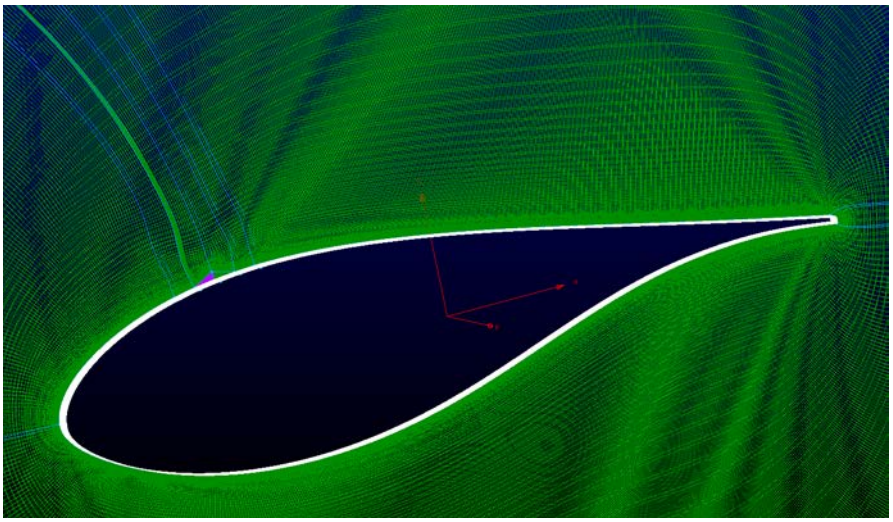

Figure D.57: Airfoil Boundary Condition

        12.3.3. Click on the tick box near the “airfoil” Boundary Condition name, to assign the Domains selected to the corresponding Boundary Condition

12.3.4. Select Domains for the "farfield" Boundary Condition

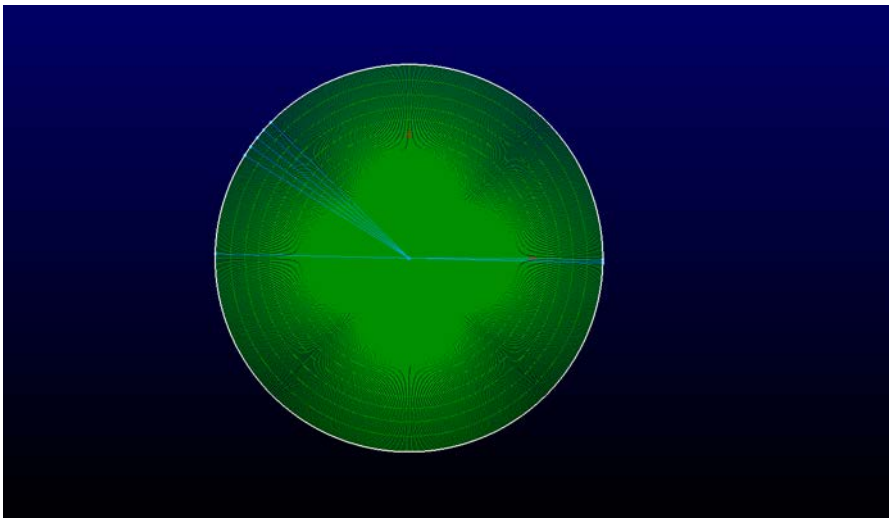

Figure D.58: Farfield Boundary Condition

12.3.5. Click on the tick box near the "farfield" Boundary Condition name, to assign the Domains selected to the corresponding Boundary Condition

12.3.6. Select Domains for the "symmetry" Boundary Condition (all the Domains with the normal to the domain pointing in the y-direction)

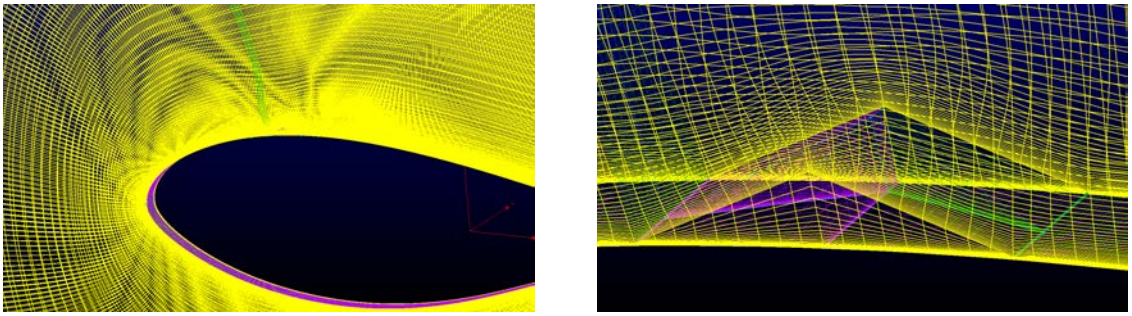

Figure D.59: Symmetry Boundary Condition

12.3.7. Click on the tick box near the "farfield" Boundary Condition name, to assign the Domains selected to the corresponding Boundary Condition

12.3.8. Select Domains for the "vg" Boundary Condition, selecting first the box Select Connections, and then the 2 domains pointing in opposite directions relatively to the VG surface

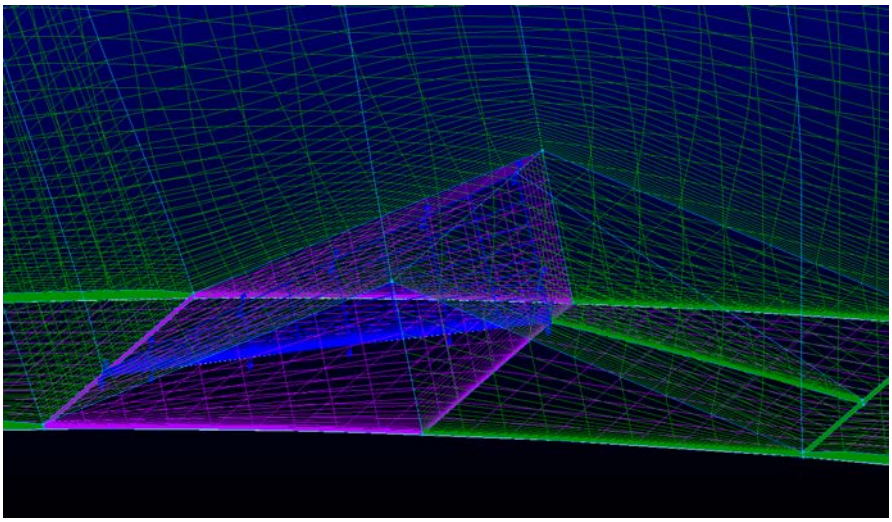

Figure D.60: VG Boundary Condition

12.3.9. Click on the tick box near the "vg" Boundary Condition name, to assign the Domains selected to the corresponding Boundary Condition

13. Export the 3D Mesh created in the SU2 format

13.1. Select all the blocks created

13.2. Go to File -> Export -> CAE

13.3. Specify name of the *.su2 file to be created

13.4. In the frame Data Precision specify Double for Double Precision

13.5. Click OK to generate the Mesh

Appendix E

Airfoil Data Extraction Script

In this Appendix, an example of a *Python* script to extract data from a 3D airfoil solution is reported.

```
# -*- coding: utf-8 -*-
"""
Created on Mon May 07 13:22:56 2018

@author: Andrea
"""

from os import getcwd, path, mkdir
import errno
from h5py import File
import numpy
import pandas
from paraview.simple import (LegacyVTKReader,
                             servermanager, Slice)
from vtk.util.numpy_support import vtk_to_numpy
from math import fmod

def merge_reshape_coordinates(MeshGrid):
    """
    Merges the 3 coordinate arrays into one 3D List of Tuples
    of the form (x,y,z), each one representing a point in the 3D space.

    The initial indexing of the imported coordinates from the CGNS Structured
    mesh is rearranged, to keep the correspondence with the Pointwise mesh,
    created according to the norm used in SU2 of having 'x' as 1st dimension,
    'z' as 2nd dimension, 'y' as 3rd dimension).

    For 3D Grid:
    ------------

    Initially the 3 indexes of the MeshGrid array referred to:
        - 1st MeshGrid array index K -> z direction
        - 2nd MeshGrid array index J -> y direction
        - 3rd MeshGrid array index I -> x direction
```

```
The rearrangement leads to:
    - K index was the first dimension in the original MeshGrid array
            -> I index now is for first dimension (x) of Coordinates Array
    - J index was the second dimension in the original MeshGrid array
            -> K index now is for second dimension (z) of Coordinates
                Array
    - I index was the third dimension in the original MeshGrid array
            -> J index now is for third dimension (y) of Coordinates Array

For 2D Grid (approximately parallel to x-z plane):
-----------------
Initially the 2 indexes of the MeshGrid array referred to:
    - 1st MeshGrid array index K -> z direction
    - 2nd MeshGrid array index I -> x direction

The rearrangement leads to:
    - K index was the first dimension in the original MeshGrid array
            -> I index now is for first dimension (x) of Coordinates Array
    - I index was the second dimension in the original MeshGrid array
            -> J index now is for second dimension (z) of Coordinates
                Array

N.B Doesn't work so far for other 2D Grids on different planes (K,I will
    refer to different directions in other cases)

Input
----------
MeshGrid:
    Original Structured CGNS Imported Mesh.

Function Variables
----------
x_coordinates_dataset: 3D Numpy array of floats
    x coordinates of the points in the 3D space
y_coordinates_dataset: 3D Numpy array of floats
    y coordinates of the points in the 3D space
z_coordinates_dataset: 3D Numpy array of floats
    z coordinates of the points in the 3D space
    Is2D:boolean
            Flag for 2D Input Mesh
    Is3D:boolean
            Flag for 3D Input Mesh
    I_dim:float
            Length of matrix dimension corresponding to I index
    J_dim:float
            Length of matrix dimension corresponding to J index
    K_dim:float
            Length of matrix dimension corresponding to K index
```

```
Output
-------
Points_Coordinates: 3D List of Tuples
    Coordinates of points in the 3D space.

"""

# Obtain x,y,z Mesh coordinates
x_coordinates_dataset = (MeshGrid['Base']['VG']['GridCoordinates']
                                ['CoordinateX']['_data'].value)
y_coordinates_dataset = (MeshGrid['Base']['VG']['GridCoordinates']
                                ['CoordinateY']['_data'].value)
z_coordinates_dataset = (MeshGrid['Base']['VG']['GridCoordinates']
                                ['CoordinateZ']['_data'].value)

Is3D = False
Is2D = False

if x_coordinates_dataset.ndim == 3:

    Is3D = True

elif x_coordinates_dataset.ndim == 2:

    Is2D = True

else:

    print "1D Grid Provided"
    raise SystemExit


if Is3D:

    # Obtain arrays dimensions length
    K_dim = numpy.size(x_coordinates_dataset,0) # K index -> z coordinates
    J_dim = numpy.size(x_coordinates_dataset,1) # J index -> y coordinates
    I_dim = numpy.size(x_coordinates_dataset,2) # I index -> x coordinates

    # Initialize 3D List 'Points_Coordinates', with List Comprehension
        syntax
    Points_Coordinates = [[ [() for index_J in range(0,J_dim)]
                          for index_K in range(0,K_dim)]
                      for index_I in range(0,I_dim)]

    # Populate Points_Cooordinates
    for J in range(0,J_dim):
        for K in range(0,K_dim):
```

```
                for I in range(0,I_dim):
                    Points_Coordinates[I][K][J] = (x_coordinates_dataset[K][J
                        ][I],
                                                   y_coordinates_dataset[K][J][
                                                       I],
                                                   z_coordinates_dataset[K][J][
                                                       I])

    elif Is2D:

        # Obtain arrays dimensions length
        K_dim = numpy.size(x_coordinates_dataset,0) # K index -> z coordinates
        I_dim = numpy.size(x_coordinates_dataset,1) # I index -> x coordinates

        # Initialize 2D List 'Points_Coordinates', with List Comprehension
            syntax
        Points_Coordinates = [[() for index_K in range(0,K_dim)]
                              for index_I in range(0,I_dim)]

        # Populate Points_Cooordinates
        for K in range(0,K_dim):
            for I in range(0,I_dim):
                Points_Coordinates[I][K] = (x_coordinates_dataset[K][I],
                                            y_coordinates_dataset[K][I],
                                            z_coordinates_dataset[K][I])

    return Points_Coordinates



def ExtractSurfaceData(Surface_reader,Quantity_to_extract,
                       X_Slice_Position,Y_Slice_Position):
    """
    Extract user specified surface data at user specified locations on the
        airfoil surface.
    It does that as follows:

    1) Slices the surface solution with a plane perpendicular to the x-axis
    2) Slices the result from 1) with a plane perpendicular to the y-axis
    3) From 2) select points on suction and pressure side
    4) Extract quantity of interest from 3)


    Input
    ----------
    Surface_reader: vtk Object with attribute SMProxy
        Object containing airfoil surface solution

        OutputVariables:List of strings
```

```
    Variables to extract from airfoil surface

    Quantity_to_extract:string
            Variable to extract from the airfoil surface solution

X_Slice_Position:float
    X position for slicing airfoil surface

Y_Slice_Position:float
    Y position for slicing airfoil surface

Function Variables
---------
Slice_X_Proxy: vtk Slice Object
    Slice at specified x position

Slice_Y_Proxy: vtk Slice Object
    Slice at specified y position

Slice_Y: vtk servermanager Object
    Solution Data from Slice_Y_Proxy Object

Sliced_Points:numpy array of floats
    Points Coordinates resulting from the 2nd slicing operation

    Row_Index_Suction_Point:numpy array of float
    Point index of the point on the suction side of the airfoil

    Row_Index_Pressure_Point:numpy array of float
    Point index of the point on the pressure side of the airfoil

    Point_On_Suction_Surface_Coordinates:numpy array of floats
    Coordinates of the point on the suction surface

    Point_On_Pressure_Surface_Coordinates:numpy array of floats
    Coordinates of the point on the pressure surface

Point_ID_Suction_Surface:numpy array of float
    PointID from Slice_Y of the Point_On_Suction_Surface_Coordinates

    Point_ID_Pressure_Surface:numpy array of float
    PointID from Slice_Y of the Point_On_Pressure_Surface_Coordinates

    Quantity_extracted:string
            Variable of interest to extract from the solution

Output
-------
```

```
    Quantity_Suction_Surface:numpy array of floats
    Extracted quantity corresponding to Point_ID_Suction_Surface

Quantity_Pressure_Surface:numpy array of floats
    Extracted quantity corresponding to Point_ID_Pressure_Surface


"""
################## 1) Extract Slice at X position
   ############################

Slice_X_Proxy = Slice(Input=Surface_reader)

Slice_X_Proxy.SliceType = 'Plane'
Slice_X_Proxy.SliceOffsetValues = [0.0]
Slice_X_Proxy.SliceType.Origin = [X_Slice_Position, 0.0, 0.0]
Slice_X_Proxy.SliceType.Normal = [1.0, 0.0, 0.0]
Slice_X_Proxy.UpdatePipeline()

############## 2) Extract Slice at Y position, obtaining 2 Values
   ##########

Slice_Y_Proxy = Slice(Input=Slice_X_Proxy)

Slice_Y_Proxy.SliceType = 'Plane'
Slice_Y_Proxy.SliceOffsetValues = [0.0]
Slice_Y_Proxy.SliceType.Origin = [0.0, Y_Slice_Position,0.0]
Slice_Y_Proxy.SliceType.Normal = [0.0, 1.0, 0.0]
Slice_Y_Proxy.UpdatePipeline()
Slice_Y = servermanager.Fetch(Slice_Y_Proxy)

###### 3) Obtain Points on the upper and lower surface of the airfoil
   #########

Sliced_Points = vtk_to_numpy(Slice_Y.GetPoints().GetData())
Row_Index_Suction_Point = numpy.argmax(Sliced_Points[:,2])
Row_Index_Pressure_Point = numpy.argmin(Sliced_Points[:,2])

########## 4) Obtain Surface Quantity values  ######

Point_On_Suction_Surface_Coordinates = Sliced_Points[
    Row_Index_Suction_Point]
Point_On_Pressure_Surface_Coordinates = Sliced_Points[
    Row_Index_Pressure_Point]

Point_ID_Suction_Surface = Slice_Y.FindPoint(
    Point_On_Suction_Surface_Coordinates)
Point_ID_Pressure_Surface = Slice_Y.FindPoint(
    Point_On_Pressure_Surface_Coordinates)
```

```
    Quantity_Suction_Surface = vtk_to_numpy(Slice_Y.GetPointData().
                                        GetArray(Quantity_to_extract))[
                                            Point_ID_Suction_Surface]
    Quantity_Pressure_Surface = vtk_to_numpy(Slice_Y.GetPointData().
                                        GetArray(Quantity_to_extract))[
                                            Point_ID_Pressure_Surface]


    return [Quantity_Suction_Surface,Quantity_Pressure_Surface]

######################## MAIN PROGRAM START
    ###################################


############################## File Paths
    ########################################

# Get Current Working Directory
cwd = getcwd()

# Appends trailing slash platform indipendent
path_vtk_solution = path.join(cwd, '')

# Get Input from user if consider a VG simulation
IsVGSimulation = raw_input('Is this a 3D VG simulation? (yes/no): ')

VG = False
if IsVGSimulation == "yes":

    path_VG_CGNS = path.join(cwd, "VG_GridPoints.cgns")

    # Imports VG CGNS Mesh
    MeshGrid = File(path_VG_CGNS, 'r')

    # Merges and Reshapes MeshGrid
    Points_Coordinates = merge_reshape_coordinates(MeshGrid)

    VG = True

# Create Path where to save *.csv files extracted from the solution
ExtractedNormalLinesSolutionPath = path.join(cwd, 'DataExtracted')

# Creates directory and handles errors
try:
    mkdir(ExtractedNormalLinesSolutionPath)
except OSError as e:
    if e.errno != errno.EEXIST:
```

```
        raise

# Appends trailing slash platform indipendent
ExtractedNormalLinesSolutionPath = path.join(ExtractedNormalLinesSolutionPath,
                                             '_')

###################### Setup the vtkUnstructuredGridReader
    ###################


SU2_Surface_reader = LegacyVTKReader(FileNames=[path_vtk_solution+
                                                "surface_flow.vtk"])



################### Obtain variables names
    ###################################


Variables_Names = SU2_Surface_reader.PointData.keys()

# Print Variables to screen, to let the user choose
print('List of Variables available (NumberID: Variable)')
for counter, name in enumerate(Variables_Names):
    if fmod(counter,3) == 0 :
        print('\n')
    print("{counter:02d}: {name:30s}\t".format(counter=counter,name=name)),
print('\n')


OutputVariables = Variables_Names


######################### Compute Surface Normals
    ##############################


Surface_reader_servermanager = servermanager.Fetch(SU2_Surface_reader)

x_start,x_end=Surface_reader_servermanager.GetPoints().GetData().GetRange(0)
y_start, y_end=Surface_reader_servermanager.GetPoints().GetData().GetRange(1)


x_start = x_start + 0.0001
x_end = x_end - 0.0001

y_start = y_start + 0.0001
y_end = y_end - 0.0001

###################### Get x,y position for slicing
```

```
    ############################
################################ from user
    ####################################

# Variable to extract from Airfoil Surface
VariableToExtractFromAirfoilSurface = raw_input('Enter variable to extract'









VariableToExtractFromAirfoilSurface = VariableToExtractFromAirfoilSurface.
    split('"')
VariableToExtractFromAirfoilSurface = VariableToExtractFromAirfoilSurface[1]


# Consider linearly spaced points, or specific locations?
LinearlySpaced_Or_UserDefined = raw_input('Consider linearly spaced points '
                                          '(along x and y direction), '
                                          'or user defined specific locations?
                                              '
                                          '(lin: linearly spaced points, '
                                          'spec: specific locations): ')
LinearlySpaced_Or_UserDefined = LinearlySpaced_Or_UserDefined.split('"')[1]

LinearlySpaced = False
UserDefined = False
if LinearlySpaced_Or_UserDefined == "lin":
    LinearlySpaced = True
elif LinearlySpaced_Or_UserDefined == 'spec':
    UserDefined = True


if LinearlySpaced:

    # Number of X positions to consider
    Number_Of_X_positions = raw_input('Enter Number of X locations to consider
        '
                                      '(linearly spaced locations on the
                                          surface '
                                      'of the blade section will be considered
                                          , '
                                      'from Leading Edge to Trailing Edge): ')
```

```
    Number_Of_X_positions = int(Number_Of_X_positions)


    X_Slices_Positions = numpy.linspace(start=x_start,stop=x_end,
                                        num=Number_Of_X_positions).tolist()

    # Number of Y positions to consider
    Number_Of_Y_positions_raw_input = ('Enter␣Number␣of␣Y␣locations␣to␣
        consider␣'
                                       '(linearly␣spaced␣locations␣on␣the␣
                                           surface␣'
                                       'of␣the␣blade␣section␣will␣be␣considered
                                           ,␣'
                                       'from␣'+str(y_start)+'␣to␣'+str(y_end)+'
                                           ):␣')
    Number_Of_Y_positions = raw_input(Number_Of_Y_positions_raw_input)
    Number_Of_Y_positions = int(Number_Of_Y_positions)

    Y_Slices_Positions = numpy.linspace(start=y_start,stop=y_end,
                                        num=Number_Of_Y_positions).tolist()

elif UserDefined:

    X_Slices_Positions = raw_input('Enter␣Number␣of␣X␣locations␣to␣consider,␣'
                                   'separated␣by␣a␣comma␣'
                                   '(from␣Leading␣Edge␣to␣Trailing␣Edge):␣')
    X_Slices_Positions = list(X_Slices_Positions.split(','))
    X_Slices_Positions = [float(position) for position in X_Slices_Positions]


    Y_Slices_Positions_raw_input = ('Enter␣Number␣of␣Y␣locations␣to␣consider,␣
        '
                                   'separated␣by␣a␣comma␣'
                                   '(from␣'+str(y_start)+'␣to␣'+str(y_end)+'):
                                       ␣')
    Y_Slices_Positions = raw_input(Y_Slices_Positions_raw_input)
    Y_Slices_Positions = list(Y_Slices_Positions.split(','))
    Y_Slices_Positions = [float(position) for position in Y_Slices_Positions]



######################## Extract solution along PolyLines
   ########################

if VG:

        ######## Create box to avoid around VG
           ####################################
```

```
    # Round z coordinate columns, to avoid very small negative numbers in
    # the VG Mesh
    for index_row,row in enumerate(Points_Coordinates):
        for index_point,point in enumerate(row):
            Points_Coordinates[index_row][index_point] = ( point[0],point[1],
                                        abs( round( point[2], ndigits=14 ) ) )

    # Find maximum X value of the VG Mesh
    VG_Max_X = max([[point[0] for point in row]
                                for row in Points_Coordinates])
    VG_Max_X = max(VG_Max_X)

    # Find minimum X value of the VG Mesh
    VG_Min_X = min([[point[0] for point in row]
                                for row in Points_Coordinates])
    VG_Min_X = min(VG_Min_X)

    # Find maximum X value of the VG Mesh
    VG_Max_Y = max([[point[1] for point in row]
                                for row in Points_Coordinates])
    VG_Max_Y = max(VG_Max_Y)

    # Find minimum X value of the VG Mesh
    VG_Min_Y = min([[point[1] for point in row]
                                for row in Points_Coordinates])
    VG_Min_Y = min(VG_Min_Y)

    X_Slices_Positions_ToAvoid = []
    Y_Slices_Positions_ToAvoid = []
    for y in Y_Slices_Positions:
        for x in X_Slices_Positions:
            if ( (x >= VG_Min_X) and (x <= VG_Max_X) and
                 (y >= VG_Min_Y) and (y <= VG_Max_Y) ):
                    Y_Slices_Positions_ToAvoid.append(y)
                    X_Slices_Positions_ToAvoid.append(x)

    Y_Slices_Positions_ToAvoid = numpy.unique(Y_Slices_Positions_ToAvoid)
    X_Slices_Positions_ToAvoid = numpy.unique(X_Slices_Positions_ToAvoid)


Quantity_Suction_Surface_list = []
Quantity_Pressure_Surface_list = []
for x_position in X_Slices_Positions:
    for y_position in Y_Slices_Positions:
        if VG:
            if ((x_position in X_Slices_Positions_ToAvoid) and
                (y_position in Y_Slices_Positions_ToAvoid)):
                    continue
```

```
        [Quantity_Suction_Surface,Quantity_Pressure_Surface] =
            ExtractSurfaceData(Surface_reader=SU2_Surface_reader,
                                                                    X_Slice_Position=
                                                                        x_position,
                                                                    Y_Slice_Position=
                                                                        y_position)

        Quantity_Suction_Surface_list.append((x_position,y_position,
            Quantity_Suction_Surface))
        Quantity_Pressure_Surface_list.append((x_position,y_position,
            Quantity_Pressure_Surface))


Quantity_Suction_Surface_array = numpy.array(Quantity_Suction_Surface_list,
                                             dtype=[("x","f8"),("y","f8"),("
                                                 Pressure_Coefficient","f8")])
Quantity_Pressure_Surface_array = numpy.array(Quantity_Pressure_Surface_list,
                                              dtype=[("x","f8"),("y","f8"),("
                                                  Pressure_Coefficient","f8")])

pandas.DataFrame(Quantity_Suction_Surface_array).to_csv(
    ExtractedNormalLinesSolutionPath + "PressureCoefficientData_SuctionSide.csv
    ", index=None)
pandas.DataFrame(Quantity_Pressure_Surface_array).to_csv(
    ExtractedNormalLinesSolutionPath + "PressureCoefficientData_PressureSide.
    csv", index=None)

################################ MAIN PROGRAM END
    ###################################
```

Appendix F

IBL Parameters Script

In this Appendix, an example of a *R* script to create the velocity profiles plot, using the solution slices extracted from 3D results, is reported.

```
# Clear plots
if(!is.null(dev.list())) dev.off()
# Clear console
cat("\014")
# Clean workspace
rm(list=ls())



##### Requires to install following packages with install.packages('
    namepackage'):
##### -'rstudioapi'
##### -'dplyr'
##### -'rlist'
##### -'ggplot2'
##### -'scales'
##### -'cowplot'
#####-  'stringr'

### This file has to be placed outside any folder containing *.csv files to
    read from
### *.csv files need to have the following name structure "Slice_x_int(xcoord)
    _dec(xcoord)_y_int(ycoord)_dec(ycoord)"
### or "Line_x_int(xcoord)_dec(xcoord)_y_int(ycoord)_dec(ycoord)"
### where xcoord and ycoord are the x and y locations of the slice *.csv file

library(dplyr)
library(rlist)
library(ggplot2)
library(cowplot)
library(scales)
library(stringr)
```

```
################################################ Start Library
    ########################################################


Read_All_Slices <- function(path) {

  ### This function is used to read data from .csv files containing slices
      data from SU2 solution.
  ### It is meant to be used with instructions like do.call( "rbind",lapply(
      CsvFilePaths,Read_All_Slices) )


  test <- read.csv(path, header = TRUE, sep=",")

  CSVFileName <- basename(path) # Get *.csv FileName for VG case

  # Get Slice Location from case FileName
  Slice_Locations <- strsplit(x=CSVFileName,split=".csv")
  Slice_Locations <- unlist(Slice_Locations)

  # Get Slice Coordinates from Slice_Locations
  Slice_Coordinates <- strsplit(x=Slice_Locations,split="_")
  Slice_Coordinates <- unlist(Slice_Coordinates)

  ##### Files start with "Slice" or "Line" and then the coordinates,
  ##### so skip always the first element of the vector Slice_Coordinates

  # Create Plot Title
  X_position <- c(Slice_Coordinates[2],"␣",Slice_Coordinates[3],"_",Slice_
      Coordinates[4])
  X_position <- paste(X_position,collapse = "")

  Y_position <- c(Slice_Coordinates[5],"␣",Slice_Coordinates[6],"_",Slice_
      Coordinates[7])
  Y_position <- paste(Y_position,collapse = "")

  test$SliceX <- rep(X_position,times=length(test$Points.0))
  test$SliceY <- rep(Y_position,times=length(test$Points.0))

  test
}

#############################################################################

CleanAndRound <- function(DataExtracted){

  ### In this function some data rounding and column renaming is done
```

```
  # Rename columns properly
  colnames(DataExtracted)[colnames(DataExtracted)=="Points.0"] <- "X"
  colnames(DataExtracted)[colnames(DataExtracted)=="Points.1"] <- "Y"
  colnames(DataExtracted)[colnames(DataExtracted)=="Points.2"] <- "Z"

  if ( "Conservative_2" %in% colnames(DataExtracted) ) {
    colnames(DataExtracted)[colnames(DataExtracted)=="Conservative_2"] <- "u"}
  if ( "Conservative_3" %in% colnames(DataExtracted) ) {
    colnames(DataExtracted)[colnames(DataExtracted)=="Conservative_3"] <- "v"}
  if ( "Conservative_4" %in% colnames(DataExtracted) ) {
    colnames(DataExtracted)[colnames(DataExtracted)=="Conservative_4"] <- "w"}

  if ( "X.Momentum" %in% colnames(DataExtracted) ) {
    colnames(DataExtracted)[colnames(DataExtracted)=="X.Momentum"] <- "u"}
  if ( "Y.Momentum" %in% colnames(DataExtracted) ) {
    colnames(DataExtracted)[colnames(DataExtracted)=="Y.Momentum"] <- "v"}
  if ( "Z.Momentum" %in% colnames(DataExtracted) ) {
    colnames(DataExtracted)[colnames(DataExtracted)=="Z.Momentum"] <- "w"}


  # Round Points Coordinates
  DataExtracted$X <- round(DataExtracted$X,8)
  DataExtracted$Y <- round(DataExtracted$Y,8)
  DataExtracted$Z <- round(DataExtracted$Z,8)

  return(DataExtracted)
}

##############################################################################


ComputeDistanceFromAirfoilSurface <- function(DataExtracted){

  ### This function computes Distance from the airfoil surface, along a line
      normal to it
  ### It uses the coordinates data already present in the slices output from
      SU2.
  ### These slices correspond already to a normal line


  DataExtracted <- DataExtracted %>%
    group_by(SliceX,SliceY) %>%
    arrange(SliceY,SliceX) %>%
    mutate( Distance = c(0,sqrt((X[2:n()] - X[1:(n()-1)])^2 + (Y[2:n()] - Y
        [1:(n()-1)])^2 + (Z[2:n()] - Z[1:(n()-1)])^2)) ) %>%
    mutate(Distance_tot = cumsum(Distance)) %>%
    ungroup()
```

```
  return(DataExtracted)

}


##############################################################################

ComparativePlotsVelocityProfiles_ShiftedValues <- function(
DataExtracted_Smooth,DataExtracted_VG,ExtractedGroup_Plot,SliceXGroups_Elem,
    offset,
x_axis_label_flag,y_axis_label_flag,plot_title_flag,plot_title_position_flag,
legend_position_flag,scale_color_manual_flag){


  ### This function creates a comparative plot of Smooth (No VG) and VG
      Velocity Profiles

  ####### Extract data for single Slice to consider
  ExtractedGroup_Smooth_ToPlot <- DataExtracted_Smooth %>% filter(SliceX==
      SliceXGroups_Elem)
  ExtractedGroup_Smooth_ToPlot <- ExtractedGroup_Smooth_ToPlot %>% select(
      Distance_tot,u)


  ExtractedGroup_VG_ToPlot <- DataExtracted_VG %>% filter(SliceX ==
      SliceXGroups_Elem)
  ExtractedGroup_VG_ToPlot <- ExtractedGroup_VG_ToPlot %>% select(Distance_tot
      ,u)


  if (offset == 0) {

    ######## Set up generic plot object Theme
    ExtractedGroup_Plot <- ExtractedGroup_Plot +
      theme_bw() +
      theme(legend.position='none') +
      theme(plot.title = element_blank())
  }


  ######## Create Plot lines and points
  ExtractedGroup_Plot <- ExtractedGroup_Plot +

    geom_line(data = ExtractedGroup_Smooth_ToPlot, aes(x = Distance_tot,
                      y = u + offset, colour = "Smooth")) +
```

```
  geom_line(data = ExtractedGroup_VG_ToPlot, aes(x = Distance_tot,
                                y = u + offset, colour = "VG")) +
      coord_flip()

#### Add extra features to the current plot

if (x_axis_label_flag) {

  ExtractedGroup_Plot <- ExtractedGroup_Plot + xlab("d [m]")

} else if (y_axis_label_flag) {

  ExtractedGroup_Plot <- ExtractedGroup_Plot + ylab(expression( 'u'/'U'[
      infinity] ))

} else if (plot_title_flag) {

  ExtractedGroup_Plot <- ExtractedGroup_Plot + ggtitle( paste("Velocity
      Profiles") )

} else if (plot_title_position_flag) {

  ExtractedGroup_Plot <- ExtractedGroup_Plot + theme(plot.title = element_
      text(hjust = 0.5))

} else if (legend_position_flag) {

  ExtractedGroup_Plot <- ExtractedGroup_Plot + theme(legend.position = "
      bottom")

} else if (scale_color_manual_flag) {

  ExtractedGroup_Plot <- ExtractedGroup_Plot + scale_color_manual(name = "
      Case", # or name = element_blank()
      labels = c("Smooth","VG"),values = c("red","blue"))

}
```

```
  return(ExtractedGroup_Plot)

}


#########################################################################

CreateVelocityProfilesEvolution_Plot <- function(ExtractedGroup_Plot_
    Collection){

  ### In this function the Velocity Profiles evolution is displayed, creating
      a unique plot
  ### from existing plot objects, that are relative to subsets of the airfoil
      chord



  ### Define colour for each plot lines, for all the plots contained in the
      collection of group plots
  ### ExtractedGroup_Plot_Collection

  for (index in 1:length(ExtractedGroup_Plot_Collection)) {

    ExtractedGroup_Plot_Collection[[index]] <- ExtractedGroup_Plot_Collection
        [[index]] +
      scale_color_manual(name = "Case", # or name = element_blank()
                         labels = c("Smooth",
                                    "VG"),
                         values = c("red",
                                    "blue")) +
      theme(legend.title=element_text(size=15),
            legend.text=element_text(size=15))

  }

  ### Create a unique plot from plot objects contained in ExtractedGroup_Plot
      _Collection

  VelocityProfilesEvolution_Plot <- plot_grid(plotlist = ExtractedGroup_Plot_
      Collection,
                                              nrow = 2,
                                              ncol = 3)

  # Add single legend
  legend_VelocityProfilesEvolution_Plot <- get_legend(ExtractedGroup_Plot_
      Collection[[1]] + theme(legend.position="bottom") )
```

```
  VelocityProfilesEvolution_Plot <- plot_grid(VelocityProfilesEvolution_Plot,
                                              legend_VelocityProfilesEvolution
                                                _Plot,
                                              ncol = 1,
                                              rel_heights = c(1, .1))

  # Add Plot Title
  title <- ggdraw() + draw_label("Velocity Profiles", fontface='plain', size
    =15)

  VelocityProfilesEvolution_Plot <- plot_grid(title, VelocityProfilesEvolution_
    Plot, ncol=1, rel_heights=c(0.05, 1))



  return(VelocityProfilesEvolution_Plot)

}



################################ End Library ################################


##############################################################################
########################## Main Program Start ###############################

# Get and Set Current directory where this R file is been run from
Current_Working_Directory <- dirname(rstudioapi::getSourceEditorContext()$path
  )
setwd(Current_Working_Directory)

# Create Path and Directory for saving Plots
Plots_SavePath <- file.path(Current_Working_Directory,"Extracted_Plots")
dir.create(Plots_SavePath)

# Get List of all *.csv files containing the solution, traversing all
    subdirectiories
csv_files_path <- list.files(path = Current_Working_Directory, pattern = ".csv
  ", recursive = TRUE)
csv_files_path <- paste("./",csv_files_path,sep="")

# Get Indexes of Smooth and VG solutions
Smooth_FilePath_Indexes <- grep("Smooth", csv_files_path, fixed = TRUE)
VG_xc02_h6mm_FilePath_Indexes <- grep("xc02_6mm", csv_files_path, fixed = TRUE
  )
VG_xc03_h6mm_FilePath_Indexes <- grep("xc03_6mm", csv_files_path, fixed = TRUE
  )
```

```
# Create separate lists containing FilePaths names for Smooth and VG cases
Smooth_FilePath <- csv_files_path[Smooth_FilePath_Indexes]
VG_xc02_h6mm_FilePath <- csv_files_path[VG_xc02_h6mm_FilePath_Indexes]
VG_xc03_h6mm_FilePath <- csv_files_path[VG_xc03_h6mm_FilePath_Indexes]

# Create Dataframe containing all data
DataExtracted_Smooth <- do.call( "rbind",lapply(Smooth_FilePath,Read_All_
    Slices) )
DataExtracted_VG_xc02_h6mm <- do.call( "rbind",lapply(VG_xc02_h6mm_FilePath,
    Read_All_Slices) )
DataExtracted_VG_xc03_h6mm <- do.call( "rbind",lapply(VG_xc03_h6mm_FilePath,
    Read_All_Slices) )


############### Rename Columns Name and round coordinates values #########

DataExtracted_Smooth <- CleanAndRound(DataExtracted_Smooth)
DataExtracted_VG_xc02_h6mm <- CleanAndRound(DataExtracted_VG_xc02_h6mm)
DataExtracted_VG_xc03_h6mm <- CleanAndRound(DataExtracted_VG_xc03_h6mm)

################## Compute length of line segments considered #############

DataExtracted_Smooth <- ComputeDistanceFromAirfoilSurface(DataExtracted_Smooth
    )
DataExtracted_VG_xc02_h6mm <- ComputeDistanceFromAirfoilSurface(DataExtracted_
    VG_xc02_h6mm)
DataExtracted_VG_xc03_h6mm <- ComputeDistanceFromAirfoilSurface(DataExtracted_
    VG_xc03_h6mm)


######################### Create Plots  ###############


SliceXGroups <- unique(DataExtracted_Smooth$SliceX)

Case_FileName <- "VG_xc03_h=6mm"
offset_VelocityProfiles <- 2


ExtractedGroup_Plot <- ggplot()
offset_VelocityProfiles_update <- 0.0
nr_comparative_plot_ShiftedValues <- 0
count_SlicesGroup <- 0
CollectionPlotsList_number <- 1
ExtractedGroup_Plot_Collection <- list()
for (SliceXGroups_VG_Elem in SliceXGroups){
```

```
ExtractedGroup_Plot <- ComparativePlotsVelocityProfiles_ShiftedValues(
    DataExtracted_Smooth,
                DataExtracted_VG_xc03_h6mm, ExtractedGroup_Plot, SliceXGroups_VG
                    _Elem, offset_VelocityProfiles_update,
        x_axis_label_flag = TRUE, y_axis_label_flag = FALSE, plot_title_flag =
            FALSE,
        plot_title_position_flag = FALSE, legend_position_flag = TRUE, scale_
            color_manual_flag = TRUE)

offset_VelocityProfiles_update <- offset_VelocityProfiles_update + offset_
    VelocityProfiles

if ( ( offset_VelocityProfiles_update %% (offset_VelocityProfiles*5) ) == 0)
     {

  # Subset corresponding 5 slices per each time, from vector containing all
      the slices
  SliceXGroups_Plotted <- SliceXGroups[(5*count_SlicesGroup + 1):(5*(count_
      SlicesGroup + 1))]

  SliceXGroups_Plotted <- gsub("_", "␣", SliceXGroups_Plotted)
  SliceXGroups_Plotted_Split <- strsplit(SliceXGroups_Plotted, "␣")

  SliceXGroups_Plotted_new <- c()
  for (index in 1:length(SliceXGroups_Plotted_Split)){
    Slice_position_string <- paste(c(SliceXGroups_Plotted_Split[[index]][2],
        ".",SliceXGroups_Plotted_Split[[index]][3]), collapse="")
    Slice_position_number <- round(as.numeric(Slice_position_string),2)
    Slice_position_string_new <- sprintf("%0.2f", Slice_position_number)
    SliceXGroups_Plotted_new_string <- paste(c(SliceXGroups_Plotted_Split[[
        index]][1],"␣",Slice_position_string_new), collapse="")
    SliceXGroups_Plotted_new <- c(SliceXGroups_Plotted_new, SliceXGroups_
        Plotted_new_string)
  }
  SliceXGroups_Plotted_new <- gsub("X", "x/c␣=", SliceXGroups_Plotted_new)

  ExtractedGroup_Plot <- ExtractedGroup_Plot + ylab(expression( 'u'/'U'[
      infinity] ))

  ExtractedGroup_Plot <- ExtractedGroup_Plot + scale_y_continuous(
              breaks = head(seq(0, offset_VelocityProfiles*5, by=offset_
                  VelocityProfiles), -1),
      labels = SliceXGroups_Plotted_new) # It's axis y because of the coord_
          flip() before
```

```
    # Update List containing all the plots created
    ExtractedGroup_Plot_Collection[[CollectionPlotsList_number]] <-
        ExtractedGroup_Plot

    # Save Comparative Plot with Shifted Values, in A4 format
    SaveFileName <- paste("ExtractedGroup_Plot_for_Vorticity_Magnitude_",Case_
        FileName,nr_comparative_plot_ShiftedValues,".pdf",sep="")
    ggsave(file=SaveFileName, plot = ExtractedGroup_Plot, path = Plots_
        SavePath, width = 297, height = 210, units = "mm")

    # Remove Plot Object that has been just saved in the .pdf file
    rm(ExtractedGroup_Plot)

    # Re-initialize plot object
    ExtractedGroup_Plot <- ggplot()

    # Reset Offset (in the function ComparativePlotsVelocityMagnitude_
        ShiftedValues a new plot will be created each time offset == 0.0)
    offset_VelocityProfiles_update <- 0.0

    # Update counter for Slices subset to extract
    count_SlicesGroup <- count_SlicesGroup + 1

    # Update number comparative plots created
    nr_comparative_plot_ShiftedValues <- nr_comparative_plot_ShiftedValues + 1

    # Update number of plot, to use when storing all the plots in a single
        List object
    CollectionPlotsList_number <- CollectionPlotsList_number + 1

  }

  }

# Update number comparative plots created for the last curves, if the number
    of the last curves is less than 5
nr_comparative_plot_ShiftedValues <- nr_comparative_plot_ShiftedValues + 1

# Save Comparative Plot with Shifted Values, in A3 format
SaveFileName <- paste("ExtractedGroup_Plot_for_Velocity_",Case_FileName,nr_
    comparative_plot_ShiftedValues,".pdf",sep="")
ggsave(file=SaveFileName, plot = ExtractedGroup_Plot, path = Plots_SavePath,
    width = 297, height = 210, units = "mm")



####### Create Grid Plot for the evolution of Velocity Profiles
```

```
######

VelocityProfilesEvolution_Plot <- CreateVelocityProfilesEvolution_Plot(
    ExtractedGroup_Plot_Collection)


# Save Evolution Plot for Velocity Magnitude, in A3 format
SaveFileName <- paste("Evolution Plot for Velocity ",Case_FileName,".pdf",sep=
    "")
ggsave(file=SaveFileName, plot = VelocityProfilesEvolution_Plot, path = Plots_
    SavePath, width = 297 , height = 420, units = "mm")




#################### End Program Start ########################
##############################################################
```